THE MECHANICS AND MOLECULAR REGULATION OF HEART VALVE MORPHOGENESIS

A Dissertation

Presented to the Faculty of the Graduate School

of Cornell University

in Partial Fulfillment of the Requirements for the Degree of

Doctor of Philosophy

by

Philip Reuben Buskohl

August 2012

THE MECHANICS AND MOLECULAR REGULATION OF HEART VALVE MORPHOGENESIS

Philip Reuben Buskohl, Ph.D.

Cornell University 2012

Congenital heart defects (CHD) affect over 1% of the American population and are the origin of substantial healthcare costs. A majority of these defects involve malformations of the valvuloseptal apparatus, which is the precursor to the valves of the heart. Due to the necessity of valves for proper heart function, most moderate to severe valve defects require surgical intervention. Corrective surgery is costly and can result in complications and/or restrictions on the patient's lifestyle. Current genetic evidence for CHD is inadequate to explain the variety and prevalence of these defects, suggesting that misguided molecular and mechanical signaling may be responsible. Unfortunately, the role of mechanical and molecular signaling in normal valve development is only beginning to be elucidated, making the detection of defective valves difficult. An understanding of these mechanical and molecular cues and their effect on valve mechanics in normal development is essential for effective treatment of CHDs.

In this dissertation, we focus on the capacity of mechanical and molecular signals to direct valve morphology and mechanical properties. We first validate two mechanical testing techniques to characterize the mechanical properties of avian valves through development. This revealed a monotonic increase in valve stiffness which was concomitant with a rapid transition from globular to planar geometry. We then investigated the capacity of transforming growth factor beta 3 (TGFβ3) and serotonin (5-HT) to stimulate biomechanical remodeling in

avian valves. TGFβ3 significantly increased valve stiffness through cell contraction, proliferation, and extracellular matrix synthesis. 5-HT modulated TGFβ3 remodeling in both *in vitro* and *in vivo* models. This demonstrated a plausible molecular mechanism for the stiffness increase observed during development.

To investigate the role of mechanical signaling, we developed a model of growth and remodeling (shape change) that is driven by mechanical stimuli. The consequences of particular assumptions about growth were illustrated with numerical examples. We then built a computational model of valve growth involving both the fluid and solid domains of the atrioventricular (AV) canal and valve. The distribution of the fluid loads on the valve was correlated with the natural morphology of the valve. The computational framework allowed the effects of pressure and shear tractions to be individually interpreted. These results provided a potential mechanical mechanism to explain the valve morphology observed during development.

The dissertation concludes with a chapter on teaching and outreach that stemmed from my involvement in the NSF GK-12 program. Conclusions and future directions are discussed.

BIOGRAPHICAL SKETCH

Philip Buskohl grew up in the rural, farming community of Grundy Center, IA. He received his K-12 instruction from Walnut Ridge Baptist Academy, from which he graduated in May 2002. Philip went on to study mechanical engineering, with minors in Bible and Math, at Cedarville University in Cedarville, OH. Philip graduated with highest honors in May 2006. While attending Cedarville, he interned in the Air Force Research Labs Material and Manufacturing Directorate at Wright-Patterson Air Force Base in Dayton, OH. Under the direction of Dr. Michael Caton, he researched the initiation and growth of short cracks in Ni super-alloys under cyclic thermal and mechanical loading. At Cedarville, he was advised by Prof. Timothy Dewhurst, who introduced Philip to continuum mechanics, the finite element method, and his alma mater, Cornell University.

In August 2006, Philip enrolled as a PhD candidate in the field of Theoretical and Applied Mechanics at Cornell University. He worked under the direction Prof. James T. Jenkins and Prof. Jonathan T. Butcher on his dissertation that was focused on understanding the feedback between mechanical and molecular signaling in atrioventricular valve development. He was awarded a National Science Foundation GK-12 STEM fellowship for two years of his doctoral training. Through his research, he has gained experience, and increased his interest, in mechanical testing of soft tissue, nonlinear finite element techniques, and constitutive modeling of material behavior.

To my father, Mark Buskohl, my mother, Nancy Buskohl,
and my loving wife, Rebekah Beth

ACKNOWLEDGEMENTS

The completion of this dissertation and my PhD degree would not have been possible without the support and encouragement of my family, friends, and my academic mentors.

I am indebted to Prof. Jenkins for the time and insight that he has shared with me during my study at Cornell. I thank him for his willingness to journey with me into the less familiar area of biomedical research. I am grateful for his patience, wisdom, and encouragement.

I thank Prof. Butcher for introducing me to heart valve morphogenesis and other interesting mechanics problems in developmental biology. I am indebted to him for providing the tools I needed to succeed in the lab, and for generously granting the financial support for me to attend various conferences and meetings. His patience and availability during the challenges of my research have been greatly appreciated.

I thank Prof. Vladimirsky for serving as my computational science and engineering minor advisor. I have enjoyed my interactions with Alex as his student, teaching assistant, and research mentee. I also appreciate his willingness and flexibility to attend my B-exam via video conference.

Many thanks go to my colleagues in the Butcher lab for their assistance with experiments, helpful discussions, and encouragement through various setbacks. I thank them for their patience as I learned the jargon of the biology field, and as I realized that not every lab presentation needs to be an hour long. I have appreciated the coffee breaks, the lab outings, the deep cleanings of the lab, and the jovial banter that we've shared. I have greatly enjoyed our time together.

I am highly indebted to my parents, Mark and Nancy Buskohl, for their steadfast support and encouragement of my graduate studies. The hard work

and perseverance of my father has been a model for me to follow during my PhD. I thank my mother for always being interested and excited to hear about my research. I thank both of them for their love and wisdom throughout my life.

I am deeply grateful for the love and dedication of my wife, Rebekah Beth Buskohl. She has brought great joy to my life and I have been richly blessed by her. She has been a beautiful respite from the frustrations of research and has encouraged my spirit. I thank her for persevering with me in this journey and look forward to overcoming future challenges together.

I appreciate the financial support provided by the following funding agencies:

- National Science Foundation GK-12 Fellowship DGE 0841291
- American Heart Association SDG 0830384N
- National Institutes of Health RO1 HL110328

TABLE OF CONTENTS

LIST OF TABLES

LIST OF FIGURES

CHAPTER 1

INTRODUCTION

Over 1% percent of Americans possess some form of congenital heart defect (CHD) [77]. The life-time economic cost of CHD-related illness is over $1.2 billion for all of CHD births each year [184]. Malformations involving the valvuloseptal apparatus are the predominant CHD that occur [155]. Severe defects can result in embryonic lethality, or require multiple highly invasive surgeries during the first few years of life. Small to moderate valve defects may remain undetected until adulthood, when other health issues such as high blood pressure exacerbate the inferior valve. Almost all corrective therapies for valves require surgical intervention, whether repair or replacement, which run the risk of complications, and can significantly alter a patient's lifestyle.

Genetic basis of CHD formation

The causes of valve defect formation are not well established. A few gene-specific heart valve defects have been identified, such as fibrillin 1 in Marfan's syndrome [43] and elastin in William's syndrome [106]. Other examples of genetically based CHDs are shown in Table 1.1. However, such genetic evidence does not adequately explain the number and variety of CHDs currently observed [96, 167]. This suggests that the issue is not a deficient genome, but instead a misregulation of gene expression and/or signalling during development, whether by molecular, biochemical, or mechanical cues. Unfortunately there are still several gaps in our understanding of normal valve development. A thorough understanding of mechanical and molecular regulation in **normal development** is essential for effectively identifying mechanisms of CHD formation.

Table 1.1: Common CHDs with Genetic Basis, compiled from [26]

Syndrome	Gene(s)	Description	Ref.
Marfan	fibrillin1	MV prolapse, bicuspid AoV	[43, 145]
Williams	elastin	AoV stenosis, MV defects	[54, 87]
Ehlers-Danlos	col5a1	AoV & MV defects	[22]
Stickler	col2a1, col1a1	MV dysfunction	[107]
22q11 deletion	-	outflow tract defects	[162]
Holt-Oram	TBX5	MV prolapse	[132]
Noonan	PTPN11	MV defects	[68]
Legend	MV - mitral valve	AoV - aortic valve	

Basics of Atrioventricular Valve Development

Atrioventricular valve formation is thought to be regulated by dynamic interactions between molecular and mechanical signaling. The primitive valves (cushions) initiate as gelatinous masses of hyaluronan and other glycoaminoglycans extending outward from the myocardial wall of the heart tube [65]. A layer of endothelial cells line the inner surface of the heart tube, with the outer wall consisting of cardiomyocytes [67]. The endocardial cells lining the cushion invade the underlying matrix and acquire a mesenchymal phenotype through a process called the endocardial to mesenchymal transformation (EMT) (see illustrated reviews [140, 163, 27]). As the cushion matures, these mesenchymal cells remodel the matrix directing a transition from hyaluronan to collagen based matrix, and a transition from globular to planar morphology [94, 88], (see Figure 1.1). The mechanical consequences of this biomechanical remodeling are currently unknown.

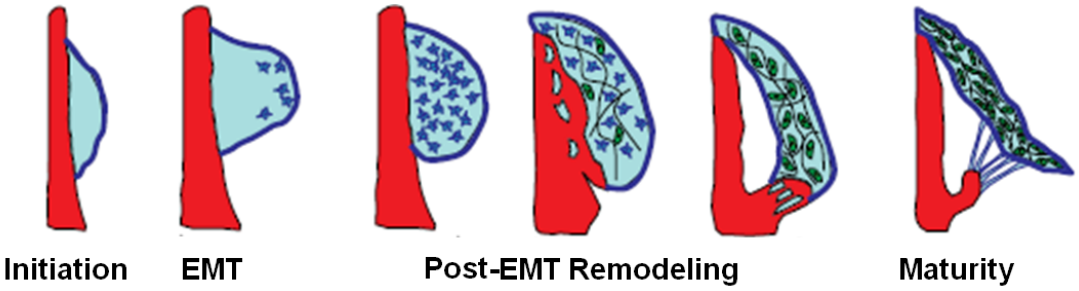

Figure 1.1: Schematic of AV valve development. Initiation: GAG rich, globular, cushion (light blue) forms as a protrusion from the myocardial wall (red). EMT: the endocardial cells lining the cushion invade and transform into mesenchymal cells. Post-EMT Remodeling: mesenchymal cell remodel the matrix, altering both composition and shape of the valve. Maturity: AV valve has planar form and consists of fibrous structural proteins. Image modified from [27]

The role of TGFβ in AV valve development

Significant advances have been made in identifying the key molecular signals needed for this initiation and maturation [27, 46, 140]. The transforming growth factor-beta (TGFβ) superfamily is critically important for a wide range of cellular processes [9, 116, 165], and is heavily involved in directing morphogenesis of AV cushions [143, 21, 29, 14, 11]. In the chick, TGFβ2 and TGFβ3 isoforms are necessary for EMT [144]. TGFβ2 induces initial cell-cell separation of valve endothelial cells, while TGFβ3 stimulates their invasion and subsequent mesenchymal phenotype shift [21, 29]. In mouse, the TGFβ2 isoform is essential for proper valve initiation [14], and is also required to achieve correct morphology during post-EMT stages [10]. As shown in Figure 1.2, the TGFβ2 KO mouse exhibits enlarged AV valves that are rich in glycoaminoglycans, which are less present in post-EMT wildtype valves.

Normally during post-EMT, the mesenchymal cells facilitate a transition in

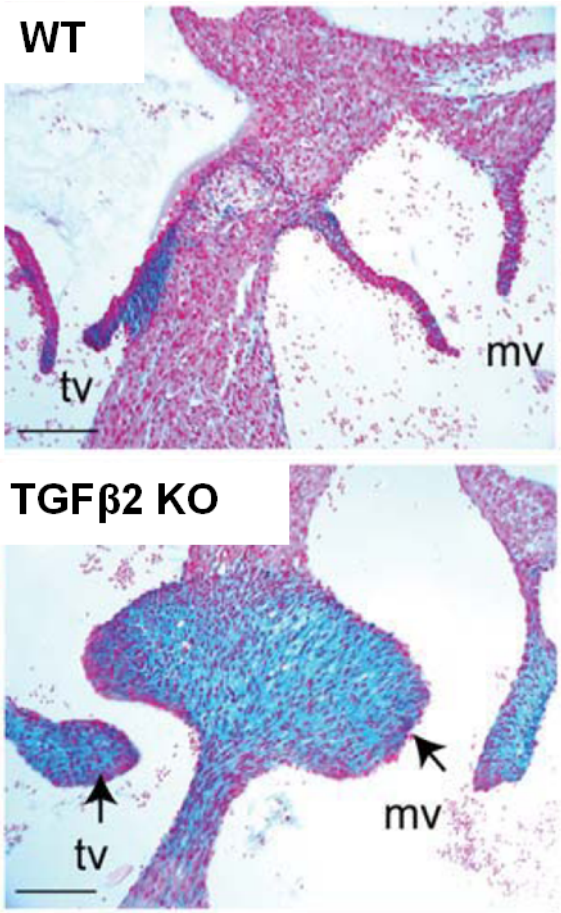

Figure 1.2: Altered molecular signals result in defective valve morphology. E18.5 WT and TGFβ2 KO AV valve sections stained with Alcian blue. Image modified from [10]

the cushion microstructure from glycosaminogylcans (GAGs) (hyaluron, versican) toward fibrous structural proteins (collagen I, V,VI, fibronectin, periostin) [94, 133, 28]. We hypothesize that this shift in extra-cellular matrix (ECM) content translates into increased valve stiffness, but this has yet to be experimentally verified. TGFβ3 expression is elevated in the AV cushions and canal during post-EMT remodeling stages in both chicken [31] and mice [29] (see Figure 1.3). Furthermore, TGFβ3 upregulates collagen I and periostin in post-EMT AV cushion explants [134], suggesting that TGFβ3 is a key modulator of cushion ECM

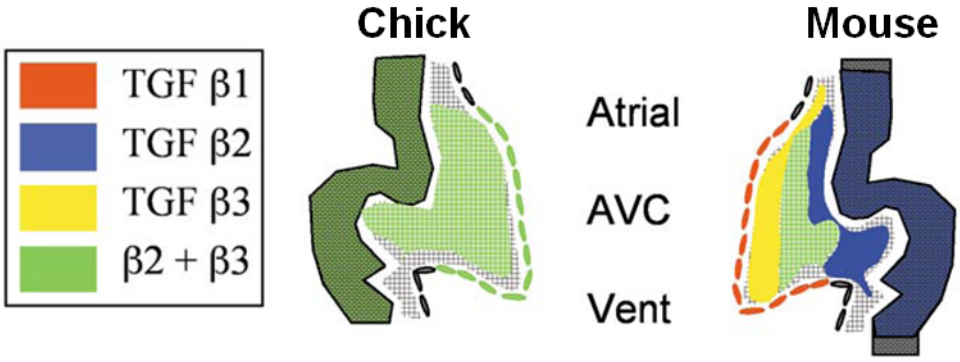

Figure 1.3: Spatial distribution of TGFβ1,2 and 3 ligands in chick and mouse AV valves during post-EMT remodeling. AVC - atrioventricular canal. Image modified from [29]

content, and consequently mechanical properties. An aim of this thesis is to determine the remodeling potential of TGFβ3 during post-EMT.

Potential interaction of serotonin and TGFβ in AV valves

Recent studies indicate that serotonin (5-HT) interacts with TGFβ signaling in adult heart valves [86, 44], and can also alter valve mechanical properties [47, 186]. 5-HT is a monoamine neurotransmitter that is derived from the essential amino acid tryptophan [156]. 5-HT has been shown to increase the stiffness of porcine aortic valves under cyclic stretch [12], or when endothelium is removed [47]. 5-HT can increase the synthesis of collagen in human and sheep valve interstitial cells (VICs) [86, 73]. Reports in adult VICs indicate that 5-HT can also upregulate TGFβ, resulting in cell differentiation and aberrant connective tissue accumulation [86, 44, 138]. This known interaction of 5-HT with TGFβ in adult valves motivates an investigation into whether a similar interaction exists during embryonic development.

Figure 1.4: 5-HT2b receptor is localized to the embryonic heart. 5-HT2b *in situ* stain of E8.0 mouse embyro. b - brain, h - heart. Image modified from [32]

The role of mechanical forces in AV valve development

The mechanical environment of the AV cushion is also critical for proper valve formation. Surgical manipulations of hemodynamic flows have resulted in defective cardiac morphology [78, 182]. The perturbed mechanical loads have included differences in local shear stress [79, 69], pressure [164], and myocardial activity [13]. For examples, Sedmera et al. [164] ligated the left atrium of chick embryos with sutures, which reduced the pressure drop across the AV canal. The reduced pressure resulted in enlarged leaflets in both the left and right AV valves at later developmental stages (Figure 1.5). These perturbations are in addition to the already significant increases in loading the valves experience during development. In the chick embryo, the heart rate nearly doubles from day 2 to day 6 of incubation, and the right ventricular systolic pressure triples in that time (see Table 1.2). The shear stresses on the AV valves due to blood flow have been approximated with fluid dynamics simulations [191, 124, 18]. The differential roles of pressure versus wall shear stresses in directing AV valve morpho-

genesis are unknown. By understanding their specific roles, we could better identify loading profiles that are defective, and/or determine which mechanosensors to target in order to block the effect of the defective mechanical loading. However, uncoupling the effects of pressure and shear tractions is difficult to do experimentally.

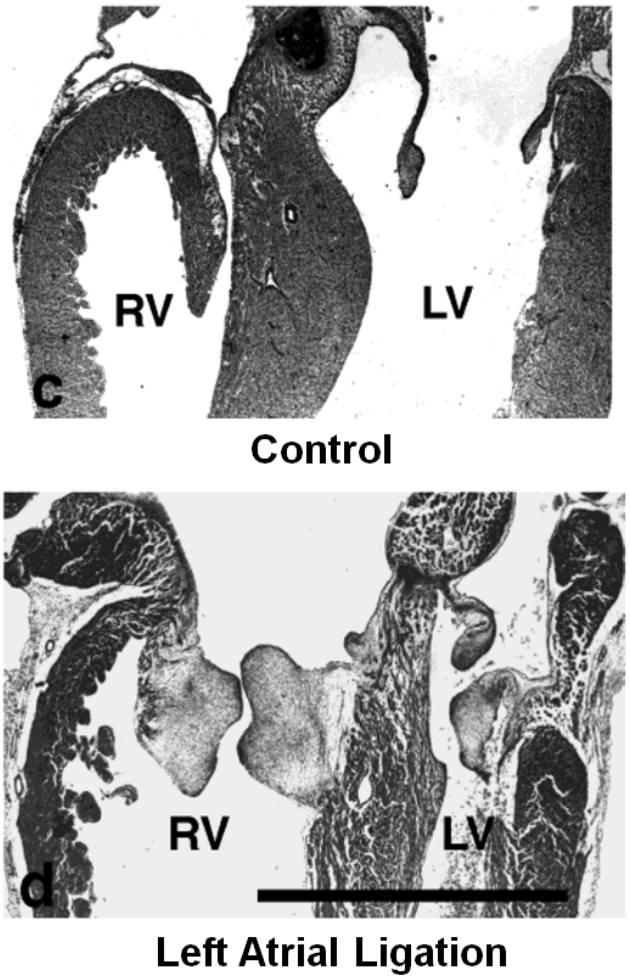

Figure 1.5: Altered mechanical loads can generate valve defects. Left atrial ligation results in enlarged left and right AV valves, as seen in these HH40 heart cross-sections. Scale bar 1 mm. Image modified from [164]

We propose studying the mechanical regulation of AV valve formation by

Table 1.2: Heart rate and right ventricular blood pressure in avian embryonic heart, taken from [111]

Stage (HH)	bpm	Systolic (mmHg)	Diastolic (mmHg)
16	110	1.15	0.25
18	147.5	1.31	0.33
21	145	1.61	0.34
24	155	1.96	0.4
27	155	2.35	0.56
29	194	3.45	0.82

Note: bpm - beats per minute; Refs: [80, 81, 141]

using a computational model of growth and shape change. Numerical models have provided insights into the fluid dynamics of the embryonic heart, such as the transition of peristaltic to pulsatile flow [178] and the distribution of normal and shear forces in AV canal [18, 124]. Previous growth models have qualitatively captured the morphology of several developmental phenomenona such as invagination [127], gastrulation [173, 174], cardiac looping [149], and ventricle growth [108]. However, no computational growth model has yet been employed to study the morphogenesis of the AV valves. In this work, we develop a theory of growth and shape change stimulated by mechanical loading, and then evaluate what insights it gives into how fluid loads may alter valve morphology.

This thesis contributes to these current knowledge gaps through experimental, analytical and computational approaches. Each chapter is motivated with an introduction section, and placed in the context of current work with a discussion section. The content and inter-relatedness of each chapter are outlined

below.

In chapter 2, pipette aspiration and deformable posts are presented as two viable micro-mechanical testing techniques for soft tissue. A new method of interpreting the experimental data from the pipette aspiration technique was validated through finite element (FE) analysis. Using these methods, we quantified the mechanical properties of avian AV valves during valvulogenesis. This data showed that valve stiffness increases monotonically during development, with leaflet-specific values. We also quantified the transition in AV valve geometry during this period, observing a distinct shift from globular to planar shape. The valve also transitioned from a relatively isotropic material toward an anisotropic material by the end of valvulogenesis. Evidence of this was seen through the substantially different magnitudes of stiffness between the in-plane and transverse plane. This chapter highlighted the rapid growth and remodeling of the embryonic valve, and provides mechanical data about this period of development that was previously unknown.

In chapter 3, we investigated a potential molecular mechanism of stiffness generation in valve development which was motivated by the mechanical data of the preceding chapter. We focused on the role of transforming growth factor beta 3 (TGFβ3) and serotonin (5-HT) signaling cascades in modulating post-EMT AV valve mechanics. Using the pipette aspiration method, we show that TGFβ3 increases AV valve stiffness over 2-fold after 24 hours of treatment. 5-HT treatment alone did not alter valve stiffness in this time frame, but did exacerbate the stiffening effect of TGFβ3 when co-treated with TGFβ. The stiffness increase was generated through increased cell contraction, elevated proliferation, and ECM synthesis. Through selective inhibition of TGFβ and 5-HT recep-

tors, we determined that the interaction between these two pathways was dependant on the 5-HT2b receptor and on canonical TGFβ signaling through the Alk5 receptor. The interaction between these pathways was further confirmed *in ovo* through systemic 5-HT treatment. This study provided direct evidence of a specific mechanism of molecular regulation of AV valve mechanical properties. Although several other genes are undoubtedly involved in post-EMT biomechanical remodeling, this study contributes to the current understanding of mechano-molecular interactions.

Having explored a molecular stimulus, we then turned our focus toward understanding the role of mechanical forces in AV valvulogenesis. In chapter 4, we developed a theoretical model of tissue growth (volume change) and shape change based primarily on mechanical stimuli. We evaluated the conservation of mass, momentum, and energy in the context of the growing body. We implemented a multiplicative split of the deformation gradient into an elastic and inelastic deformation. Then using the entropy inequality, we derived an evolution equation for the growth and remodeling deformation. Through this analysis, we encountered many open questions remaining in the growth mechanics field [5]. For instance, what is the nature of the homeostatic reference state? Is it stress based or strain based, or neither? Does new tissue enter with mechanical energy? When can growth be defined as a displacement field? Although not all were conclusively answered, these questions and others are discussed in chapter 3. This analysis contributes to the ongoing effort to connect the powerful tools of continuum mechanics with the intricate complexities of biological systems.

In chapter 5, we employed the growth law of the preceding chapter to simu-

late the role of hemodynamic loading in AV valvulogenesis. Using a previously published AV canal geometry [18] and hemodynamic parameters [191], we evaluated the relative effects of pressure, shear, and the homeostatic state on valve morphology. The model showed that the fluid forces were capable of directing the initial globular valve toward an elongated and condensed shape. Interestingly, as the valve evolved the distribution of fluid forces on the valve surface became increasingly more favorable for valve elongation. We also identified regions of residual stress due to growth, and evaluated how these stresses affected the overall evolution of the valve. The simulations were all implemented in the ANSYS, a commercial FE package, through a custom material subroutine. This growth model provides a useful theoretical and computational framework upon which to incorporate more biological details and to analyze other clinically relevant loading situations.

In chapter 6, I discuss my experience in the NSF GK-12 STEM teaching fellowship program which was facilitated by the Cornell BME department. Through this program, I assisted with science activities at a regional high school and discussed current research trends with the students. I developed two teaching curriculums on embryonic development using the shell-less chick culture technique (*ex ovo*) used in my lab. I treated embryos with elevated levels of retinoic acid which is a metabolite of vitamin A. The development of the embryo and the surrounding vasculature was stunted. The students compared this treatment to control embryos through image analysis. The teaching concepts of the lesson included, 1) how environmental factors, even good ones like vitamin A, need to be regulated, 2) that the embryo is highly sensitive to perturbations in the mechanical and molecular environment, 3) that local treatment can have a global consequence because of the vasculature system, and 4) that

animal research is importanct for gaining a mechanistic understanding of how living systems operate. This was a particularly meaningful experience because while the practical applications of my research are several years away, the attitude and excitement of these students toward science was immediately affected by my work.

The thesis is concluded with a summary of the major contributions of this work, and possible future research directions are discussed.

CHAPTER 2

MECHANICAL TESTING TECHNIQUES FOR SOFT TISSUES

Tissue assembly in the developing embryo is a rapid and complex process. While much research has focused on genetic regulatory machinery, understanding tissue level changes such as biomechanical remodeling remains a challenging experimental enigma. In the particular case of embryonic atrioventricular valves, micro-scale, amorphous cushions rapidly remodel into fibrous leaflets while simultaneously interacting with a demanding mechanical environment. In this study we employ two microscale mechanical measurement systems in conjunction with finite element analysis to quantify valve stiffening during valvulogenesis. The pipette aspiration technique is compared to a uniaxial load deformation, and the analytic expression for a uniaxially loaded bar is used to estimate the nonlinear material parameters of the experimental data. Effective modulus and strain energy density are analyzed as potential metrics for comparing mechanical stiffness. Avian atrioventricular valves from globular Hamburger-Hamilton stages HH25-HH34 were tested via the pipette methods, while the planar HH36 leaflets were tested using the deformable post technique. Strain energy density between HH25 and HH34 septal leaflets increased 4.6 $\pm$ 1.8 fold ($\pm$ SD). The strain energy density of the HH36 septal leaflet was four orders of magnitude greater than the HH34 pipette result. Our results establish morphological thresholds for employing the micropipette aspiration and deformable post techniques for measuring uniaxial mechanical properties of embryonic tissues. Quantitative biomechanical analysis is an important and underserved complement to molecular and genetic experimentation of embryonic morphogenesis.

2.1 Introduction

Morphogenetic events in the developing embryo are the result of dynamic interactions between cells and their environments. Many technologies exist to decipher the molecular and genetic regulation of cell behavior, but far less is known about the role of micro-environmental signaling. In the case of the heart, it is well known that virtually all mechanically relevant indices increase over development (e.g. blood pressure, wall shear stress, myocardial wall strain [37, 80, 191]). While it is appreciated that the resident tissue must somehow strengthen to withstand these increased loads, quantifying these material properties is extremely challenging. In the case of heart valve development, globular gelatinous masses, dubbed cushions, are rapidly remodeled into thin, fibrous leaflets, rich in matrix fiber striation [29, 140]. In common animal models such as chick and mouse, these tissues barely reach beyond 1 mm in length, which is much too small for traditional uniaxial testing. Conversely, in using micro-scale techniques such as atomic force microscopy [85] or optical trapping methods [98], the continuum approximation is lost as the devices are probing individual cells or extracellular matrix components. Previous experiments have shown that many embryonic tissues including valves are super-compliant, with elastic moduli less than 40 Pa [28, 183]. Unlike relatively stable postnatal tissues, the constant and significant shape and size change over time may selectively invalidate some testing methodologies.

Many techniques have been developed to assess the biomechanics of micro-scale tissues (generally a few millimeters or less in length). Pipette aspiration (PA) applies a local vacuum pressure and monitors resultant tissue displacement within the tip. PA has previously been used to measure material proper-

ties of early embryonic valve cushion primordia [28], as well as adult pig and mice valves [93, 195], and blood vessel walls [136]. The ability to relate experimental data in these studies to meaningful material properties has varied. Early work derived Young's modulus, E, of a linear elastic material in terms of the applied pressure, ΔP, and aspirated length, L, for an infinite half-space undergoing small strain [180]. While some recent studies utilize this model directly for tissues [93], others have modified the approach for such factors as viscoelasticity [120, 161], different material layers [3], or accounting for pipette-tissue adhesion [20]. A previous finite element (FE) analysis of the pipette method developed a similar small-strain expression for E for a finite tissue geometry [8]. Such soft tissues, however, predominantly demonstrate marked nonlinear material behavior with large deformations, and therefore need to be considered in a finite elasticity context. Recent inverse FE simulations enable nonlinear material property identification [196, 195], but with significant time and computational resource cost. To overcome these challenges, we will compare the pipette technique to a uniaxial load and use the analytical solution of a uniaxially loaded bar to fit our experimental data.

A second common technique is the use of deformable microfabricated posts that measure applied force via traditional cantilever deflection. Deformable posts (DP) are commonly fabricated in a subcellular array to measure local cell traction forces [102, 179]. We hypothesized that a similar system could function for planar embryonic soft tissues like heart valve leaflets. Furthermore, by analyzing the two techniques (PA and DP) with the same nonlinear material law, we should be able to relate the material parameters between each device. We here establish the appropriate morphological regimes where each device is viable for stiffness measurement, and demonstrate their utility for soft, short

length scale embryonic heart valve tissues. We further present strain energy as an alternative metric for representing stiffness for nonlinear materials.

2.2 Materials and Methods

2.2.1 AV Cushion Geometry Transition

The geometries of AV valve primordia were measured for HH25, HH29, HH34, and HH36 embryonic stages. Cushion length, L_c, was taken to be the dimension protruding perpendicular from the AV canal wall. Thickness, t_c, was the cushion dimension perpendicular to L_c along the anterior-posterior axis. Lastly cushion width, w_c, was defined as the maximum dimension of the cushion along the dorsal-ventral axis of the heart. Measurements were taken from magnified images of cushions immediately after isolation using Zeiss Discovery v20 stereo microscope and ImageJ.

2.2.2 Pipette Aspiration Experiments

PA Simulation

A FE model of the pipette technique was developed to: 1) characterize the effects of tissue geometry on the experimental measurements of applied pressure and aspiration length, and 2) construct an analytical model to interpret the experimental data. In all simulations the tissue was modeled as an incompressible, isotropic, hyperelastic disk with thickness D, and radius R (see Figure

2.1). A vacuum pressure, ΔP, was applied to the tissue surface in the pipette interior, and all exterior surfaces were assumed traction free. The pipette was modeled as an analytically rigid surface with filleted edges for smooth tissue contact. The pipette thickness was 25% of the pipette inner radius, r_p, comparable to the pipettes used in the experiments. Free-sliding contact was assumed between the tissue and pipette tip. An axisymmetric model using 2D, 8-node quadrilateral, second order elements with displacement-pressure (u-p) hybrid formulation were used for optimal handling of the incompressibility condition. FE simulations were performed in ANSYS v12.1 (ANSYS Inc., Canonsburg, PA) using approximately 3600 elements.

First, using a Neo-Hookean material law, the effect of tissue geometry was investigated by varying the ratio of tissue thickness and radius relative to the pipette radius, $\bar{D} = \frac{D}{r_p}$, and $\bar{R} = \frac{R}{r_p}$, respectively. The slopes of the ΔP versus λ curves, where $\lambda = \frac{L+r_p}{r_p}$ and L is the aspirated length, were evaluated to determine $\bar{D}$ and $\bar{R}$ regimes where PA yields consistent slope values. Second, to interpret the pipette data, FE simulation results were compared to the analytical expression for the axial stress of a uniaxially loaded, incompressible bar (Eq. 2.2.2). The Neo-Hookean material was implemented to evaluate the ΔP versus λ curve behavior relative to the Cauchy, 1st Piola Kirchhoff (PK) and 2nd PK stress measures for a uniaxial load, as it was unclear which stress measure the ΔP would best mimic. Third, given the exponential nature of the experimental data, an exponential material law [195],

$$W = \frac{C}{2}\left[exp\left(\alpha(I_B - 3)\right) - 1\right], \tag{2.2.1}$$

was also analyzed numerically via the USERHYPER subroutine (see Appendix C), where $I_B = tr(\boldsymbol{F}\boldsymbol{F}^T)$, $\boldsymbol{F}$ is the deformation gradient, and α, C are material parameters. Agreement between the axial Cauchy stress, σ_{yy} , and the ΔP

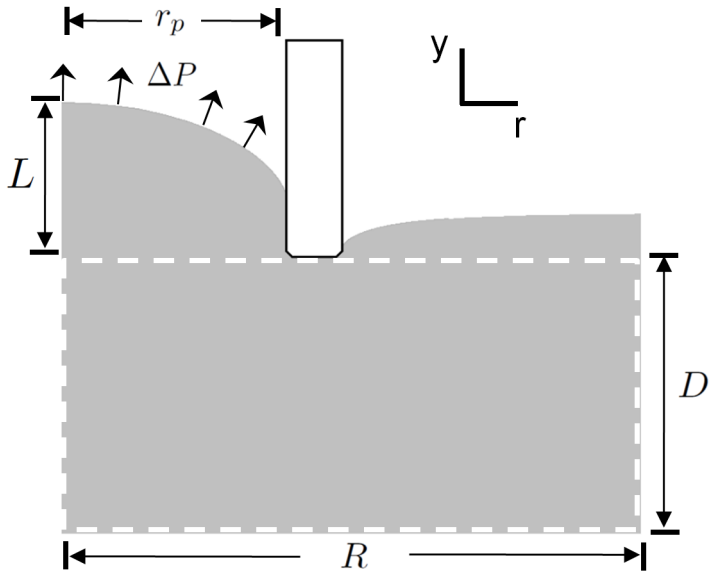

Figure 2.1: Axisymmetric schematic of a pipette-aspirated tissue disk. The reference tissue is denoted by the dashed box and has dimensions of radius, R, and thickness, D. The region inside of the pipette with radius, r_p, is loaded with aspiration pressure, ΔP, resulting in an aspirated length, L.

versus λ curve was quantified for the exponential material law.

PA Experimental Technique

Avian left atrioventricular (AV) valve primordia mechanical properties were quantified using PA. Hamburger-Hamilton (HH) stages 25-34 septal and mural leaflets were isolated and placed directly in phosphate-buffered saline (PBS, Gibco) prior to testing. A glass micropipette ($r_p \leq 35$ μm) was placed adjacent to the cushion surface collinear with the AV canal axis for HH25, while it

was placed on leaflet surface facing the atrium for HH29 and HH34. Vacuum pressure was incrementally applied via a 200 μL pipetter calibrated with a custom manometer. Previous strain history was mitigated by preconditioning with $\approx$ 20 cycles of low pressurization ($<$ 1 Pa). The preconditioning step ensured the tissue and pipette tip were in full contact. Incremental pressure loads were then applied, at which images were captured for each static load at 150x magnification using a Zeiss Discovery v20 stereo microscope (Spectra Services, Inc.). The aspirated length was measured using calibrated images in NIH ImageJ.

An experimental "stretch ratio", $\lambda = \frac{L+r_p}{r_p}$, was defined by normalizing the aspirated length to the pipette radius. The experiment stretch ratio is a measure of geometry change during aspiration, which is related, but not identical to the local stretch of the tissue (see Supplemental Fig. S3B). The ΔP versus λ curves were fitted using the axial Cauchy stress for a uniaxial load of an incompressible material with an assumed exponential material law (Eq. 2.2.1), specifically,

$$\sigma_{yy} = \alpha\, C\, exp\left[\alpha\left(\lambda^2 + \frac{2}{\lambda} - 3\right)\right]\left(\lambda^2 - \frac{1}{\lambda}\right) \tag{2.2.2}$$

The fitting parameters α and C were determined by minimizing the sum of the errors squared between Eq. 2.2.2 and the ΔP versus λ data curves. The C parameter was modified using a scale factor determined from FE simulation, $C_{mod} = \gamma(\alpha)\, C$. Effective modulus, $E_{Eff} = \alpha\, C_{mod}$, and strain energy density were evaluated as metrics for comparing mechanical testing data. Strain energy density (Pa or kPa) was calculated as the stored energy of the uniaxial deformation with axial stretch ratio ranging from λ= 1 to 2, namely,

$$W_{1-2} = \frac{C_{mod}}{2}\left[exp(2\alpha) - 1\right]. \tag{2.2.3}$$

Data is presented with representative stress response curves and strain energy density values presented as mean $\pm$ SD with n=8-11. Statistical comparisons

were performed using ANOVA with Tukey post-tests or Student's t-test, *p $<$ 0.05.

2.2.3 Deformable Post Experiments

DP Experimental Technique

To measure the mechanical properties of planar tissue, a custom device was fabricated which measures force based on beam deflection theory. Deformable cantilevers constructed from polydimethylsiloxane (PDMS, Sylgard 184) were used to determine the forces in the micro-milliNewton range (μN-mN). To create the DPs, negative molds were machined into a Teflon block. We generated three different post sizes, but each had the same height, h_p, to diameter, ϕ_p, ratio (ϕ_p/h_p = 3 mm/1 mm = 6 mm/2 mm = 9 mm/3 mm = 3). However, the 3mm/1mm cantilever was optimal, due to the size and generated force range of the HH36 valves. The PDMS was mixed at a ratio of 10:1 (base/curing agent), poured into mold geometry, cured at 65 °C for 12 hours, and then autoclaved to complete the curing process. Post bending stiffness and batch variability were measured using a previously described method [160]. Filter paper patches (CFP4, Whatman) were secured to the top of each post to provide a substrate for tissue attachment. The silicone posts were mounted on two horizontal sliding arms which were capable of positive and negative translation. The freshly isolated HH36 valves were delicately transferred to a glass slide using a transfer pipette, and the residual saline was wicked away. The glass slide was then inverted, placed over the DP, and leaflet edges brought in contact with filter paper. Once the valve was placed across the DPs in a planar fashion, two small drops

of cyanoacrylate (454 Prism, Loctite) applied with micropipette (100 μm diameter) secured the valve to the DP. The mechanical testing was then conducted in PBS at 20 °C. Deflection was determined as half the difference between the displacements of the base and the tip of the post, specifically,

$$\nu = \frac{x_b - x_t}{2}\,, \tag{2.2.4}$$

(Figure 2.12A). From the deflection and the bending stiffness calibration, the axial force in the plane of the tissue was approximated. The axial force was normalized to the initial reference area, approximated as the product of the unloaded thickness and width. An average stretch ratio for the deformable post tissue was defined as,

$$\lambda_p = \frac{x_t - x_0}{x_0}\,. \tag{2.2.5}$$

The 1st PK form of the axial stress for a uniaxial load, Eq. 2.2.2 , was used to fit the post data. The 1st PK stress versus λ_p curves are presented for the HH36 septal leaflet along with the average W_{1-2} value for n=9.

DP Simulation

A FE model of a post with fixed base and transverse applied force at tip was investigated. The post was modeled as an incompressible, Neo-Hookean material using 8-node 3D solid-structural elements with u-p formulation. Force-deflection profiles were calculated for differing post geometries by varying post height and diameter. Scaling of bending stiffness between differing post geometries was compared to Euler beam theory. The analysis was performed to determine maximum tissue contact area within the required force transduction range. Maximal contact area is beneficial for the attachment of tissue to the DPs.

2.3 Results

Pipette stiffness results sensitive to tissue geometry

The geometry of aspirated tissues, both thickness and radius, can influence pipette technique's stiffness measurements. FE simulations with a Neo-Hookean material demonstrate that the slope of ΔP versus λ decreases as tissue thickness, $\bar{D} = \frac{D}{r_p}$, goes to zero (Figure 2.2). The measured stiffness decreases rapidly for $\bar{D} < 2$, with a 50 % decrease between $\bar{D} = 2$ and $\bar{D} = 0.75$. The decrease in stiffness is a direct result of higher aspirated lengths, due to contributions from tissue bending. Evidence for bending is seen in the change of sign ($\pm$) of the radial stress ($\hat{\sigma}_{rr}$) along the axis of symmetry for tissue thickness $\bar{D} \leq 2$ (Figure 2.3). The pipette aspiration method assumes local stretching at the location of applied pressure, not bending of the global tissue. While the error in stiffness measurement between $\bar{D} = 2$ and $\bar{D} = 4$ may be small (2%), the assumption of no tissue bending is not valid until $\bar{D} \geq 4$. Similarly, measured stiffness decreases as tissue radius $\bar{R} = \frac{R}{r_p}$ approaches unity (Figure 2.4). Measured stiffness values converged for $\bar{R} \geq 2$, but errors were introduced for smaller $\bar{R}$. The maximum error calculated was 9.7% between $\bar{R} = 1.25$ and $\bar{R} = 2$.

PA approximates uniaxial deformation in tissue interior

FE simulations of the pipette method, using either Neo-Hookean or exponential material laws (Eq. 2.2.1), demonstrate a heterogeneous strain field, with maximum magnitudes located at the contact surface between the tissue and the pipette (Figure 2.5). Near the axis of symmetry the strain field is more uniform,

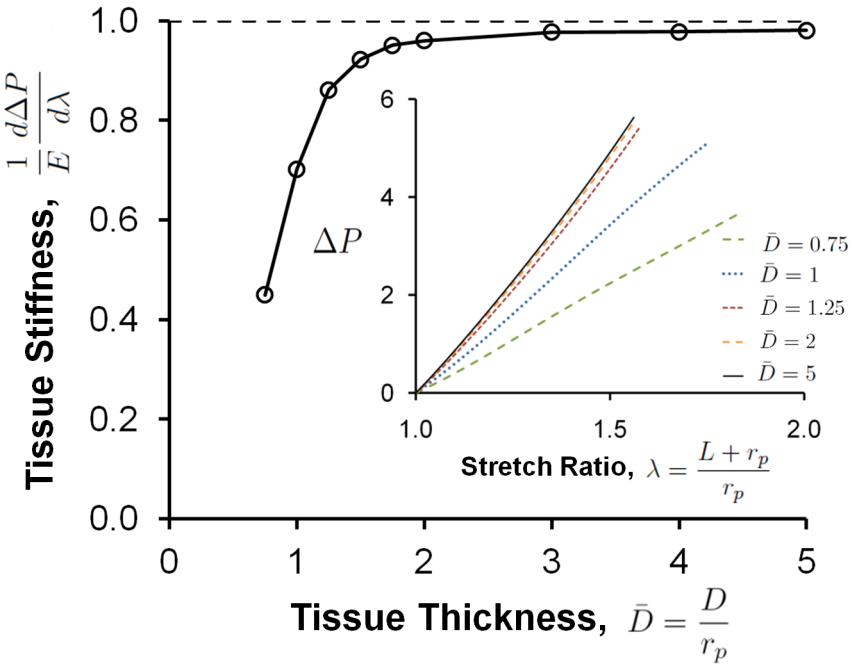

Figure 2.2: Plot of measured tissue stiffness normalized to Young's Modulus, E, of a Neo-Hookean material versus tissue thickness, $\bar{D}$. Inset: FE generated ΔP versus λ curves from which stiffness was calculated as the slope.

with the only significant gradient in the y direction. The radial and meridian stretch ratios, λ_r and λ_θ respectively, along the axis of symmetry were equal and transitioned from elongation to compression with depth into tissue (Figure 2.6A). Conversely, the stretch in the y direction, λ_y, was in compression at the pressurized tissue surface, but transitioned toward elongation in the tissue interior. This depicts a transition from equibiaxial extension (gray region Figure 2.6A) toward uniaxial with depth. The y location of this transition, y_{trans}, varies with applied load, but remains near the surface, never exceeding $\frac{r_p}{2}$ in any of the simulations and therefore lying within the initial "cap" of distended tissue (Figure 2.7A). The geometric "stretch ratio" $\lambda = \frac{L+r_p}{r_p}$ was implemented to

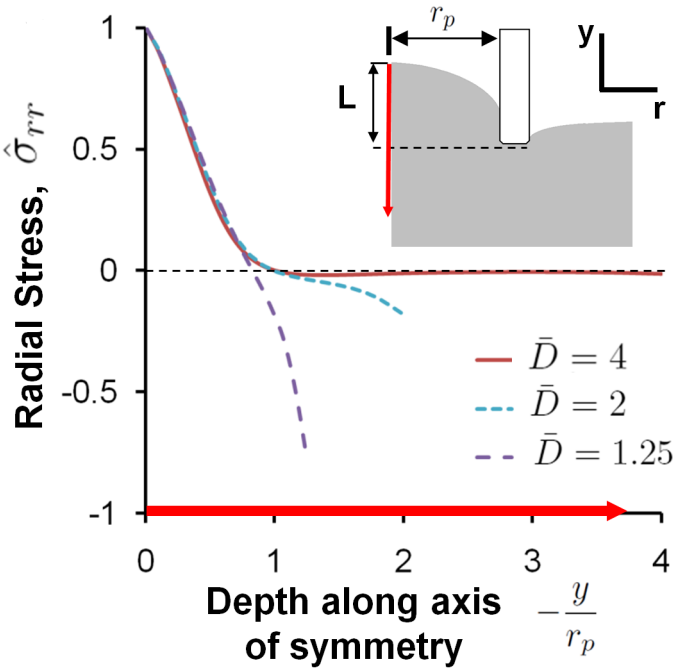

Figure 2.3: Plot of radial stress normalized to stress at applied load surface as a function of depth along the axis of the symmetry. For $\bar{D} < 4$, the radial component (likewise meridianal) experiences a compressive stress at the bottom edge, evidence of the tissue undergoing bending. Inset: Schematic of axi-symmetric pipette geometry

approximate the y-axis stretch which varied with depth along the axis of symmetry. The average of λ_y along the axis of symmetry was always greater than or equal to one, and was linearly related to λ (Figure 2.7B). We calculated the average of λ_y through the entire depth of the tissue ($\bar{D} = 4$). The stretch ratio values away from the pipette interface were near unity, which explains why the slope of avg(λ_y) in Figure 2.7B is less than one.

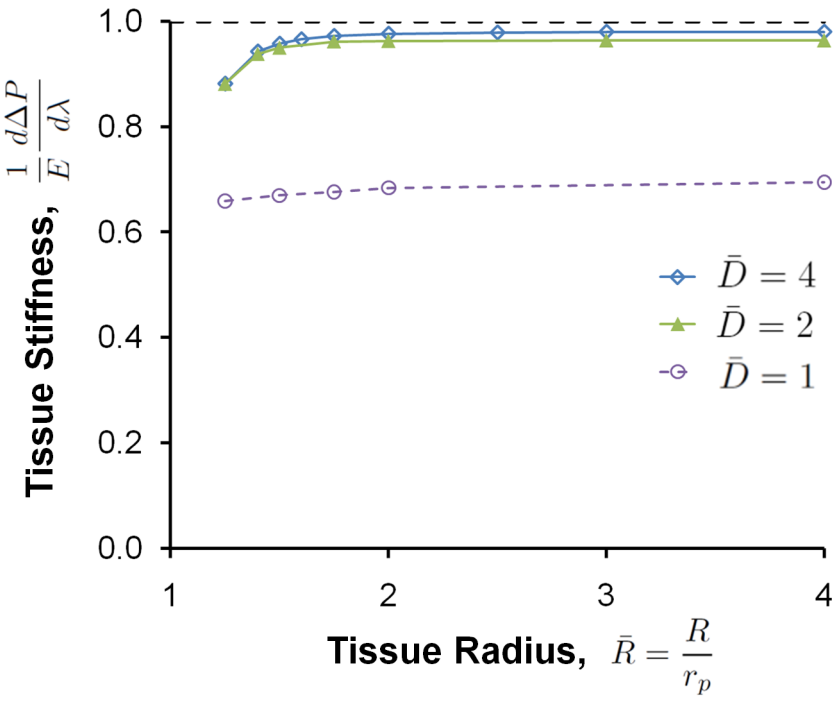

Figure 2.4: Pipette stiffness measurement consistent for $R > 2r_p$. Slope of ΔP versus λ profiles for varying $\bar{R}$ and $\bar{D}$. The error introduced by small tissue thickness dominates the error that results from small tissue radius. Yet a minimum tissue radius is required for the pipette technique to even work.

ΔP proportional to axial stress of uniaxial deformation

An analytic model was developed for the purpose of interpreting the experimental data by comparing the pipette pressure ΔP versus λ to the axial stress versus axial stretch of a uniaxial load (Eq. 2.2.2). FE-generated ΔP versus λ curves aligned closest to the axial Cauchy stress, σ_{yy}, for the Neo-Hookean material, and poorly with the 1st PK (Figure 2.6B). The slopes of the ΔP versus λ and the σ_{yy} versus λ curves differed by a factor,γ, which correlated with the stiffness offset from unity for $\bar{D} > 4$ in Figure 2.4A. Similarly, with the exponential material, the ΔP versus λ curve differed only by a scalar factor from

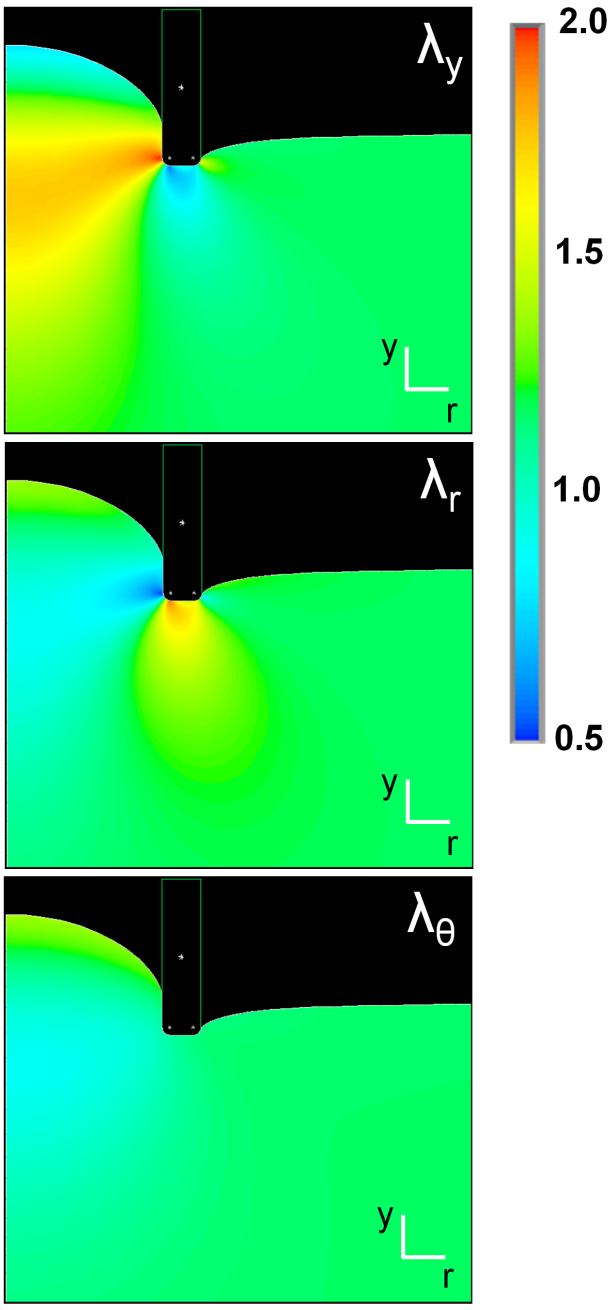

Figure 2.5: Axial component is the dominant stretch ratio in the tissue interior. Contour images of the elastic stretch ratio fields, presented as stretch ratios along the orthogonal reference axes. Note λ_r and λ_θ have identical strain profiles along the axis of symmetry. The axial stretch transitions from elongation at load surface to compression in the tissue interior. Data was generated from FE simulation run with exponential material law with C=10, α = 0.5 evaluated at $\Delta P = 21$, and tissue geometry $\bar{R} = 3$ and $\bar{D} = 4$.

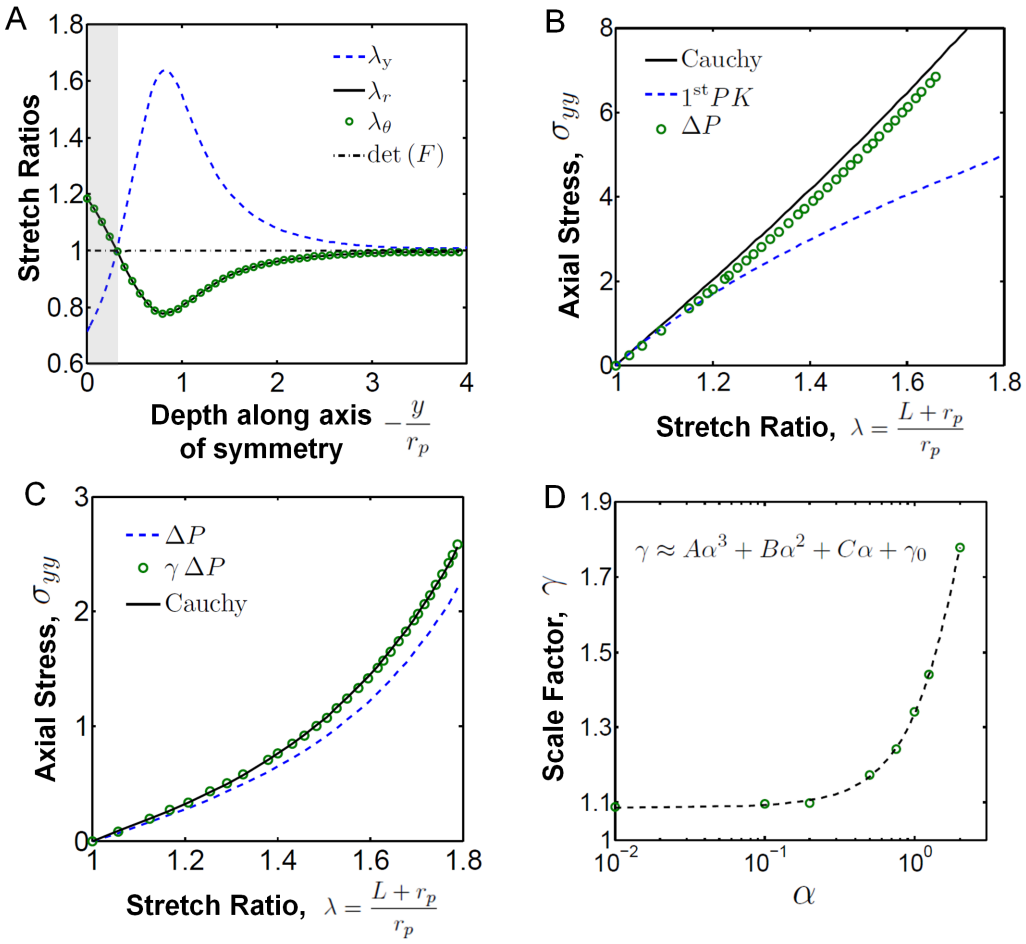

Figure 2.6: Pipette aspiration is approximately a uniaxial load. A) Along the axis of symmetry, the deformation transitions from equi-biaxial (gray region) extension toward uniaxial extension with depth into the tissue. B) The ΔP versus λ curve of an incompressible, Neo-Hookean material closely aligns with the Cauchy stress of a uniaxially loaded bar, not the 1st Piola Kirchhoff stress. C) The ΔP versus λ curve of an exponential material differs by a scale factor, γ, from the axial stress of a uniaxial load compared at the same stretch ratios. D) The scale factor, γ, is a function of α only, which is approximated with a cubic polynomial shown for $\alpha = [0, 2]$. A = -0.052, B = 0.252, C = 0.053, γ_0 = 1.09

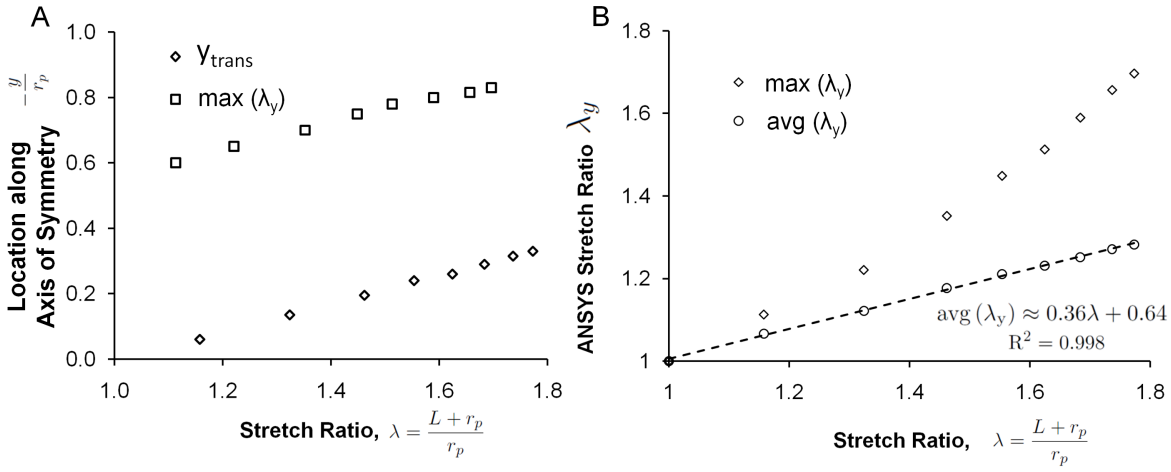

Figure 2.7: Location of stretch ratio features depend on applied load. A) The y location along the axis of symmetry where the deformation transitions from equibiaxial to uniaxial is a function of the observed stretch ratio, $\lambda = \frac{(L+r_p)}{r_p}$. Similarly, the location of maximum λ_y also depends on λ. B) The average of λ_y along the axis of symmetry is linearly related with λ, and is greater than unity for all λ. The observed stretch ratio λ overestimates the maximum of λ_y, and is nonlinearly related. Data was generated from FE simulations using an exponential material law with C=10, α = 0.5 evaluated from $\Delta P = [0, 21]$, and tissue geometry $\bar{R} = 3$ and $\bar{D} = 4$.

the assumed uniaxial model (Figure 2.6C). A parameter sweep of both α and C demonstrated that the scale factor γ was a function solely of α (parameter range $C \in [0.01 - 100]$ and $\alpha \in [0.01 - 5]$). The relationship between α and the scale factor was fitted to a cubic order polynomial: $\gamma = A\alpha^3 + B\alpha^2 + C\alpha + \gamma_0$, where $A = -0.052, B = 0.252, C = 0.053, \gamma_0 = 1.09$ (Figure 2.6D). For $\alpha > 2$, the fit quality between the simulation and analytic model was unsatisfactory, hence $\alpha = 2$ was considered an upper bound for relating PA to a uniaxial load test.

Strain energy density as an alternative to effective modulus

An effective modulus, $E_{Eff} = \alpha C$, has been suggested as a stiffness metric for two-parameter exponential models [28, 195]. For small α, ($\alpha < 0.2$), E_{Eff} approximates the slope of the ΔP versus λ curve, as the exponential term is near one. Unfortunately, $\alpha < 0.2$ is too strict a condition for sufficient curve fitting of experimental data, and E_{Eff} loses its physical significance outside this range. Furthermore, E_{Eff} is not a unique parameter, as an infinite combination of α and C values will equal the same E_{Eff} value. Strain energy density is therefore proposed as an alternative, physically significant, metric for comparing mechanical properties. Continuing with the uniaxial analog, the strain energy density from $\lambda = [1, 2]$ has a simple form for the pipette deformation: $W_{1-2} = \frac{C_{mod}}{2}[exp(2\alpha) - 1]$. This strain energy parameter is also not unique, but for a given set of α values it produces a narrower range of material response curves compared to fixed E_{Eff} over the same range (Figure 2.8). For $\alpha = [0.5, 1, 1.5, 2]$, the range of material response curves with fixed $E_{Eff} = 1$ is quite wide with approximately a 3-fold difference in strain energy density, while for fixed W_{1-2} the curve spread is tighter. The enhanced consistency of strain energy density at these higher α values gives it an advantage over E_{Eff}, even if not a direct measure of stiffness.

Globular to planar geometry transition concomitant with stiffness increase

The leaflet thickness decreased 3-fold from stage HH25 to HH36 (Figure 2.9), ending with a thickness of 110.4 9.7 μm (mean $\pm$ SD) at HH36. With the $\bar{D} \geq 4$ criteria and assuming continuum measurements require $r_p \geq 35\mu$m, the pipette method is best suited for leaflet thickness greater than 140 μm. Hence HH36 tis-

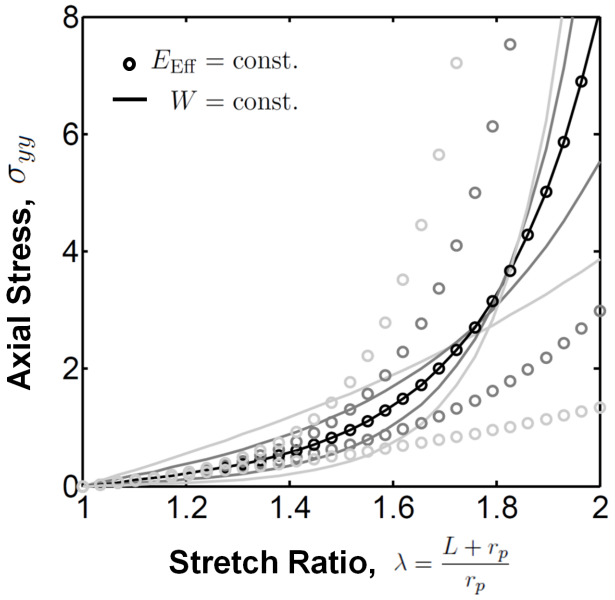

Figure 2.8: Strain energy density is a meaningful parameter for nonlinear material comparison. Plot of Cauchy axial stress for an exponential material with 1) fixed effective modulus, $E_{Eff} = \alpha C$ (circles), and 2) fixed strain energy density from W_{1-2} (solid lines) evaluated for $\alpha = [0.5, 1, 1.5, 2]$. Though both parameters are non-unique, the strain energy density generates a tighter range of material response curves for the same set of α values, while E_{Eff} has a larger spread of material response curves and no physical meaning for large α.

sue was tested using the deformable post test device. The significant decrease in leaflet thickness was concomitant with 2.46 $\pm$ 0.28 and 1.85 $\pm$ 0.18 (fold $\pm$ SD) increases in leaflet length, L_c and width, w_c, respectively. The thickness to length ratio, $\frac{t_c}{L_c}$, decreased 6-fold from HH25 to HH36 as the globular cushion transitions into a planar leaflet (Figure 2.9B). This shift of aspect ratio occurs over five days of incubation, underscoring the rapidity of this complex morphogenesis. The ΔP versus λ curves from the pipette data demonstrate a nonlinear, exponential behavior (Figure 2.10A), exhibiting an increased slope with development. The strain energy density increased 4.6 $\pm$ 1.8 (fold $\pm$ SD) between HH25 inferior and HH34 septal cushions (Figure 2.10B). Similarly, the HH29

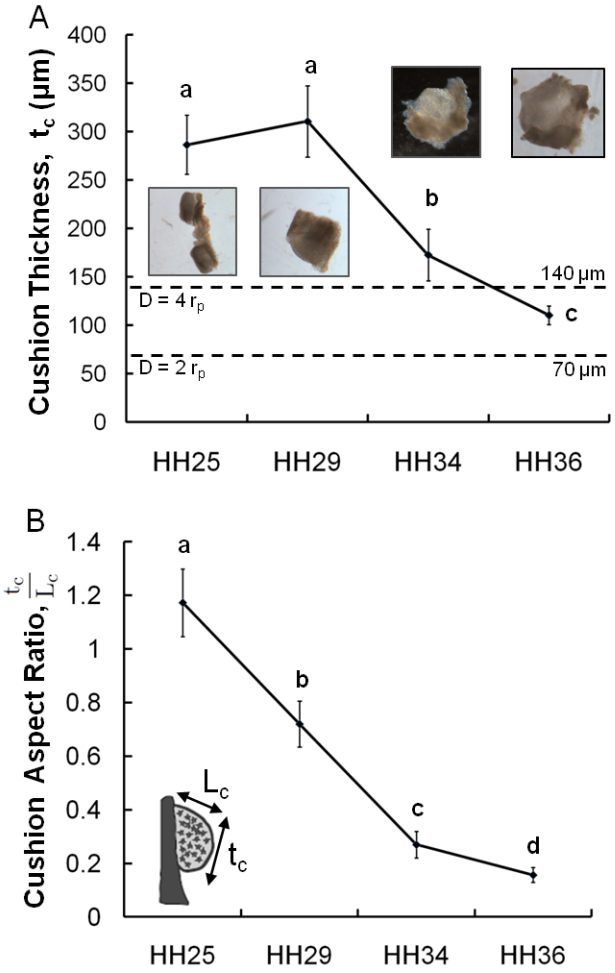

Figure 2.9: AV cushion geometry transition necessitates alternative mechanical testing devices. A) Cushion thickness, t_c, relative to pipette placement decreases during development. HH36 violates the $D = 4\,r_p$ testing criteria for 70 μm pipette diameter. B) Ratio of thickness to cushion apex to base length, L_c, shows a transition to a more planar configuration at the completion of valvulogenesis (HH36). n = 8-10 mean $\pm$ SD, all pairs of different letters are statistically significant, ANOVA, $p < 0.001$

septal cushion increased 2.5 $\pm$ 0.9 fold from the HH25 inferior cushions. The HH25 superior cushion was slightly stiffer than the inferior cushion with strain energy density of 0.44 $\pm$ 0.14 Pa versus 0.34 $\pm$ 0.08 Pa (mean $\pm$ SD). Mural leaflet strain energy increased from 0.69 $\pm$ 0.11 Pa to 0.96 $\pm$ 0.21 Pa between HH29 and HH34. The mural and septal leaflet strain energies differed statistically only at HH34. The HH36 septal material behavior well fit the 1st PK stress for a uniaxial load of the exponential material law used to model the pipette experiment (Figure 2.11). The average strain energy density of the HH36 cushion in the plane of the tissue was W_{1-2}= 59.2 $\pm$ 14.2 kPa. The in-plane strain energy density at HH36 was 4 orders of magnitude greater than the strain energy density in the transverse direction measured by PA.

DP force range is tunable according the Euler beam theory

The HH36 AV leaflets were tested with a DP uniaxial testing device (Figure 2.12B,C). FE simulations demonstrated that for ratios of post height to diameter, $\frac{h_p}{\phi_p} > 2$, the force versus deflection curve agreed with the Euler bending theory up to a deflection of $\nu = \frac{h_p}{4}$. For constant $\frac{h_p}{\phi_p}$, the bending stiffness scales linearly with cantilever diameter (Figure 2.12D). For diameters 1, 2, 3 mm, the bending stiffness was measured as 10.3 $\pm$ 1.5, 20.2 $\pm$ 1.9, and 29.9 $\pm$ 0.9 mN/mm, respectively (mean $\pm$ SD n=6). The small deviations in bending stiffness demonstrate the consistency of the fabrication technique and the low variability between silicone batches.

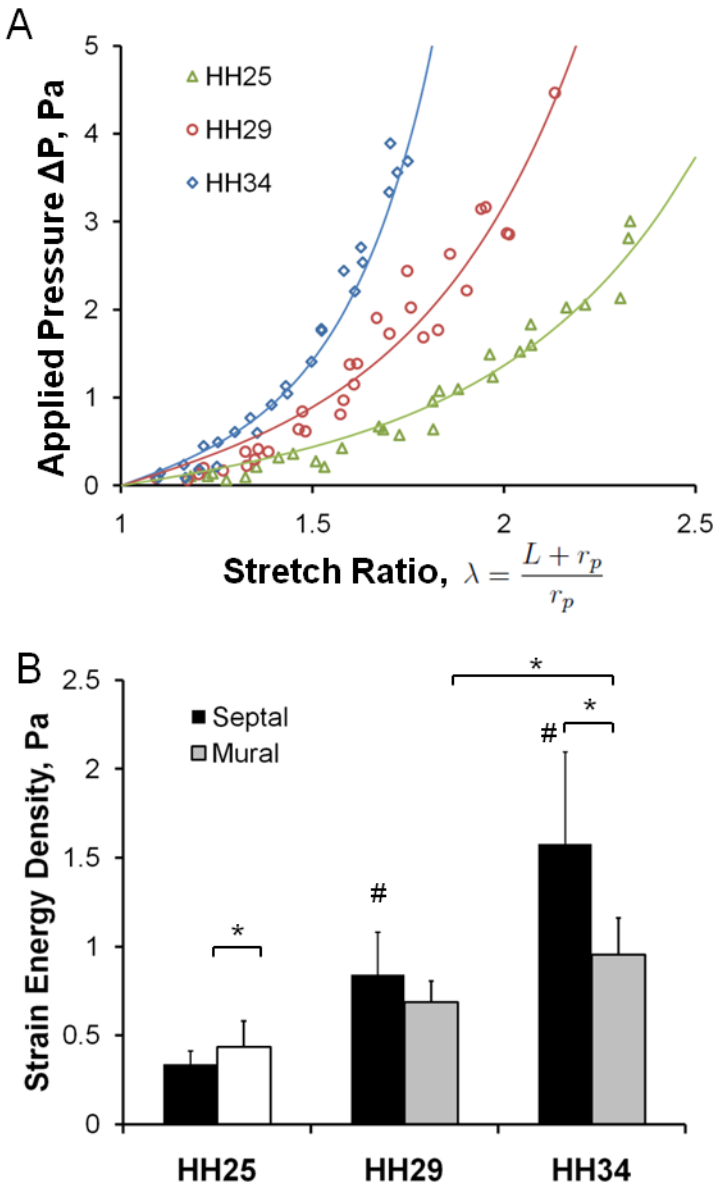

Figure 2.10: Monotonic increase in AV cushions stiffness during development. A) Representative septal leaflet aspiration data for stages HH25-HH34, (n=4) B) Calculated strain energy data for septal (black), mural (gray) cushions. HH25 inferior denoted as septal (black) and superior (white) bar. n = 8-11 mean $\pm$ SD 1-way ANOVA or t-test *$p<0.05$, # $p<0.001$ wrt. HH25 septal

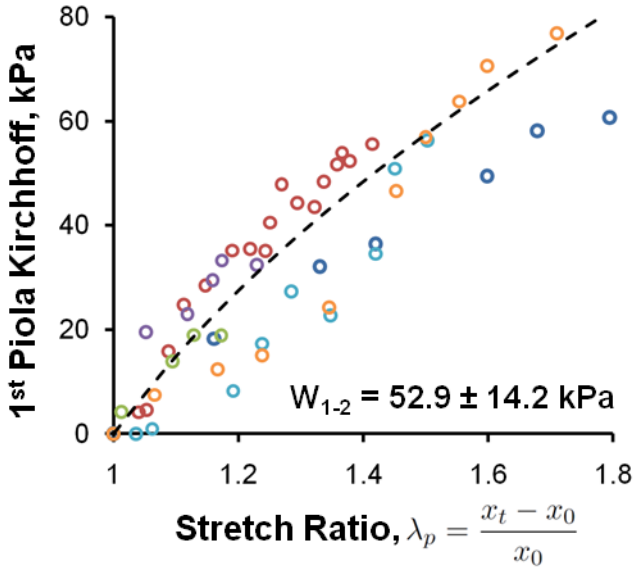

Figure 2.11: In-plane stiffness is much higher than trans-planar stiffness. Plot of applied force over initial cross-sectional area (≈1st PK) for HH36 septal leaflet measured using deformable posts. Average strain energy density denoted on figure as mean ± SD [kPa]. The in-plane tissue stiffness is 4 orders of magnitude greater than normal stiffness, suggesting material anisotropy.

2.4 Discussion

Increasing evidence in developmental biology suggests that mechanical cues from the microenvironment are instrumental in directing cardiogenesis [79, 164]. Furthermore, the pivotal role AV valves play in manipulating blood flow highlights the importance of understanding their mechanical behavior even in the embryonic period [182]. The results of this study demonstrate that PA and DP techniques are effective and complimentary for quantifying the ultra-compliant properties of complex-shaped, microscale, embryonic tissues.

We confirmed the previously shown result that tissue thickness less than two

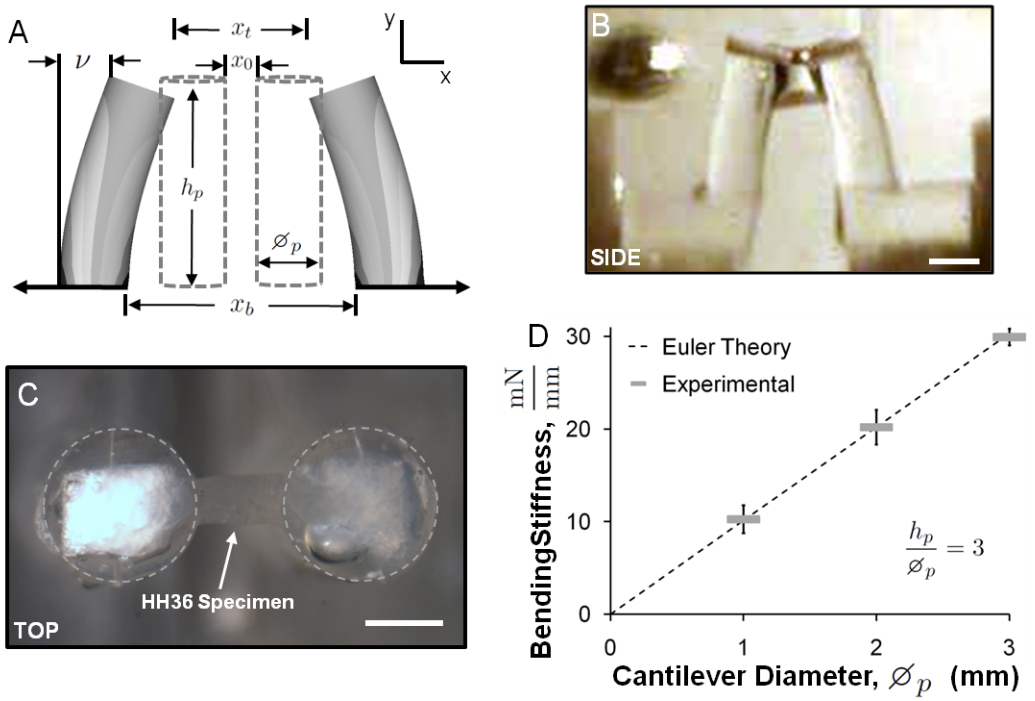

Figure 2.12: Deformable post testing device for planar tissues. A) Schematic of deformable cantilevers of height, h_p, and diameter, ϕ_p, in reference (dashed) and deformed configurations (solid). Cantilever deflection equals $\nu = (x_b - x_t)/2$, where x_t is the distance between the top of the posts, and x_b is the distance between the bases. B) Side view of DP device, scale bar = 1 mm C) Top view of device with attached HH36 septal leaflet, and tip of posts highlighted for reference (dashed circles). Scale bar = 500 μm. D) Euler beam theory (dashed line) predicts a linear increase in bending stiffness with diameter for a fixed h_p/ϕ_p . Measured bending stiffness for three diameters with h_p/ϕ_p =3 showed agreement with theory, n = 6 (3 silicone batches) mean $\pm$ SD

pipette radii influences measured aspiration length [8, 195]. However, as shown in Figure 2B, compressive stress occurs in the radial direction when $\bar{D} < 4$. The compressive stress denotes global bending which elevates the measured aspiration length because tissue is deflecting, as well as stretching into the pipette. Therefore a $\bar{D} \geq 4$ criterion ensures no error due to tissue thickness. This criterion was satisfied for HH25-HH34 AV cushions, but the more planar HH36 tis-

sue required a different technique. Furthermore, we showed that the radial dimension of the tested tissue must exceed $R = 2r_p$ for consistent results, though the errors introduced are not as large as those for the thickness criteria. This supports and extends recent work by Zhao et al. [195], who considered material nonlinearity through the implementation of an exponential hyperelastic material law in an inverse FE analysis. In the current approach, we related the ΔP versus λ data from the pipette experiment to the Cauchy stress curve of a uniaxial load through a numerically determined scale factor. This result simplified the determination of α and C to an error minimization of an analytic expression, potentially saving significant post-testing computation time employed in inverse approaches. It is important to note that our uniaxial approximation was valid for $\alpha < 2$. Although this range satisfactorily fit the AV cushion data, an FE inverse approach would be necessary for tissues with larger α. Examples of this would be tissues with a short toe region and a steep exponential region, where the non-linear parameter $\alpha >> 1$

PA has previously been compared to equibiaxial loading [53], which was in the context of red cell mechanics, where in-plane membrane surface tensions were assumed to dominate. For solid tissues with finite thickness, deformation along the pipette axis must be considered. Our FE simulations determined that the mode of deformation quickly transitioned from equi-biaxial at the pressurized surface to uniaxial within the tissue along the axis of symmetry (Figure 2.6A). The equibiaxial regime was very narrow ($y_{trans} < \frac{r_p}{2}$), and did not experience the high stretch ratios seen in λ_y in the tissue interior. This supports and extends the previous findings by Aoki et al, who suggested that the normal extension and shear components in the axial direction were the dominant contributions to the strain energy [8]. Taken together, these results support the

uniaxial model as an intuitive and computationally inexpensive way to identify the material parameters of nonlinear materials. Nonlinear material models lack direct, simple stiffness metrics for comparing test samples. Exponential, or Fung-like, materials are particularly difficult, as even linear fitting of sections of the stress-strain curve require tedious (and arbitrary) conditions to consistently apply fits (i.e., where does the toe region end, does a bi-linear fit effectively capture material nonlinearity, etc.). Others have compared stress values at a particular stretch [112], but this does not adequately represent the stress response curve nonlinearity. An effective modulus, E_{Eff}, defined as the product of the fit parameters, has previously been used as a stiffness measure for an exponential material model [28, 195]. Yet E_{Eff} relates directly to stiffness only for small α and is non-unique, prompting instead our analysis of strain energy densities under a given deformation between samples. Our results determined that strain energy was a much more consistent metric of tissue stiffness for a given material response. This parameter is similar to toughness measures used in fracture mechanics, except here it is integrated to a non-failure strain to approximate material behavior in physiological conditions.

Experiments using the PA method showed a stiffness increase over the course of embryonic AV cushion valvulogenesis. The over 4-fold stiffness increase between HH25 and HH34 septal cushions is indicative of substantial biomechanical remodeling of the microstructure. Similar rates of stiffness increases in earlier embryonic stage AV cushions have been reported [28]. AV valves of fetal chick and mice have demonstrated an increase in extra-cellular matrix (ECM) protein synthesis, particular in the collagen and elastin structural protein families [94, 140], as well as an increase in their structural organization [88, 83]. The mural leaflet stiffness lags the septal leaflet stiffness at HH34. This

is possibly because the mural leaflet orginates from a myocardial sheet in the AV canal wall after the superior and inferior cushions, which form the septal leaflet, have fused [40]. The in-plane stiffness of the HH36 valves was approximately four orders of magnitude larger than all the pipette data sets. This indicates that tissue anisotropy is significant by HH36, with in-plane stiffness the dominant player. FE simulations of a linear elastic, transversely isotropic material showed that the transverse stiffness contributed one-fifth of the measured stiffness compared to four-fifths from the stiffness in the direction of the pipette axis [136]. The effect of a nonlinear, highly aniosotropic tissue on measured tissue stiffness with the pipette method is unclear, but could potentially be teased out with a more complicated FE simulation.

As the valve transitions toward a planar geometry, the tissue thickness criteria and continuum testing assumption become mutually exclusive. The DP device effectively measured tissue stiffness in this planar regime. Tan, et al., first used this approach at the cellular scale, to measure sub-cellular traction forces [179]. By constructing an array of micro-fabricated DPs (length 11 μm), mechanical interactions between cells and their underlying substrates were possible to measure through the DP deflection. Furthermore, DP bending rigidity could be easily tuned by altering their geometry [56]. DPs have also been used to test the mechanical properties of microscale constructs of cells embedded within 3D matrices [103, 102]. During the remodeling of 3D collagen matrices, cellular contractile forces and changes in tissue morphology were quantified through the deflection of DPs of length 250 μm. By securing the HH36 embryonic tissue between DPs of length 3 mm, deflection of the silicone cantilevers provided a precise measurement of force within the mN range. Although this system was used for embryonic valves, it could be easily applied to other embryonic tissues.

In conclusion, PA and the DP techniques are two viable methods for evaluating the mechanical properties of ultra-soft, small-sized globular and planar tissues, respectively. AV cushions rapidly increase in stiffness during valvulogenesis, keeping pace with the demanding mechanical loading of its microenvironment. Selection of pipette dimension and point of application on tissue surface require consideration of an appropriate continuum approximation and specimen geometry, especially thickness. Strain energy density is a physically meaningful parameter for which to compare tissue stiffness, and can translate to any material model. Both techniques are applicable to soft, short-length scale tissues, and further integration of the devices' data sets will provide a richer understanding of other tissues with complex material properties.

CHAPTER 3

SEROTONIN POTENTIATES TRANSFORMING GROWTH FACTOR-BETA3 INDUCED BIOMECHANICAL REMODELING IN AVIAN EMBRYONIC ATRIOVENTRICULAR VALVES

Embryonic heart valve primordia (cushions) maintain unidirectional blood flow during development despite an increasingly demanding mechanical environment. Recent studies demonstrate that atrioventricular (AV) cushions stiffen over gestation, but the molecular mechanisms of this process are unknown. Transforming growth factor-beta (TGFβ) and serotonin (5-HT) signaling modulate tissue biomechanics of postnatal valves, but less is known of their role in the biomechanical remodeling of embryonic valves. In this study, we demonstrate that exogenous TGFβ3 increases AV cushion biomechanical stiffness and residual stress, but paradoxically reduces matrix compaction. We then show that TGFβ3 induces contractile gene expression (RhoA, αSMA) and extracellular matrix expression (col1α2) in cushion mesenchyme, while simultaneously stimulating a two-fold increase in proliferation. In this way, local compaction increased because of the elevated contractile phenotype, but global compaction appeared reduced because of proliferation and ECM synthesis. Blockade of TGFβ type I receptors via SB431542 inhibited the TGFβ3 effects. We next showed that exogenous 5-HT does not influence cushion stiffness by itself, but synergistically increased cushion stiffness with TGFβ3 in physiological ranges. 5-HT increased TGFβ3 gene expression and also potentiated TGFβ3 induced gene expression in a dose dependent manner. Blockade of the 5HT2b receptor, but not 5-HT2a receptor or serotonin transporter (SERT), resulted in complete cessation of TGFβ3 induced mechanical strengthening. Finally, 5-HT administration to *in ovo* cultured embryos induced cushion remodeling related

defects, including thickened/atretic AV valves, ventricular septal defects, and outflow rotation defects. Elevated 5-HT *in ovo* resulted in elevated remodeling gene expression and increased TGFβ3 signaling activity, supporting our *ex vivo* findings. Collectively, these results highlight TGFβ/5-HT signaling as a potent mechanism for control of biomechanical remodeling of AV cushions during development.

3.1 Introduction

Biomechanical remodeling is the process by which living tissues reorganize, reshape, and refit their microstructure in adaptation to changing internal and external forces. This process defines much of embryogenesis, during which initially indistinct cellular masses acquire shape and functional specificity through production and manipulation of the extracellular matrix (ECM). This is particularly important for the morphogenesis of the heart, which is critically responsible for distributing nutrients as the embryo grows. The heart transitions rapidly from a tubular structure into a multi-chambered pumping organ, simultaneously growing over 100 fold in volume [28]. The hemodynamic environment inside the heart increases dramatically in severity during this process [80, 89, 191], which necessitates precisely tuned biomechanical properties of the forming valves to maintain efficient unidirectional blood flow. Atrioventricular (AV) valve morphogenesis is characterized by rapid ECM accretion and turnover [94, 88], which is hypothesized to be stimulated by a dynamic interaction of molecular and mechanical signaling. While numerous molecular agents important for valve morphogenesis have been identified [140, 35, 27, 46], less is known about how these signals affect valve mechanics, which is a key readout

of valve function.

The transforming growth factor-beta (TGFβ) superfamily is critically important for a wide range of cellular processes [9, 116, 165], and is heavily involved in directing morphogenesis of AV cushions [143, 21, 29, 14, 11]. In the chick, TGFβ2 and TGFβ3 isoforms are necessary for the endothelial to mesenchymal transition (EMT) which initiates AV cushion development [144]. TGFβ2 induces initial cell-cell separation of valve endothelial cells, while TGFβ3 stimulates their invasion and subsequent mesenchymal phenotype shift [21, 29]. During post-EMT, these mesenchymal cells facilitate a transition in the cushion microstructure from glycosaminogylcans (GAGs) (hyaluron, versican) toward fibrous structural proteins (collagen I, V,VI, fibronectin, periostin) [94, 133, 28]. This shift in ECM content translates into increased valve stiffness [24], and coincides with elevated expression of TGFβ3 in the cushions and AV canal [31]. Furthermore, TGFβ3 upregulated collagen I and periostin in post-EMT AV cushion explants [134], suggesting that TGFβ3 is a key modulator of cushion ECM content, and consequent mechanical properties. An aim of this study is to better understand this remodeling potential of TGFβ3 through a combined analysis of cushion stiffness, matrix compaction, cell proliferation, and ECM synthesis.

The capacity of TGFβ3 to stimulate valvular remodeling events underscores the importance of identifying molecular signals which modulate TGFβ activities. Recent studies indicate that serotonin (5-HT) interacts with TGFβ signaling in adult heart valves [86, 44], and can also alter valve mechanical properties [47, 186]. 5-HT, which is a monoamine neurotransmitter derived from the essential amino acid tryptophan [156], increased the stiffness of porcine aortic valve cusps with the endothelial layer denuded [47], and under cyclic stretch [12].

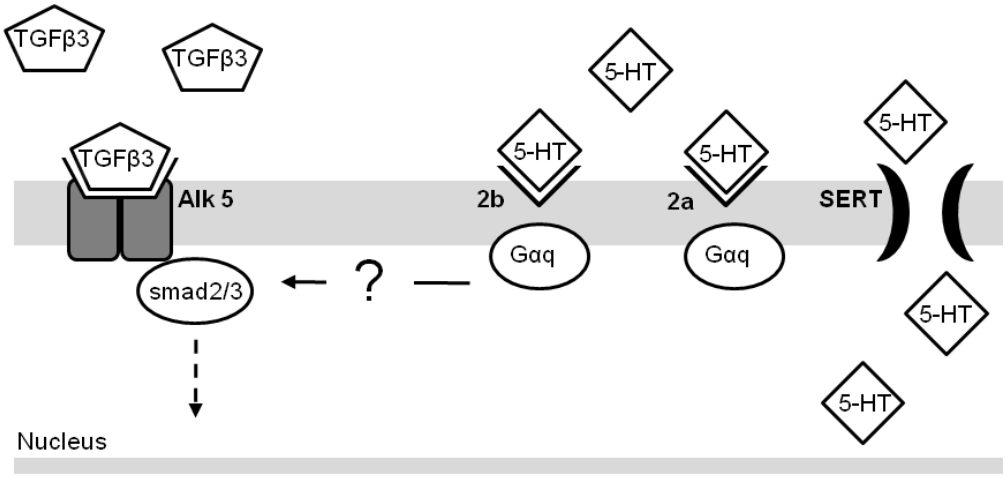

Figure 3.1: Schematic of TGFβ and 5-HT signaling pathways. TGFβ phosporylates Smad2/3 which localizes to the nucleus to activate gene expression. 5-HT binds to the $G_{\alpha q}$ receptors 5-HT2a and 5-HT2b, or may be transported into the cytosol via the serotonin transporter, SERT.

Serotonin also increased collagen synthesis in human and sheep valve interstitial cells (VICs) [86, 73]. Reports in adult VICs indicate that 5-HT can upregulate TGFβ, resulting in cell differentiation and aberrant connective tissue accumulation [86, 44, 138]. In development, serotonin is active in key events such as cardiac progenitor patterning, left-right laterality, and migration of the neural crest [99, 105, 125, 57, 158]. Murine AV cushions express the serotonin receptors 5-HT2a and 5-HT2b, and the serotonin transporter (SERT) (Figure 3.1 by the completion of EMT [100, 32], which is when TGFβ3 expression increases in the cushions [11, 122]. Latent TGFβ binding protein and serotonin binding protein are also expressed in murine post-EMT endocardial cushions [193, 129], highlighting each pathway's capacity to regulate expression of their ligands. The proximity of these TGFβ and 5-HT signaling components suggests that may be interacting partners in post-EMT cushion development. Furthermore, a recent study reported TGFβ1 upregulation in murine SERT KO hearts at near fetal

stages, which was hypothesized to be a consequence of excess 5-HT signaling due to SERT inhibition [139]. In light of these signaling interactions in both adult and development models, we hypothesize that this mechanically relevant crosstalk of TGFβ and 5-HT may play a role in modulating embryonic AV cushion biomechanics.

The objectives of this study therefore were to characterize the remodeling capacity of TGFβ3 in AV cushions, and determine how TGFβ3 and 5-HT may act together to regulate cushion biomechanical remodeling. Chick AV cushion biomechanics, compaction, and candidate gene expression were quantified through implementation of an *ex vivo* cushion culture system. We determined that TGFβ3 induces AV valve stiffening through increases in cell proliferation, myofibroblastic differentiation, and collagen synthesis. 5-HT enhances the AV valve stiffening effect of TGFβ3 in a dose dependent manner. Crosstalk between TGFβ3 and 5-HT signaling was investigated via molecular inhibition studies. The *ex vivo* results were then tested *in ovo* through an elevated 5-HT model. These results suggest that 5-HT may be an important potentiator of TGFβ3 signaling in embryonic valve morphogenesis and biomechanical stiffening.

3.2 Materials & Methods

AV cushion organ culture model

Fertilized leghorn chicken eggs were incubated until Hamburger and Hamilton (HH) stage 25 (Day 4.5). The AV cushions were isolated from their myocardial attachment in ice-cold sterile Earle's Balanced Salt Solution (EBSS; Quality Biological, Inc.). Single cushions were cultured in 20L hanging drops for 24

hours at 38 °C in a 5% CO_2 environment. Control culture media consisted of Medium 199 (M199 w/ phenol red and L-glutamine; Gibco) with 1% concentrations of penicillin/streptomycin (Gibco), Insulin-Transferrin-Selenium (ITS, Gibco), and chick serum (Gibco). For experiments, control media was treated with one or more of the following reagents: human recombinant TGFβ3 (1 ng/ml, Sigma), serotonin hydrochloride (0.47 - 47 μM, Sigma), Cytochalasin D (1 μM, Sigma), 5-HT2a inhibitor MDL100,907 (0.01 - 1 μM, Axon Medchem BV), 5-HT2b inhibitor SB204741 (0.35-35 μM, Sigma), serotonin transporter inhibitor Fluoxetine (10 μM), and Alk 4,5, and 7 inhibitor SB431542 hydrate (0.26 - 26 μM, Sigma). TGFβ3 was reconstituted in 4 mM HCL solution containing 1 mg/ml BSA, all other reagents were dissolved in DMSO. Figure 3.1 contains a schematic of the TGFβ and 5-HT signaling pathways considered in this study. The 470nM 5-HT dose was considered physiological, based on HPLC measured concentrations in 10% fetal bovine serum media (100 nM [187]). The 47 μM 5-HT dosage is similar to prior in vitro/ex vivo studies in postnatal valves [86, 47, 186, 12, 84], so we conservatively considered this dose high for our studies.

Micromechanical testing

Cushion mechanical properties were measured after 24 hour treatment in the *ex ovo* study and at HH25 in the *in ovo* study using the micromechanical pipette aspiration technique [24, 8, 195]. A glass micropipette (70-100 μm in diameter) was placed adjacent to the cushion surface, and a small vacuum pressure was incrementally applied. The pressure source was a 200 μL pipetter calibrated with a custom manometer. Previous strain history was mitigated by preconditioning with approximately 20 cycles of low pressurization ($<$ 1 Pa). The tissue was then monotonically loaded with increasing static pressure loads, at which

images were captured. Aspirated length L, measured as the length from the tip of the pipette to tip of the tissue furthest inside the pipette, was converted into an experimental "stretch ratio", λ, by normalizing to the pipette radius, r_p. The cushion was assumed to be an isotropic, incompressible, hyperelastic material with an exponential free energy law,

$$W = \frac{C}{2}\left[exp\left(\alpha(I_B - 3)\right) - 1\right], \tag{3.2.1}$$

where I_B is the first invariant of left Cauchy Green stretch tensor. AV cushion material isotropy at HH25 was supported by a lack of preferred matrix orientation as determined by ubiquitous protein stain 5-DTAF (50 μM Invitrogen; Figure 3.2). The ΔP vs. λ data was then fit to the axial stress equation of a uni-axially loaded bar of this exponential material, specifically,

$$\sigma_{axial} = \alpha\, C\, exp\left[\alpha\left(\lambda^2 + \frac{2}{\lambda} - 3\right)\right]\left(\lambda^2 - \frac{1}{\lambda}\right) \tag{3.2.2}$$

From previous analysis [24] (see chapter 2), the ΔP vs. λ curve differs from the uniaxial load expression by a scale factor, γ. This scale factor was numerically determined to be a function of only the material parameter α. Due to the nonlinear nature of the data, the mechanical testing data is presented as strain energy density. This was calculated as the area under the ΔP vs. λ curve fit from $\lambda = [1, 2]$ (Figure 3.3A), which from our assumed material model is $W_{1-2} = \frac{C_{mod}}{2}\left[exp(2\alpha) - 1\right]$, where $C_{mod} = \gamma(\alpha)\, C$. See Section 2 for more details of this analysis.

Compaction & Opening Angle Assays

Compaction of the AV cushions was quantified as the ratio of cross-sectional area before (A_0) and after (A) 24 hours of culture in the different treatment con-

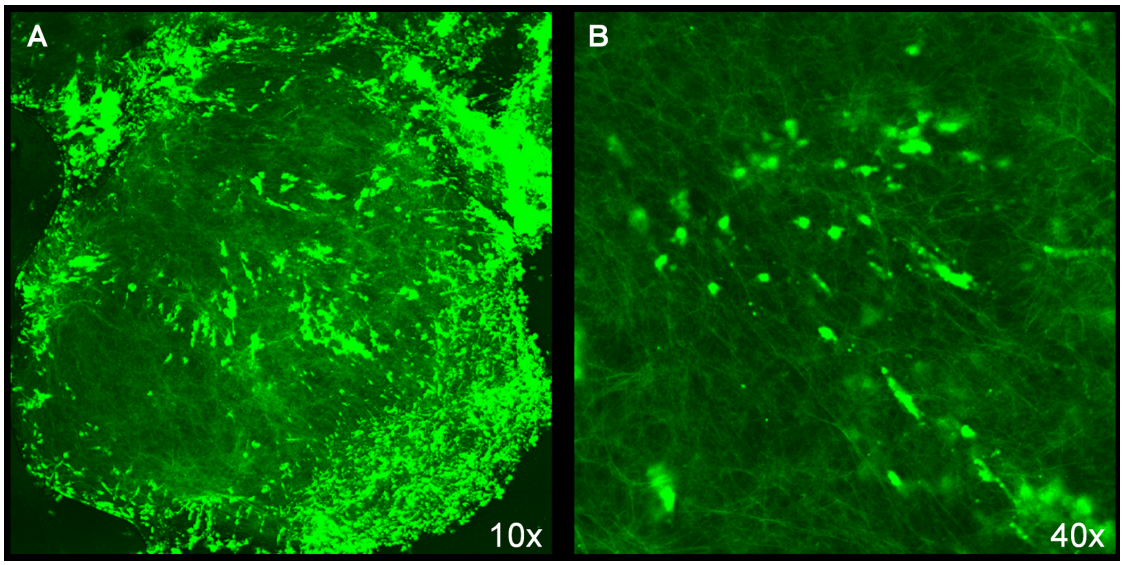

Figure 3.2: Minimal ECM organization in HH25 cushion supports use of an isotropic mechanical testing technique. A) Confocal image of a HH25 cushion with ECM labeled via 5-DTAF protein stain at 10x magnification. B) 40x magnification. Note the lack of matrix fiber density or preferential fiber orientation at this stage of development.

ditions, denoted $\frac{A}{A_0}$. This ratio measures the combined biomechanical remodeling effects of cell traction, proliferation, and ECM synthesis. To isolate cell traction effects, we quantified the opening angles created by micro-slit incision in AV cushions after 24 hours of treatment. The incision was made along the centerline of the spherical cushion mass, extending approximately one radius into the cushion, and immediately created a pie-wedge with defined opening angle. Opening angles are an established indicator of tissue residual stress [58], which is primarily a function of cell traction forces in our culture system. Images were taken at 150x magnification using Zeiss Discovery v20 stereomicroscope (Spectra Services, Inc.) and QImaging Retiga 4000R Fast camera (Spectra Services, Inc). Cross-sectional area and opening angle were measured from calibrated images using NIH ImageJ image analysis software.

Immunohistochemistry (IHC)

Proliferation was assessed through bromodeoxyuridine (BrdU) incorporation into HH25 AV cushion hanging drops. BrdU reagent (Invitrogen) was added at 1:100 dilution in culture medium 6 hours prior to completion of 24 hour culture. AV cushions were then rinsed and fixed in 4% paraformeldehyde (PFA). BrdU incorporation was assessed via immunofluorescent antibody staining and confocal microscopy using anti-BrdU 488 (1:100, Invitrogen), with DRAQ5 (1:1000, Biostatus) as a DNA counterstain. Images were processed via ImageJ, and BrdU incorporation was quantified as the ratio of BrdU positive cells to total cell count. IHC was also used to label phosphorylated Smad2/3 (pSmad2/3) complex in HH25 cushions isolated from the systemic 5-HT *in ovo* model. Isolated cushions were fixed in 4% PFA and then stained via standard whole mount IHC protocol. The cushions were stained with primary pSmad2/3 polyclonal goat anti-human antibody (1:50, Santa Cruz) followed with 488 fluorescent secondary (1:100, Santa Cruz) and cell nuclei counter stain DRAQ5 (1:1000). pSmad2/3 was quantified as the number of cell nuclei with localized pSmad2/3 divided by the total number of cell nuclei.

PCR quantification of gene expression

At the end of 24 hour treatment, AV cushion mRNA was isolated and purified using RNEasy Isolation Kit (Qiagen). A set of 8-10 cushions were pooled per test sample. RNA integrity was determined by NanoDrop spectrometry, using A260/A280 ratio between 1.8 and 2.2 as quality control. cDNA synthesis was completed using SuperScript III first strand RT-PCR kit (Invitrogen) with oligo(dT) primers. Amplification reactions were as follows: (95 °C 15s), (54 °C

Table 3.1: RT-PCR Primers & Accession Number Summary

Gene	Size	Primer Sequence
18s	275	5′- CGGAGAGGGAGCCTGCGAA - 3′
AF173612.1		5′ - CGCCAGCTCGATCCCAAGA - 3′
TGFβ3	142	5′ - GGCTTGTACAACACGCTGAA - 3′
NM205454.1		5′ - TGCAGGATTTCACCACCATA - 3′
ACTA2	126	5′ - CAGTTTTCCCTTCCATCGTG - 3′
NM001031229.1		5′ - TGGGGTATTTCAAGGTCAGG - 3′
Col1α2	201	5′ - GGCAGCAGGTTTCTGCTAAG - 3′
NM001079714.2		5′ - CTCACATGTTGGCTTGTTGC - 3′
Cyclin b2	167	5′ - AGGGGTGGAGAATGCCGTGA - 3′
NM001004369		5′ - TGCCAGGTCCTTTCGTAGCCTT - 3′
RhoA	159	5′ - GTTGGCTTTGTGGGATAC - 3′
NM204704.1		5′ - CAGAAATGCTTCACTTCCG - 3′
SERT	146	5′ - GCAGTGGCTTGGTTCTACGGCAT - 3′
AY573844		5′ - TTGGACAGAAAGCTGCAAGTGACA - 3′
TGM2	120	5′ - GGTGGACAAACTCGCCTTCGACG - 3′
NM205448.1		5′ - TGCAACACTGCACTCCAGGTCC - 3′

15s), (72 °C 30s). Power Syber Green (Applied Biosystems) replication indicator was read at the completion of each 72 °C stage. Standard curves for all primers (listed in Figure 3.1) were generated from HH34 brain mRNA and normalized to 18s ribosomal RNA. Threshold cycle count, C(t), was used to calculate gene expression via the $\Delta\Delta$Ct method using 18s rRNA as a housekeeping reference gene [19].

5-HT administration *in ovo*

HH17 stage fertilized leghorn chicken eggs were windowed on their blunt side. Up to 1.0 mg of serotonin (Sigma) was diluted into 100 μL of PBS and dispensed directly onto the chorionic membrane at HH17, HH25, or HH31. The max 5-HT dosage was equivalent to 18 mg/kg which is comparable to other elevated 5-HT animal models (25 mg/kg and 75 mg/kg) [48, 76]. After 5-HT treatment, chicks were then sealed and cultured at 55% humidity and 38 C until HH36 (Day 10). Preliminary experiments demonstrated that 5-HT treatment sometimes resulted in an ectopic heart, so additional embryos were alternatively subjected to a thoracotomy that mimicked an ectopic heart without serotonin administration as a control. Embryos were then dissected and analyzed for gross anatomical defects. Hearts with intact great artery connections were then removed, cleared, and analyzed with 3D confocal microscopy or serial section histology using Movat's pentachrome stain. Optical fluorescence tomography (OFT) of ventricular, valve, and outflow vessel anatomy was performed as previously described [123, 90]. Briefly, HH36 hearts were freshly isolated and rinsed with 1% lidocaine in PBS buffer. Following rinse, hearts were perfused with fluorescein isothiocyanate-poly-L-lysine(Sigma) via micro injection and then fixed in 4% PFA. The poly-L-lysine binds to the negatively charged endothelial glycocalyx. Hearts were then cleared using Murray's Clear, followed by deep tissue 3D imaging via fluorescence confocal microscopy. Hearts were screened for major defects, and valve morphometry were quantified from this using ImageJ. Valve measurements included leaflet length, average thickness, and minimal thickness with control n=3 and 5-HT treatment n=6. Average thickness (t_{avg}) was calculated as $t_{avg} = \frac{A_L}{L}$, where L is the annulus-tip length of the leaflet, and A_L is cross-sectional area of leaflet. The location of minimum thick-

ness was generally the same for all specimens regardless of treatment.

Statistical Analyses

All data is presented as mean $\pm$ standard error of the mean for the number of samples reported. Statistical comparisons between groups were performed using ANOVA for data sets involving more than two groups, or two-tailed t test when only two groups were compared. Defect prevalence in the *in ovo* model was compared using a chi-squared statistical test. In all comparisons, differences between groups was considered statistically significant for p valves smaller than 0.05.

3.3 Results

TGFβ3 increases AV cushion stiffness

Ex vivo cultured AV cushions exhibited nonlinear mechanical behavior that was well described by the exponential constitutive model (Figure 3.3A). Administration of exogenous TGFβ3 (1ng/ml) increased cushion stiffness 2.5 fold over controls ($W_{TGF\beta3}$ = 0.965 $\pm$ 0.051 vs. W_{Contr} = 0.378 $\pm$ 0.021, p$<$0.0001 Figure 3.3B). Inhibition of canonical TGFβ signaling via the TGFβ type 1 receptor Alk5 (2.6 μM SB431542 [54]) blocked the increase in cushion stiffness (W_{T+TI} = 0.245 $\pm$ 0.043 Figure 3.3B). The Alk5 inhibitor alone had no effect on cushion biomechanics. TGFβ3 treated cushions compacted less than controls, with compaction quantified as the ratio of cross-sectional area before and after treatment (A/A_0 = 0.925 $\pm$ 0.028 vs. A/A_0 = 0.508 $\pm$ 0.017, p$<$0.0001 Figure 3.4A). This

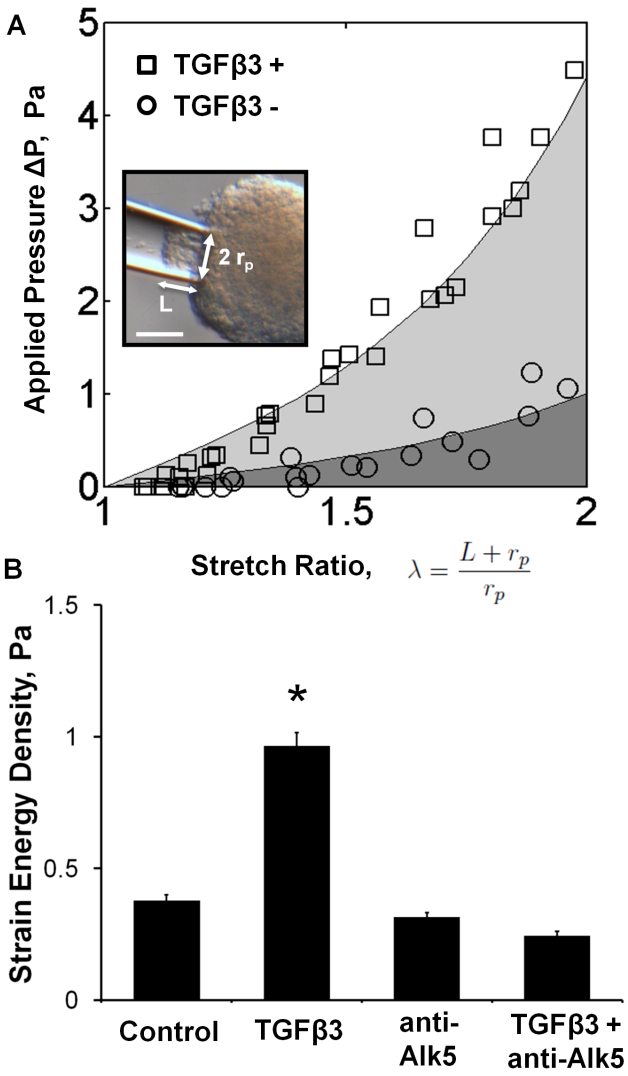

Figure 3.3: TGFβ3 treatment increases stiffness of AV cushions through Alk5 mediated pathway. A) Representative pipette test data for TGFβ3 (1ng/ml, TGFβ3+) and control media (TGFβ3-) treated cushions, n = 4. Strain energy density was calculated from the shaded regions beneath the ΔP vs λ curves. Inset: image of aspirated HH25 AV cushion after 24 hours of culture. The pipette radius, r_p, and the aspirated length, L are indicated. Scale bar = 70 μm. B) AV cushion strain energy density increased with TGFβ3 treatment, but was blocked by Alk5 inhibition (SB431542, 2.6 μM). mean $\pm$ SEM, n $\geq$ 7, *p $<$ 0.0001, 2-way ANOVA.

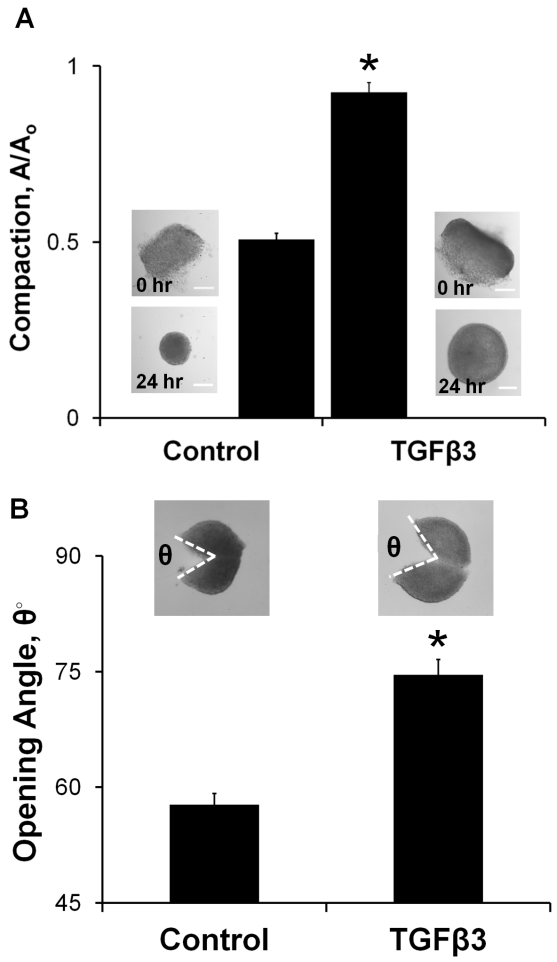

Figure 3.4: TGFβ3 treated cushions compact less than controls, but are under more residual tension. A) Bar graph of area ratios calculated from before and after images of 24 hour TGFβ3 treated cushions. Representative cushion images shown, scale bar = 100 μm. mean $\pm$ SEM, n $\geq$ 12, *p $<$ 0.0001, t-test B) Opening angle of 24 hour TGFβ3 treated cushions is greater than control, indicating tissue is under greater residual tension. Inset shows representative images with opening angle, θ. mean $\pm$ SEM, n = 10-11, *p $<$ 0.001 t-test.

was unexpected because the Cytochalasin D (CytD, 1 μM) results suggested that compaction and stiffness are directly related. CytD inhibited cytoskeletal actin polymerization which resulted in a 5.3 fold decrease in strain energy density of the AV cushions relative to control (W_{CytD} = 0.072 $\pm$ 0.016, Figure

3.5A). Without actin polymerization the AV cushion cells did not compact the matrix, and the cushion did not remodel into the spherical configuration observed in all other treatments. Instead, the post treatment cushion area was significantly larger than initial area, suggesting a relaxation of pre-treatment actin forces (A/A_0 = 1.60 $\pm$ 0.03, Figure 3.5B). The TGFβ3 results of stiffness increase with compaction decrease did not align with this trend. Alk5 inhibition did return compaction behavior to control levels (A/A_0 = 0.570 $\pm$ 0.035 Figure 3.6), indicating that the stiffness and compaction results are both dependent on activation of canonical TGFβ3 signaling. To better understand the relationship between stiffness and compaction, cushion opening angles were quantified to approximate difference in cell traction forces. The opening angle of TGFβ3 cushions was 1.29 fold larger than controls (74.6° $\pm$ 2.0° vs. 57.7° 1.4°, $p<0.001$ Figure 3.4B), indicating that TGFβ3 treated cushions did indeed have higher cell traction forces. Together, these results demonstrate that TGFβ3 induces cushion stiffening through Alk5, but with a concurrent reduction in tissue compaction that suggests other processes are also affected.

TGFβ3 increases AV cushion proliferation and mesenchymal phenotype

Contractile phenotype markers αSMA and RhoA were significantly upregulated with TGFβ3 treatment, 5.3 $\pm$ 0.4 and 2.1 $\pm$ 0.3 fold ($\pm$ SEM) respectively (Figure 3.7), suggesting that TGFβ3 induced residual tension is partially due to an increased migratory/contractile phenotype of resident cushion mesenchyme. TGFβ3 treatment also upregulated mRNA expression of col1α2 mRNA (3.8 $\pm$ 0.9, $p<0.05$) and cyclin b2 (3.9 $\pm$ 0.7 fold, $p< 0.05$), indicative of increased collagen I synthesis and cell proliferation, respectively. BrdU incorporation confirmed that TGFβ3 increased cushion cell proliferation 2.26 $\pm$ 0.36

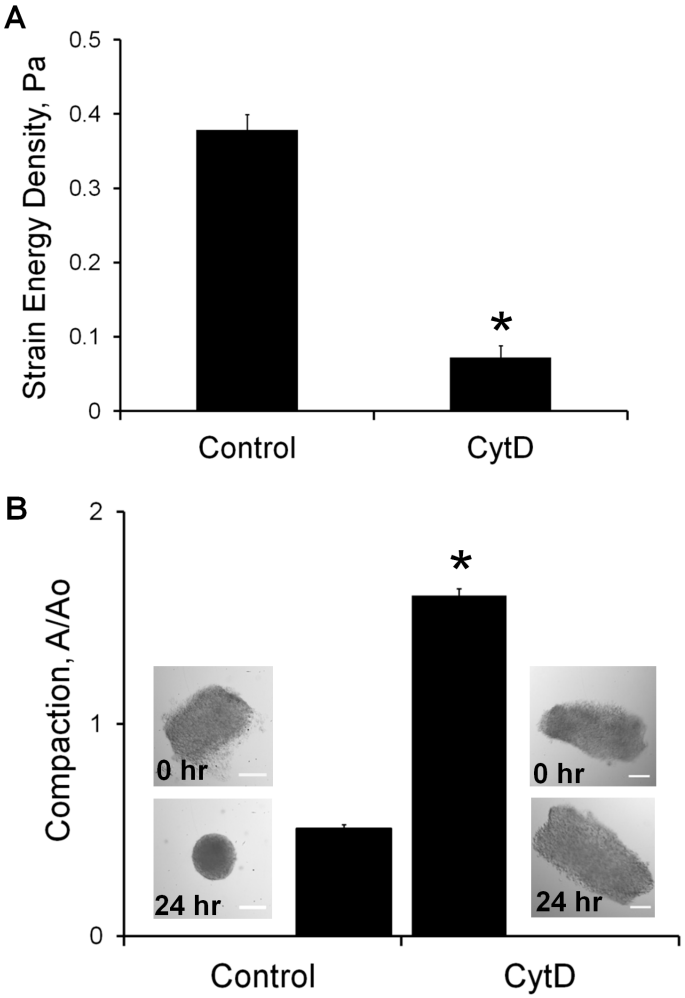

Figure 3.5: Compaction related stiffness control. A) Molecular inhibition of actin polymerization (Cytochalasin D, 1 μM) caused an 80-85% reduction in effective modulus. mean $\pm$ SEM, n $\geq$ 6 *p<0.0001, t-test B) Cushion area increased with actin inhibition, resulting in a 3 fold decrease in measured compaction compared to control. Insets: Representative images of AV cushions before and after treatment, scale bar = 100 μm. mean $\pm$ SEM, n $\geq$ 12, *p<0.0001, t-test

fold over controls (p<0.0001, Figure 3.8). Collectively, these results strongly suggest that while TGFβ3 treated AV cushion mesenchyme are more migratory/contractile, concomitant increases in cell proliferation and matrix synthesis work to counteract aggregate matrix compaction. This explains how the TGFβ3

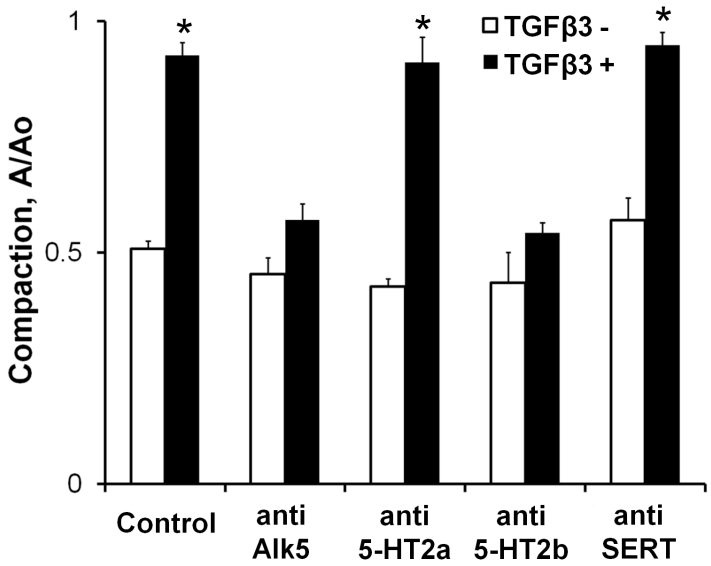

Figure 3.6: TGFβ3 induced decrease in compaction was blocked through inhibition of Alk 5 (SB431542, 2.6 μM) or 5-HTR2b (SD204741 35 μM, anti-5-HT2b). Neither 5-HTR2a inhibitor (MDL100907 10 nM, anti-5-HT2a) nor serotonin transporter inhibitor (Fluoxetine 10 μM, anti-SERT) affected TGFβ3 compaction behavior. mean $\pm$ SEM, n $\geq$ 7, *p$<$0.05, t-test with respect to untreated controls.

treated cushions are biomechanically stiffer, but appear minimally compacted. Furthermore, TGFβ3 treatment increased TGFβ3 transcription (2.2 $\pm$ 0.6 fold, p$<$ 0.05), indicating a potential positive feedback loop for TGFβ3 control of AV cushion biomechanical remodeling.

5-HT potentiates TGFβ3 signaling through 5-HT2b receptor

The effect of 5-HT dose on biomechanical remodeling, independently and in combination with TGFβ3, was systematically evaluated through the stiffness and compaction metrics of the AV cushion organ culture system. 5-HT administration by itself had no statistically significant effect on cushion stiffness. Combined treatment of TGFβ3 with physiological 5-HT (470 nM) increased AV

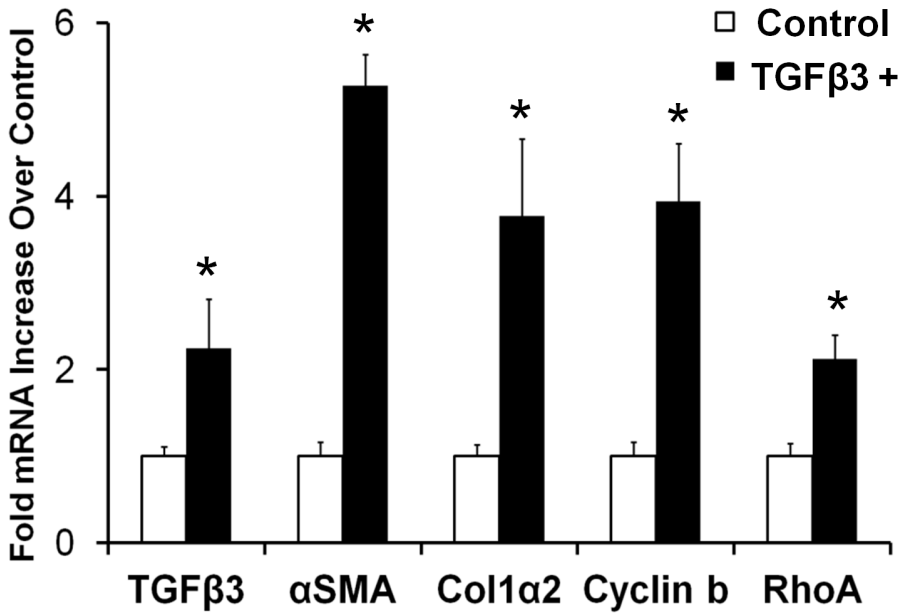

Figure 3.7: 24 hour TGFβ3 treated cushions upregulate contractile (αSMA, RhoA), proliferation (cyclin b), and extracellular matrix protein (col1α2) encoding genes. TGFβ3 administration also significantly stimulated its own production. mean $\pm$ SEM, n=3-4 pooled samples of 8-10 cushions, *p < 0.05, t-test

cushion stiffness (W_{T+5-HT} = 1.136 $\pm$ 0.035), but high 5-HT dose (5-HT+ = 47 μM) eliminated any TGFβ3 induced stiffening effect ($W_{T+5-HT+}$ = 0.457 $\pm$ 0.025, Figure 3.9). Neither selective inhibition of the 5-HT2a (MDL100907 10 nM), 5-HT2b (SB204741 2.6 μM) receptors, or the serotonin transporter SERT (Flouxetine 10 μM) alone affected cushion stiffness (Figure 3.9). Yet in combination with TGFβ3, the anti-5-HT2b treatment completely blocked TGFβ3 dependent stiffness and compaction behavior (Figure 3.9 and Figure 3.6). Inhibition of the 5-HT2a receptor or SERT had no measurable effect on TGFβ3 induced cushion biomechanics. The compaction and stiffness changes induced by 5-HT potentiated TGFβ3 followed the same trend of TGFβ3 treatment alone, with compaction decreasing as stiffness increased and vice versa (Figure 3.9 and Figure 3.6). The additional stiffening effect of 5-HT with TGFβ3 was also eliminated

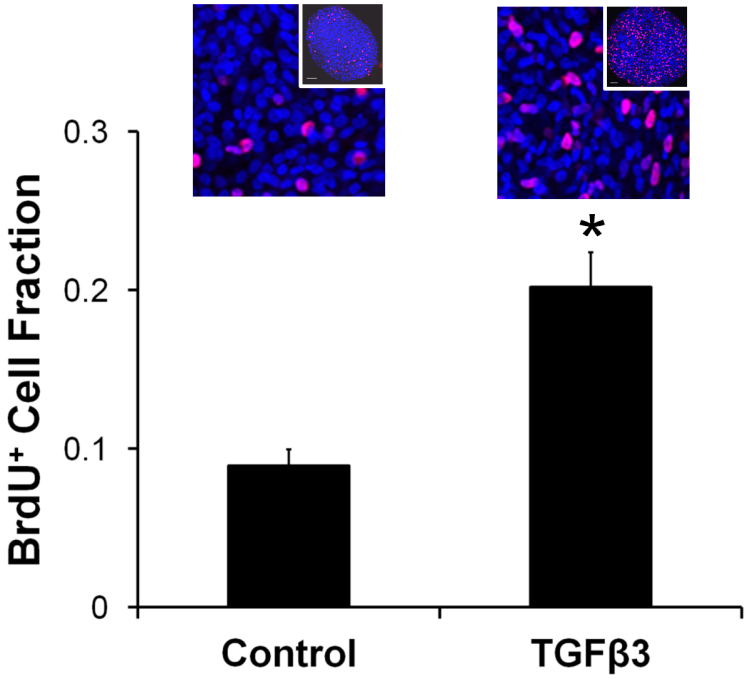

Figure 3.8: BrdU incorporation data (red) of TGFβ3 treated cushions normalized to DRAQ5 cell nuclei counter stain (blue). BrdU was administered 6 hours prior to completion of 24 hour treatment. Representative confocal images are shown above each bar, with a global view of cushion contained in the inset. mean $\pm$ SEM, n = 12, *p$<$ 0.0001, t-test

with Alk5 inhibition, as shown through the combined treatment of TGFβ3 + 5-HT + anti-Alk5 in Figure 3.10. This combined treatment generated a strain energy density similar to the TGFβ3 + anti-Alk5 treatment (0.209 $\pm$ 0.023 Pa vs 0.245 $\pm$ 0.16 Pa, respectively), and further supported that the effects of 5-HT signaling on AV valve remodeling is dependent on canonical TGFβ signaling. Together, these findings suggest that exogenous 5-HT acts through the 5-HT2b receptor to augment or impair TGFβ3 induced cushion stiffening and compaction in a dose dependent manner.

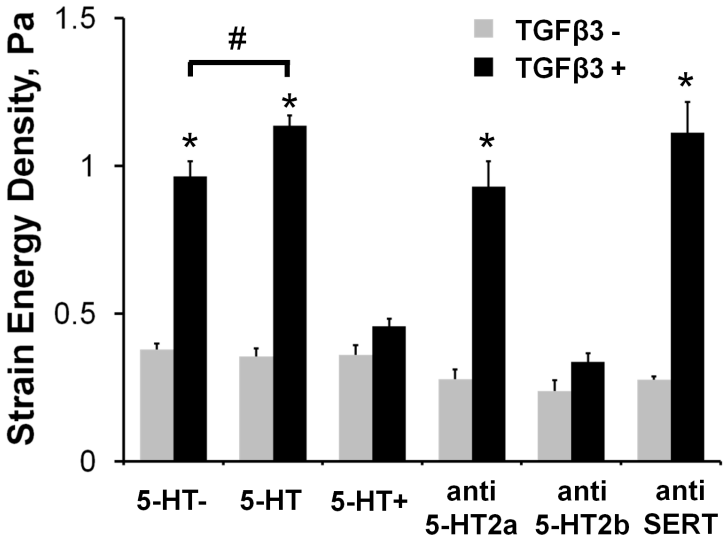

Figure 3.9: 5-HT signaling modulates TGFβ3 induced AV cushion stiffness. Physiological dosages of 5-HT (470 nM, 5-HT) exacerbated TGFβ3 stiffening, while elevated dosages (47 μM, 5-HT+) eliminated it. Molecular inhibition of the 5-HT2a receptor (MDL100907 10 nM, anti-5-HT2a) and the serotonin transporter (Fluoxetine 10 μM, anti-SERT) did not affect TGFβ3 mediated biomechanical stiffening. Inhibition of the 5-HT2b receptor (SB204741 35 μM, anti-5-HT2b) however eliminated the stiffening effect of TGFβ3. mean $\pm$ SEM, n $\geq$ 6, *p $<$ 0.0001 t-test relative to control, # p $<$ 0.05 2-way ANOVA with Tukey post-hoc test.

5-HT modulates TGFβ3 regulation of AV cushion mesenchyme phenotype

Exogenous 5-HT administration potentiated remodeling relevant gene expression in organ cultured AV cushion mesenchyme. TGFβ3 mRNA transitioned from 1.9 $\pm$ 0.1 fold upregulation over controls at physiological 5-HT to 0.40 $\pm$ 0.16 down regulation at high 5-HT dose (Figure 3.11A). The physiological 5-HT dose had no statistically significant effect on αSMA, col1α2, cyclin b2, and RhoA expression. In contrast, high 5-HT significantly decreased transcription of αSMA (0.18 $\pm$ 0.09), collagen1α2 (0.22 $\pm$ 0.07), and RhoA (0.46 $\pm$ 0.11 Figure 3.11A). No effect on cyclin b2 expression was observed at either dose, suggest-

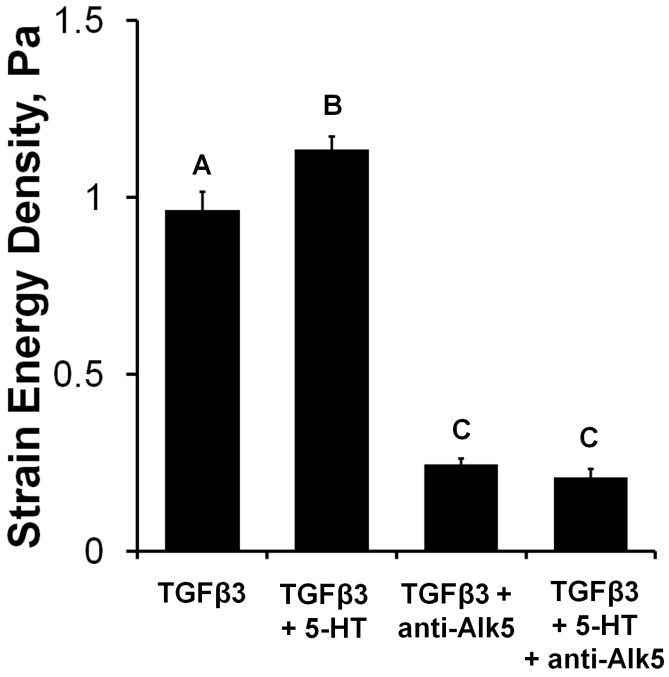

Figure 3.10: TGFβ3 and 5-HT stiffness generation is dependent on Alk5 signaling pathway. Strain energy density (Pa) of cushions treated with TGFβ3 (1ng/ml) only, TGFβ3 + Alk5 inhibitor (SB431542, 2.6 μM anti-Alk5), TGFβ3 + 5-HT (470 nM), and TGFβ3 + 5-HT + anti-Alk5. mean $\pm$ SEM, n $\geq$ 8, Different letter pairings denotes statistically significant p $<$0.05, 2-way ANOVA.

ing proliferation was not directly regulated by 5-HT. Physiological 5-HT did not affect TGFβ3 induced gene expression (Figure 3.11B), but high dose 5-HT markedly reduced gene expression of TGFβ3 (0.86 $\pm$ 0.20 vs. 2.2 $\pm$ 0.6), αSMA (1.4 $\pm$ 0.4 vs. 5.3 $\pm$ 0.4), collagen1α2 (1.3 $\pm$ 0.3 vs. 3.8 $\pm$ 0.9), and RhoA (1.3 $\pm$ 0.2 vs. 2.1 $\pm$ 0.3) (Figure 3.11B). Proliferation related gene cyclin b2 was not significantly affected by 5-HT in combination with TGFβ3. These results suggest that exogenous 5-HT potentiates TGFβ3 more likely through interaction with upstream activation points and/or TGFβ3 synthesis, rather than interacting with TGFβ3 downstream targets, such as αSMA, RhoA, or col1α, directly. We also analyzed the mRNA expression of intracellular 5-HT (i5-HT) related

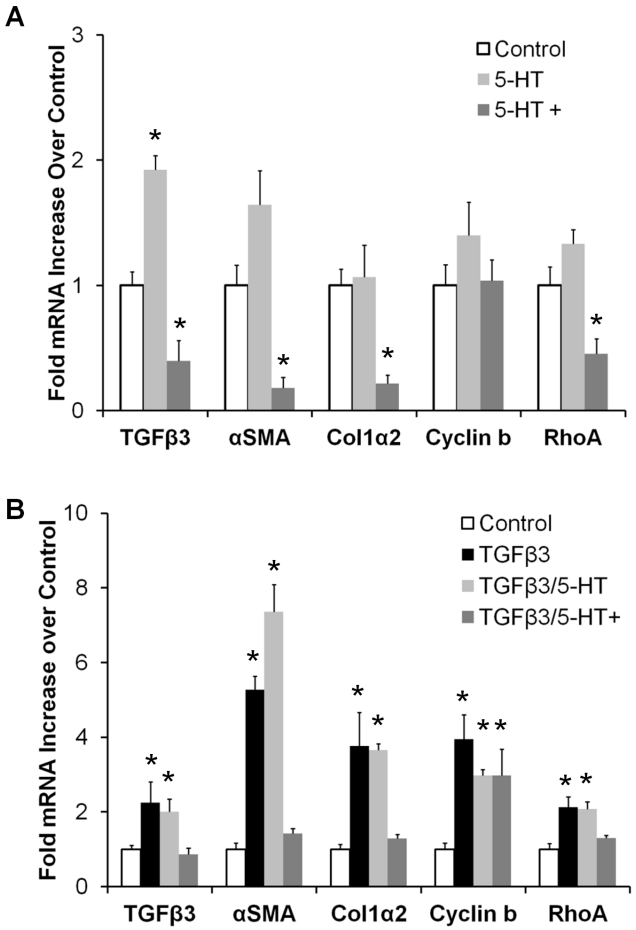

Figure 3.11: 5-HT treatment modulates TGFβ3 mediated gene expression. A) TGFβ3 mRNA transcripts increase with physiological 5-HT (470 nM, 5-HT), but decrease at high dose (47 μM, 5-HT+). αSMA, RhoA, and col1α2, were not affected by physiological 5-HT dose, but were significantly down regulated with high 5-HT treatment. B) High 5-HT treatment mitigates exogenous TGFβ3 induced contractile gene expression, while TGFβ3 induced proliferation was independent of 5-HT dose. mean $\pm$ SEM, n = 3-5 pooled samples of 8-10 cushions, *p$<$ 0.05 via ANOVA comparisons with controls.

genes transglutanminase 2 (TGM2) and the serotonin transporter (SERT). i5-HT transamidates small GTPases and matrix proteins, in a process called "serotonylation" [187]. Tranglutaminase 2 (TGM2) is a i5-HT binding partner which assists transamidation of RhoA [70] and fibronectin [113], altering tissue mechan-

ics through GTPase activation and matrix protein cross-linking, respectively. SERT mRNA expression was significantly increased with 5-HT treatment (1.5 ± 0.2 fold, $P<0.05$), but was downregulated with the 5-HT+ dose (0.46 ± 0.12 fold, Figure 3.12). TGFβ3 treatment stimulated a 4.0 ± 1.0 fold increase in TGM2, but SERT transcription remained near control levels (0.70 ± 0.11 Figure 3.12B). Addition of 5-HT with TGFβ3 significantly decreased SERT and TGM2 mRNA, regardless of 5-HT dose. Though TGFβ3 treatment did upregulate TGM2, the down regulation of SERT by 5-HT treatment and the lack of mechanical changes seen with the SERT inhibitor suggest that serotonylation is not a primary mechanism of stiffness increase in the *ex vivo* culture remodeling results.

Elevated 5-HT induces atrioventricular valvuloseptal defects *in ovo*

As the effects of TGFβ signaling on valve formation are well studied [14, 11, 181], we here test whether exogenous 5-HT administration *in ovo* alters valve morphogenesis. 5-HT administration *in ovo* at HH17 induced a spectrum of cardiac defects by HH36 (Day 10) as summarized in Table 3.2. Temporal and dosage dependant viability curves (Figure 3.13) showed that 0.7mg dose was over 50% lethal at HH36, but administration of the same dose of 5-HT at HH25 or HH31 did not result in further lethality or defect formation (data not shown). The only gross malformations observed were localized to the heart and chest wall. Approximately 42% (24/57) of affected embryos exhibited an ectopic heart which protruded through an incomplete chest wall closure (Figure 3.13). To confirm that interior defects resulted specifically from 5-HT exposure and not secondarily from the ectopia, an experimental thoracotomy was performed to model the ectopic condition. We found no statistically significant occurrence of any cardiac defects with experimental ectopia, supporting that 5-HT was re-

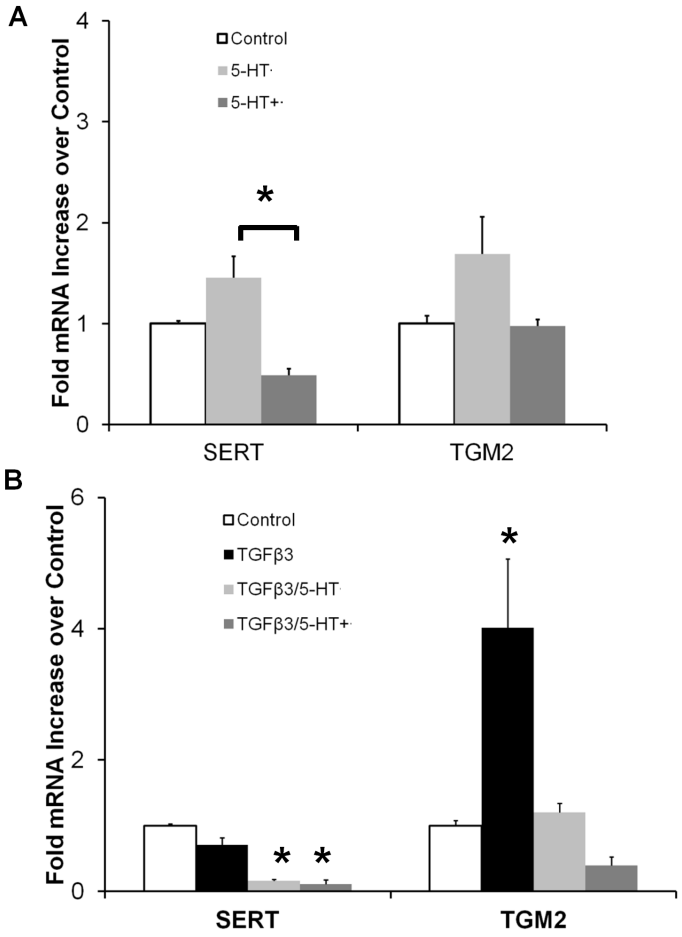

Figure 3.12: Intracellular 5-HT uptake is modulated by 5-HT dose. A) 5-HT transporter (SERT) gene expression was downregulated via high 5-HT (47 μM, 5-HT+) dose, while transglutaminase 2 (TGM2) was not affected. Physiological dose of 5-HT (470 nM, 5-HT) had no effect on either SERT or TGM2 gene expression. B) TGFβ3 (1ng/ml) stimulated 4-fold increase in TGM2, which was mitigated by either doses of 5-HT. TGFβ3 had no effect on SERT expression. mean $\pm$ SEM, n = 3-4, *p$<$0.05, t-test.

sponsible for the cardiac defects observed. A ventricular septal defect (VSD or SVSD) occurred in 42% (24/57) of the defective embryos. Approximately 18% (10/57) of the embryos exhibited double outlet right ventricle (DORV) defects. 5-HT administration also resulted in significantly enlarged atria with thinned walls in 35% (20/57) of the defective embryos (Table 3.2, Figure 3.15A). All of

Table 3.2: Cardiac Defect Summary of *in ovo* 5-HT Administration

	Control	Serotonin	Thoracotomy
# of embryos treated (HH17)	35	133	107
# of embryos survived (HH36)	34	60	49
# of defective embryos (HH36)	0	57*	27
Ectopic	-	24*	25*
VSD	-	5	-
SVSD	-	19*	1
DILV	-	3	-
DOLV	-	1	-
DORV	-	10*	-
Enlarged Atria	-	20*	3

the embryos with DORV also exhibited highly stenotic or atretic atrioventricular (AV) valves (Figure 3.15B), with the normally muscular flap valve in the right AV canal appearing thin and fibrous like the left AV valve. Regardless of gross cardiac defect identified, the average (0.144 ± 0.009 mm, mean $\pm$ SEM) and minimal (0.080 ± 0.007 mm) thickness of the left AV septal leaflet was thinner in 5-HT treated embryos than controls (0.191 ± 0.009 and 0.165 ± 0.023 mm respectively, Figure 3.15C). No differences were found in mural leaflet thickness, or in the length of either leaflet. The reduction in AV valve thickness with 5-HT treatment indicated an increase in tissue compaction, and may possibly be a recapitulation of the migratory/contractile phenotype observed *ex vivo*.

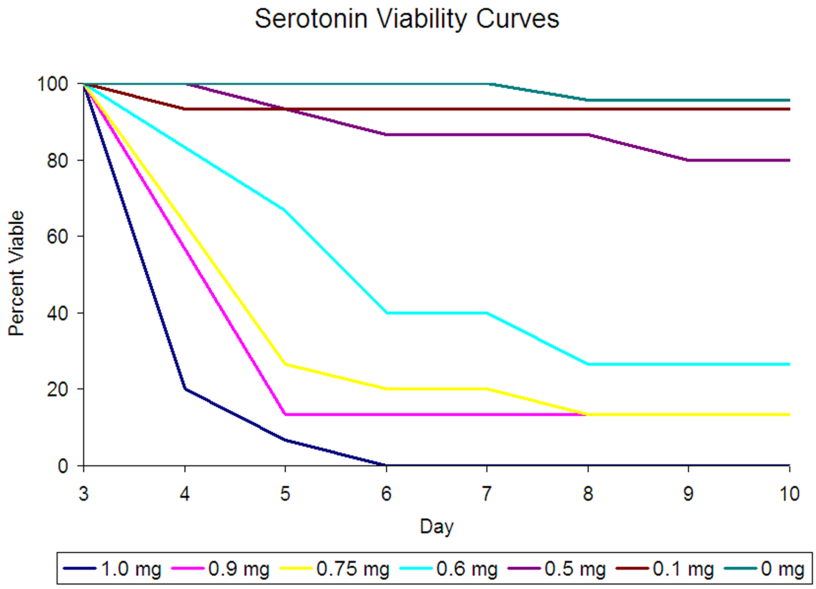

Figure 3.13: Plot of avian embryo viability as a function of time and 5-HT dose. 5-HT administration to the surface of HH17 chick embryos resulted in greater than 70% lethality at dosages above 0.75 mg. The majority of deaths occurred within 48 hours of incubation. Doses of 0.5 mg and below were over 80% viable with virtually no morphological defects. Doses administered at later incubation times (Day 5, Day 7) did not result in lethality or defects by HH36 (data not shown). 5-HT administration at the predicted 50% lethality dose (0.7 mg/100 l) resulted in 55% lethality by Day 10.

Exogenous 5-HT increases AV cushion stiffness through TGFβ signaling *in ovo*

Systemic 5-HT treatment at HH17 resulted in a statistically significant 1.4 ± 0.2 fold increase in AV cushion stiffness over control at stage HH25 (strain energy density of 0.43 ± 0.06 Pa vs. 0.31 ± 0.03 Pa, *$p<0.05$, Figure 3.16). We next analyzed the mesenchymal gene expression patterns in this *in ovo* system. 5-HT significantly upregulated TGFβ3 (1.7 ± 0.1), αSMA (1.5 ± 0.1), col1α2 (1.5 ± 0.1), cyclin b (1.6 ± 0.2), and RhoA (1.7 ± 0.2) (*$p<0.05$, Figure 3.17). Interestingly, the TGFβ3 mRNA expression was comparable to that observed in the *ex ovo* or-

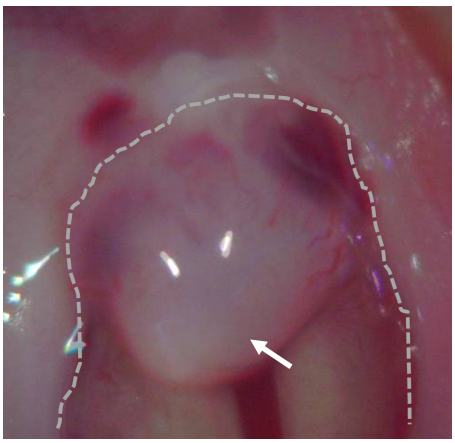

Figure 3.14: Representative image of ectopic heart (arrow) and unclosed chest (dashed line) observed with both 5-HT treatment and thoracotomy sham controls.

gan culture treatment of TGFβ3 alone (2.2 $\pm$ 0.6), 5-HT alone (1.9 $\pm$ 0.1), and TGFβ3 + 5-HT (2.0 $\pm$ 0.3). αSMA and col1α2 mRNA were also upregulated *in ovo* with 5-HT, but less than with direct TGFβ3 administration in *ex vivo* culture (αSMA - 1.5 vs 5.7, RhoA - 1.7 vs 2.1). The similar mRNA profiles of the candidate genes in both models suggested that 5-HT also potentiates TGFβ signaling in AV cushions *in ovo*. To confirm that the 5-HT treatment was indeed modulating TGFβ signaling activity *in ovo*, we quantified nuclear pSmad2/3 expression in HH25 cushions with and without 5-HT treatment (Figure 3.18). 5-HT treatment increased the number of cell nuclei with localized pSmad2/3 expression 2.6 $\pm$ 0.8 fold over control embryos (0.28 $\pm$ 0.04 vs. 0.11 $\pm$ 0.03, $p<0.01$). Together these results demonstrate that 5-HT potentiates TGFβ signaling in AV cushions to control contractile differentiation, proliferation, and biomechanical remodeling.

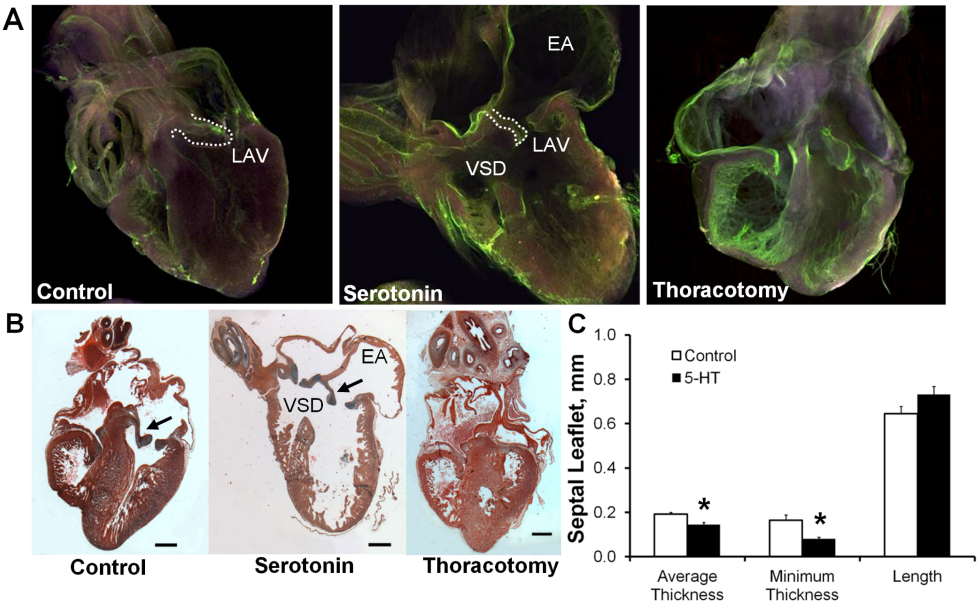

Figure 3.15: 5-HT administration *in ovo* induces cardiac defects. A) Representative virtual sections of control, 5-HT treated, and thoracotomy sham control hearts at HH36 via Endopainting and confocal microscopy. B) Representative Movat's pentachrome stained sections of hearts with the same conditions. Prominent cardiac defects, including enlarged atria (EA) and ventricular septal defect (VSD), were associated with malformed and malfunctioning AV valves (arrows). 25x, scale bar = 500 μm. C) Left septal leaflet average thickness and minimum thickness are both statistically thinner in 5-HT treated leaflets than control. mean $\pm$ SEM, n = 3-6 hearts per treatment, *p$<$0.05, t-test.

3.4 Discussion

In this study we implemented a quantitative organ culture assay that simultaneously interrogated the contributions of cellular and molecular signaling to drive cushion tissue-level remodeling and biomechanical strengthening. TGFβ3 stimulated a 2.5 fold increase in biomechanical stiffness (Figure 3.3), generated in part by an increase in cell traction. This contractile phenotype is a common outcome of TGFβ signaling in postnatal valve tissue. For instance, porcine aor-

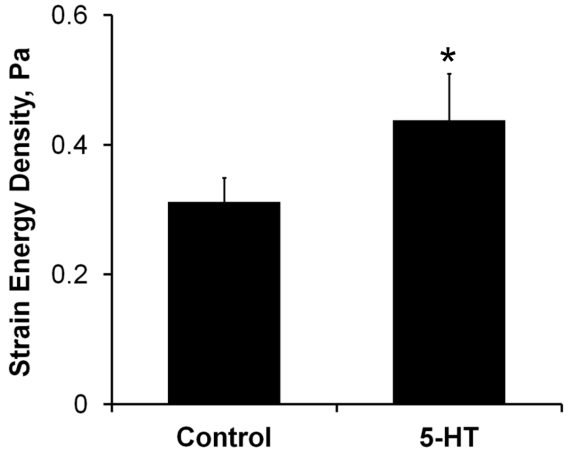

Figure 3.16: Exogenous 5-HT increases AV cushion stiffness. The strain energy density (Pa) of HH25 cushions increased 1.4 fold with systemic 5-HT treatment *in ovo*, mean $\pm$ SEM, n = 8-10 cushion, *p < 0.05, t-test.

tic valves express contractile marker αSMA when stimulated by TGFβ1 in situ [121]. Porcine aortic valve interstitial cells (VICs) embedded in collagen gels expressed αSMA in response to TGFβ1, and demonstrated significant gel compaction over untreated gels [185]. Similarly, TGFβ3 treated embryonic AV progenitors compacted collagen gels to 10% of initial area [31]. Yet in contrast to these reports, TGFβ3 induced contractility did not result in hyper-compacted AV cushions (Figure 3.4), but instead compacted less than controls. A key distinction between these two assays is that *in vitro* collagen gel cultures have much lower cell densities than our *ex vivo* system. The effect of proliferation on volume change is virtually undetectable in these gels, and cell traction dominates the compaction behavior. In native tissues, especially in the embryo, changes in cell proliferation and/or apoptosis have a significant impact on resulting tissue volume and apparent compaction. *Ex ovo* culture of AV cushions enables precise control of the biochemical environment while maintaining the natural structural and cellular composition of the cushion. The lack of compaction with

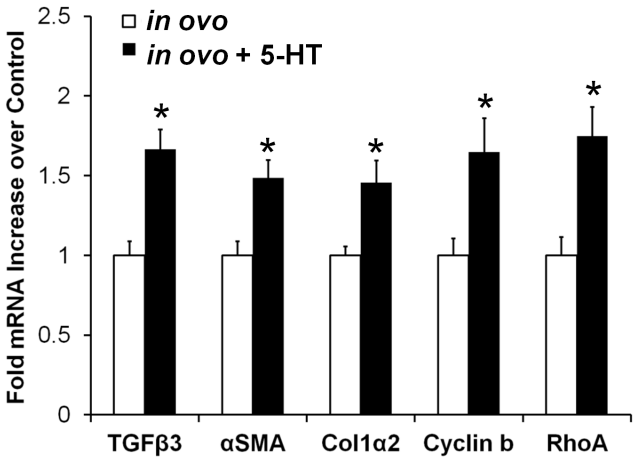

Figure 3.17: Exogenous 5-HT increases AV cushion TGFβ related remodeling genes *in ovo*. Gene expression levels of HH25 AV cushions isolated from embryos treated with 5-HT at HH17 (48 hours). mean $\pm$ SEM, n= 6-10 samples, each of 8-10 pooled HH25 cushions, *p$<$0.05, t-test.

TGFβ3 treatment is therefore most likely due to a counterbalancing from increases in cell proliferation and ECM synthesis. This supports a mechanism of simultaneous tissue growth, matrix reorganization, and biomechanical stiffening during embryonic valve formation that is driven by a complex coordination of cell tractions, matrix synthesis, and cell proliferation. These findings underscore that embryonic valve tissue biomechanical remodeling, which is critical for proper valve function, cannot be inferred strictly from isolated compaction, proliferation, or matrix synthesis data, but is best measured directly from an integrated system.

The interplay of TGFβ3 and 5-HT signaling was most notably seen through the potentiation of TGFβ3 gene expression by 5-HT dose (Figure 3.7). The physiological 5-HT concentration upregulated TGFβ3 expression, while the high concentration down regulated expression. Upregulation of TGFβ expression by 5-HT has been observed in several cardiac cells and tissues, though through

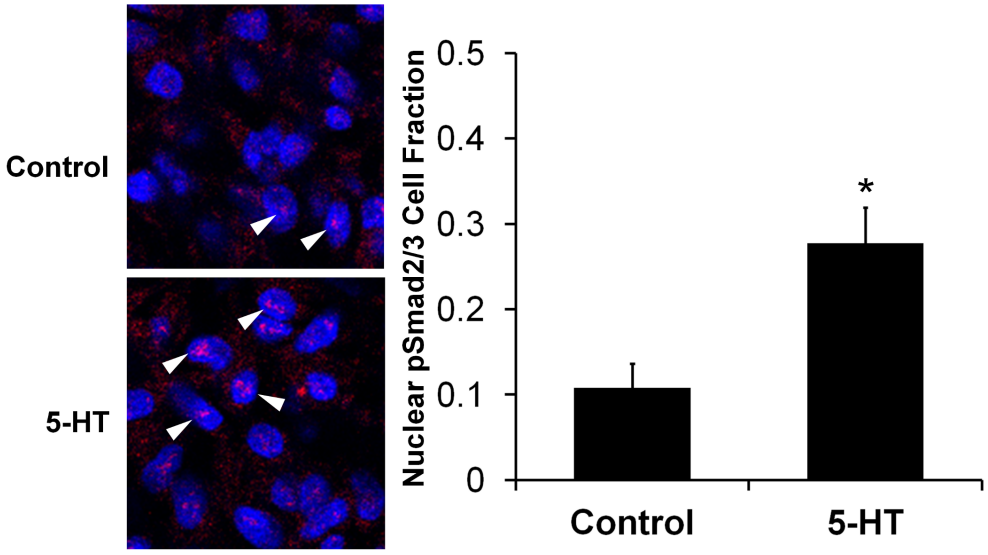

Figure 3.18: 5-HT increases AV cushion pSmad2/3 expression *in ovo* Embryos treated with systemic 5-HT at HH17 have increased pSmad2/3 expression at HH25 indicating elevated TGFβ signaling. n=6, mean $\pm$ SEM *p<0.01, t-test. Arrows denote representative cells with pSmad2/3 nuclear staining. Cell nuclei - blue, pSmad2/3 - red

which molecular pathways is still unclear. Adult aortic valve interstitial cells treated with 5-HT have increased TGFβ1 activity, predominantly through the 5-HT2a receptor [86, 189]. Neo-natal rat cardiac fibroblasts treated with 5-HT and 5-HT2a agonists upregulated αSMA protein expression, a marker for fibroblast differentiation and a gene induced by TGFβ signaling [190]. Similarly, TGFβ1 and αSMA expression were elevated in SERT cre-lox KO mice hearts through heightened 5-HT2a signaling in late embryonic stage mice, purportedly due to excess 5-HT from SERT inhibition [139]. Other reports point to 5-HT2b as the key mechanism. 5-HT administration in adult rats increased 5-HT2b mRNA expression in both aortic and mitral valves, demonstrating a positive response to 5-HT treatment[48]. SERT mRNA was down regulated in these valves denoting a negative response to elevated 5-HT, which our results also demon-

strate (Figure 3.12B). The 5-HT2b receptor, TGFβ receptor type I and II, and the TGFβ latent binding protein were all more expressed in canine myxomatous mitral valves than normal valves, suggesting a coupling of these two pathways through 5-HT2b [44]. Longterm 5-HT treatment of rats generated valve related echocardiographic and histology defects [72], but these defects did not occur in rats simultaneously treated with a 5-HT2b inhibitor [76]. This suggests that the 5-HT2b receptor may be a key pathway for cardiac and valve tissue remodeling. Cardiac fibroblast studies indicate that the 5-HT upregulates TGFβ1 through a mutual transactivation of the epidermal growth factor (EGF) and 5-HT2b pathways [84, 126]. Our results support a 5-HT2b dependant mechanism, as seen by 5-HT2b inhibition effectively blocking TGF?3 stiffening. The TGFβ stiffening effect was independent of 5-HT2a and SERT. Although TGFβ3 upregulated TGM2 expression, 5-HT treatment mitigated this expression, which suggests TGM2 activity does not contribute to the enhanced stiffening of TGFβ/5-HT signaling. High 5-HT also mitigated the TGFβ3 stiffening, though desensitization of the 5-HT2b receptor by a sustained high 5-HT dose may explain this effect. 5-HT directly increased pSmad2/3 phosphorylation in cushion mesenchyme, and its potentiating effect was abrogated through Alk5 blockade. This suggests that 5-HT signaling through 5HT2b may interact with Smad2/3 signaling, but further studies are warranted to clarify potential roles of other intermediate or downstream targets.

In our *in ovo* model, systemic 5-HT elevation induced severe heart defects, including failure of the ventricular septum to close, ballooned atria, DORV, and hyper-contracted AV valves. Variations of these defects have been observed in other TGFβ and 5-HT related studies. VSDs are the most prevalent congenital heart defects observed, occurring in approximately 50% of all clinical cardiac

malformations [77, 151]. Selective serotonin uptake inhibitors (SSRI) taken during the first trimester of pregnancy were associated with a statistical increase in VSD prevalence in newborns [119]. Our data supports elevated extracellular 5-HT as a possible cause of this correlation. Removal of TGFβ secondary messenger smad4 causes VSDs and other lethal congenital defects, which are presumed to be consequence of decreased TGFβ signaling [146]. Yet removal of TGFβ inhibitory messenger smad7 also generates VSDs [30], indicating that exacerbated TGFβ signaling can also generate significant cardiac defects. The dilated atria observed in our model are not explicitly reported in other 5-HT studies, suggesting the defect may result from secondary effects, such as altered hemodynamics from valve incompetence. For instance, enlarged atria defects have been induced in zebrafish embryos through mechanical obstruction of the AV canal [79]. Our avian model exhibited a small (18%), but statistically significant, penetrance of DORV, which is a predominant congenital defect in TGFβ2 KO mice (87% penetrance) [14]. Collectively these defects highlight the morphogenetic potential of 5-HT in early cardiac development, and the similar spectrum of defects generated across 5-HT and TGFβ related animal models.

An interaction of TGFβ and 5-HT signaling was observed *in ovo* through the upregulation of TGFβ3 and contractile genes in the AV cushions (Figure 3.17), the increase in pSmad2/3 expression (Figure 3.18), and the resulting thinned valve morphology (Figure 3.15C). While the pSmad2/3 and mRNA expression confirms that aspects of the *ex vivo* results occur *in ovo*, it is unclear whether elevated TGFβ signaling at HH25 is solely responsible for the thinned valve morphology observed at HH36. Hyperplastic and thickened AV valves occur in TGFβ2 KO (31% penetrance) [14, 10], and TGFβ latent binding protein KO (81% penetrance) [181] animals, which supports this hypothesis. However, adult rats

treated with subcutaneous 5-HT injections for 7 days developed thickened AV valves rich in GAGs [48], while 3 month treatment increased valve thickness, but consisted primarily of collagen [72]. Thickened, collagen rich valves are also reported in adult SERT KO mice [118], and at late embryonic stage SERT KO pups [139]. Together these results indicate that elevated 5-HT signaling can instigate valvular remodeling *in vivo*, but changes in valve microstructure and morphology are clearly dependent on other factors such as treatment duration, specimen age, or secondary effects from accompanying congenital malformations. Altered hemodynamic loading can also generate defects, as evidenced through the serious malformations stimulated by mechanical perturbation [192, 164]. Yet hemodynamic loading is simultaneously a consequence and stimulant of molecular signaling, interacting in a cyclical rather than linear cause-effect manner. This again emphasizes the importance of direct assessment of mechanical stiffness, because it can distinguish the influence of these microstructure and microenvironment variations on valve performance.

Embryonic valve formation and maturation utilizes multiple TGFβ isoforms in spatially and temporally restricted ways that are also somewhat different between species [29, 11]. We chose to focus on TGFβ3 over either TGFβ1 or TGFβ2 because of its principal role in cell invasion during chick cushion EMT [29], and confirmed increase in expression during post-EMT [31]. Our results establish a molecular mechanism for short-term (24 hours) TGFβ3 stimulation on AV cushion biomechanical remodeling, but the effects of prolonged signaling on biomechanical and morphological changes remain unclear. This could be addressed with a combined *in vivo*/*in vitro* experimentation over more time points using a system like the approach presented here. The *ex vivo* culture system contains both endocardial and mesenchymal cells, but lack of antibodies

reactive in chick prohibited the determination of cell specific responses. Our *in ovo* exogenous 5-HT administration model data complements existing data on genetic mutant animal models of TGFβ and 5-HT related signaling in cardiac development [14, 130]. Future studies will need to investigate whether the serotonin effects of TGFβ3 change with TGFβ3 dose.

In conclusion, tissue mechanics, cell phenotype, and molecular signaling all simultaneously direct and control tissue morphogenesis. Our results suggest that TGFβ is a potent stimulator of cushion stiffening, and 5-HT is a key regulator of this stimulating effect. Connecting signaling networks with cell and tissue level responses will become increasingly important for understanding post-EMT valve remodeling and potentially other embryonic remodeling events. The quantitative experimental systems presented herein are an attractive approach for elucidating these multi-scale mechanisms and their downstream consequences.

CHAPTER 4

A MODEL OF MECHANICALLY STIMULATED GROWTH AND SHAPE CHANGE

4.1 Introduction

Embryonic development is characterized by rapid transitions in tissue size, function, and morphology. Examples of this in heart development include the folding of the heart tube into four chambers [115] and the elongation and condensation of the atrioventricular valve leaflets [94]. Experimental studies have demonstrated that abnormal mechanical loading in the early heart can generate defects. As examples, the ligation of the left atrium of a chick embryo resulted in reduced blood flow and a decrease in left ventricle volume [164], and obstruction of blood flow in a zebrafish embryo generated enlarged atrias and impaired valves [79]. Even in less mechanically robust environments, such as neural tube formation [131] or torsion of the early cardiac tube [188], residual stresses develop that are essential for proper formation. These examples emphasize the need for mathematical frameworks in which to connect mechanical loading with changes in tissue size, shape, and function during embryogenesis.

Development of biological tissue may be divided into three categories: mass addition ("growth"), material property change ("remodeling"), and shape change ("morphogenesis") [172]. Growth involves the cellular processes of extra-cellular matrix production, cell proliferation, and cell enlargement. In these processes, mass is converted and redistributed in and by the cells. Sources of mass include soluble factors, such as those present in the blood stream or cell culture media, or assembled protein structures, such as glycoaminoglycan or

collagen networks from neighboring tissues. Growing systems are generally modeled as open, at least with respect to mass, because the origin of the incoming mass is external to the mechanical element(s) being modeled [114, 49, 62]. Remodeling broadly includes a change in material properties, such as stiffness, anisotropy, constituent volume fractions, and/or chemical reactivity. Rarely does remodeling occur in the absence of mass addition or shape change. We do not consider remodeling in this study, but instead focus on growth and shape change using a single constituent model.

Morphogenesis is the dynamic process in which embryonic tissues form, change shape, and mature into functional organs. Kinematic descriptions of morphogenesis as a mapping of material points have been considered in research on plant growth [152, 166]. In the context of bone remodeling, Cowin and Van Buskirk introduced a mechanically driven, small strain, surface growth model that related the normal velocity of the bone surface to the difference in current and referential strain experienced by the tissue [36]. Skalak and others formalized finite strain growth using a velocity field description, and considerated of both volumetric and surface additions [168]. Rodriguez and others [154] extended this work with a multiplicative decomposition of the deformation gradient into inelastic and elastic components, borrowing ideas from metal plasticity [101]. In their approach, tissue growth and shape change occurs through a stress free evolution of the reference configuration, which is defined by the inelastic deformation. With this decomposition, growth and shape change are prescribed through evolution equations for the inelastic deformation. Here, we use the multiplicative decomposition to derive evolution equations for growth and shape change.

The determination of the appropriate form of the evolution equations for growth and shape change has been the focus of recent research [114, 49, 41, 6, 62]. With limited experimental data available, research has employed thermodynamic arguments from the entropy inequality or a dissipation principle to motivate appropriate forms of the evolution equations. Regardless of the means used to satisfy the inequality, such as the assumption of maximal dissipation [148, 61], or the introduction of a quadratic form for the dissipative parts, it is necessary to consider the influence mass addition has on the thermodynamics. For example, does new mass enter with mechanical energy equal to the energy at that material point, with no mechanical energy (stress-free), or with an intermediate, constituent-specific energy? External sources of mass or entropy associated with the incoming mass are sometimes neglected [41, 64]. In this paper, we evaluate how these different assumptions influence the evolution.

Various assumptions have been made regarding the mechanical stimuli of growth and shape change, including strain [75, 36], stress [60, 154], and strain energy [74]. Experimental evidence suggests that certain plants and embryos maintain a target, or homeostatic, stress state [17, 15]. At the homeostatic stress state, growth and shape change do not occur. Evidence for a homeostatic stress is also seen in arteries, where the residual stress distribution promotes a uniform stress field through the artery wall when fully loaded [33]. This uniformity suggests the existence of an inherent mechanical loading preferred by the tissue. We assume the existence of a homeostatic stress state and incorporate it into the evolution equations through an expression for the balance of biochemical forces [42, 41].

Shear forces are a significant part of the mechanical environment in cer-

tain instances of development. In particular, blood flow through the primitive heart generates significant wall shear stress on the valve and vascular structures [191, 18, 79]. Experiments suggest that these shear forces are important for activating biochemical cascades within the cell that drive the production and rearrangement of extra-cellular matrix proteins, proliferation, cell contraction, and other mechanically relevant processes [69]. While previous growth models have the capacity to evolve in shear [150, 6], examples of growth and shape change under shear loading are limited. We present some simple examples to demonstrate the shearing behavior of the model tissue.

4.2 Kinematics

Consider a stress-free body in the reference configuration at $t = 0$, denoted as the initial configuration β_0 in Fig. 4.1. The body undergoes a combined elastic-inelastic deformation from the initial to current configuration β defined by the mapping $\boldsymbol{x} = \boldsymbol{x}(\boldsymbol{X}, t)$. The observable deformation,

$$\boldsymbol{F} = \frac{d\boldsymbol{x}}{d\boldsymbol{X}} \tag{4.2.1}$$

includes elastic and inelastic deformations. We assume $\boldsymbol{F}$ may be expressed as a multiplicative decomposition (Eq. 5.2.1) of the elastic, $\boldsymbol{f}$, and inelastic, $\boldsymbol{\mathcal{F}}$, deformation:

$$\boldsymbol{F} = \boldsymbol{f}\boldsymbol{\mathcal{F}}. \tag{4.2.2}$$

The multiplicative decomposition was introduced in the study of biological growth by Rodriguez et al [154]. The advantage of this decomposition is that it provides access, at least mathematically, to the inelastic deformation. Growth and shape change due to biological processes may be prescibed in terms of, $\boldsymbol{\mathcal{F}}$,

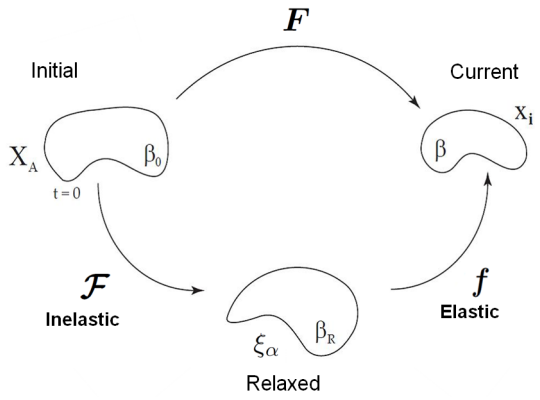

Figure 4.1: Multiplicative decomposition of the overall deformation into inelastc and elastic components

or by defining the inelastic deformation rate,

$$\boldsymbol{\mathcal{L}} = \dot{\boldsymbol{\mathcal{F}}}\boldsymbol{\mathcal{F}}^{-1}, \tag{4.2.3}$$

where a dot denotes the derivative with respect to time, t, at a fixed point in the initial configuration. Although the ultility of this decomposition is generally accepted [5], there exist a few issues worth mentioning. First, the decomposition is not unique [114]. Any rigid body rotation of the stress-free, relaxed configuration is permissible, as this will not contribute any stress. To avoid this issue, we assume the initial configuration is known, and we incrementally update the relaxed configuration relative to it through integration of the inelastic deformation rate. The rotational component of $\boldsymbol{\mathcal{F}}$ is, therefore, always known and is unique to the specific evolution being modeled. Second, material points are being added and/or removed from the initial configuration throughout the evolution. How does this mass enter? At what density should it be added? Here, we assume that density is constant; in this case mass addition is equal to volume change. Finally, it is not clear whether the multiplicative decomposition accurately describes how elastic and inelastic deformations interact.

Previous research has demonstrated the ability of the decomposition to capture the shape and volume change of developing tissues [154, 175, 150]. However,including more biological features could provide better mechanistic insight into how growth occurs. We will explore ways to incorporate such details in the inelastic deformation rate in Section 4.5.

Inhomogeneous growth can produce incompatibilities. Incompatibilities are isolated elements of growth or shape change which do not fit together in a stress-free configuration [169]. An example of this is differential expansion between two elements. In this case, both elements occupy the same space in the stress-free configuration, resulting in a displacement field from the original configuration to the relaxed configuration that is no longer one-to-one. Consequently, the elastic deformation is also incompatible in this case in order to maintain the compatibility of the total deformation. This compensation by the elastic deformation gives rise to growth-induced residual stresses. Residial stresses occur in several developing tissues [188, 194].

In the special case when growth is compatible the inelastic deformation may be defined as the gradient of a growth displacement, ξ_α, with respect to the initial position, specifically,

$$\boldsymbol{\mathcal{F}} = \frac{d\boldsymbol{\xi}}{d\boldsymbol{X}}\,, \tag{4.2.4}$$

or, in indicial notation as

$$\mathcal{F}_{\alpha A} = \xi_{\alpha,A}\,.$$

In this decomposition, the elastic deformation is influenced by two mechanisms, 1) the total, observable deformation, $\boldsymbol{F}$, and 2) the evolution of the reference configuration due to inelastic deformation, $\boldsymbol{\mathcal{F}}$. In a compatible growth situation, the primative quantities would be the observable displacement, x_i, and

the inelastic displacement, ξ_α. However, in general the inelastic deformation, not the displacement, will be the primitive quantity that defines the growth and shape change of the tissue. This distinction will be important for the variational calculation of Section 4.4.

From this decomposition, the deformation rates are related as follows,

$$L_{ik} = l_{ik} + f_{i\alpha}\mathcal{L}_{\alpha\beta}f^{-1}_{\beta k}, \tag{4.2.5}$$

where $\boldsymbol{L} = \dot{\boldsymbol{F}}\boldsymbol{F}^{-1}$, $\boldsymbol{l} = \dot{\boldsymbol{f}}\boldsymbol{f}^{-1}$, and $\boldsymbol{\mathcal{L}} = \dot{\boldsymbol{\mathcal{F}}}\boldsymbol{\mathcal{F}}^{-1}$. The overall deformation rate, $\boldsymbol{L}$ may be separated into the symmetric stretching tensor,

$$\boldsymbol{D} = \boldsymbol{d} + \frac{1}{2}\left[\boldsymbol{f}\boldsymbol{\mathcal{L}}\boldsymbol{f}^{-1} + \boldsymbol{f}^{-T}\boldsymbol{\mathcal{L}}^{T}\boldsymbol{f}^{T}\right]$$

and the skew-symmetric spin tensor,

$$\boldsymbol{W} = \boldsymbol{w} + \frac{1}{2}\left[\boldsymbol{f}\boldsymbol{\mathcal{L}}\boldsymbol{f}^{-1} - \boldsymbol{f}^{-T}\boldsymbol{\mathcal{L}}^{T}\boldsymbol{f}^{T}\right].$$

The varibles $\boldsymbol{d}$ and $\boldsymbol{w}$ are, similarly, the symmetric and skew-symmetric parts of $\boldsymbol{l}$. The product of the inelastic determinant, $\mathcal{J} = \det(\boldsymbol{\mathcal{F}})$, and the elastic determinant, $j = \det(\boldsymbol{f})$ equals the overall volume change. That is,

$$\det(\boldsymbol{F}) = \det(\boldsymbol{f})\det(\boldsymbol{\mathcal{F}}), \tag{4.2.6}$$

or,

$$J = j\,\mathcal{J}. \tag{4.2.7}$$

4.3 Field Equations

4.3.1 Conservation of Mass

In a growing system, the amount of mass present in the tissue depends on the time of the evolution. The calculation of mass density is further dependent of a choice of volume. Following the notation of Lubarda and Hoger [114], we define three measures of density:

$$\rho_0 = \frac{dm^0}{dV}\,, \tag{4.3.1a}$$

$$\rho = \frac{dm}{dv}\,, \tag{4.3.1b}$$

and,

$$\rho_g = \frac{dm}{dV} = \rho J\,, \tag{4.3.1c}$$

where Eq. 4.3.1a gives the density of initial mass per initial volume, Eq. 4.3.1b gives current mass per current volume, and Eq. 4.3.1c gives the current mass per initial volume.

We express the mass balance in an integral form over the initial volume, V,

$$\frac{d}{dt}\int_V \rho_g\, dV = \int_V \rho J\kappa\, dV\,, \tag{4.3.2}$$

where κ is the rate of mass addition per unit current mass. In local form, this reduces to

$$\dot{\rho_g} = (\dot{\rho J}) = \rho J\kappa\,,$$

which, upon carrying out the differentiation becomes,

$$\dot{\rho} + \rho d_{kk} + \rho\mathcal{D}_{\alpha\alpha} = \rho\kappa\,, \tag{4.3.3}$$

where $\boldsymbol{d}$ and $\boldsymbol{\mathcal{D}}$ are the symmetric parts of the elastic and inelastic deformation rates defined in Section 4.2. All mass enters through the inelastic deformation, therefore, $\mathcal{D}_{\alpha\alpha} = \kappa$. This reduces the continuity equation to,

$$\dot{\rho} + \rho\, d_{kk} = 0\,. \tag{4.3.4}$$

We further assume that the elastic deformation is isochoric ($j = 1$ and $d_{kk} = 0$), which simplifies Eq. 4.3.4 to,

$$\dot{\rho} = 0\,.$$

Hence, the ratio of current mass to current volume remains constant and equal to the ratio of initial mass to initial volume. In this case,

$$\rho = \rho_0 \equiv const\,,$$

and the new mass enters the tissue with the same density as the original material. Furthermore, with the elastic deformation incompressible, the total and inelastic Jacobians are equal,

$$J = \mathcal{J}\,,;$$

so

$$\rho_g = \rho J = \rho \mathcal{J}\,. \tag{4.3.5}$$

4.3.2 Conservation of Linear Momentum

The balance of linear momentum requires that the change in momemtum of a body is equal the sum of external forces applied to it. In a growing system, an additional external force term that balances the momentum of the incoming mass is, in general, present. We express this balance law in an integral represen-

tation over the initial configuration,

$$\frac{d}{dt}\int_V \rho\mathcal{J}\dot{x}_i\,dV = \int_V \rho\mathcal{J}\left[b_i + \kappa\,\dot{\tilde{x}}_i\right]\,dV + \int_{\partial V}\mathcal{T}_{iA}N_A dS_0$$
$$\int_V \rho\mathcal{J}\ddot{x}_i\,dV = \int_V \mathcal{T}_{iA,A} + \rho\mathcal{J}b_i + \rho\mathcal{J}\left(\dot{\tilde{x}}_i - \dot{x}_i\right)\mathcal{D}_{\alpha\alpha}\,dV\,, \tag{4.3.6}$$

where b_i is the external body force per unit mass, $\mathcal{T}_{iA}$ is the external surface traction per unit area in the initial configuration, N_A is the unit normal vector of the reference configuration surface, x_i is the displacement of the body, ξ_α is the growth and remodeling displacement (see Section 4.2), and $\dot{\tilde{x}}_i$ is the velocity of the incoming mass.

There is currently no experimental data on the velocity of the incoming mass. To circumvent this, a common approach is to assume that the mass enters (or leaves) with the same velocity of the body ($\dot{\tilde{x}}_i = \dot{x}_i$) [114, 91]. Another approach is to consider growth to be a quasi-static process; in this case, all of the dynamic terms in the balance law are neglected [42]. These two approaches are effectively equal. A third approach is to represent the momentum of the incoming mass with a "reversible" and an "irreversible" term [49]. The reversible term balances the momemtum of the new mass in the system, $\dot{\tilde{x}}_i = \dot{x}_i$ as in the preceding approaches. The irreversible term is the momemtum associated with other physical forces, potentially dissipative, involved in the growth process. For example, if the velocity of the incoming mass differred from the current velocity of the tissue, the momentum difference would be represented in this irreversible term. Here, we assume that mass enters with the same velocity as that of the body ($\dot{\tilde{x}}_i = \dot{x}_i$). This is motivated by the difference in time scales between mechanical loading (seconds) and tissue growth (days), which suggests that momentum due to growth does not significantly influence the balance of linear momentum. In this way, the local form of Eq. 4.3.6 in the initial configu-

ration reduces to

$$\mathcal{T}_{iA,A} + \rho\mathcal{J}b_i = \rho\mathcal{J}\ddot{x}_i\,. \tag{4.3.7}$$

4.3.3 Conservation of Angular Momentum

We next evaluate the balance of angular momentum. As with linear momentum, we introduce an external source of angular momentum to balance the change in velocity of the mass entering the system. With this term, the balance law in integral form over the initial volume becomes,

$$\frac{d}{dt}\int_V \rho\mathcal{J}\,\epsilon_{ijk}\,x_j\,\dot{x}_k\,dV = \int_V \rho\mathcal{J}\,\epsilon_{ijk}\,x_j\,\left(b_k + \kappa\,\dot{\bar{x}}_k\right)\,dV + \int_{\partial V}\epsilon_{ijk}\,x_j\,\mathcal{T}_{kA}N_A dS_0\,, \tag{4.3.8}$$

where ϵ_{ijk} is the permutation tensor. We again assume $\dot{\bar{x}} = \dot{x}$. Appling the divergence theorem to the surface terms,

$$\int_V \rho\mathcal{J}\epsilon_{ijk}x_j\,\left(\ddot{x}_k + \dot{x}_k\,\dot{\mathcal{D}}_{\alpha\alpha}\right)\,dV = \int_V \epsilon_{ijk}\,x_j\,(\mathcal{T}_{kA,A} + \rho\mathcal{J}b_k + \kappa\,\dot{\bar{x}}_k) + \epsilon_{ijk}x_{j,A}\mathcal{T}_{kA}\,dV\,,$$

and using Eq. 4.3.7, we arrive at the local form

$$\epsilon_{ijk}F_{jA}\mathcal{T}_{kA} = 0\,. \tag{4.3.9}$$

Eq. 4.3.9 requires that,

$$F_{jA}\mathcal{T}_{kA} = \mathcal{T}_{kA}F_{jA}\,. \tag{4.3.10}$$

4.3.4 Balance of Biochemical Forces

The multiplicative decomposition of the deformation gradient facilitated the expression of growth and shape change as an inelastic deformation. Although the

stress is not directly dependent on $\mathcal{F}_{\alpha A}$, this deformation represents the evolution of the reference for the elastic deformation, on which the stress does directly depend. This evolution is fundamentally driven by the biochemical and/or cellular forces of growth. Recently, Dicarlo and Quiligotti [42] proposed a balance of accretive forces to describe the relationship between these forces and the tissue evolution. This provided a formal method in which to incorporate biological details into the mechanics. Prior to this, Klisch et al. [91] equated the stress-work of growth to the extra energy needed for growth using the energy equation, but did not describe this relation as a balance law. Here, we include the balance of biochemical forces as a balance law; and, then, demonstrate its derivation from a variational principle.

We first state the balance of biochemical energy associated with the evolution of the reference configuration in integral form over the initial configuration,

$$\int_V \mathbb{C}_{\alpha\beta}\mathcal{L}_{\alpha\beta}\, dV = \int_V \mathbb{B}_{\alpha\beta}\mathcal{L}_{\alpha\beta}\, dV\,,$$

where we have borrowed the notation of Dicarlo and Quilligotti [42] for the internal growth and shape-change, symmetric couple, $\mathbb{C}_{\alpha\beta}$, and the external biochemical force couple, $\mathbb{B}_{\alpha\beta}$. A consequence biochemical forces is homeostasis, which is the propensity of a living system to maintain its physical environment. For instance, when an artery is pressurized beyond the homeostatic pressure, it will grow to mitigate the elevated loading [59]. Cells are responsible this change in reference configuration, and their activity is regulated by biochemical gradients. In the context of a growing tissue, a biological force could be the production of extra-cellular matrix proteins. The synthesis of these proteins do not elastically deform the tissue, but instead change the reference configuration of the elastic deformation. Another example of a biochemical force is the inhibition of actin polymerization through treatment with Cytochalasin D. Without actin,

the cells can no longer exert forces on the extra-cellular matrix, which results in its relaxation. Biochemical forces evolve the reference configuration, but do not contribute momentum. We adopt a balance of biochemical forces in order to include these biochemical effects [42, 41]. Assuming that Cauchy's localization principle applies to the biological process represented in the this balance law, we arrive at the reference configuration local form

$$\mathbb{C}_{\alpha\beta} - \mathbb{B}_{\alpha\beta} = 0\,. \tag{4.3.11}$$

This algebraic formulation is identical with that employed by previous works [42, 6, 41].

4.3.5 Balance of Energy

We now consider the balance of mechanical, thermal, and biochemical energy for this system using a integral representation in the initial configuration. The external work terms include work done by both the mechanical forces and biochemical couples. As growth of a single phase is intrinsically an open system, in that it is influenced by parts of the system that are not being modeled, the energy balance includes the kinetic ($\frac{1}{2}\dot{\bar{x}}_i\dot{\bar{x}}_i$) and internal energy ($\Sigma_h$) associated with the mass entering the system:

$$\frac{d}{dt}\int_V \rho\mathcal{J}\left[\frac{1}{2}\dot{x}_i\dot{x}_i + \Sigma\right]\,dV = \int_V \left[\rho\mathcal{J}\,b_i\dot{x}_i + \mathbb{B}_{\alpha\beta}\mathcal{L}_{\alpha\beta} + r + \rho\mathcal{J}\,\kappa\,\left(\frac{1}{2}\dot{\bar{x}}_i\dot{\bar{x}}_i + \Sigma_h\right)\right]\,dV + \int_{\partial V}\left(\mathcal{T}_{iA}\dot{x}_i - q_A\right)N_A dS_0$$

or, after applying the divergence theorem,

$$\begin{aligned}\int_V \rho\mathcal{J}\left(\frac{1}{2}\dot{x}_i\dot{x}_i+\Sigma\right)\mathcal{D}_{\alpha\alpha}+\rho\mathcal{J}\ddot{x}_i\dot{x}_i+\rho\mathcal{J}\dot{\Sigma}\,dV &= \int_V \rho\mathcal{J}\,b_i\dot{x}_i+\mathbb{B}_{\alpha\beta}\mathcal{L}_{\alpha\beta}+r-q_{A,A}\\ &\quad+\rho\mathcal{J}\,\kappa\,\left(\frac{1}{2}\dot{\bar{x}}_i\dot{\bar{x}}_i+\Sigma_h\right)+\left(\mathcal{T}_{iA}\dot{x}_i\right)_{,A}\,dV\\ &= \int_V \rho\mathcal{J}b_i\dot{x}_i+\mathbb{B}_{\alpha\beta}\mathcal{L}_{\alpha\beta}+r-q_{A,A}\\ &\quad+\rho\mathcal{J}\,\kappa\,\left(\frac{1}{2}\dot{\bar{x}}_i\dot{\bar{x}}_i+\Sigma_h\right)+\mathcal{T}_{iA,A}\,\dot{x}_i+\mathcal{T}_{iA}\,\dot{x}_{i,A}\,dV\,.\end{aligned}$$

Upon grouping terms with corresponding velocities and assuming $\dot{\bar{x}}_i = \dot{x}_i$, we can solve for the internal energy rate:

$$\int_V \rho\mathcal{J}\dot{\Sigma}\,dV = \int_V \mathcal{T}_{iA}\,\dot{x}_{i,A}+\mathbb{C}_{\alpha\beta}\mathcal{L}_{\alpha\beta}+\rho\mathcal{J}\Delta\Sigma\,\mathcal{D}_{\alpha\alpha}+r-q_{A,A}\,dV \tag{4.3.12}$$

where we have used,

$$\begin{aligned}\mathcal{T}_{iA,A}+\rho\mathcal{J}b_i-\rho\mathcal{J}\ddot{x}_i &= 0\\ \mathbb{C}_{\alpha\beta} &= \mathbb{B}_{\alpha\beta}\\ \mathcal{D}_{\alpha\alpha} &= k\end{aligned}$$

and,

$$\Delta\Sigma = \Sigma_h - \Sigma\,.$$

The local form of the rate of internal energy in reference configuration is, then,

$$\rho\mathcal{J}\dot{\Sigma} = \mathcal{T}_{iA}\,\dot{x}_{i,A}+\mathbb{C}_{\alpha\beta}\mathcal{L}_{\alpha\beta}+\rho\mathcal{J}\Delta\Sigma\,\mathcal{D}_{\alpha\alpha}+r-q_{A,A}\,. \tag{4.3.13}$$

In Eq.4.3.13, the current internal energy may differ from the internal energy of the newly removed or deposited tissue ($\Delta\Sigma \neq 0$). This is motivated by the extra-cellular matrix proteins, which are the predominant structural components of tissue. Such proteins are initially secreted by cells as individual fiber strands, which coil with other strands to form a mature collagen fiber. Eventually the protein is removed through an enzymatic degradation process. This

suggests that the internal energy from growth is unlikely to enter in with the current energy. Also, by permitting different internal energies, we provide a means to incorporate kinetic rates of turnover of newly acquired mass, such as those proposed in mixture-theory approaches [82, 66].

4.4 Principle of Virtual Work

We now derive balances of linear momentum and biochemical forces through the variation of the internal and external energy. Neglecting changes in thermal energies, the first variation of the internal energy is,

$$\begin{aligned} \delta W_{int} &= \delta \int_V \rho\psi J \, dV \\ &= \int_V \delta\bar{\psi} \, J + \bar{\psi} \, \delta J \, dV \, , \end{aligned} \tag{4.4.1}$$

where $\bar{\psi} = \rho \, \psi$ is the free energy per unit current mass and V is the initial volume.

The variation of the total and inelastic deformation gradients are,

$$\delta F_{iA} = \delta x_{i,A} \, , \tag{4.4.2}$$

and,

$$\delta \mathcal{F}_{\alpha A} = \mathcal{L}_{\alpha\beta} \mathcal{F}_{\beta A} \, . \tag{4.4.3}$$

The external energy includes the work done by external forces on the observable displacements, x_i and the external biochemical stress-work associated with the evolution of the reference configuration, $\mathbb{B}_{\alpha\beta}\mathcal{L}_{\alpha\beta}$, where,

$$\mathbb{B}_{\alpha\beta}\mathcal{L}_{\alpha\beta} = \mathbb{B}_{\alpha\beta}\mathcal{F}^{-1}_{A\beta}\delta\mathcal{F}_{\alpha A} \, . \tag{4.4.4}$$

The variation of the external energy is,

$$\delta W_{ext} = \int_V \rho J b_i \, \delta x_i + \mathbb{B}_{\alpha\beta} \mathcal{F}^{-1}_{A\beta} \delta \mathcal{F}_{\alpha A} \, dV + \int_{\partial V} \mathcal{T}_{iA} \, \delta x_i N_A \, dS_0 \,, \tag{4.4.5}$$

where b_i is the body force per unit current mass, $\mathcal{T}_{iA}$ is the physical stress applied to the initial configuration surface, S_0, which is defined by the normal vector N_A.

The variation of the internal energy is equivalent to the variation of the external energy.

$$\delta W_{int} = \delta W_{ext} \tag{4.4.6}$$

From incompressibility, the total and inelastic Jacobians are equal ($J = \mathcal{J}$, Eq. 4.3.5), which requires that their variations are equivalent:

$$\delta J = \delta \mathcal{J} \,,$$

$$J F^{-1}_{iA} \, \delta x_{i,A} = \mathcal{J} \mathcal{F}^{-1}_{\alpha A} \, \delta \mathcal{F}_{\alpha A} \,,$$

and,

$$J \delta x_{i,i} = \mathcal{J} \mathcal{F}^{-1}_{\alpha A} \delta \mathcal{F}_{\alpha A} \,. \tag{4.4.7}$$

The variation of the current density, $\delta\rho$, is zero. The variation of the internal energy, $\bar{\psi}$, is

$$\begin{aligned} \delta \bar{\psi} &= \delta \bar{\psi} \left(f_{i\alpha} \right) \\ &= \frac{\partial \bar{\psi}}{\partial f_{i\alpha}} \left[\frac{\partial f_{i\alpha}}{\partial F_{jA}} \, \delta x_{j,A} + \frac{\partial f_{i\alpha}}{\partial \mathcal{F}_{\beta A}} \, \delta \mathcal{F}_{\beta A} \right] \\ &= \frac{\partial \bar{\psi}}{\partial F_{iA}} \delta x_{i,A} + \frac{\partial \bar{\psi}}{\partial \mathcal{F}_{\beta A}} \, \delta \mathcal{F}_{\beta A} \,. \end{aligned} \tag{4.4.8}$$

Using the above relations, we may now evaluate the internal and external variations. Note that we have replaced the total Jacobian with the inelastic Jacobian.

$$\begin{aligned} \int_V \mathcal{J} \, \frac{\partial \bar{\psi}}{\partial F_{iA}} \delta x_{i,A} + \mathcal{J} \, \frac{\partial \bar{\psi}}{\partial \mathcal{F}_{\beta A}} \, \delta \mathcal{F}_{\beta A} + \, \bar{\psi} \, \mathcal{J} \mathcal{F}^{-1}_{\alpha A} \, \delta \mathcal{F}_{\alpha A} \, dV \\ = \int_V \rho J b_i \, \delta x_i + \mathbb{B}_{\alpha\beta} \mathcal{F}^{-1}_{A\beta} \delta \mathcal{F}_{\alpha A} \, dV + \int_{\partial V} \mathcal{T}_{iA} \, \delta x_i N_A \, dS_0 \end{aligned} \tag{4.4.9}$$

The following identity facilitates the use of the divergence theorem.

$$\frac{\partial \psi}{\partial F_{iA}} \delta x_{i,A} = \left[\frac{\partial \psi}{\partial F_{iA}} \delta x_i \right]_{,A} - \left(\frac{\partial \psi}{\partial F_{iA}} \right)_{,A} \delta x_i \tag{4.4.10}$$

We employ Eq. 4.4.10 in the internal energy variation on the left side of Eq. 4.4.9 and apply the divergence theorem.

$$\begin{aligned} \delta W_{int} = \int_V -\mathcal{J} \left(\frac{\partial \bar{\psi}}{\partial F_{iA}} \right)_{,A} \delta x_i + \mathcal{J} \frac{\partial \bar{\psi}}{\partial \mathcal{F}_{\beta A}} \delta \mathcal{F}_{\beta A} + \bar{\psi} \mathcal{J} \mathcal{F}^{-1}_{\alpha A} \delta \mathcal{F}_{\alpha A} \, dV \\ + \int_{\partial V} \mathcal{J} \frac{\partial \bar{\psi}}{\partial F_{iA}} \delta x_i N_A \, dS_0 \end{aligned} \tag{4.4.11}$$

Upon combining Eq. 4.4.11 and 4.4.9 and grouping terms associated with their respective virtual displacments yields the balance laws and boundary conditions as coefficients of the variations in the integrands:

$$0 = \int_V -\mathcal{J} \left[\left(\frac{\partial \bar{\psi}}{\partial F_{iA}} \right)_{,A} + \rho b_i \right] \delta x_i \, dV \tag{4.4.12}$$

$$+ \int_V \left[\mathcal{J} \frac{\partial \bar{\psi}}{\partial \mathcal{F}_{\alpha B}} \mathcal{F}_{\beta B} + \bar{\psi} \mathcal{J} \delta_{\alpha\beta} - \mathbb{B}_{\alpha\beta} \right] \delta \mathcal{F}_{\alpha A} \mathcal{F}^{-1}_{A\beta} \, dV \tag{4.4.13}$$

$$+ \int_{\partial V} \left[\mathcal{J} \frac{\partial \bar{\psi}}{\partial F_{iA}} - \mathcal{T}_{iA} \right] N_A \, \delta x_i \, dS_0 \tag{4.4.14}$$

The first condition, Eq. 4.4.12, is the balance of momentum expressed in the initial configuration,

$$\left(\frac{\partial \bar{\psi}}{\partial F_{iA}} \right)_{,A} + \rho b_i = 0 \, . \tag{4.4.15}$$

The second balance law, Eq. 4.4.13, is similar in form to the conservation of momentum, but, instead, represents the balance of biochemical forces associated with the evolution of the relaxed configuration (Section 4.3.4),

$$\mathcal{J} \frac{\partial \bar{\psi}}{\partial \mathcal{F}_{\alpha B}} \mathcal{F}_{\beta B} + \bar{\psi} \mathcal{J} \delta_{\alpha\beta} - \mathbb{B}_{\alpha\beta} = 0 \tag{4.4.16}$$

Comparing Eq. 4.4.16 to the proposed biochemical balance law, Eq. 4.3.11, we infer that in equilibrium,

$$\mathbb{C}_{\alpha\beta} = \mathcal{J} \frac{\partial \bar{\psi}}{\partial \mathcal{F}_{\alpha B}} \mathcal{F}_{\beta B} + \bar{\psi} \mathcal{J} \delta_{\alpha\beta} \, . \tag{4.4.17}$$

Evaluating the surface integrals in Eq. 4.4.14 results in:

$$\mathcal{T}_{iA} = \mathcal{J}\frac{\partial \bar{\psi}}{\partial F_{iA}}\,. \tag{4.4.18}$$

4.5 Entropy Inequality

We now consider the entropy inequality to determine an evolution equation for the inelastic deformation. We recall that

$$\psi = \Sigma - \theta\eta \tag{4.5.1}$$

where ψ is the Helmholtz energy per unit mass, Σ is the internal energy per unit mass, θ is the absolute temperature, and η the entropy per unit mass. The Helmholtz energy is a thermodynamic potential representing the extractable work from a system. Taking the time derivative of Eq. 4.5.1 and solving for the entropy rate yields Eq. 4.5.2.

$$\dot{\eta} = -\dot{\psi}\theta^{-1} + \dot{\Sigma}\theta^{-1} - \dot{\theta}\theta^{-1}\eta \tag{4.5.2}$$

We now assume the Helmholtz free energy is a function of the constituitive variables $F_{iA}, \mathcal{F}_{\alpha A}, \theta,\ \theta_{,A}$ and $\mathcal{D}_{\alpha\beta}$. $\theta_{,A}$ is the temperature gradient in the initial configuration. $\mathcal{D}_{\alpha\beta}$ is the $sym\left(\mathcal{L}_{\alpha\beta}\right) = sym\left(\dot{\mathcal{F}}_{\alpha A}\mathcal{F}^{-1}_{A\beta}\right)$ which is an objective quantity. The time derivative of ψ yields,

$$\begin{aligned}\dot{\psi} &= \frac{d}{dt}\left[\psi\left(F_{iA}, \mathcal{F}_{\alpha A}, \theta, \theta_{,A}, \mathcal{D}_{\alpha\beta}\right)\right] \\ &= \frac{\partial\psi}{\partial F_{iA}}\dot{x}_{i,A} + \frac{\partial\psi}{\partial\mathcal{F}_{\alpha A}}\dot{\mathcal{F}}_{\alpha A} + \frac{\partial\psi}{\partial\theta}\dot{\theta} + \frac{\partial\psi}{\partial\theta_{,A}}\dot{\theta}_{,A} + \frac{\partial\psi}{\partial\mathcal{D}_{\alpha\beta}}\dot{\mathcal{D}}_{\alpha\beta}\end{aligned} \tag{4.5.3}$$

The Clausius-Duhem entropy inequality in integral form is as follows,

$$\frac{d}{dt}\int_V \rho\mathcal{J}\,\eta\,dV - \int_V \theta^{-1}\,r + \rho\mathcal{J}\,\kappa\,\eta_h\,dV + \int_{\partial V}\theta^{-1}q_A N_A dS_0 \geq 0\,,$$

or, after applying the divergence theorem,

$$\int_V \rho\mathcal{J}\dot{\eta} - \rho\mathcal{J}\Delta\eta\,\dot{\mathcal{F}}_{\alpha A}\mathcal{F}^{-1}_{A\alpha} - \theta^{-1}\,r + \left(\theta^{-1}q_A\right)_{,A}\,dV \geq 0\,.$$

where we have used,

$$\Delta\eta = \eta_h - \eta \tag{4.5.4}$$

We have added a source of entropy, η_h, which is associtated with the change of mass in the system. In local form, the inequality reduces to,

$$\rho\mathcal{J}\left[\dot{\eta} - \Delta\eta\dot{\mathcal{F}}_{\alpha A}\mathcal{F}^{-1}_{A\alpha}\right] - \theta^{-1}\,r + \theta^{-1}q_{A,A} - \theta^{-2}\theta_{,A}\,q_A \geq 0 \tag{4.5.5}$$

where r and q_A are volume and surface heat sources, respectively. We now insert Eq. 4.3.13 into Eq. 4.5.5 and expand yielding,

$$\rho\mathcal{J}\left[-\dot{\psi} + \dot{\Sigma} - \dot{\theta}\eta\right] - \rho\mathcal{J}\theta\,\Delta\eta\,\dot{\mathcal{F}}_{\alpha A}\mathcal{F}^{-1}_{A\alpha} + q_{A,A} - \theta^{-1}\theta_{,A}q_A - r \geq 0$$

$$-\rho\mathcal{J}\dot{\psi} + \mathcal{T}_{iA}\dot{x}_{i,A} + \mathbb{C}_{\alpha\beta}\dot{\mathcal{F}}_{\alpha A}\mathcal{F}^{-1}_{A\beta} + \rho\mathcal{J}\,\Delta\psi\dot{\mathcal{F}}_{\alpha A}\mathcal{F}^{-1}_{A\alpha} - \rho\mathcal{J}\dot{\theta}\eta - \theta^{-1}\theta_{,A}q_A \geq 0$$

where we have used,

$$\Delta\psi = \Delta\Sigma - \theta\,\Delta\eta\,. \tag{4.5.6}$$

Upon insertion of and Eq. 4.5.3 and grouping like terms, we arrive at the following:

$$\left[-\rho\mathcal{J}\frac{\partial\psi}{\partial F_{iA}} + \mathcal{T}_{iA}\right]\dot{x}_{i,A} + \left[\mathbb{C}_{\alpha\beta}\mathcal{F}^{-1}_{A\beta} - \rho\mathcal{J}\frac{\partial\psi}{\partial\mathcal{F}_{\alpha A}} + \rho\mathcal{J}\,\Delta\psi\mathcal{F}^{-1}_{A\alpha}\right]\dot{\mathcal{F}}_{\alpha A}$$
$$-\rho\mathcal{J}\left[\frac{\partial\psi}{\partial\theta} + \eta\right]\dot{\theta} - \rho\mathcal{J}\frac{\partial\psi}{\partial\theta_{,A}}\dot{\theta}_{,A} - \rho\mathcal{J}\frac{\partial\psi}{\partial\mathcal{D}_{\alpha\beta}}\dot{\mathcal{D}}_{\alpha\beta} - \theta^{-1}\theta_{,A}q_A \geq 0$$

To ensure this inequality holds for all possible $\dot{x}_{i,A}, \dot{\theta}, \dot{\theta}_{,A}$ and $\dot{\mathcal{D}}_{\alpha\beta}$, we require that,

$$\rho\mathcal{J}\frac{\partial\psi}{\partial F_{iA}} = \mathcal{T}_{iA}\,, \tag{4.5.7}$$

$$\frac{\partial\psi}{\partial\theta} = \eta\,, \tag{4.5.8}$$

$$\frac{\partial\psi}{\partial\theta_{,A}} = 0\,, \tag{4.5.9}$$

$$\frac{\partial\psi}{\partial\mathcal{D}_{\alpha\beta}} = 0\,. \tag{4.5.10}$$

With these requirements, the remainder of the inequality, Γ, is,

$$\Gamma = \left[\mathbb{C}_{\alpha\beta}\mathcal{F}^{-1}_{A\beta} - \rho\mathcal{J}\frac{\partial\psi}{\partial\mathcal{F}_{\alpha A}} + \rho\mathcal{J}\,\Delta\psi\mathcal{F}^{-1}_{A\alpha}\right]\dot{\mathcal{F}}_{\alpha A} - \theta^{-1}\theta_{,A}q_A \geq 0\,. \tag{4.5.11}$$

Notice that the difference in current and incoming Helmholtz free energy, $\Delta\psi$, appears in the remainder. We now phrase the entropy inequality in terms of the elastic deformation constituitive variables using the following definitions.

$$\bar{\psi} = \rho\psi \qquad\qquad P_{i\beta} = \frac{\partial\bar{\psi}}{\partial f_{i\beta}}$$

$$\sigma_{ij} = P_{i\beta}f_{j\beta} \qquad\qquad \rho\frac{\partial\psi}{\partial\mathcal{F}_{\alpha A}} = -P_{j\beta}\,f_{j\alpha}\,\mathcal{F}^{-1}_{A\beta}$$

With these identities, the entropy remainder can alternatively be expressed as,

$$\Gamma = \left[\mathbb{C}_{\alpha\beta}\mathcal{F}^{-1}_{A\beta} - \mathcal{J}\frac{\partial\bar{\psi}}{\partial\mathcal{F}_{\alpha A}} + \mathcal{J}\rho\Delta\psi\mathcal{F}^{-1}_{A\alpha}\right]\dot{\mathcal{F}}_{\alpha A} - \theta^{-1}\theta_{,A}q_A \geq 0$$

$$\left[\mathbb{C}_{\alpha\beta} + \mathcal{J}f_{i\alpha}P_{i\beta} + \mathcal{J}\rho\Delta\psi\delta_{\alpha\beta}\right]\mathcal{F}^{-1}_{A\beta}\dot{\mathcal{F}}_{\alpha A} - \theta^{-1}\theta_{,A}q_A \geq 0$$

$$\left[\mathbb{C}_{\alpha\beta} + \mathcal{J}f_{i\alpha}\sigma_{ij}f^{-1}_{\beta j} + \mathcal{J}\rho\Delta\psi\delta_{\alpha\beta}\right]\mathcal{L}_{\alpha\beta} - \theta^{-1}\theta_{,A}q_A \geq 0$$

where $\mathcal{L}_{\alpha\beta}$ is the deformation rate of $\boldsymbol{\mathcal{F}}$ as defined in Section 4.2. At thermodynamic equilibrium $\Gamma = 0$, and the first partial derivatives of Γ also equal zero. We define equilibrium as,

$$\mathcal{L}_{\alpha\beta} = 0$$

$$\theta_{,A} = 0$$

and evaluate thier first partial derivatives equal zero. First, the partial with respect to the deformation rate, which yields:

$$\left.\frac{\partial \Gamma}{\partial \mathcal{L}_{\alpha\beta}}\right|_0 = 0$$

$$\mathbb{C}^0_{\alpha\beta} + \mathcal{J} f_{i\alpha} \sigma_{ij} f^{-1}_{\beta j} + \rho \mathcal{J} \Delta\psi \delta_{\alpha\beta} = 0$$

$$\mathbb{C}^0_{\alpha\beta} = -\mathcal{J}\left(\rho\, \Delta\psi \delta_{\alpha\beta} + f_{i\alpha} \sigma_{ij} f^{-1}_{\beta j}\right) . \tag{4.5.12}$$

Note that this is equivalent to the equilibrium result from the variational calculation when $\psi_h = 0$ (see Eq. 4.4.17).

Then, taking the partial derivative with respect to the temperature gradient,

$$\left.\frac{\partial \Gamma}{\partial \theta_{,A}}\right|_0 = 0$$

$$-\theta^{-1}\, q^0_A = 0$$

$$q^0_A = 0\,. \tag{4.5.13}$$

We now assume that $\mathbb{C}_{\alpha\beta}$ can be represented as the sum of its equilibrium, $\mathbb{C}^0_{\alpha\beta}$, and dissipative parts, $\mathbb{C}^{'}_{\alpha\beta}$,

$$\mathbb{C}_{\alpha\beta} = \mathbb{C}^0_{\alpha\beta} + \mathbb{C}^{'}_{\alpha\beta} \tag{4.5.14}$$

We further assume a form of the dissipative stress to be

$$\mathbb{C}^{'}_{\alpha\beta} = a\, \mathcal{L}_{\alpha\beta} \tag{4.5.15}$$

where $a \geq 0$ and may depend on the independent constitutive variables. From this we can now define an evolution equation for $\mathcal{L}_{\alpha\beta}$ through the balance of biochemical forces (Eq. 4.3.11),

$$\mathbb{C}_{\alpha\beta} - \mathbb{B}_{\alpha\beta} = 0 \tag{4.5.16}$$

Inserting Eq. 4.5.12 and Eq. 4.5.15 into Eq. 4.5.16, we determine a relation for $\mathcal{L}_{\alpha\beta}$.

$$-\mathcal{J}\left(\rho\, \Delta\psi \delta_{\alpha\beta} + f_{i\alpha} \sigma_{ij} f^{-1}_{\beta j}\right) + a\, \mathcal{L}_{\alpha\beta} + \mathbb{B}_{\alpha\beta} = 0$$

$$\mathcal{L}_{\alpha\beta} = \frac{1}{a}\left[\mathcal{J}\left(f_{i\alpha}\sigma_{ij}f^{-1}_{\beta j} + \rho\Delta\psi\delta_{\alpha\beta}\right) - \mathbb{B}_{\alpha\beta}\right] \tag{4.5.17}$$

We now define the homeostatic state as an external biochemical force,

$$\mathbb{B}_{\alpha\beta} = \mathcal{J}\, f_{i\alpha}\sigma^{*}_{ij}f^{-1}_{\beta j}$$

where σ^{*}_{ij} is the homeostatic Cauchy stress in the current configuration. With this assumed form, $\mathcal{L}_{\alpha\beta}$ reduces to a linear function that depends on the difference between current and homeostatic stress states.

$$\mathcal{L}_{\alpha\beta} = \frac{1}{a}\mathcal{J}\left[f_{i\alpha}\left(\sigma_{ij} - \sigma^{*}_{ij}\right)f^{-1}_{\beta j} + \rho\Delta\psi\delta_{\alpha\beta}\right] \tag{4.5.18}$$

The evolution equation proposed in Eq (4.5.18) represents a hybrid between two accountings of the energy entering or leaving the system via mass addition or subtraction. The incoming mass is often assumed to enter with the free energy of the current body, namely, $\psi_h = \psi$ [49, 114, 92]. This results in $\Delta\psi = 0$ in the Eq. (4.5.18) leaving only the Cauchy stress difference as the mechanism of growth and shape change. Alternatively, others have not included an external source term ($\psi_h = 0$) [6, 42]. This assumes that the creation of new mass reduces the rate of internal energy production by consuming energy from other external sources, specifically the biochemical stress-work, $\mathbb{C}_{\alpha\beta}\,\mathcal{L}_{\alpha\beta}$. This results in evolution equations that contain an Eshelby stress term (see Section 4.7),

$$\mathbb{E} := \psi\boldsymbol{I} - \boldsymbol{f}^{T}\psi'\,. \tag{4.5.19}$$

The external biochemical force is then assumed to be a homeostatic Eshelby tensor, $\mathbb{E}_0 = \mathbb{B}$, creating a set of evolution equations which are driven by the difference of two Eshelby tensors. The homeostatic Eshelby tensor, $\mathbb{E}_0$, is related to the homeostatic Cauchy stress through the following relation,

$$\mathbb{E}^{0}_{\alpha\beta} = \rho\psi^{*}\delta_{\alpha\beta} - f_{i\alpha}\sigma^{*}_{ij}f^{-1}_{\beta j} \tag{4.5.20}$$

where $\psi*$ is the homeostatic free energy. We now evaluate the physical significance of $\Delta\psi \neq 0$ through a series of numerical examples.

4.6 Numerical Examples of Evolution Equations

To demonstrate the behavior of the model, we first analyze a set of homogenous deformations applied to a solid, incompressible, hyperelastic cube. We use a Neo-Hookean material with free energy potential,

$$\bar{\psi} = \mu \left(I_b - 3 \right) , \tag{4.6.1}$$

where μ is the shear modulus and $I_b = tr(\boldsymbol{b})$ is the first invariant of the left Cauchy-Green tensor of the elastic deformation. From the hyperelastic potential, we obtain the Cauchy stress as

$$\sigma_{ij} = 2\mu \left(b_{ij} - \frac{1}{3} b_{kk} \delta_{ij} \right) - p\, \delta_{ij} , \tag{4.6.2}$$

where the first term is the deviatoric part of the stress and p is the hydrostratic pressure associated with incompressibility. The value and form of the homeostatic stress, σ^*_{ij}, will be defined as needed. Using this material law, the evolution equation (Eq. 4.5.18) is,

$$\begin{aligned}
\mathcal{L}_{\alpha\beta} &= \frac{2\mu\mathcal{J}}{a} \left[f_{i\alpha} \left(b_{ij} - \frac{1}{3} b_{kk} \delta_{ij} - \frac{p}{2\mu}\, \delta_{ij} - \frac{\sigma^*_{ij}}{2\mu} \right) f^{-1}_{\beta j} + \frac{\Delta\bar{\psi}}{2\mu} \delta_{\alpha\beta} \right] \\
&= \frac{2\mu\mathcal{J}}{a} \left[f_{i\alpha} f_{i\gamma} f_{j\gamma} f^{-1}_{\beta j} - \left(\frac{1}{3} b_{kk} + \theta \right) \delta_{\alpha\beta} + \frac{1}{2\mu} \left(\Delta\bar{\psi}\, \delta_{\alpha\beta} - f_{i\alpha} \sigma^*_{ij} f^{-1}_{\beta j} \right) \right] \\
&= \frac{2\mu\mathcal{J}}{a} \left[c_{\alpha\beta} - \left(\frac{1}{3} b_{kk} + \theta \right) \delta_{\alpha\beta} + \frac{1}{2\mu} \left(\Delta\bar{\psi}\, \delta_{\alpha\beta} - f_{i\alpha} \sigma^*_{ij} f^{-1}_{\beta j} \right) \right] .
\end{aligned} \tag{4.6.3}$$

In this, we have rephrased the hydrostatic pressure as a strain, $\theta = p/(2\mu)$. Note that because the Cauchy stress of a Neo-Hookean material is linear in b_{ik}, the evolution equation becomes a function of the right Cauchy Green tensor, $c_{\alpha\beta}$.

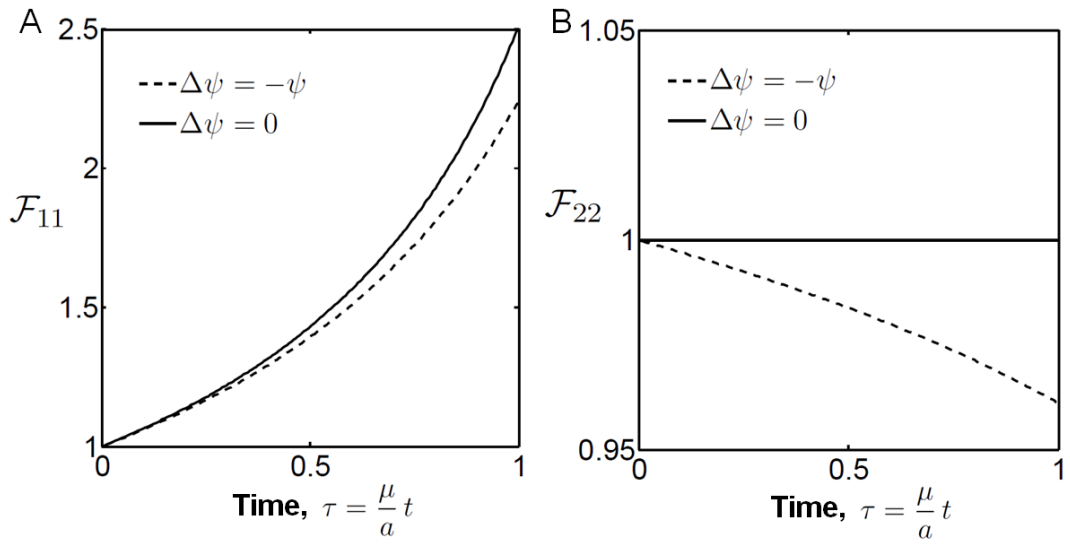

Figure 4.2: Non-zero $\Delta\bar{\psi}$ results in isotropic volume addition or subtraction depending on its value. A) Plot of the axial inelastic component versus normalized evolution time. B) Plot of non-axial normal components versus normalized time. $\alpha = 1.1$, $\mu = 10$, $a = 10$

4.6.1 Fixed Stress

Consider now the situation where the elastic stretch ratios are held fixed, $\boldsymbol{f} = const$. As a consequence of this, the stress is fixed, and we expect continuous growth of the inelastic components. We first consider the stress state associated with uniaxial elongation,

$$\boldsymbol{f} = \text{diag}\left(\alpha, \alpha^{-1/2}, \alpha^{-1/2}\right)$$

and

$$\boldsymbol{b} = \text{diag}\left(\alpha^2, \alpha^{-1}, \alpha^{-1}\right) ,$$

with the initial conditions

$$\boldsymbol{F}(\boldsymbol{X}, \tau_0) = \boldsymbol{f} \qquad \text{and} \qquad \boldsymbol{\mathcal{F}}(\boldsymbol{X}, \tau_0) = \boldsymbol{I} .$$

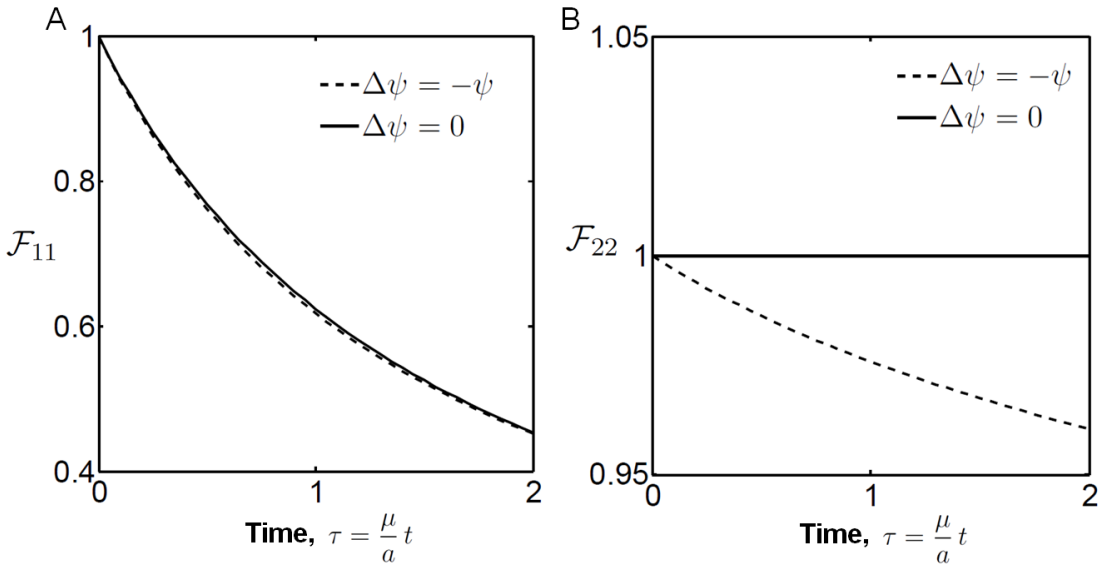

Figure 4.3: Inelastic Jacobian $\mathcal{J}$ affects qualitative behavior of growth under compression A) Plot of the axial inelastic component versus normalized evolution time. B) Plot of non-axial normal components versus normalized time. $\alpha = 0.9$, $\mu = 10$, $a = 10$

The hydrostatic pressure is determined by assuming the stress in the x_3 direction is zero, resulting in

$$p = 2\mu\left(\alpha^2 - \alpha^{-1}\right).$$

For this problem, we assume that the homeostatic stress is zero, $\boldsymbol{\sigma}^* = \mathbf{0}$, and, instead, focus on $\Delta\bar{\psi}$. We employ two different levels of incoming free energy,

$$\Delta\bar{\psi} = -\bar{\psi} \qquad \text{no incoming energy},$$

and

$$\Delta\bar{\psi} = 0 \qquad \text{equal incoming energy}.$$

These are the two extremes currently discussed in the literature. It is unlikely that new tissue enters the body with a free energy exceeding the current free energy, $\Delta\psi > 0$. We then solve for the components of $\boldsymbol{\mathcal{F}}$ over time by integrating Eq. 4.6.3 using the Matlab function ode45.

A fixed uniaxial stress state associated with $\alpha = 1.1$ causes the cube to elongate indefinitely in the direction of loading (Figure 4.2). When $\Delta\bar{\psi} = 0$, no in-

elastic deformation occurs in the stress-free directions (x_2 and x_3). In constrast, when no incoming energy is included, these directions slightly retract (dashed line Figure 4.2B). The rate of axial elongation is also reduced by the $\Delta\psi$ term. Similar behavior was observed under uniaxial compression ($\alpha = 0.9$, Figure 4.3), except that the growth rate was further reduced by the diminishing inelastic Jacobian. This limited the divergence between the $\mathcal{F}_{11}$ curves for $\Delta\bar{\psi} = 0$ and $\Delta\bar{\psi} = -\bar{\psi}$, compared to the elongation case. The Jacobian is also responsible for the difference in concavity of the evolution of $\mathcal{F}_{22}$ between tensile and compressive loading.

The effect of $\Delta\bar{\psi}$ is similar in a homogeneous shear deformation,

$$\boldsymbol{f} = \begin{bmatrix} 1 & k & 0 \\ 0 & 1 & 0 \\ 0 & 0 & 1 \end{bmatrix} \qquad \text{and} \qquad \boldsymbol{b} = \begin{bmatrix} 1+k^2 & k & 0 \\ k & 1 & 0 \\ 0 & 0 & 1 \end{bmatrix},$$

in which k is a constant shear deformation and $p = (2/3)\mu\, k^2$. The growth rate of the normal components decreased when $\Delta\bar{\psi} = -W$, including the stress-free x_3 direction. The shear components were affected by $\Delta\bar{\psi}$ (Figure 5.23A). This is a consequence of the Jacobian in Eq. 4.6.3, which relates the volume change due to normal component growth to the remodeling rate of the shear component.

4.6.2 Fixed Displacement

We now investigate a situation in which the total deformation is fixed. Consider the shear deformation,

$$\boldsymbol{F} = \begin{bmatrix} 1 & k & 0 \\ 0 & 1 & 0 \\ 0 & 0 & 1 \end{bmatrix},$$

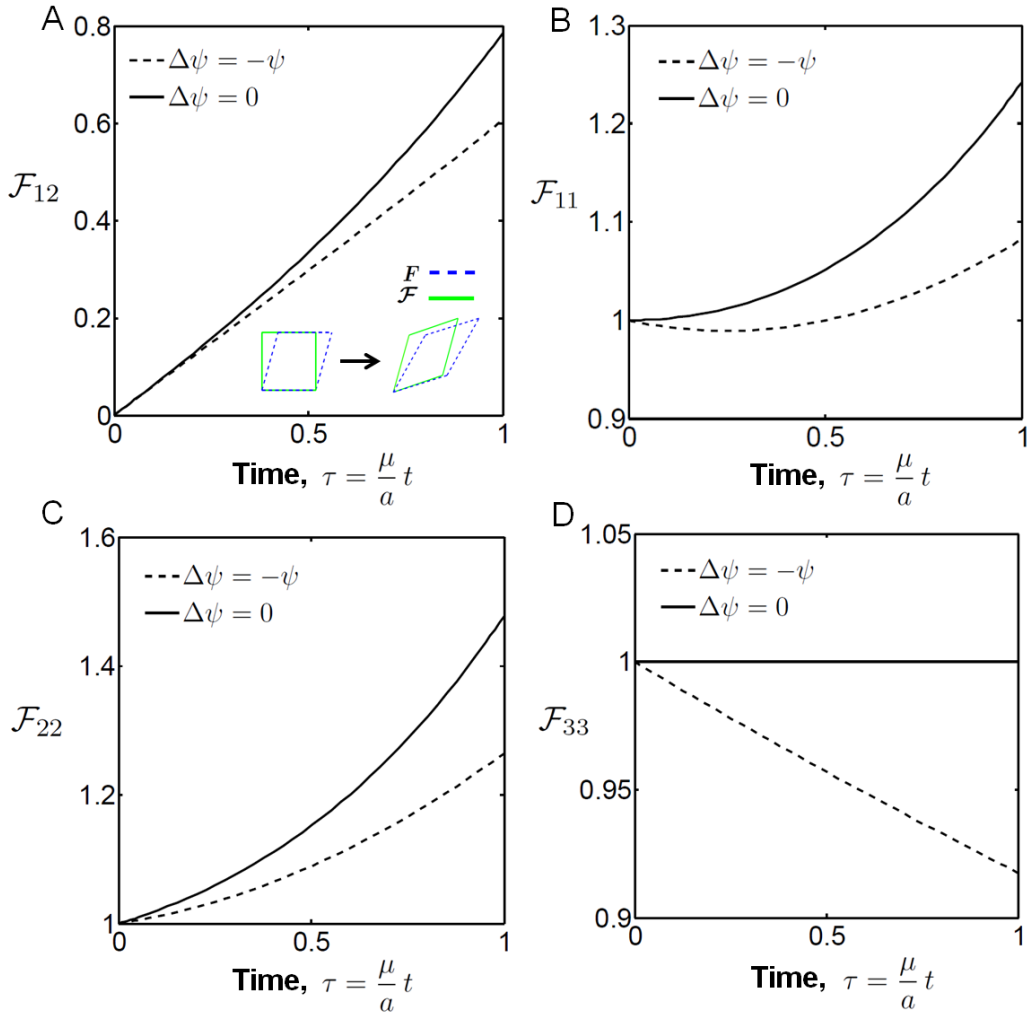

Figure 4.4: Fixed Shear Stress A) Inelastic shear deformation over time B) Evolution of inelastic shear component, $\mathcal{F}_{12} = \mathcal{F}_{21}$. C) $\mathcal{F}_{11}$ component D) $\mathcal{F}_{22}$ component. $k = 0.3$, $\mu = 10$, $a = 10$

where at time equal zero,

$$\boldsymbol{f}(\boldsymbol{X}, \tau_0) = \boldsymbol{F} \qquad \text{and} \qquad \boldsymbol{\mathcal{F}}(\boldsymbol{X}, \tau_0) = \boldsymbol{I}\,.$$

Because $\boldsymbol{F}$ is fixed, the deformation rate of the total deformation is zero. Using a kinematic relation (Eq. 4.2.5) we see that,

$$l_{ik} + f_{i\alpha}\mathcal{L}_{\alpha\beta}f^{-1}_{\beta k} = 0\,, \tag{4.6.4}$$

which describes how the elastic and inelastic deformations will trade-off as the evolution occurs. The incompressibility assumption requires that $l_{kk} = 0$, which, from Eq. 4.6.4, implies that $\mathcal{L}_{\alpha\alpha} = 0$. Therefore, shape change occurs without growth. As a consequence of this condition, the hydrostatic pressure becomes,

$$\begin{aligned}
\mathcal{L}_{\alpha\alpha} = 0 &= \frac{2\mu\mathcal{J}}{a}\left[c_{\alpha\alpha} - \left(\frac{1}{3}b_{kk} + \theta\right)\delta_{\alpha\alpha} + \frac{1}{2\mu}\Delta\bar{\psi}\,\delta_{\alpha\alpha}\right] \\
0 &= \frac{2\mu\mathcal{J}}{a}\left[c_{\alpha\alpha} - b_{kk} - 3\theta + \frac{3}{2\mu}\Delta\bar{\psi}\right] \\
0 &= -\theta + \frac{1}{2\mu}\Delta\bar{\psi}\,.
\end{aligned}$$

The hydrostatic pressure is, therefore, equal to the free energy difference:

$$p = \Delta\bar{\psi}\,. \tag{4.6.5}$$

The evolution of the inelastic deformation is unaffected by the choice $\Delta\bar{\psi}$ in this fixed displacement situation. However, because of Eq. 4.6.5, the stress state evolution is affected. In Figure 4.5F we see that the negative incoming free energy induces a negative hydrostatic pressure; that is, the tissue is under tension. All of the normal stress components are shifted by this pressure. The tissue is attempting to retract, which requires a tensile restoring force to maintain the position of the surface. Interestingly, the nature of σ_{22} and σ_{33} is exchanged between the two $\Delta\bar{\psi}$ cases. For instance, notice that when $\Delta\bar{\psi} = 0$, the approach to equilibrium is shallow for σ_{22} and steep for σ_{33}. The opposite is true when $\Delta\bar{\psi} = -\bar{\psi}$. This case study demonstrates how shape change can relieve stress in displacement-constrained situations.

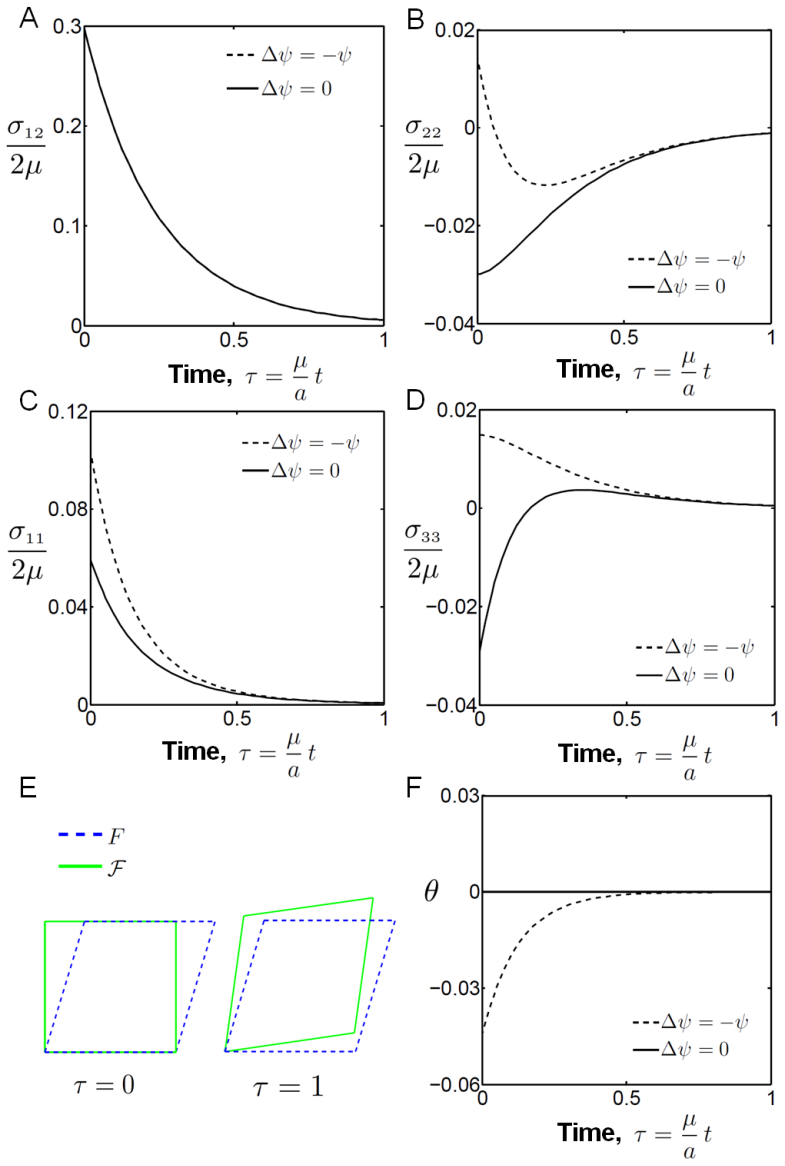

Figure 4.5: Stress relaxes under fixed shear deformation. A) The shear stress evolution was unaffected by the choice of free energy term. Interesting nonlinear effects occur in B) σ_{22} C) σ_{11} and D) σ_{33} components. The negative free energy essential inverts the evolution of these two components. The negative hydrostatic pressure F) initially increases the σ_{11} stress. E) Schematic of the initial and equilibrium states of the inelastic deformation. Note that the elastic deformation contains rotation. $k = 0.3$, $\mu = 10$, $a = 10$

4.7 Discussion

Computational and experimental approaches to understanding tissue growth have significantly expanded in recent years. With the increase of investigators

in this area, the perspectives on growth and remodeling mechanisms have become increasingly diverse [5]. Debated entities range from whether the multiplicative decomposition adequately captures growth behavior to what is the fundamental mechanical measure of homeostasis. In this paper, we analyzed how the thermodynamic assumptions regarding the incoming mass affect the evolution of tissue shape and volume. We included the potential for growth in shear and evaluated the consequence of this through some numerical examples. These results provide a possible mechanism for how tissue growth and shape change may be directed by mechanical loading.

Although some have adopted the "accretive force balance" approach to derive specific constitutive relationships for the inelastic evolution [6, 137], the formulation has yet to acquire broad acceptance. The necessity of this "configurational" force balance has been questioned by Ganghoffer et al [62], who suggest instead that the intermediate configurational forces naturally arise from the change in integration domains and from defining stress in terms of the free energy per unit initial volume, $\bar{\psi}_0 = \rho_0 \psi$. In a strictly mechanical theory this is true, but in our view, a biochemical and/or biomolecular forces must be postulated [41]. The biochemical force balance provides a natural means to incorporate bio-related forces and their conseqeunces, such as the homeostatic stress state implemented in this work and others [175, 150]. A form of this balance law has also been used to relate the growth rate to the concentration of nutrients, which introduces a more concrete example of a bio-chemical force [7] Future implementations of this balance law with mechanistic biological data will determine whether this construction is physically justified.

The occurrence of an Eshelby-like tensor in the evolution equations for the

inelastic deformation has been the focus of recent discussion in growth mechanics [117, 49, 42]. Originally derived to determine the energy change associated with the translocation of a material inhomogeneity [50, 51], the Eshelby stress tensor is considered the key driving force of elastoplasticity [34], crack propagation [52], and volumetric growth [49, 62]. In our formulation, the presence of an Eshelby-like term depends on whether or not a source of free energy was included in the energy balance. If no external energy source was included the evolution equation included an isotropic free energy term. If the external energy source was equal to the current internal free energy, only the physical and biochemical stress-work terms and thermal terms would remain in the entropy inequality. The numerical examples demonstrated that the free energy source primarily affected the amount of volume change. This was particularly clear in the case of uniaxial loading with no source term, in which the directions orthogonal to the loaded axis retracted, even though they were stress free (Figure 4.2B).

The magnitude of the free energy of newly created tissue is still an open question. Newly synthesized fibronectin, a key extra-cellular matrix protein, must be stretched in order expose sites for binding to other matrix proteins [170, 104, 95]. This supports the inclusion of a non-zero free energy source. In the assembly of collagen, a ubiquitous and critical extra-cellular matrix protein, applied stretch increases the density and organization of fibers which resulted in increased mechanical stiffness [142]. This suggests that the magnitude of the incoming free energy may depend on the current stretch. In a homogeneous, single constituent model, spatially varying amounts of incoming free energy translates into spatially-dependent volume change. Although a limitation of the current model, the single constituent formulation made the physical signifi-

cance of the free energy source term clear.

The biomechanical loads that regulate the homeostasis are still debated [5]. Stress, strain, and strain energy criteria have been proposed [135, 36], but have been difficult to experimentally distinguish. Evidence from artery mechanics, plant remodeling, and embryonic development point to stress as the response stimulus [33, 15, 16], however several *in vitro* studies show elevated cellular activity under strain [71]. In this work, we employ a homeostatic Cauchy stress state, which has been implemented in several previous works [154, 173, 175]. This is distinct from an Eshelby homoestatic stress proposed in recent works [6, 7]. In the Eshelby formulation the homeostatic Cauchy stress and the isotropic free energy term are related by evaluating the free energy at the same deformation. Our formulation allows the homeostatic Cauchy stress and the homeostatic free energy to vary independently, allowing for both a cell specific stress response and an extra-cellular matrix protien specific entrance of free energy.

Inelastic shear deformations have been underrepresented in examples employed to illustrate growth and shape change. Examples of growth often constrain it to material principal axes, which is justified by either the symmetry of the loading conditions or by the underlying microstructure [150, 6, 4]. It is important to consider shear deformations in high shear environments, such as fluid flow in the developing heart and vascular structures [124, 191]. A recent growth model of avian valve development showed a decrease in valve elongation and condensation when inelastic shear deformation was not included [23] (see chapter 5). Inelastic shear deformations may also be involved in the torsion seen in blastomeres of cleaving Xenopus zygotes [38] and the looping of

the primitive heart tube [177]. Furthermore, there is increasing evidence that cells can sense shear stresses [69], suggesting that growth models should have the capacity to evolve into a sheared configuration in response to this stimulus.

In conclusion, we have presented a self-contained derivation of a finite elastic-inelastic model of growth. In doing this, we have engaged the current question of the need for a biochemical force balance and the question of how the free energy of the incoming mass affects the evolution of the tissue. A limitation of our study is the implementation of a single constituent theory, which does explicitly treat interactions between difference constituents. An incompressible, single constituent theory also requires a spatially constant density, which is unrealistic for some tissues. Our examples includes inelastic shear deformations, that involve shape changes but not growth. Future variants growth models with more biological detail, including multiple constituents, molecularly based remodeling forces, and variable growth rates are needed to better capture mechanisms of growth and shape change observed in embryonic development.

CHAPTER 5

COMPUTATIONAL SIMULATION OF HEMODYNAMIC DRIVEN GROWTH AND REMODELING OF EMBRYONIC ATRIOVENTRICULAR VALVES

Embryonic heart valves develop under continuous and demanding hemodynamic loading. The particular contributions of fluid pressure and shear tractions in valve morphogenesis are difficult to decipher due to an inability to decouple them experimentally. In this study, we present a computational model of HH27 atrioventricular (AV) embryonic valve (cushion) growth and remodeling, incorporating experimentally derived physiological hemodynamic and tissue mechanics inputs. Fluid loads on an axisymmetric AV cushion/myocardial section were derived through a semi-iterative scheme of fluid simulation, followed by evolution of the cushion, and then an update of fluid forces in response to the new geometry. We demonstrate that the hemodynamic loads place the AV cushion in a compressive stress state. We assumed the cushions possessed an intrinsic homeostatic stress state that was isotropic, homogeneous, and compressive. Simulations determined that the homeostatic stress magnitude modulated the rate of volume addition during the evolution, but not the re-shaping of the cushion. We found that the pressure distribution on the AV cushion was sufficient to generate the elongated and condensed leaflet-like morphology through inducing tissue resorption on the inflow side of cushion and expansion on the outflow side. Conversely, shear tractions minimally altered tissue volume, but regulated the remodeling of tissue near the cushion surface, particular at the leading edge. Significant shear and circumferential residual stresses developed as the cushion evolved in shape. This model provides insight into how natural and perturbed mechanical environments may direct AV

valvulogenesis, and suggests mechanobiological mechanisms for valve growth, remodeling, and malformation.

5.1 Introduction

Atrioventricular valve formation is thought to be regulated by dynamic interactions between molecular and mechanical signaling. The primitive valves (cushions) initiate as gelatinous masses of hyluronan from the myocardial wall of the heart tube. A layer of endothelial cells line the inner surface of the heart tube, with the outer wall consisting of cardiomyocytes [67]. The endocardial cells lining the cushion invade the underlying matrix and acquire a mesenchymal phenotype through a process called the endocardial to mesenchymal transformation (EMT) (see illustrated reviews [140, 163, 27]). As the cushion matures, these mesenchymal cells remodel the matrix directing a transition from hyluronan to collagen based matrix, and a transition from globular to planar morphology [94, 88]. Significant advances have been made in identifying the key molecular signals needed for this initiation and maturation [27, 46, 140], yet little is known about the role of mechanical signaling in cushion development. The hemodynamic environment of the embryonic cushion rapidly increases in pressure over development, resulting in an exponential increase in cardiac output and heightened wall shear stresses [80, 191]. Concomitant with this increase in mechanical load, the AV cushions elongate to form thin, fibrous leaflets with increased extracellular matrix (ECM) proteins and greater mechanical stiffness [25, 28, 94].

These findings motivate the hypothesis that hemodynamic forces direct valve morphology and stimulate the turnover and remodeling of the internal

valve constituents. Surgical manipulations of heart development have demonstrated that altered hemodynamic flows result in defective cardiac morphology [78, 182]. The perturbed mechanical loads have included differences in local shear stress [79, 69], pressure [164], and myocardial activity [13]. The differential roles of pressure gradients or wall shear stress in directing AV valve morphogenesis are unknown. By understanding their specific roles, we could identify loading profiles that are defective, and/or determine which mechano-sensors to target in order to block the effect of the defective mechanical loading. However, uncoupling the effects of pressure and shear tractions is difficult to do experimentally.

Computational approaches to the study of the mechanical regulation of morphogenesis are an attractive alternative to address these issues of coupled loading and predictability. Numerical models have provided insights into the fluid dynamics of the embryonic heart, such as the transition of peristaltic to pulsatile flow [178] and the distribution of normal and shear forces in AV canal [18, 124]. Recent gains in fluorescent and ultrasound imaging have enhanced these computational studies by providing critical information on the magnitude and temporal nature of *in vivo* hemodynamic loads [55, 79, 191]. Previous stress-driven growth models have qualitatively captured the morphology of several developmental phenomenona such as invagination [127], gastrulation [173, 174], cardiac looping [149], and ventricle growth [108]. Stress-based growth laws assume that tissue morphology is a direct response to the current stress state, or to the difference in current stress from a homeostatic stress state. This is in contrast to growth models phrased in terms of strain or strain energy, with corresponding homeostatic states assumed as functions of these quantities [36]. Experimental evidence in plants and embryos supports stress as the mechanical criterion

to which living organisms respond [16, 15]. Stress-based evolution equations for growth also arise naturally when the entropy inequality is employed [7, 63], further supporting this form of growth law.

The objective of this study was to develop and implement a computational framework incorporating both fluid-structure interaction and growth mechanics to identify mechanical mechanisms sufficient to reproduce valve-like morphology. Physiological fluid flow parameters and cushion material properties were utilized. The results indicate that fluid pressure directs spatially dependant volume addition and removal resulting in valve elongation. Shear tractions do not significantly alter volume, but instead stimulate tissue distortion, particularly near the cushion surface. Growth and remodeling induces residual stresses which may significantly alter (or guide) cushion formation over time. This model provides an initial framework of mechanically induced valve development on which further biological detail may be incorporated.

5.2 Methods

5.2.1 Kinematics

Consider a stress-free body in the reference configuration at $t = 0$, denoted as the initial configuration β_0 in Fig. 5.1. The body undergoes a combined elastic-inelastic deformation from the initial to current configuration β defined by the mapping $\boldsymbol{x} = \boldsymbol{x}(\boldsymbol{X}, t)$. The observable, total deformation, $\boldsymbol{F} = \frac{d\boldsymbol{x}}{d\boldsymbol{X}}$, includes components of growth, remodeling and elastic deformation. We assume $\boldsymbol{F}$ can be expressed as a multiplicative decomposition of the elastic components and

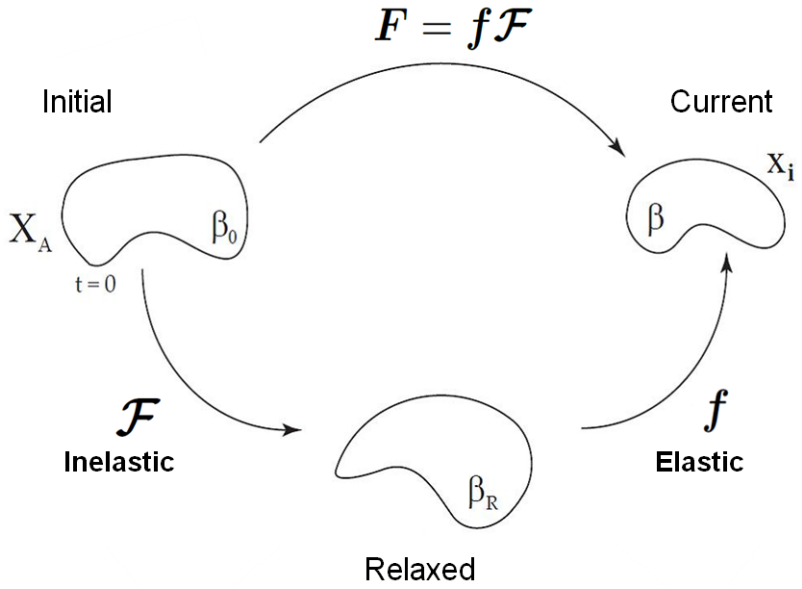

Figure 5.1: Multiplicative decomposition of the deformation gradient. The observable deformation, $\boldsymbol{F}$, is decomposed into an elastic, $\boldsymbol{f}$, and inelastic, $\boldsymbol{\mathcal{F}}$, deformation. All volume change occurs through $\boldsymbol{\mathcal{F}}$ as the elastic deformation is assumed to be isochoric, $\det(\boldsymbol{f}) = 1$. All growth and remodeling is described by the inelastic deformation. The initial, relaxed, and current bodies are referred to as β_0, β_R, and β, respectively.

growth and remodeling (inelastic) components as done in several preceding works [154, 114, 150]. The total deformation is thereby defined as the product of the inelastic, $\boldsymbol{\mathcal{F}}$, and the elastic, $\boldsymbol{f}$, deformations.

$$\boldsymbol{F} = \boldsymbol{f}\boldsymbol{\mathcal{F}} \tag{5.2.1}$$

The elastic deformation is considered nearly incompressible, $\det(\boldsymbol{f}) \approx 1$, and is the deformation used to calculate the elastic stress. The inelastic deformation comprises both volumetric changes representative of growth and shape changes representative of remodeling. This deformation will be prescribed through a constituitive relation. Although the inelastic deformation does not directly contribute to the elastic stress, the geometric incompatibilities from differential growth and remodeling induce elastic residual stresses required to maintain

material continuity.

5.2.2 Material Law

The material properties of the avian AV cushions have previously been characterized by fitting an isotropic, exponential hyperelastic material law (Eq. $5.2.2$) to experimental data [25].

$$W = \frac{C}{2}\left\{exp\left(\alpha\left[I_1 - 3\right]\right) - 1\right\} + \frac{1}{D}\left(J-1\right)^2 \tag{5.2.2}$$

Parameters C and α are the linear and nonlinear material constants, respectively, of the material law, while D is inversely related to the bulk modulus which enforces the incompressibility constraint. I_1 is the first invariant of the left Cauchy-Green stretch tensor $\boldsymbol{b} = \boldsymbol{f}\boldsymbol{f}^T$, and $J = \det(\boldsymbol{f})$ is the Jacobian of the elastic deformation. From the strain energy function (Eq. 5.2.2), the Cauchy stress is derived as

$$\boldsymbol{\sigma} = \frac{1}{J}\frac{\partial W}{\partial \boldsymbol{f}}\boldsymbol{f}^T \tag{5.2.3}$$

$$= \frac{\alpha C}{J} exp\left[\alpha\left(I_1 - 3\right)\right]\boldsymbol{b} + \frac{2}{D}\left(J-1\right)\boldsymbol{I}. \tag{5.2.4}$$

Using the pipette aspiration technique, Buskohl et al [25] quantified the stiffness of HH25, HH29 and HH34 AV cushion and presented the data in terms of strain energy density. The strain energy density was defined as the area under the stress-stretch ratio curve of a uni-axial loaded bar from $\lambda = [1, 2]$, with closed form expression shown in Eq. 5.2.5.

$$W_{12} = \frac{C}{2}\left[exp\left(2\alpha\right) - 1\right] \tag{5.2.5}$$

Buskohl et al [25] reported significantly stiffer material properties in the plane of the tissue versus that in the trans-planar direction at HH36, indicating the

Table 5.1: Fluid/Solid Material Parameters

Item	Value	Units
Density	1060	$\frac{kg}{m^3}$
Viscosity	0.003	[Pa − s]
R	0.5	mm
Re	5	–
α	0.3	–
C	100	Pa
D	2 E-03	Pa^{-1}
W_{12}	41	Pa
a_0	1 E-02	$\left[\frac{1}{Pa\,t}\right]$

development of material aniostropy (see chapter 2). As the pipette data for the HH29 cushion was likely underestimating the cushion stiffness, we attempted to compensate for this by increasing the linear parameter, C, from C = 2 Pa to C = 100 Pa. This increased the strain energy density of the tissue from $W_{avg} = 0.84$ Pa to W_{avg} = 41 Pa. We chose C = 100 Pa because it approximately halved the four orders of magnitude difference between the in-plane and trans-planar stiffness measurements. The nonlinear parameter, $\alpha = 0.3$, at HH29 was retained (Table 5.1).

5.2.3 Growth Law

In this growth model, the Cauchy stress is assumed to the key driver the growth and remodeling processes. The deformation rate of the inelastic tensor, $\mathcal{F}$, is

prescribed through the constituitive relation,

$$\boldsymbol{\mathcal{L}} = \dot{\boldsymbol{\mathcal{F}}}\boldsymbol{\mathcal{F}}^{-1} = a(r)\,\boldsymbol{f}^{T}\left(\boldsymbol{\sigma} - \boldsymbol{\sigma}^{*}\right)\boldsymbol{f}^{-T} \tag{5.2.6}$$

where $\boldsymbol{\sigma}^{*}$ is the homeostatic stress state and a is the radially dependent growth rate parameter. The concept of a homeostatic, or target stress, has been employed in several other growth models [154, 82, 150]. The homeostatic stress provides a non-zero stress state at which no growth occurs. In light of limited experimental data, we assumed the homeostatic stress to be a homogenous, isotropic compressive stress of magnitude p, (Eq. $5.2.7$).

$$\boldsymbol{\sigma}^{*} = -p\boldsymbol{I} \tag{5.2.7}$$

A compressive homeostatic state was chosen because the hemodynamic loads on the AV cushion are compressive in this simulation. We emphasize that this simulation models the average flow through the AV canal over one cardiac cycle. At specific times of the cardiac cycle, blood flow may produce regions of negative pressure on the cushion surface. These negative pressures have been observed in peak-flow simulations of avian AV canal [18], and in *in vivo* imaging of zebrafish heart tubes [55]. However, we hypothesize that growth and shape change are a result of the average mechanical loading because they occur on a much longer time scale than the peak loads of the cardiac cycle. An isotropic stress state was chosen to avoid any directional bias that distortional components would have introduced. The growth rate parameter was assumed to vary linearly in the radial direction of AV canal, promoting more growth near the surface of the cushion. This was motivated by the increased cell density near the cushion surface observed from hematoxylin stained histology sections of HH27 AV valves (Fig. 5.2). The exact formulation used in finite element (FE)

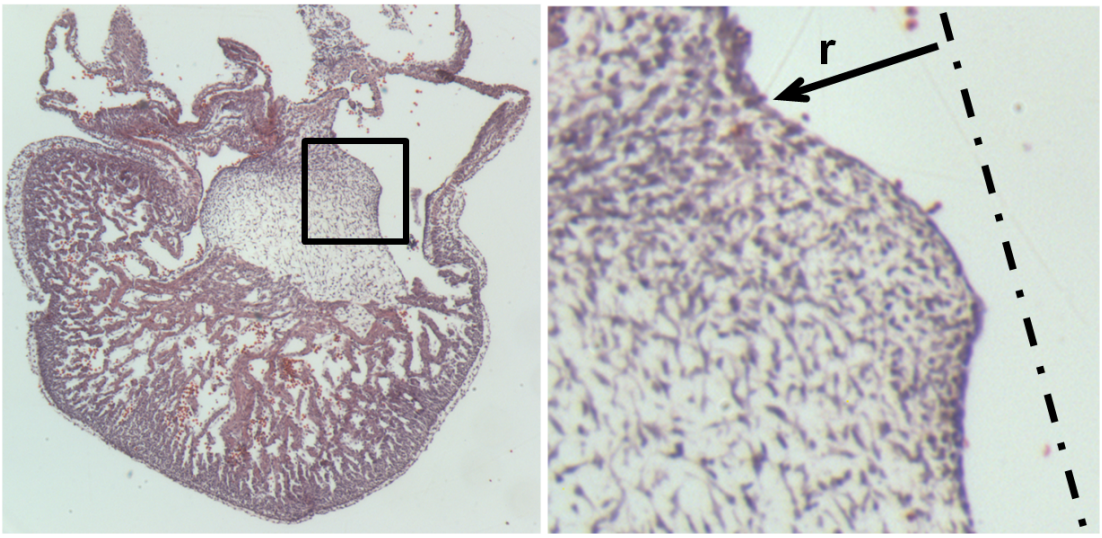

Figure 5.2: Increased cell density near the valve surface supports a gradient in the growth rate parameter, $a(r)$. Representative histology image of HH27 left AV valves stained with Weigerts hematoxylin. Magnification: 94x, 150x

implementation was

$$a(r) = \begin{cases} a_0 \left(1 - \frac{r}{R}\right) & : r \leq R \\ 0 & : r > R \end{cases}$$

where R is the radius of the AV canal (R=0.5 mm), and r the radial position from the axis of symmetry. A colormap of the growth rate parameter is presented in Fig.5.3B.

5.2.4 FE Implementation of the Fluid/Solid Model

The mechanical environment of the AV cushion is primarily defined by the hemodynamic forces generated through the pump action of the embryonic heart. To approximate these fluid loads, the AV canal and cushion were modeled together through an idealized axisymmetric geometry (Figure 5.3A). A

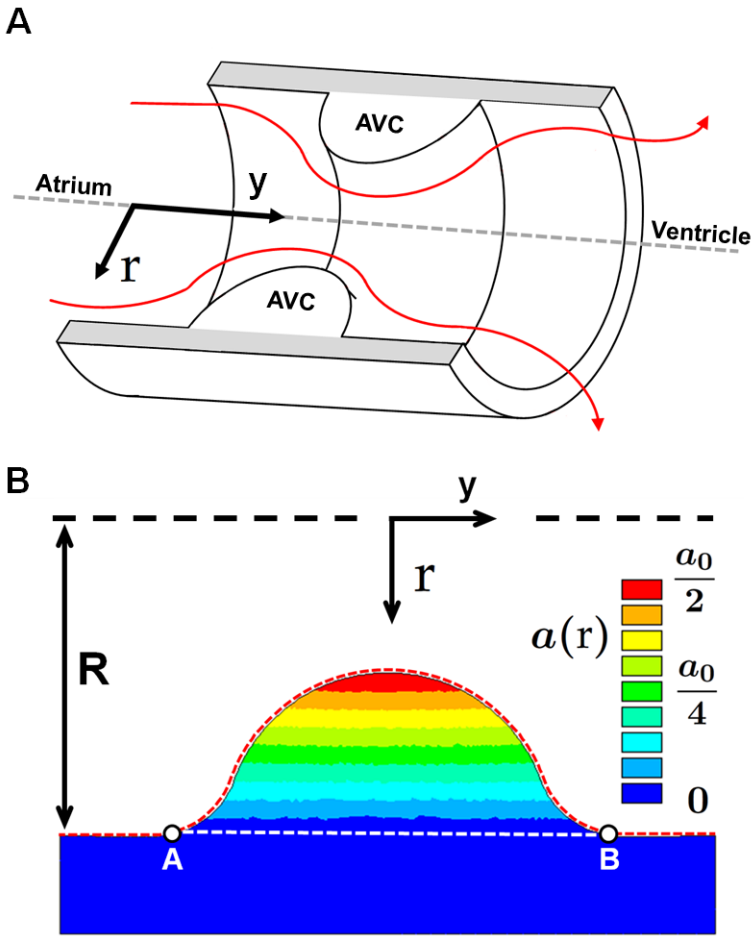

Figure 5.3: AV canal model geometry and growth rate gradient. a) Cross-section of the AV canal model geometry with AV cushions (AVC) shown inside. Red lines indicated blood flood from the atrium to ventricle. Gray band denotes myocardial wall. b) Colormap of growth rate parameter $a(r)$ over the 2D AVC cross-section. R is the radias of the AV canal and r is the radial coordinate as referenced from the axis of symmetry. The dashed red line from A to B denotes the cushion surface normalized from 0 to 1 in future figures. The AVC cross-sectional area is the area bounded by the red and white dashed lines. a_0 = 0.01 $[1/(\text{Pa}\,t)]$

cylindrical coordinate system was defined with the axial direction, y, oriented in the direction of flow and the radial direction, r, orthogonal to the axis of symmetry (Figure 5.3). The length to diameter ratio of the AV canal was 4 mm to 1

mm and the cushion was a near semi-circular cap of radius 0.25 mm. These dimension are supported by micro-CT images of AV canals [191] and a previously implemented computational model of AV canal blood flow [18]. The surface of the cushion and myocardial wall interface was smoothed to mitigate potential stress concentrations. The blood was simulated as an incompressible, Newtonian fluid, with density and viscosity of 1060 kg/m^3 and 0.003 Pa-s, respectively. Although blood is non-Newtonian, the viscosity is nearly constant in the range of shear rates used in our simulation [2].

The pressure and velocity profiles were determined using the axisymmetric Navier Stokes equations for the conservation of momentum and the continuity equation. All interior surfaces of the canal, including the cushions, had no slip boundary conditions (Figure 5.4 Step 1). The inflow and outflow pressures were selected to match experimental data of the time averaged velocity through the AV orifice (3.08 cm/s $\pm$ 0.99 cm/s , Yalcin et al [191]). The time averaged velocity was calculated by averaging AV orifice velocities over one cardiac cycle, or heartbeat. This is the mean loading velocity experienced by the cushion, and was considered a reasonable approximation of the loading range which directs cushion growth.

The peak velocity blood flow was simulated to compare the AV orifice velocities profiles from the experimental data and our model. This comparison was only used to validate our idealized geometry for the AV canal and cushion. The pressure drop across the AV canal necessary to match the AV orifice velocity for the average and peak flow conditions was 62 and 1200 dynes/cm^2, respectively. Reynolds numbers for each condition were Re = 5 and Re = 65 using the AV orifice diameter (0.5 mm) as the characteristic length. Both Reynolds numbers

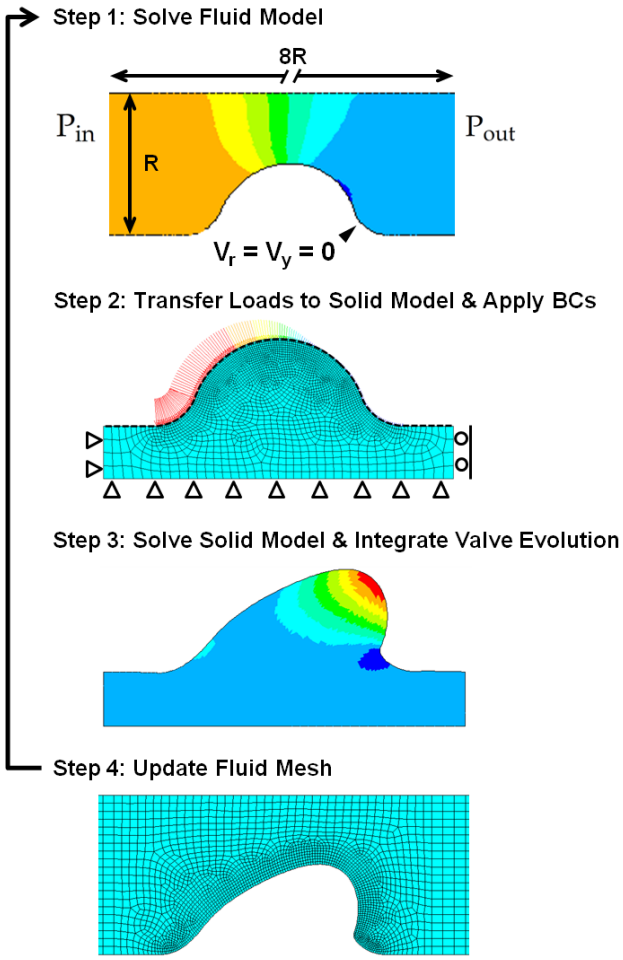

Figure 5.4: Schematic of fluid/solid interaction algorithm and boundary conditions(BC). Each iteration followed this process, Step 1: Simulate the fluid flow in the AV canal with no slip velocity BCs along the fluid/solid interface and a pressure drop, $\Delta P = P_{in} - P_{out}$, across the canal. Step 2: Transfer the pressure and wall shear stress loads from the fluid model to the cushion surface using the 1D surface elements (black dashed line). Apply displacement BCs to myocardium as shown. Step 3: Calculate the elastic stress and inelastic deformation for a set time of growth and remodeling, and then remove load. Step 4: Update the fluid mesh using the new relaxed cushion geometry. Repeat Steps 1-4.

are within the laminar range for flow in round tube ($Re_L < 2100$) [128]. The entrance length, l_e for fully developed flow in a tube with laminar flow is,

$$\frac{l_e}{D} = 0.06Re\,. \tag{5.2.8}$$

In the peak flow condition, the minimum entrance length needed is $l_e = 1.95$ mm. The entrance length used in the simulation was $l_e = 2$ mm.

The fluid/solid model was decoupled in the FE implementation, and solved through a semi-iterative approach. First the pressure and velocity profiles were determined from the fluid problem. The flow induced pressure and shear tractions on the AV cushion surface were then transferred to the solid model to simulate the elastic and inelastic deformations. After a set time of inelastic deformation, the fluid simulation was rerun with the evolved geometry, and the fluid forces were updated (see Figure 5.4).

The FE simulations were computed in ANSYS v12.1 using four-node quadrilateral elements in both the fluid and solid domains (meshes are shown in Figure 5.4). A series of two-node surface elements were used to transfer the normal and shear components of the fluid load onto the solid model (black dashed line in Figure 5.4, step 2). A total of 3400 fluid elements and 2400 solid elements were used in the simulations. The exponential material law and the growth law were implemented through the USERMAT subroutine (see Appendix C.2). At every integration point, the USERMAT subroutine would determine the elastic deformation gradient ($\boldsymbol{f} = \boldsymbol{F}\boldsymbol{\mathcal{F}}^{-1}$) and calculate the Cauchy stress and the spatial elasticity tensor. The growth tensor would also be updated through the following explicit integration scheme,

$$\mathcal{F}_{ij}\left(t+\Delta t\right) = \mathcal{F}_{ij}\left(t\right) + \mathcal{L}_{im}(t)\mathcal{F}_{mj}(t)\Delta t. \tag{5.2.9}$$

To assess the importance of the shear deformations in capturing the valve morphology, a simulation was performed in which the shear components of $\boldsymbol{\mathcal{F}}$ were

not allowed to evolve. In this case, the update of the growth tensor was

$$\mathcal{F}_{ij}\left(t+\Delta t\right)=\begin{cases}\mathcal{F}_{ij}\left(t\right)+\mathcal{L}_{im}(t)\mathcal{F}_{mj}(t)\Delta t & :i=j\\ 0 & :i\neq j\end{cases}$$

Computations were performed until $0.6 \leq \det(\boldsymbol{\mathcal{F}}) \leq 2.6$. Outside this range convergence difficulties occurred due to the accumulation of large inelastic deformations or large gradients of inelastic deformation. Simulation results were compared by using cross-sectional area, orientation angle, and color maps of computed mechanical outputs. The orientation angle was defined as the angle between the myocardial wall and the line that connects the bottom center of the cushion to the displaced position of the top-center point on the cushion surface (see Figure 5.17D).

5.2.5 Mesh Sensitivity

Some modifications were made to the cushion geometry to improve convergence. First, the intersection between the cushion and myocardial regions was filleted. This interface orginally formed a right angle, as highlighted by the red circles in Figure 5.5. The fillets reduced the stress concentrations in these regions. Secondly, the growth rate parameter, $a(r)$, was linearly varied, from zero at the myocardial wall, to unity at the axis of symmetry. While this was motivated by the heightened cell density near the cushion surface, as explained earlier, this also benefited the computation by reducing the jump between growth and no growth conditions at the myocardium interface. These two changes led to the final geometry used in the simulation.

A mesh sensitivity test was performed to determine if there were mesh de-

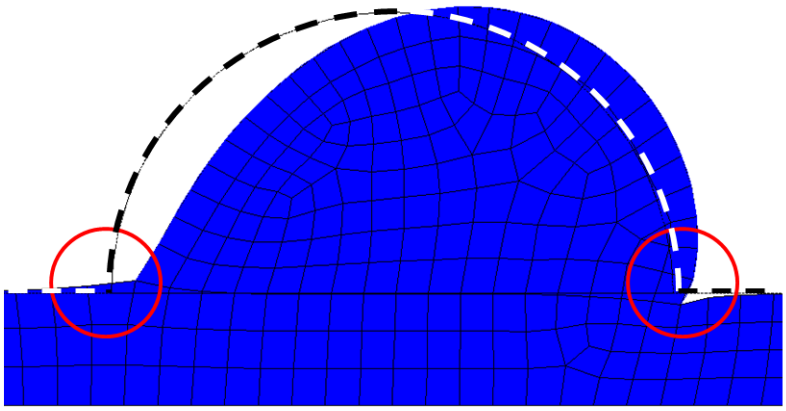

Figure 5.5: Early version of AV cushion geometry and mesh. Undeformed configuration is denoted by the dashed outline. The red circles highlight the initial sharp corners between the cushion and myocardium wall.

pendent effects. We varied the element density of the mesh relative to the mesh used for the simulation (MD=1). We evaluated a two-fold increase (MD=2) and a four-fold decrease (MD=0.25) in mesh density. The fluid and solid meshes for each mesh density are shown in Figure 5.6 and Figure 5.7, respectively.

Effect of mesh density on fluid results

We compared the initial fluid force profiles between the different meshes. The pressure profile did not differ significantly between any of the meshes (Figure 5.8). In contrast, the wall shear stress differed significantly between MD=0.25 and MD=2. The MD=0.25 shear stress profile lacked the symmetry present in the other curves (Figure 5.9). The MD=2 shear stress differed from MD=1 only at the center of the cushion surface, where the shear stress is maximal. The shear stress is more sensitive to the mesh density because it is deter-

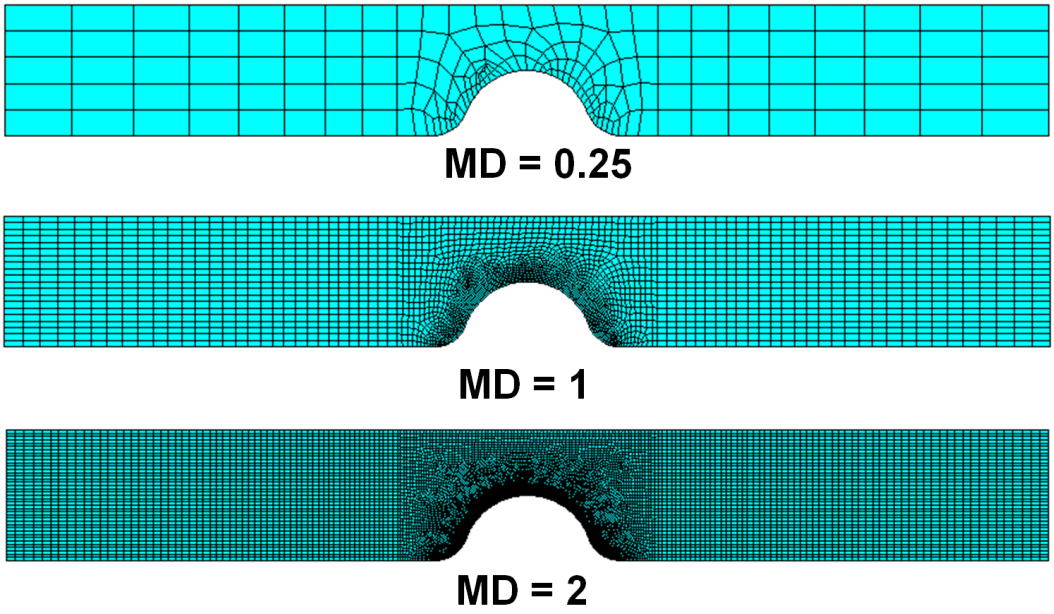

Figure 5.6: Fluid domain meshes used in the sensitivity analysis.

mined from a spatial derivative, specifically,

$$WSS = \mu \left(\frac{\partial u}{\partial y} \right)_{y=0}, \tag{5.2.10}$$

where μ is the dynamic viscosity, u is the fluid velocity parallel to wall surface, and y is the distance perpendicular to the wall. The approximation of this spatial derivative is less accurate with a coarse mesh than a fine mesh. The agreement between the MD=1 and MD=2 meshes suggested that the MD=1 mesh was sufficient for our analysis.

Effect of mesh density on solid results

We evaluated the effect of mesh density on the solid model through two metrics: 1) comparing the evolution of the cushion cross-sectional area with time, and, 2) comparing of the residual stress fields. The cross-sectional area

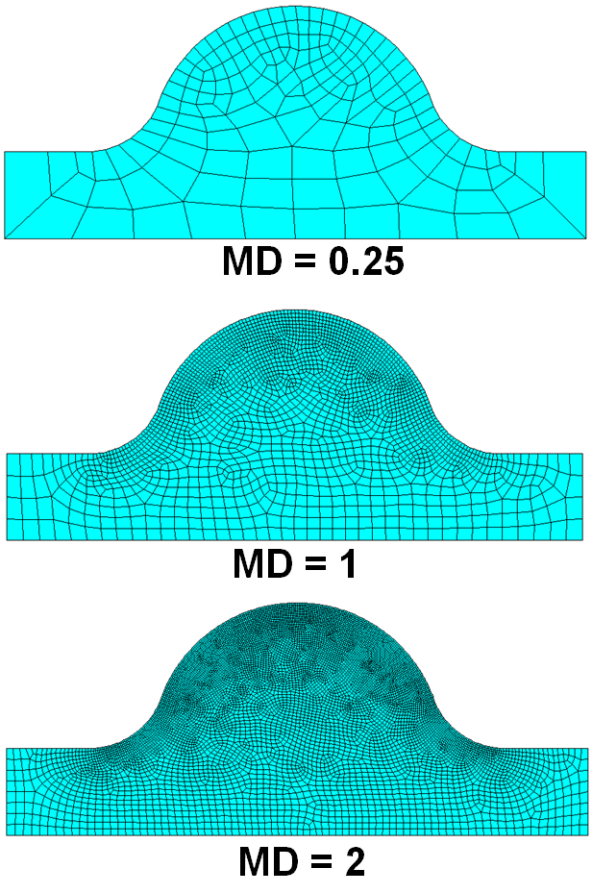

Figure 5.7: Solid domain meshes used in the sensitivity analysis.

evolutions for MD=0.25, MD=1, and MD=2 are shown in Figure 5.10. Mesh refinement beyond MD=1 did not alter cushion evolution. The evolution of the coarser mesh (MD=0.25) did not agree with the other mesh densities. However, the trend of the evolution agrees, as evidenced by the increasing area due to growth. Also, the evolved shape of the MD=0.25 is similar to the evolved shape of the MD=1 and MD=2 cushions shown in the Figure 5.11. The residual stress fields between MD=1 and MD=2 at time, $t = 1$, were minimally different. The higher resolution of the refined mesh resulted in slightly smoother contours. The coarser mesh inadequately approximated the residual stress, especially in the stress concentration regions at the cushion/myocardial interface. The consistency between the residual stress fields of the MD=1 and MD=2 meshes indicated that mesh refinement beyond MD=1 was not necessary.

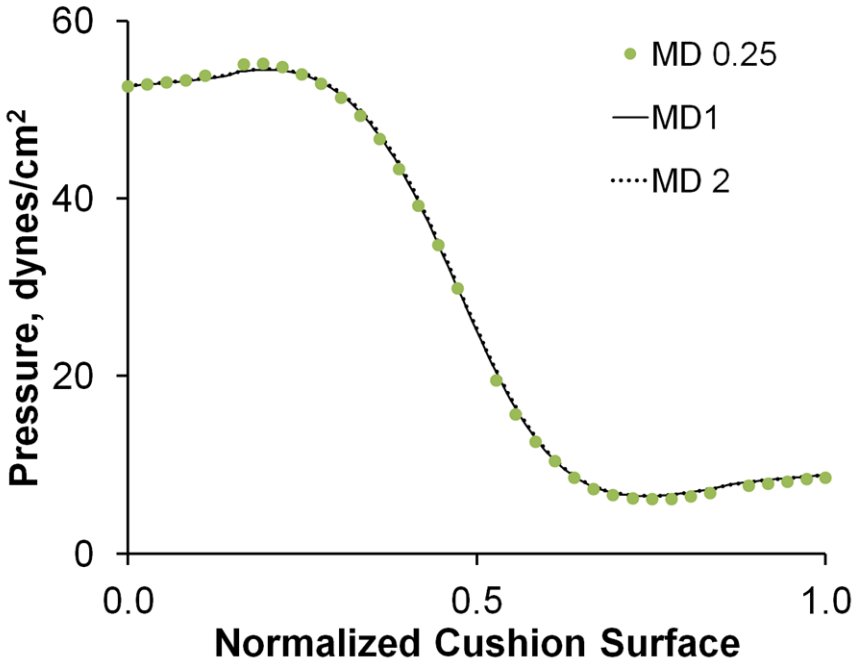

Figure 5.8: Initial fluid pressure profiles were minimally affected by variations in mesh density. Cushion surface normalized as shown in Figure 5.3

As mentioned at the end of Section 5.2.4, all simulations had convergence difficulties as the inelastic deformation evolved. Convergence predominantly failed on the exit flow surface in the region where the inelastic Jacobian reached a minimum. In this region, the Newton-Raphson residuals did not satisfy the convergence tolerance within the maximum number of Newton-Raphson iterations allowed (50) (Figure 5.12). The coarse mesh displayed a larger region of unconvergent NR residuals, but this region still coincided with the NR residual regions of the other meshes. This suggests that the cause of the convergence difficulties is similar for all the meshes.

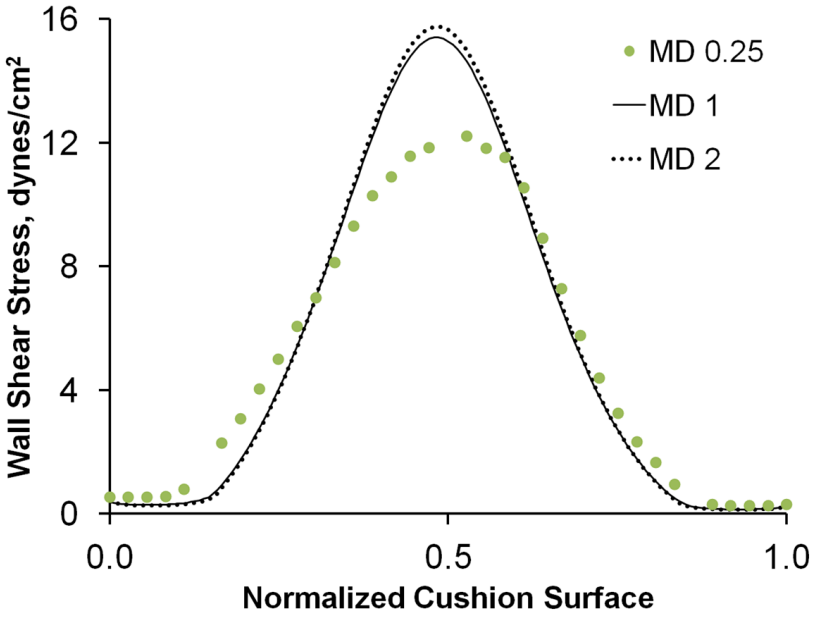

Figure 5.9: Wall shear stress distribution is sensitive to mesh density. Cushion surface normalized as shown in Figure 5.3

5.3 Results

Fluid forces apply compressive load to AV cushion

In our simulations, the pressure drop across the AV canal was adjusted to match the experimental average velocity at the AV orifice (3.08 $\pm$ 0.99 cm/s) [191]. A pressure drop of 62 dynes/cm^2 (0.046 mmHg) generated a parabolic velocity flow profile through the AV orifice with an average velocity of 3.07 cm/s (Figure 5.13). The Reynolds number through the AV orifice was Re=5 which can be considered laminar for tube flow. The flow profile in the AV orifice during peak velocity was previously calculated by using actual HH27 AV canal geometries (36.6 cm/s, Yalcin et al. [191]). To validate our idealized geometry, we simulated peak flow through the orifice (ΔP = 1200 dynes/cm^2, V_{avg} = 36 cm/s, Figure 5.13B). The velocity profile resembled a plug flow, and agreed well with the prior study. This indicated that the axisymmetric AV canal

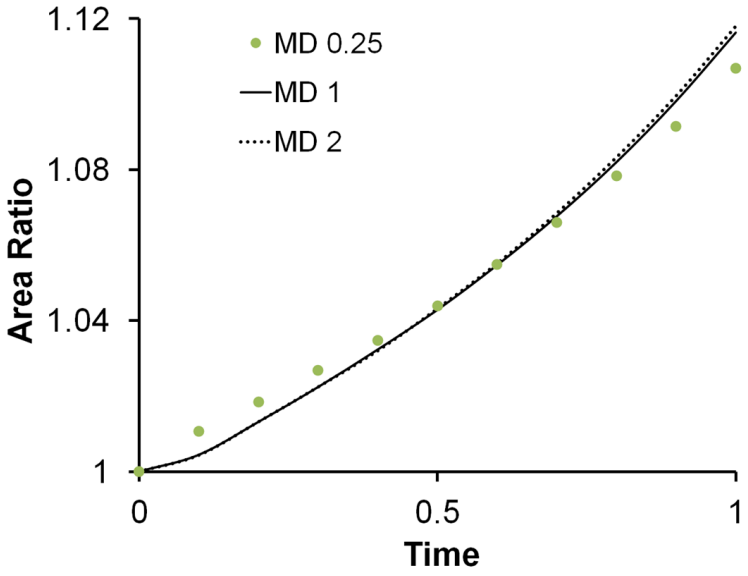

Figure 5.10: Evolution of cushion cross-sectional area with time for varying mesh densities. MD=1 and MD=2 are consistent, but MD=0.25 does not agree.

and semi-circular cushion geometries were adequate approximations. The AV canal pressure rapidly dropped from 52 dynes/ cm^2 on flow entrance surface to 7 dynes/cm^2 on the flow exit surface of the cushion, mainly due to the narrowing of the valve orifice. The shear tractions were oriented in the direction of flow, and their magnitude was symmetrically distributed about the cushion surface (solid, Figure 5.14B). As the cushion evolved, the fluid loads would change based on the evolved cushion geometry. Expansion of the cushion increased the pressure drop across the cushion surface, while retraction decreased the pressure drop (dash and dash-dot respectively, Figure 5.14A). A similar trend was seen in the shear traction, with the magnitude of maximum shear increasing with cushion expansion and decreasing with retraction (Figure 5.14B). The symmetry of the shear traction profile declined as the initial geometric symmetry of the cushions degenerated. Together, the average hemodynamic loads put the

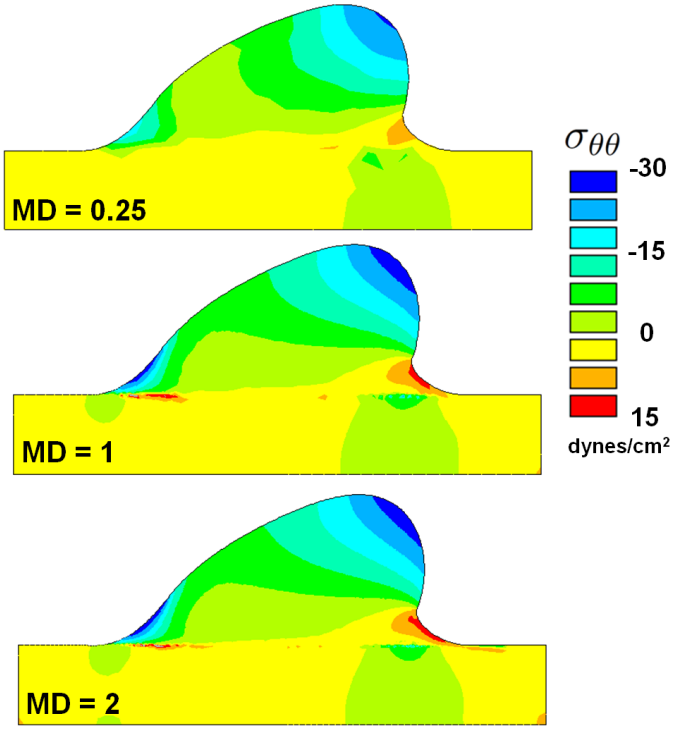

Figure 5.11: Circumferentual residual stress at time, $t = 1$, for varying mesh densities.

AV cushion in a compressive and sheared state throughout the cardiac cycle.

While clearly the geometry of the cushions affects the fluid force profile, the high to low pressure drop across the AV cushion should still occur even with irregularly shaped valves. However, the effect of irregular cushion geometry or cushion asymmetry was not analyzed in this study.

AV cushion volume change rate is negative under fluid loading

The time derivative of the inelastic jacobian ($\mathcal{J} = det(\boldsymbol{\mathcal{F}})$), or dilatation rate (Eq. 5.3.1), determines the rate at which material is introduced or removed during the inelastic deformation.

$$\dot{\mathcal{J}} = tr\,(\boldsymbol{\mathcal{L}})\,\mathcal{J} \tag{5.3.1}$$

Included in Eq. 5.3.1 is the growth rate parameter $a(r)$ which varies in the radial

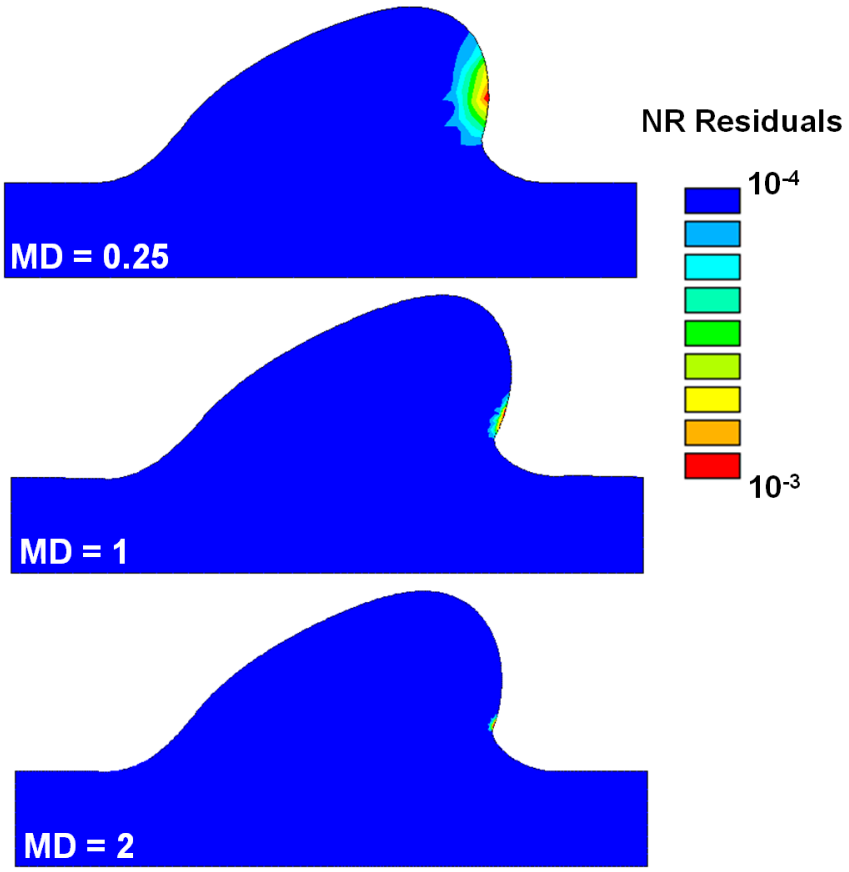

Figure 5.12: Newton-Raphson (NR) residuals were localized to the high resorption region on the flow exit surface. The non-convergent area increased with reduced mesh density (MD).

direction from a value of zero at the cushion/myocardium interface to a value of one on the axis of symmetry. The initial dilatation rate of the entire cushion under only the pressure load is negative, with the highest resorption rate at the top of the entrance surface (arrow 1, Figure 5.15A). The shear tractions induced a positive dilatation rate on the inflow side and a negative on the exit, but the rate is an order of magnitude less than the pressure induced dilatation rate. The difference in magnitude of the rates is due to 1) the difference in applied load magnitude, and 2) the nature of shear deformations to intrinsically drive distortion and not dilatation. This is seen in the case of a pure shear deformation,

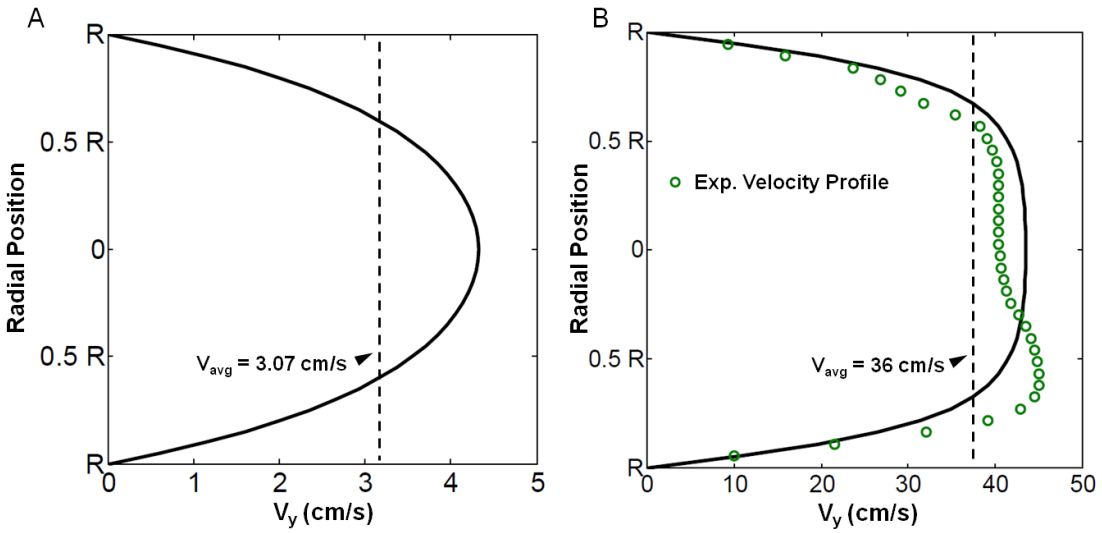

Figure 5.13: Average velocity over the cardiac cycle generates low Reynolds flow (Re = 5). A) Parabolic velocity profile at AV orifice under average flow condition, with approximated 3.07 cm/s spatial average. B) Plug flow velocity profile across the AV orifice when experimental peak velocity used in simulation. Plug flow agrees with calculated velocity profile using innate AV orifice geometry [191]. This indicates that the idealized initial geometry of this model is an appropriate approximation. (Re=65)

k, which contributes k^2 terms to the diagonal components of the stress, where typically $k < 1$. Though the pressure is the dominant load on the entrance side of the cushion, it is of the same order of magnitude as the shear tractions on the exit side of cushion near the top (Figure 5.14). It is in this region that the shear tractions modulate the inelastic dilatation rate, by increasing the resportion rate near the myocardial interface on flow exit side of the cushion (arrows 2a-b, Figure 5.15 A,C). The hemodynamic loads initially place the cushions into a state of resorption, which is only exacerbated by cushion expansion (dash-dot Figure 5.14).

We propose the tissue responds to this compressive load by acquiring a pref-

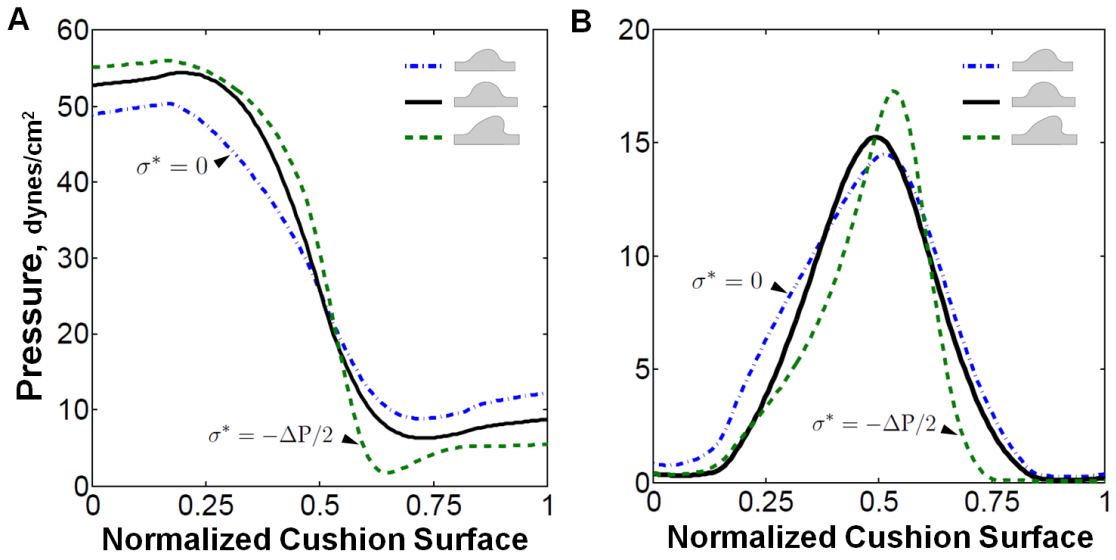

Figure 5.14: Valve-like morphology generates fluid force profiles that promote further valve elongation and condensation. A)Plot of pressure distribution on the AV cushions at initial loading (solid) and after evolution with $\boldsymbol{\sigma}^* = \mathbf{0}$ (dash-dot) and $\boldsymbol{\sigma}^* = -\frac{\Delta P}{2}\boldsymbol{I}$ (dash). B) The shear traction distribution becomes less symmetric as the cushion evolves asymmetrically. The maximal shear stress occurs at the leading edge of cushion. Normalized cushion surface denoted by red dashed line between point A and B in Figure 5.3B

erential, homeostatic, compressive stress state. With limited data on the magnitude and spatial distribution of the homeostatic stress, we assume a homogenous, isotropic stress state with a magnitude proportional to the pressure drop across the AV canal (ΔP). As this pressure largely determines the stress state of the AV cushions, it is plausible that the homeostatic stress state would be sensitive to this load. With the incorporation of this homeostatic stress state, the initial dilatation rate uniformly increases in the cushion, resulting in volumetric expansion on the flow exit side of cushion, while maintaining resorption on flow entrance side (Figure 5.15D). The combination of the fluid forces with homoestatic stress provides an initial rate of dilatation conducive to generate AV cushion morphology.

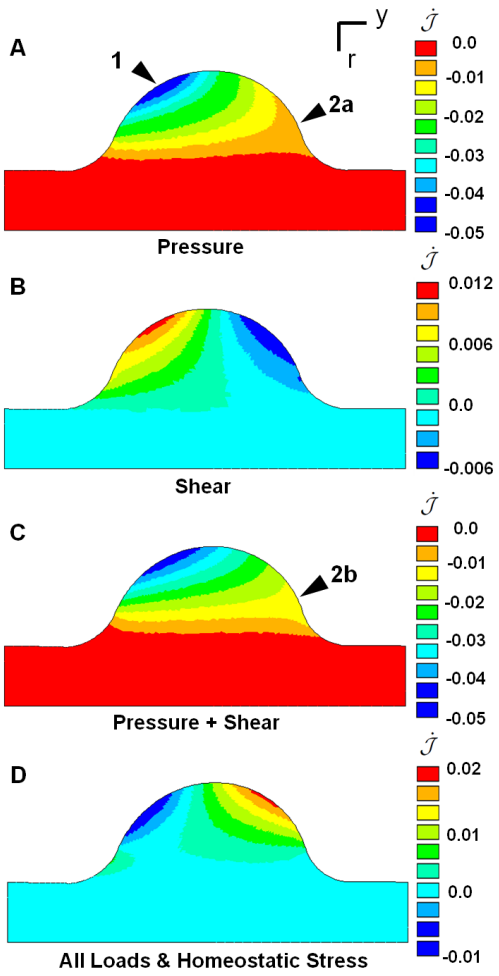

Figure 5.15: Compressive fluid loads stimulate negative dilation of AV cushion. Color maps of $\dot{\mathcal{J}} = \mathcal{J}\mathcal{L}_{\alpha\alpha}$ after initial loading with A) pressure load only, B) shear tractions only, C) all applied loads, and D) all loads with homogenous homeostatic stress $\boldsymbol{\sigma}^* = -\frac{\Delta P}{2}\boldsymbol{I}$. The resorption rate was highest at leading of inflow cushion surface (arrow 1). The shear tractions increase the rate of resorption on the back side of the cushion at the interface with the myocardium (arrow 2a-b). Compressive homeostatic stress shifts dilatation rate into a positive growth range. Color map in units of $[1/t]$.

Valve-like morphology generated with time averaged fluid forces and isotropic homoestatic stress conditions

The evolution of the AV cushion under different load conditions was ana-

lyzed through comparison of cross-sectional area and the migration of the top-center point of the cushion surface. As anticipated, without a homestatic stress the AV cushion volume contracted (Figure 5.16A), but in a spatially dependant manner. More volume was removed on inflow side of cushion than outflow, and the cushion even expanded in a small region on the inflow side at the cushion/myocardial interface (Figure 5.16C). The area ratio increased as the magnitude of the compressive homeostatic stress increased. A net increase in area was seen at magnitudes of $-\Delta P/2$ and ΔP, while $-\Delta P/4$ was still a net decrease. These area changes are evident from the evolved configurations shown in Figure 5.16B (t=0.6).

With $\boldsymbol{\sigma}^* = -\Delta P/2\, \boldsymbol{I}$ and no fluid load applied (NL), the AV cushion ballooned into the AV canal (Figure 5.16B). The cross-sectional area increased significantly, while maintaining a constant orientation angle of $\pi/2$. This determined that an isotropic homeostatic stress contributes directly to the volume change of the evolved cushion, and not the orientation. All loaded simulations had the same initial rate of change of the orientation angle, regardless of homeostatic tissue stress value. This indicated that the hemodynamic forces, not the homeostatic stress, directed the cushion shape change. The orientation angle began to diverge between the simulations after t=0.5, with large homeostatic stress magnitudes generating smaller angles (Figure 5.16D). This is a consequence of the elevated hemodynamic loads experienced by cushions with net volume addition.

The combination of the fluid forces with $\boldsymbol{\sigma}^* = -\Delta P/2\, \boldsymbol{I}$ resulted in increased cushion volume and elongated morhophology, similar to that of later stage valves. The other homeostatic stress magnitudes tested resulted in either de-

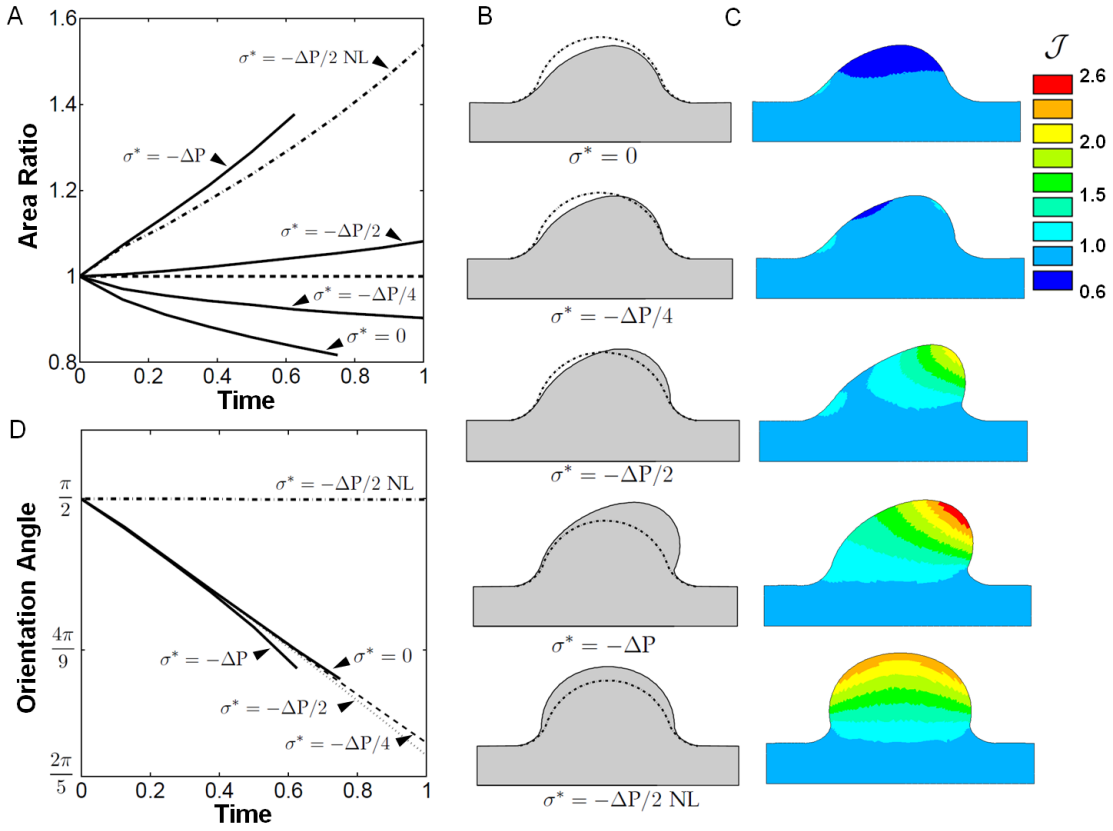

Figure 5.16: Fluid force distribution and homeostatic stress state generate valve-like morphology. A) Plot of AV cushion cross-sectional area normalized to initial area versus evolution time. Several compressive, isotropic, homeostatic stress states are shown. Note that a non-zero homeostat will stimulate remodeling when no load (NL) is applied. B) Plots of evolved configurations after removal of load for all scenarios. C) Colormap of the inelastic jacobian, $\mathcal{J} = det(\boldsymbol{\mathcal{F}})$, which details the spatial distribution of cushion expansion or resorption. D) The top center cushion surface evolves in the direction of flow as seen by the decrease in orientation angle over time. The orientation angle is defined as the angle between the y-axis and the line connecting the bottom center of the cushion with the deformed position of the top center cushion surface.

ficient or excessive in volume addition, creating retracted or thickened cushions (Figure 5.16B). New tissue was primarily introduced at the cushion tip, with tissue resorption occurring on the inflow cushion surface (Figure 5.16C). The evolved cushion geometry increases the fluid pressure on inflow surface and

reduces the pressure on the exit surface of the cushion (Figure 5.14A), encouraging this elongated shape. This suggests that cushion growth and remodeling is supported by a positive feedback process, whereby hemodynamic forces created by the asymmetric fin shape promote further condensation and elongation of the cushion.

Differential roles of pressure and shear traction in cushion formation

The hemodynamic loads on the AV cushion are sufficient to remodel a cushion with $\boldsymbol{\sigma}^* = -\Delta \mathrm{P}/2\, \boldsymbol{I}$ into a valve-like shape. Thiselongated and condensed shape is primarily a consequence of the fluid pressure, as evidenced by the pressure only simulations (Figure 5.17). As seen in the dilatation rates (Figure 5.15), the pressure stimulates tissue removal on the flow entrance side of cushion, and expansion on the flow exit side. The pressure significantly decreased the rate of volume increase compared to the no load evolution (Figure 5.17A). The shear tractions had little effect on cushion volume, although a slight increase was observed at the leading edge of the cushion in the full load model versus the pressure only model (Figure 5.17B). The magnitude of the shear tractions are maximal in this region, and promote distortion and thinning of the cushion leading edge.

The fluid pressure had little effect on orientation angle, while the shear tractions were the dominant stimuli of this metric (Figure 5.17C). The pressure directed the valve-like morphology, but did so without significant displacement of the top center cushion surface (Figure 5.17D). In this way, volume was selectively removed or added about the center line of the cushion. The top center point significantly migrated under shear loading. This may indicate that shear

tractions are still important for the remodeling of the AV cushion surface, even if not important for overall cushion volume change.

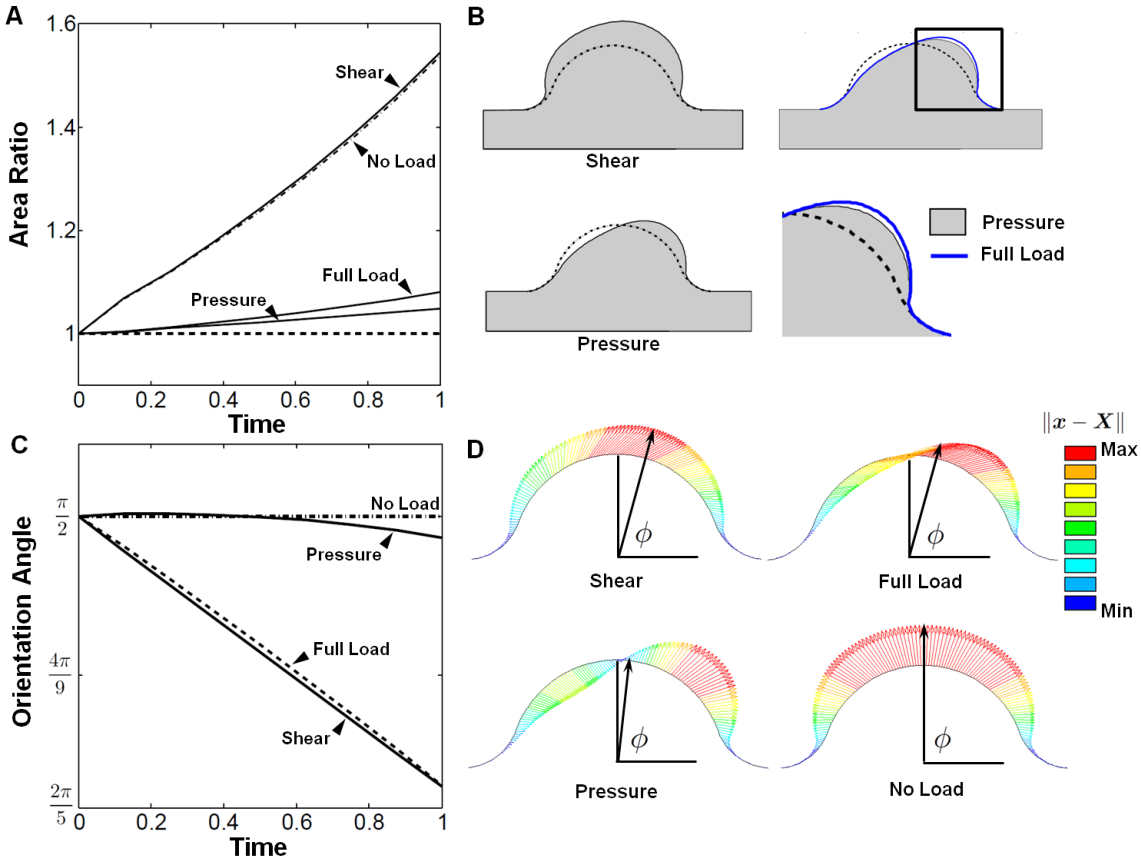

Figure 5.17: Pressure modulates volume change while shear directs surface remodeling. A) Area ratio plot for simulations with pressure only, shear tractions only, no load, and full load. B) Deformed configuration of each load scenario. The difference between full load and pressure only is shown in enlarged image of cushion leading edge. C) The shear traction directed migration of top center point. The pressure remodeled the cushion by removing and adding volume about the centerline of the cushion, displacing the center point very little. D) Vector plots depicting the displacement of cushion surface nodes and the orientation angle, ϕ. Vector length and color indicate displacement magnitude ($\|\boldsymbol{x} - \boldsymbol{X}\|$). Note that the isotropic growth due to the homoestatic stress does not affect the orientation angle.

Growth and remodeling induces residual stress

Radial and axial stress concentrations develop during the evolution at the cushion/myocardium interface on the flow exit cushion surface (arrows Figure 5.18 & 5.19). Both the pressure and shear tractions contribute to the location and intensity of this stress. After removal of the fluid load, the cushion relaxes to the evolved configuration, which is not stress free. The stresses in this configuration, termed residual stresses, are introduced by differential tissue growth and remodeling during the evolution. The cushion/myocardium interface develops residual stresses because of the difference in growth rate across that boundary, as the myocardium does not grow in this simulation. Even in the loaded state,

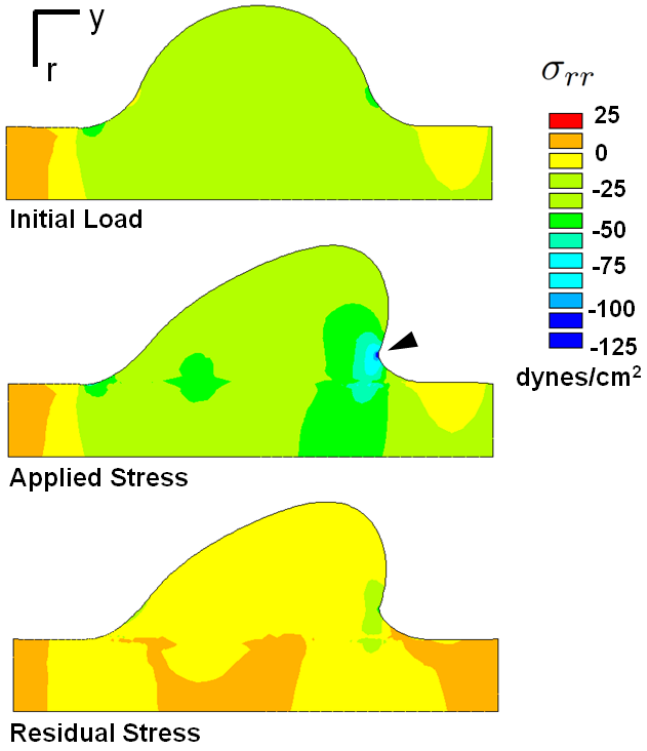

Figure 5.18: Radial residual stress. The residual stress in this direction is minor when compared to the applied stress state values. Significant compressive radial stress occurs at the cushion/myocardial interface on the flow exit side (arrow).

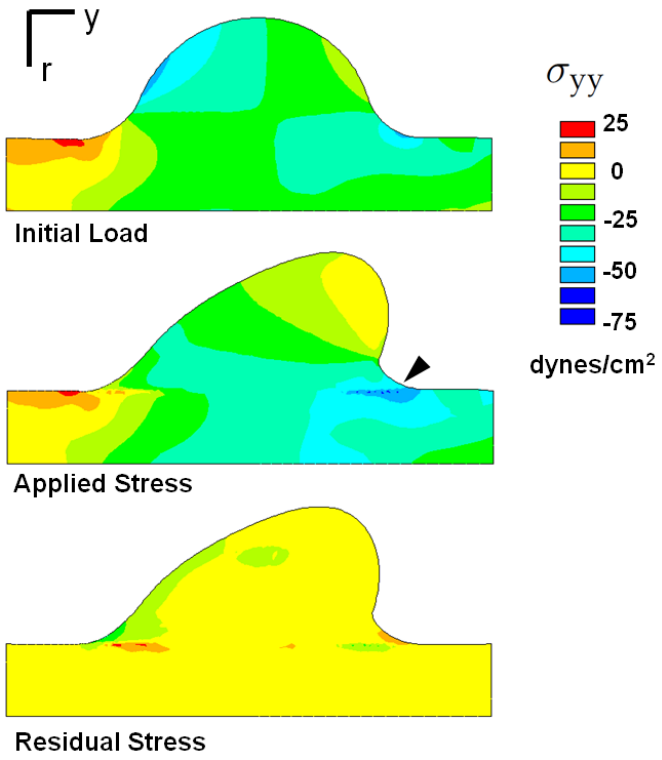

Figure 5.19: Axial residual stress. Residual stress is insignificant when compared to the applied stress, but stress concentrations do exist along the cushion/myocardium interface (arrow).

the continuity of the stress field is disrupted along this interface by prior inelastic deformations. The radial and axial residual stresses are small relative to their counterparts in the loaded configuration (Figure 5.18 & 5.19). In contrast, the circumferential residual stresses are of the same sign and order of magnitude of the loaded stress state (Figure 5.20). The compressive residual stress is due to 1) growth in the radial direction placing tissue closer to the axis of symmetry under higher compressive stress, and 2) the homeostatic stress tempering the negative growth rate induced by the compressive hemodynamic load which in effect stimulates growth where retraction would have happened without the homeostatic stress. The converse is true in the simulation with no homeostat, where a tensile residual stress accrues in the circumferential direction. The magnitude

and sign of the circumferential residual stress appears to be predominantly a consequence of the cushion growing in a tube.

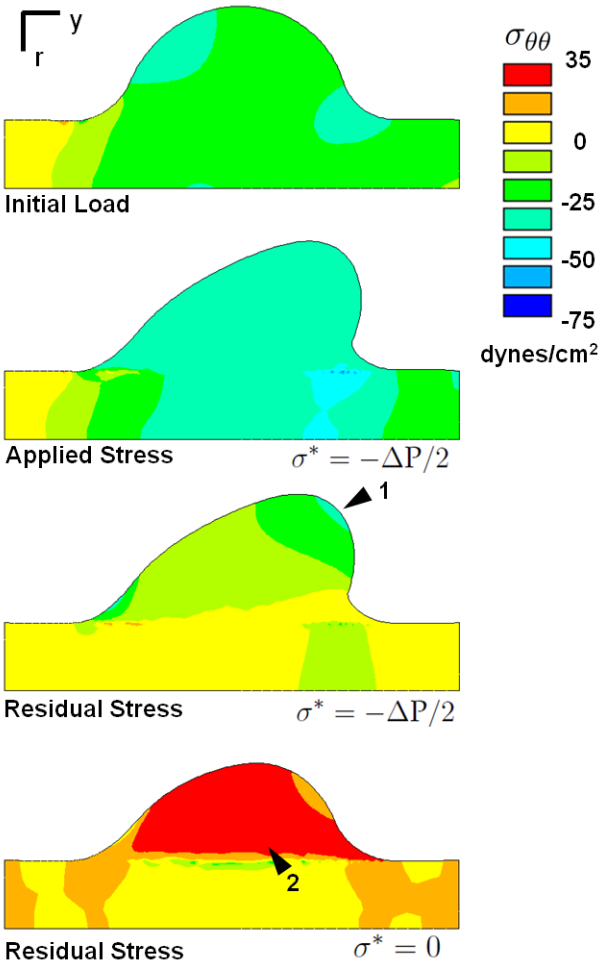

Figure 5.20: Growth and remodeling induces residual stress. Circumerential residual stress is influenced by growth in the radial-axial plane. The residual stress is maximal at the cushion leading edge, where the radial position in the AV canal is shortest (arrow 1). It is compressive because 1) circumferential stress is higher than the homeostatic stress which stimulates growth, and 2) the circumferential retractions are insufficient to match the reduced space due to radial growth toward axis of symmetry. With $\boldsymbol{\sigma}^* = \mathbf{0}$, the applied compressive load stimulated circumferential resorption which resulted in a tensile residual stress (arrow 2).

The residual shear stress in r-y direction is also of similar magnitude to the

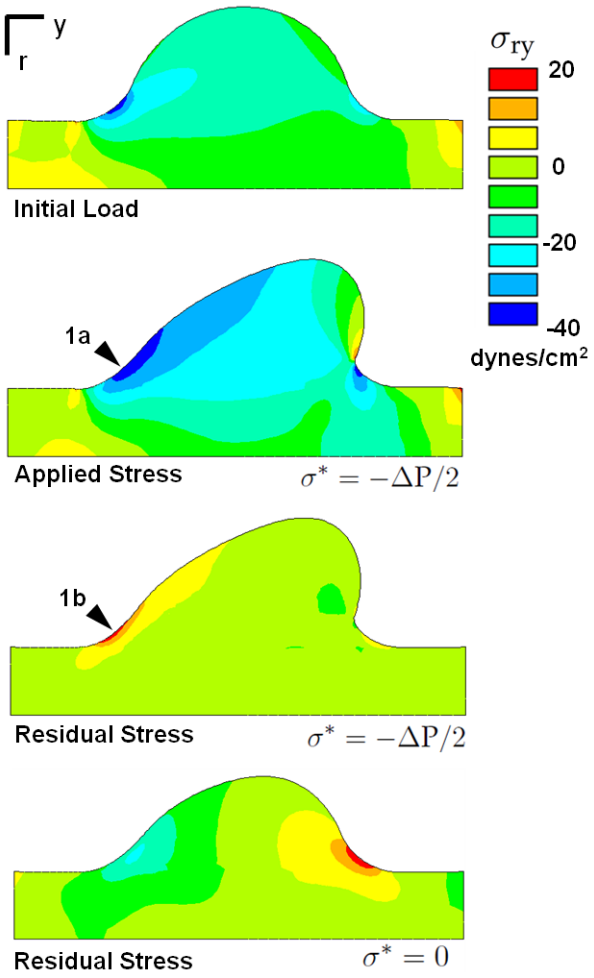

Figure 5.21: Residual shear stress. The residual shear stress is mainly localized to the cushion/myocardium interface on the inflow surface (arrows 1a-b). The negative applied shear stress results in a positive residual stress due to the accruement of inelastic shear deformation in that region.

loaded shear stress near the cushion/myocardium interface on the inflow side of cushion (arrow, Figure 5.21). The applied load induces a negative shear stress in that region, which results in an inelastic shear deformation. When the load is removed, the tissue attempts to return to its original configuration, which creates a positive shear stress in this remodeled region. In this stress-based growth model, the residual stress does influence the evolution of the cushion. Relaxation of the residual stress was investigated by incrementally updating the stress-free reference configuration to the unloaded evolved configuration.

The residual stresses were then disregarded at each update. In this relaxed model, the cross-sectional area and cushion morphology began to diverge from the non-relaxed model (Figure 5.22). Though the differences were small for the evolution times investigated, these results support the possibility that residual stresses may induce distinct and functional differences at longer times.

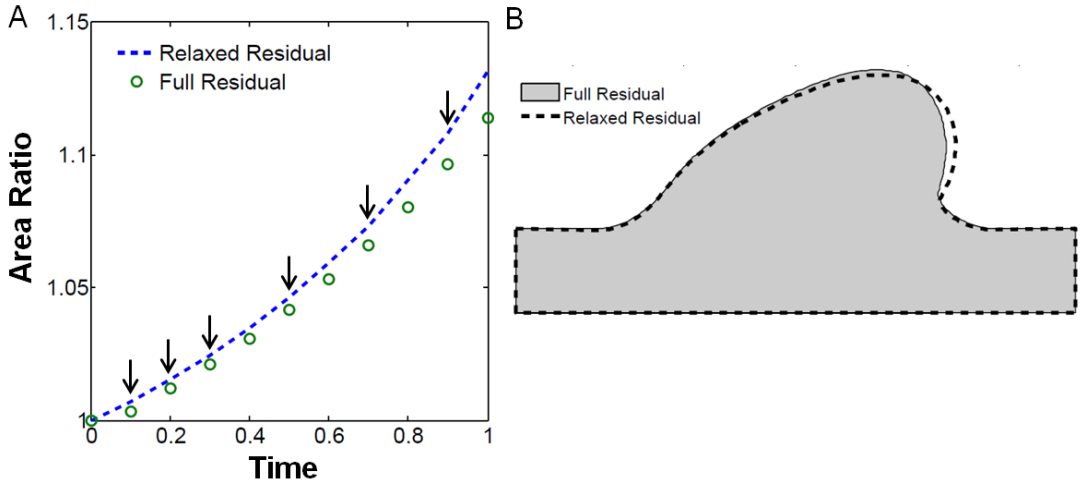

Figure 5.22: Residual stress alters AV cushion evolution. A) Plot of normalized cushion area vs. normalized simulation time. Arrows denote the reset of the stress-free reference configuration to the unloaded evolved state, which in effect eliminates the residual stresses. The relaxed residual model increased the cross-sectional area at a faster rate than the simulation with residual stress maintained. B) Reduced residual stress stimulated evolution of more tissue in the direction of blood flow. Simulation details: Full Load, $\boldsymbol{\sigma}^* = \Delta P/2\boldsymbol{I}$

Inelastic shear deformations are important for driving valve-like morphogenesis

The morphogenesis of the AV cushion includes not only an increase in tissue volume at this stage, but also significant change in shape. The inelastic shear deformations play a pivotal role in reproducing shape change in this growth

model. The shear components of the growth and remodeling tensor are maximal at the tip of the AV cushion (Figure 5.23C). The fluid shear tractions and tissue growth rate are also maximal in this region. A simulation was run in which the shear components did not evolve. In this situation the cushion grew in the direction of flow, but did not remodel as efficiently into the elongated and condensed valve shape (Figure 5.23B). The cross-sectional area also increased at a slower rate in this simulation (Figure 5.23A). This is most likely due to the difference in applied fluid forces between the two remodeled geometries. These results suggest that shear deformations, or shear remodeling, may be important in controlling valve morphology.

5.4 Discussion

The hemodynamic environment of the embryonic heart applies morphologically significant mechanical loads to the developing AV valves (review [159]). Experimental studies both support and contest shear stress as a mechanical stimulus of cushion development. The reduced shear tractions due to occluded blood flow in zebrafish resulted in defective cardiac looping, bulbus formation, and inflow/outflow tract fusion, which occur in hearts without AV cushions [79]. Another study suggested that shear tractions are secondary effects compared to myocardial function [13]. Myocardial force was reduced through myofibrillar ATPase inhibition to the point of stagnant blood flow, but the AV cushions still developed. Our computational model indicated that fluid shear tractions do not significantly change cushion volume, but are instead responsible for cushion surface remodeling. Maximum shear tractions, and consequently inelastic shear deformation, were localized to the leading edge of the cushion

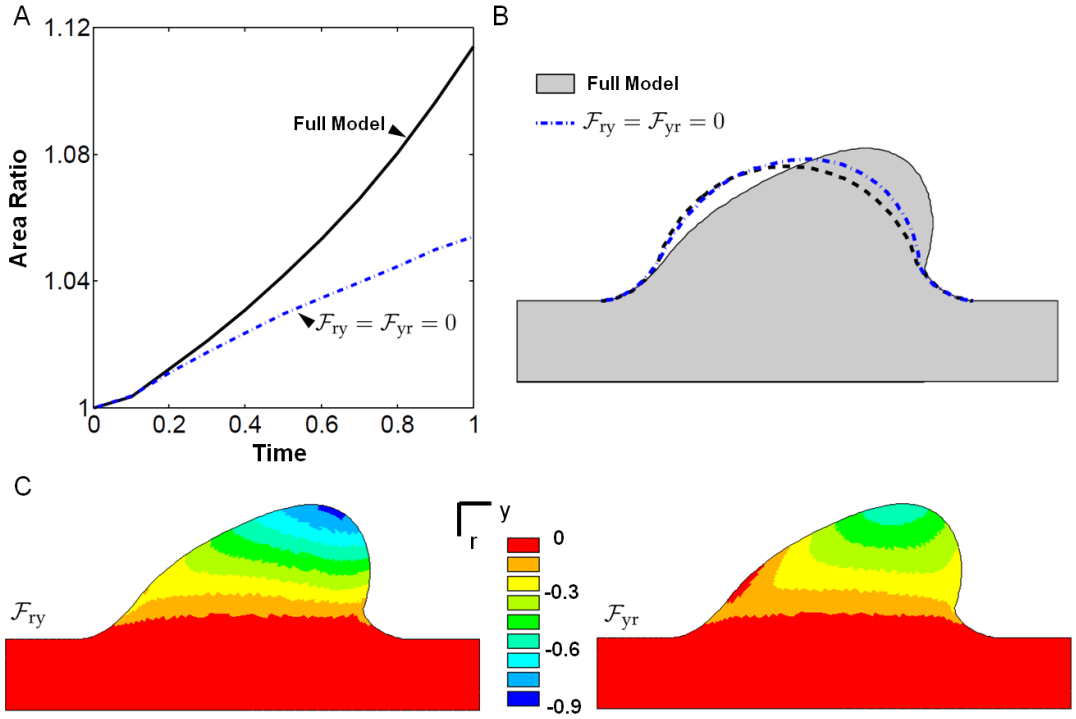

Figure 5.23: Inelastic shear deformations are key to recapitulating valve morphology. A) Removal of the inelastic shear components results in reduced cross-sectional area growth compared to the full growth law. B) Without shear components the cushion does evolve in the direction of flow (dash-blue), but has limited shape change. C) Color maps of the $\mathcal{F}_{ry}$ and $\mathcal{F}_{yr}$ display the large inelastic shear deformations throughout the cushion.

(Figure 5.14B,5.23C). The fluid pressure predominantly directed the valve-like morphology through selective removal and addition of volume, in conjunction with a compressive, homeostatic stress state. Interestingly, the pressure had little effect on the evolution of the top center region of the cushion, while the shear tractions significantly elongated this region (Figure 5.17D). Although the fluid shear tractions did not significantly alter cushion volume, their role in stimulating cellular and molecular signaling may be instrumental to the growth process [69], but this is not represented in the current model.

Homeostatic reference states, defined in terms of both stress and strain, have

become common features of tissue growth models [82, 154, 173]. Evidence of a homeostatic stress state has been previously investigated in arteries [33, 82, 176]. Opening angles of excised arteries show a non-homogenous residual stress distribution, which promotes a uniform circumferential and axial stress when the artery is loaded [33]. This suggested the existence of a uniform, preferential stress state maintained by the tissue. Although there is no data on the homeostatic stress state for AV cushions, the compressive fluid forces and the need of a directionally unbiased model motivated the use of a homogenous, isotropic, compressive stress state. This homeostatic stress was essential in generating a net increase in cushion volume needed to reproduce the growth of the cushion. In the present model, cessation of growth or remodeling would occur only if the internal and external pressure of the AV canal were constant and equal to the homeostatic stress of the AV cushion. The loading conditions for this growth equilibrium state are incompatible with fluid flow, indicating that at least remodeling, if not growth, is persistently active. Continuous growth and remodeling would not be appropriate for modeling homeostatis of an adult valve, but is a plausible feature of a morphogenesis model.

The isotropic homeostatic stress functionally represented an active growth process in the AV cushion, which was modulated by the distribution of the stress from the fluid loads. Where the applied stress was less than the homeostatic stress, the tissue retracted; where it was higher, volume was added. This type of response is observed in left atrial ligation studies, where the left AV valve thickens due to a decrease in blood inflow and AV canal pressure [164]. In our model this is seen in the ballooning of the cushion that occurs when no loads are applied, but the homeostatic stress is non-zero (Figure 5.16). Thickened valves are a common phenotype seen in gene knockout (KO) mice, such as

TGFβ2 [14], periostin [171], and collagen 11α1 [110]. While it is possible that genetic aberrations may perhaps modulate the homeostatic stress, resulting in incorrect cushion volume, no method to measure the homeostatic stress in valves is currently known. It may be possible to infer cushion residual stresses, and then relate to the homeostatic stress, through incision methods similar to those used to study arteries. At the same time, it is important to note that the biological rational of stress-based growth and consequently a stress-based homeostat is still a subject of debate in the morphomechanics community [5]. Different mechanical or molecular criteria may better define the nature of the tissue homeostatic state.

Several biological details were incorporated in the growth model. Fluid loads were determined from *in vivo* velocity measurement acquired from ultrasound imaging. The material law parameters were acquired from previous mechanical testing. The model also included a gradient in growth rate, which was motivated by cell distributions seen from AV cushion histology sections. More experimental work is needed to verify whether mass addition and ECM production is spatially dependant in this way. Although significant experimental data was incorporated in the model, additional biological features would enhance the predictability and insight of the simulation. Inclusion of multiple constituents through mixture theory is a step in this direction. Mixture theory approaches have successfully modeled constituent turnover and mechanical feedback responses in models of arteries [82, 147]. Incorporating molecular details into future growth and remodeling similations is essential for defining the relationships between cellular and tissue scale events. This is particular relevant for valve development as there are several gene specific defective valve phenotypes with both physiologic and clinical significance.

In this study, we have correlated the distribution of the fluid loads and an isotropic homeostatic stress state with valve-like morphology of the AV cushions. Pressure appears to be the key load responsible for cushion growth and remodeling, but shear tractions may serve an important role in surface remodeling. Inelastic shear deformations were shown to be important for acquiring the valve-like evolved configuration. The model also indicated that the mechanical aspects of valvulogenesis may be self-propagating, as the elongated valve shape generated fluid force profiles which promoted further cushion elongation. While this elongated morphology is appropriate for modeling the AV cushion, it may not accurately portray growth and remodeling in other valves of the heart [40, 109]. Additional refinements, such as increasing the degree of freedom of the cushion material at myocardium interface and including growth of the AV canal, may be necessary to reproduce the morphology of other leaflets. Novel *in vitro* and *in vivo* experiments are needed to establish the nature of the homeostatic state, which could be analyzed with this growth law. This model may also inform researchers on the optimal location or magnitude of mechanical perturbation needed to generate disease state animal models. For instance, the shear stress could be modulated by using blood viscosity modifiers, or the AV canal pressure drop increased through left atrial ligation. In all, our growth model provides a useful framework on which to investigate morphological aspects of valve development, and motivates further experimental studies toward understanding mechanical signaling *in vivo*.

CHAPTER 6

EDUCATIONAL OUTREACH AND BROADER IMPACTS

6.1 Introduction

Early connections to and appreciation for physical processes in biology are key motivators for students to pursue biomedical engineering careers. Yet encouraging this science passion among students is difficult, and requires techniques to assist students in identifying themselves as science learners. As a NSF GK-12 fellow, I had the unique privilege of addressing these issues as a mentor and "resident scientist" for at-risk middle school students. I was paired with a middle school teacher for one year, and high school teacher for a second year at Elmcrest Children's Center in Syracuse, NY. Focusing primarily on my research area of heart valve development, I engaged the students through interactive lectures, extensive Q & A sessions, and a hands-on curriculum involving data sets from my work. The curriculum module has culminated in a manuscript submission to the *American Biology Teacher* (see Sec. 6.4), which is a practitioner journal focused toward life science teachers. This outreach experience demonstrated that embryonic development can effectively connect students to biology, and instill wonder as students realize that they themselves were formed through a similar process.

6.2 Ask a Scientist

Questions are an important instrument students utilize to broaden their understanding of the world. Students are naturally interested in knowing the answer to their own questions, and hence question formation engages students in science. To encourage scientific thinking and question asking, our teaching team constructed an "Ask a Scientist" box for student submitted questions. The box allowed questioned to be asked with anonymity, removing the sometimes intimidating situation of asking a question in the classroom. More often than not though, students signed their questions and wanted others to know what they had asked. Questions ranged from simple and silly to more technical and complex. Others were more reflective, with students asking me personal questions about why I chose to be a scientist and what I liked about science. Though not comprehensive, below is a list of questions submitted to the "Ask a Scientist" box which gives a snapshot into the thoughts of the science students.

- Do you have any experiments with explosions? Have you made explosives?
- How do you know that the chick's heart starts the same way that the mammalian heart?
- Can you dissect a frog for us?
- What tools do you need to dissect a chicken?
- How can people live so long? Who was the first person who was on the earth?
- If an elevator was coming down the shaft and broke and you jump right before the elevator hits the floor, assuming the elevator doesn't crush like

a can, could you still not get hurt?

- Mr. B, how is penicillin made?
- How many beats does a chicken heart have in a second? Why do people research on chick hearts and what's so important about chick hearts?
- Why do you like science? Do you like the field of work you do?
- Why are you so happy with your job? What's so special about it?

6.3 Informal Lectures

In a more traditional teaching approach, I also gave short talks on a variety of topics throughout the year. Students were free to ask questions at any point during the talk, which consequently morphed the talk into an interactive Q&A session. Corralling the sometimes scattered and unrelated question back to the discussion was a recurring challenge, yet was also great practice for me in managing conversations. Some representative lectures are presented below.

Collaboration in Science

Science is becoming an increasingly more fluid and networked career area. Disciplines which had little to no crossover 50 years ago, now find that their interface is on the cutting edge of current research trends. Heart disease is an example of a research problem which requires a collaboration of many different fields in both the pure and applied sciences, as seen in Figure 6.1. Biology and biochemistry investigate the initiation of valve calcification, while clinicians and pharmacologists seek therapies to reverse its progression. Biophysicists and

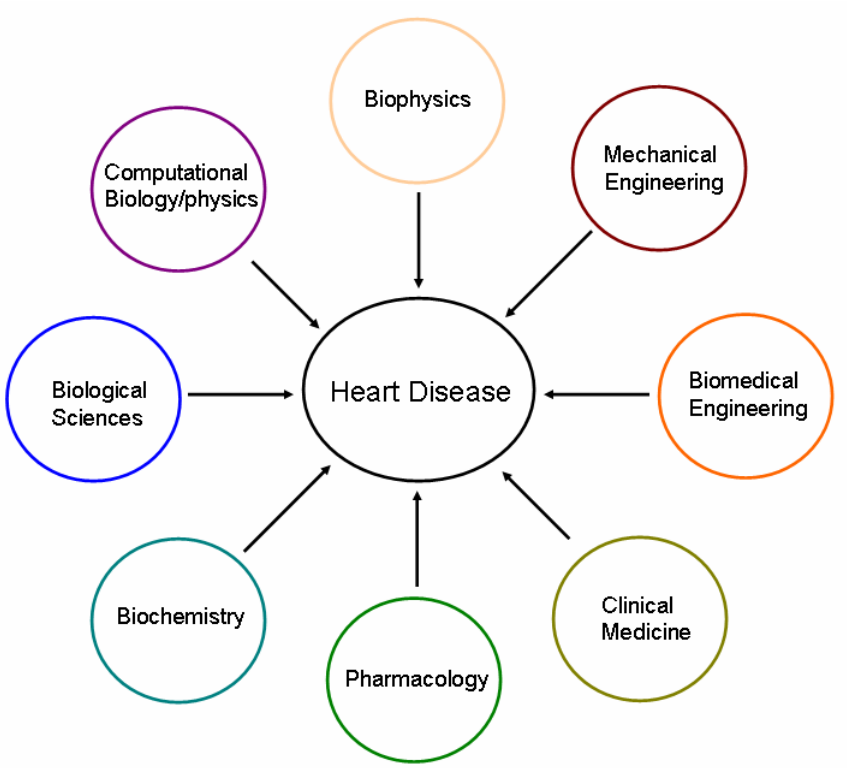

Figure 6.1: Schematic of scientific collaboration which emphasises the interdisciplinary nature of science. Heart disease is presented as an example of a scientific problem.

mechanical engineers study the role of the mechanical environment in exacerbating disease states, and provide models which computational biology scientists can simulate numerically. The exciting thing about such collaborations is that solutions to difficult problems are systematically discovered by utilizing the strengths of every participant.

Importance of Animal Models

Biological systems share common life sustaining processes. The study of one species can provide general insights into many others. In the context of understanding and preserving human life, animal models are of prime value. Without

these models, we would not have the medical advances taken for granted today. For example, genetic alterations in mice have uncovered the necessity, function, and significance of a plethora of proteins leading to our knowledge of hereditary diseases and direction towards effective treatments in humans. Likewise, animal research benefits veterinary science in treatment of animal diseases with applications in animal population control and domestic animal care. For students, however, animal research is often a difficult topic because the study of vital organ systems or development necessitates the ultimate death of the animal studied. The discussion moves quickly from matters of scientific interest to one of ethical and moral dilemma. It was my observation that teachers, administrators, and students are hesitant to engage in dialogue over these issues. This hesitancy to broach the ethical dilemma in fact prevented my bringing one of the more hands-on portions of my research to the classroom.

The topic of animal models provides an opportunity for students to wrestle with their understanding of the world and their value systems. A more formal discussion would reveal the unconscious double standard among most students, namely that scientific research on animals is wrong, yet consumption of animals for food and comfort is completely appropriate. In the discussions I did have in the classroom regarding animal research, I emphasized that the scientific community has established strict standards for humanely treating animals, and how the results of this research have benefited animal medicine, as well as human medicine. Unjustified animal cruelty was condemned, and I affirmed the professional and respectful nature scientists are called to exercise when dealing with animal specimens. The approach the teacher and I took in handling these discussions with our students was a good start. In future classes, a more formal and intentional treatment of the topic would, in my mind, better serve the

students.

Relating to the Microscale

Much of life science research works around the 1-100 micron length scale, which is a nebulous unit of measurement for students who relate best to everyday length scales of inches and meters. To assist the students in relating to the size of a micron, I constructed a slideshow of images of the back of a penny taken at different magnifications. Starting at the highest magnification, I had the student guess what the object was, reminding them to consider the scale bar. After revealing the penny's identity, the student now had a reference point for the micron scale, namely: Abraham Lincoln's thumbnail is approximately 200 μm long.

Modeling Projectile Motion

Mathematical modeling of physical phenomena is an important tool in scientific research. To practice this skill, the students and I teamed up to model projectile motion. Due to the student's lack of calculus background, the discussion focused on specifying the governing laws involved, appropriate assumptions about the projectiles properties, and nature of the forces acting on the projectile. Table 6.1 summarizes the key components of the modeling discussion. Without the knowledge of integration, the students predicted the trajectory of two different objects. The first was a wad of notebook paper, whose behavior is dominated by the gravitational force, and the other a slightly compacted tissue, which has resistive air forces on the order of the gravitational force when launched with a high initial velocity (see Figure 6.3). Of course, testing the

Table 6.1: Key Consideration in Modeling of Projectile Motion

- Governing Laws: Newton's Laws of Motion
  - Objects in motion stay in motion unless acted upon by an external force
  - The change in momentum is proportional to the motive force

$$\Sigma \boldsymbol{F} = \frac{d}{dt}(m\boldsymbol{v})$$

  - For every action there is an equal and opposite reaction
- Forces Involved: gravity and air resistance
- Relevant Physical Properties
  - Shape: affects air resistance and center of mass location
  - Density: mass distribution affects center of mass
  - Surface Area: affects the air resistance
- Assumptions:
  - Object is not magnetic
  - Color or chemical composition of object does not affect trajectory

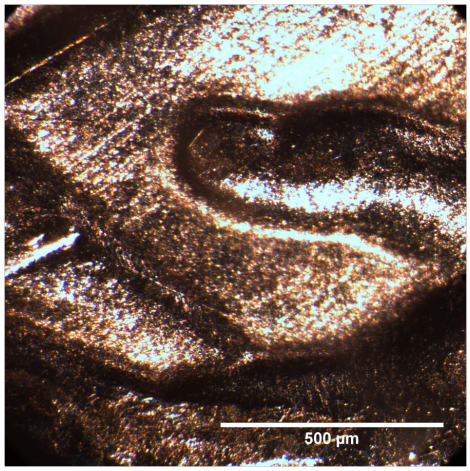

(a)

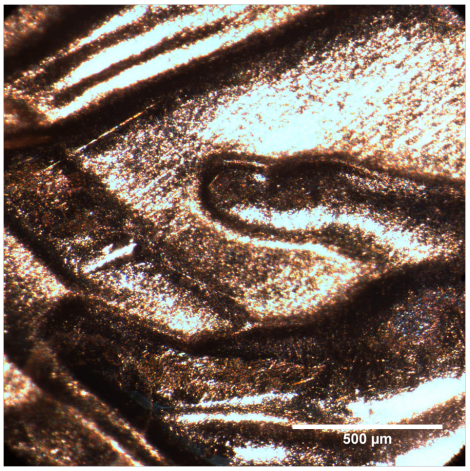

(b)

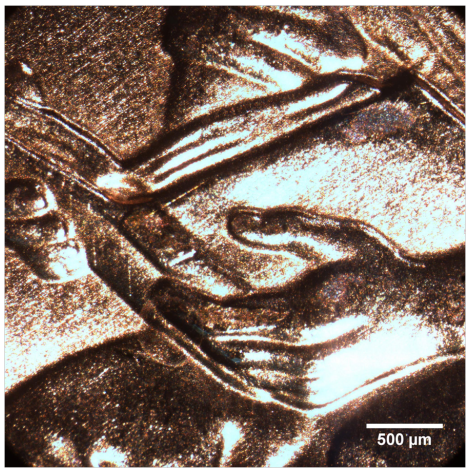

(c)

(d)

Figure 6.2: Progression of magnified images of the Abraham Lincoln penny. This established a reference point of the microscale for the students.

hypothesis was the most interesting part of the exercise as selected students were allowed to launch the wad of pad and the wad of tissue and compare the trajectories. In the gravity-dominant case, the projectile's trajectory follows a parabolic path as expected. Interestingly, the wad of tissue had a triangular tra-

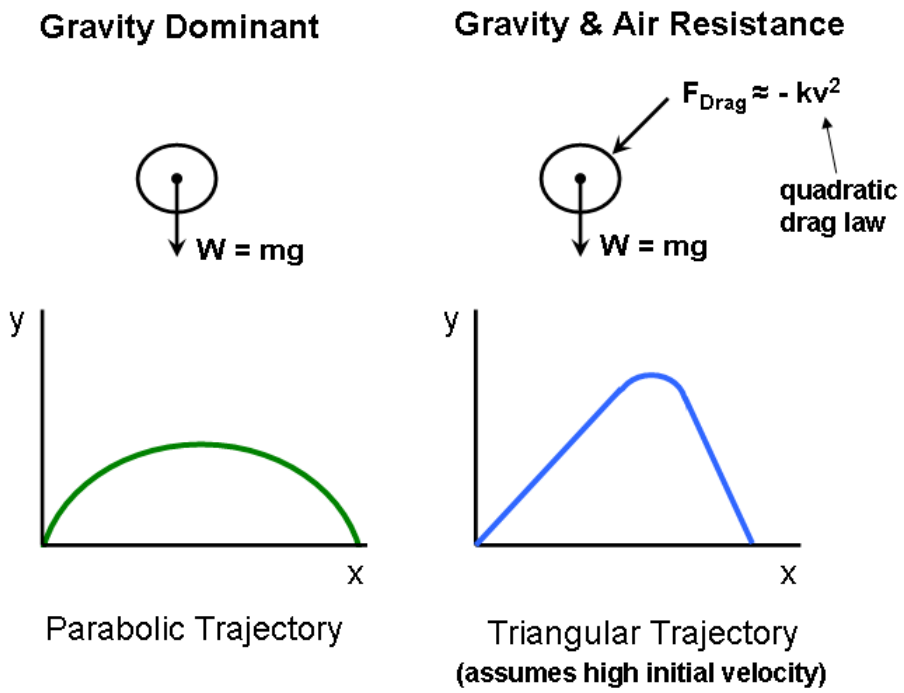

Figure 6.3: Schematic of projectile motion models and resulting trajectories

jectory, which was a consequence of the air resistance. This modeling exercise strengthened the students' intuition for knowing what is necessary to consider when describing a system. Projectile motion proved to be a great case study as all students had previous experience with flying objects and were naturally interested.

Biomedical Engineering Imaging Tools

Advancements in imaging technology have led to breakthroughs in the biomedical sciences. Two imaging techniques used in the Cardiovascular Engineering lab at Cornell University are ultrasound and micro-computed tomography (micro-CT). Possessing the ability to non-invasively probe inside spec-

imens, these tools are ideal for continuation studies of living systems, such as the study of embryonic heart development. Ultrasound technology defines the spatial boundaries between acoustically different media in the specimen by interpreting the scattering of high frequency sound waves of a source probe. Micro-CT is a high- resolution (25 μm x 25 μm) x-ray machine which maps the specimen's 3D geometry by interpreting the diffraction pattern of radioactive particles colliding with the specimen.

6.4 Retinoic Acid and Embryonic Development Curriculum

As required by the NSF GK-12 Fellowship program, I developed a curriculum module related to my area of research. The aim of this work was not only to communicate important scientific concepts, but also to instill a sense of discovery and excitement in my students. The *ex ovo* culture system was an ideal approach to achieve both of these goals. The following article was a collaborative effort amoung Russell Gould, Susan Curran, Shivaun Archer, Jonathan Butcher and myself. The article has been submitted to the *The American Biology Teacher*, which is a practitioner's journal for primary and secondary teachers in the life sciences.

Multidisciplinary inquiry-based learning using an *ex ovo* chicken culture platform - Role of vitamin A on embryonic morphogenesis

Embryonic development offers a unique perspective on the function of many biological processes and their heightened sensitivity to environmental factors. This hands-on lesson investigates the effects of elevated vitamin A on the morphogenesis of chicken embryos. The active form of vitamin A (retinoic acid)

is applied to shell-less (*ex ovo*) cultured chick embryos, which are highly accessible and intrinsically spawn inquiry. The student activities mirror the scientific research process, including review of the scientific literature, hypothesis formation, experimental design, interpretation of data, and re-evaluation of initial hypothesis. This exercise supports instruction on developmental biology, biophysics, animal research, and experimental design, and is motivated by a clinically relevant health issue.

6.4.1 Introduction

Major congenital defects occur in 2.5% of all near or full-term babies [45]. These malformations affect multiple body systems, and are caused by both genetic and environmental factors. Chromosomal rearrangements or local mutations within the genome can disrupt normal development, such as with Down and Patau syndromes. Environmental factors are chemical, molecular, and mechanical stimuli which can guide or misdirect embryonic development. Common negative environmental factors include maternal substance abuse, pollutants, nutritional deficiencies, and/or medications. In this exercise, we investigate the role of a nutritional environmental factor (vitamin A metabolite), in directing embryonic chicken development.

Retinoic Acid (RA) is the active form of vitamin A and has been correlated with severe congenital defects at both surplus and deficient levels of maternal consumption [1, 197]. RA regulates cell differentiation, proliferation, and development-related gene expression through interactions with retinoic acid receptors located on the DNA [97]. The specific RA signaling mechanisms for tis-

sue morphogenesis are still an active area of research. Excessive consumption of vitamin A supplements has been correlated with increased risk of congenital defects of newborns [157]. Furthermore, the increased use of RA for medicinal purposes, such as treatment of acne (tretinoin) underscores the importance of clarifying the role of RA in birth defect formation.

The chick embryo is an excellent animal model in which to study human morphogenesis of the heart, limbs, and eyes [39]. Advantages of using the chick embryo for research include short development times, no maternal sacrifice, and ease of access for observation and treatment administration. Shell-less (*ex ovo*) chick culture furthers this access by allowing real-time observation of the whole chick and its complement of extraembryonic vasculature. *Ex ovo* culture is an intrinsically inquiry-based classroom activity as the natural response of students is to ask, "How can a chick embryo develop without a shell?" The high school lesson engages this enthusiasm by exploring the role of vitamin A in development, and the negative consequences of vitamin A excess. The teaching activities include an interactive background of RA scientific literature, hypothesis-driven experiments, hands-on ex-ovo culture with RA treated embryos, systematic measurement of growth, and interpretation of data in the context of the reviewed literature. This exercise supports instruction in developmental biology, molecular signaling, animal research, experimental design, and is motivated by a clinically relevant health issue using current scientific research.

6.4.2 Preparing for the Study

Materials and Methods:

- Fertilized white Leghorn chicken eggs (local poultry farm)
- Egg Incubator & Rocker (HovaBator, GQF Mfg. $60- $100)
- Cling Wrap
- 70% ethanol
- Rubber bands (#16, 2.5 in)
- Rubber gloves & Safety Glasses
- 9 oz plastic cups (Dia. 3in)
- 100 mm diameter Petri dish
- Whatman Filter Paper Size 3
- 1.5 ml centrifuge tubes (optional)
- Forceps
- All-trans-Retinoic Acid (Sigma-Aldrich R2625 $30)
- Dimethyl Sulfoxide (DMSO, $<$10ml)
- USB Microscope Veho VMS-100 ($\approx$ $70) or alternative large working distance scope
- Bleach

Preparation of Incubator and Chick Embryos

Fertilized white Leghorn chicken eggs should be obtained from your local poultry farms. These fertilized embryos can be stored in a cooler maintained at 13 °C (55 °F) for up to 3-4 days until ready for use. Prior to the start of your activity, clean out incubator with soap and water to remove contaminates. Dilute bleach or 70% ethanol may be used to sterilize incubator. Line base of incubator with aluminum foil for easy clean up and place thermometer inside. Pre-heat incubator to 37 °C (99 °F), and let stand 1 hour to confirm constancy of temperature. Place eggs blunt side up in incubator and turn on rocker to start chick incubation (day 0). Include a $\frac{3}{4}$ filled 9 oz cup of water inside incubator to maintain humidity.

***Ex ovo* Culture of Chick Embryos**

After 72 hours (day 3), prepare hammocks for ex-ovo culture (Figure 6.4). Fill the 9 oz plastic cups $\frac{3}{4}$ full with warm water. Cut about 20 x 20 cm (8 x 8 in) square of cling wrap and place loosely inside the cups. Cling wrap should be in contact with water and form loose hammock. Secure cling wrap to cup with a rubber band (Figure 6.4A). Spray the plastic wrap with 70% ethanol to prevent contamination. Remove eggs from incubator after 72 hours of incubation. Sterilize eggs by spraying surface with 70% ethanol. Lay the eggs horizontally on egg carton for 1-2 minutes to allow the embryo to rotate (Figure 6.4B). Using a sharp edge (like the edge of a metal bucket or a glass beaker), tap the egg gently until there is a small dent on the underside of the egg (Figure 6.4C). Put thumbs in opposite sides of the dent and open the shell directly above hammock (Figure 6.4D). The entire yolk, egg white, and embryo should fall into the hammock

softly (Figure 6.4E). If the embryo is not on the top side of yolk, gently rotate egg yolk with fingers (using gloves). Place a 100 mm diameter Petri dish on top of the cup to seal the embryo. Transfer the embryo back into the incubator set at 37 °C with water cup to maintain humidity (Figure 6.4F). Observe embryos as long as you would like or directed by the activity. We recommend that the students perform the *ex ovo* culture under close supervision of an instructor or teaching aide.

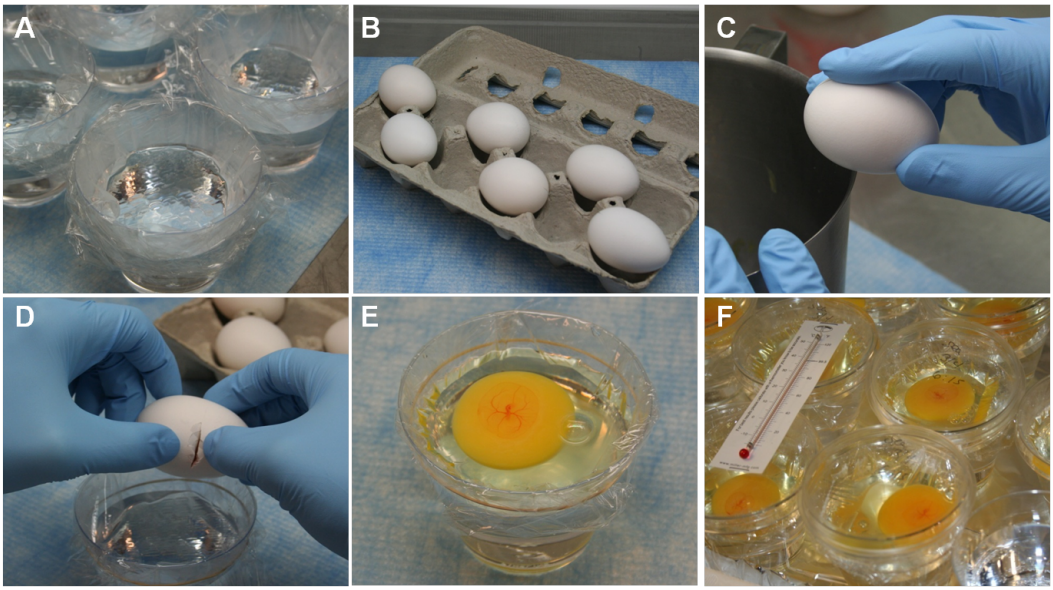

Figure 6.4: Step-by-step ex-ovo culture technique. A) Prepare hammocks in plastic cups; B) Lay eggs on side to prep for cracking; C) Use sharp edge to create narrow crack on center of egg; D) Carefully open egg shell directly above hammock and cup; E) Rotate embryo to top side of egg yolk, F) Place in incubator at to 37 °C (99 °F)

Motivate Study and Discuss Background

Before investigating the effect of vitamin A on the embryonic chick, it is important to motivate this study. Using the information outlined in the introduction, attempt to connect the overuse of vitamins and/or congenital birth defects with the students' experience with or perceptions of either issue. We found this was best done through a brief, but interactive large group discussion. In addition, we recommend discussing normal embryonic development, particularly pertaining to chick development (Hamburger and Hamilton embryo atlas images provided in the supplement and/or online at www.butcherlab.com).

Sufficient background information is needed to further place excess vitamin A exposure in context and facilitate the students' hypothesis formation. The students were given excerpts from introduction sections of scientific and medical journal articles to analyze. Field-specific literature was paraphrased to increase the readability of the excerpts. With each excerpt we included a series of questions which assessed reading comprehension and the acquisition of scientific concepts. Though reading technical literature can be difficult for students, completion of the exercise empowered the students and broke down the false notion that scientific research can only be understood by scientists. The exercise is similar to scientific reading comprehension questions on many standardized tests. It may also be used as a graded activity, which provides early feedback for both student and teacher on the progress of the project. We recommend small groups of two or three students, preferably with a range of ability, for this exercise. An initial read-through as a large group can remove any class-wide gaps in understanding. An example excerpt and questions are shown below, and additional excerpts can be found online: http://climb.bme.cornell.edu/embryo.php

Background Information Excerpt Example

Read the following excerpt from Ritchie et al [153] and answer the questions.

"Vitamin A is an essential nutrient required for normal embryonic development. Both an excess and deficiency during gestation will result in abnormalities. Vitamin A (in its more common metabolic form, retinoic acid [RA]) is teratogenic when orally administered to pregnant rats, mice, hamsters, guinea pigs, rabbits and dogs. The induced malformations occur in all body systems including the central nervous system (CNS), the face, the cardiovascular system (ventricular septal defect, aortic arch anomalies), the limbs, the urogenital system, the respiratory system, and the gastrointestinal system. [...] The question then arises, would similar malformations be induced in humans exposed to RA? Teratogenic outcomes have reportedly been associated with exposures >40,000 IU [IU - international unit of biological activity] or >10,000 IU. Equally reports have also suggested that supplemental RA intakes of <10,000 IU have no increased risk of major malformation. This contradictory data in humans highlights the importance of laboratory animal data in risk estimation."

Background Questions to Help with Hypothesis Generation

- Q#1) List the stages of chick embryonic development and illustrate normal morphology.
- Q#2) List the reported body systems that are affected by vitamin A excess during development.
- Q#3) What does this excerpt indicate about the role of vitamin A in development?
- Q#4) The authors indicate there is a "contradiction" in the human data.

What is the contrary/conflicting data?

- Q#5) Why is the contradiction important to settle?
- Q#6) What are the animal models for vitamin A research mentioned in this excerpt?
- Q#7) Why are animal models important for this research?
- Q#8) Why are different animal species important for this research?

Experimental Design

After reading the background material and discussing it as a class, divide the students into groups of 3-4 to prepare for experiment. Ask each group to formulate and record a hypothesis on what will happen when RA is applied to the vasculature network of the ex-ovo cultured embryo as compared to a normal embryo. Remind the students to develop a testable hypothesis, considering ahead of time which metrics they will use to evaluate the hypothesis. In this module, embryo "tip-to-tail" length and eye diameter were the two morphological parameters used to compare between treatments. "Tip-to-tail" length is defined as the longest straight line drawn between a point on the head and a point on the tail of the embryo (Figure 6.5). Other measurement ideas include wing bud length, limb bud length, embryo area, heart rate, and vasculature branching.

Example Hypothesis & Proposed Metrics

We hypothesize that excess vitamin A administered to the embryo vasculature will affect the entire embryo and will result in stunted growth and reduced

eye size. We will use "tip-to-tail" length as a metric of embryo growth and directly measure eye diameter. Control experiments are an essential component

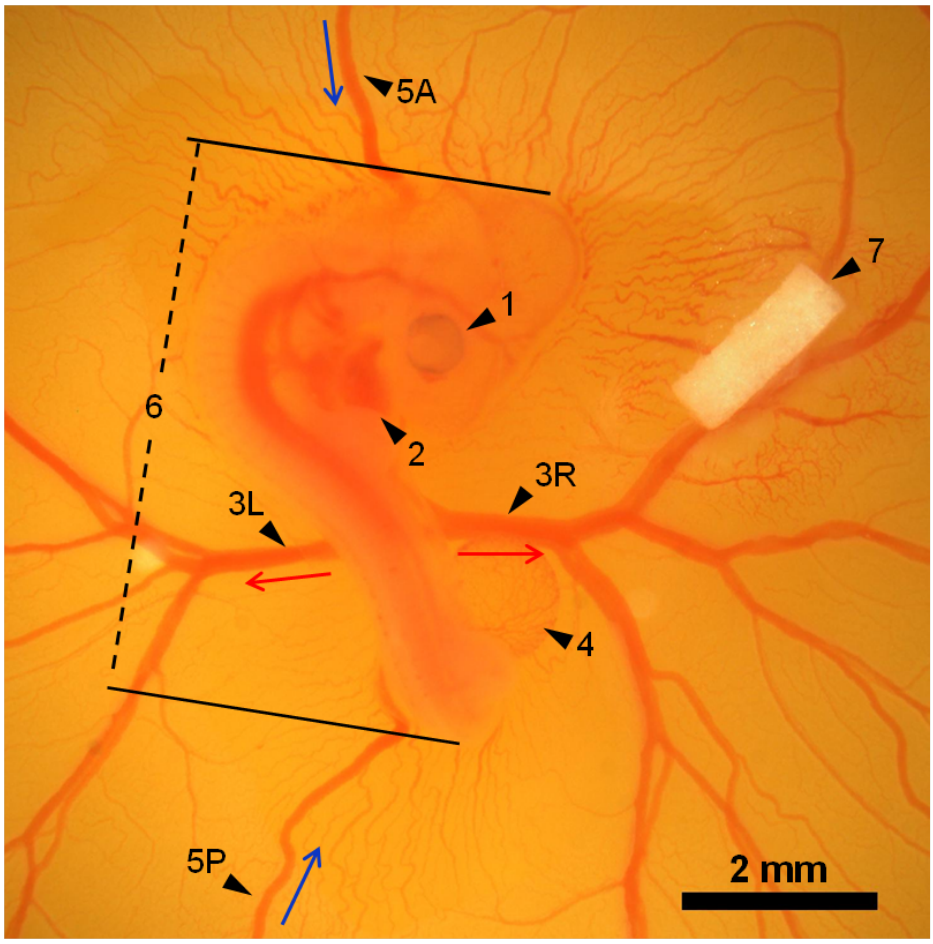

Figure 6.5: Image of chick embryo in ex-ovo culture at 4.5 days of incubation. Annotations: 1) Eye; 2) Heart; 3L) Left vitelline arterty; 3R) Right vitelline artery; 4) Chorioallantoic membrane; 5A) Anterior vitellene vein; 5P) Posterior vitellene vein; 6) Tip-to-tail length; 7) RA filter paper

to any well-designed scientific study. Spend a brief, but thorough time explaining the types and purpose of controls with the students. Solicit their assistance in identifying the most appropriate controls for this study. We recommend two controls: an untreated group (standard control), and a filter paper with DMSO only (sham control). The standard control will provide the benchmark of nor-

mal development to compare with RA treated, and the sham control to verify that the effects observed are not due to the filter paper or the RA solvent, DMSO.

6.4.3 Conducting the Investigation

Environment Perturbation Study: Addition of Vitamin A (Retinoic Acid)

From previous dose-dependent and temporal responses, we have determined that a RA concentration of 1mg/ml applied at day 4 of incubation induces morphological changes by day 7 of incubation. We recommend that the teacher mix and administer the RA treatment to the embryo. RA and DMSO should be handled with gloves and safety glasses. Cut the Whatman filter paper into 2-5 mm diameter circles or strips. Dilute 1mg of RA in 1ml of DMSO in a 1.5ml tube. Place the filter paper sections in the 1.5ml tube and let soak for 10-15 minutes. Using forceps, remove filter paper from RA solution and place on the ex-ovo culture. We suggest placement of the filter paper on the right side of the embryo, within the vasculature (Figure 6.5). Capture images of the embryo and vasculature sequentially at day 4, day 5, day 6, and day 7 using the USB-microscope (Veho VMS-100, Figure 6.6 and 6.7). Measure the chosen metrics of tip-to-tail length and eye diameter from these images using open source software ImageJ (NIH, http://rsbweb.nih.gov/ij/). Simple instructions for ImageJ are available at http://climb.bme.cornell.edu/embryo.php. Hand measurement using a caliper or ruler is a viable alternative. Finally, record the measurements in tables for each metric (Figure 6.8).

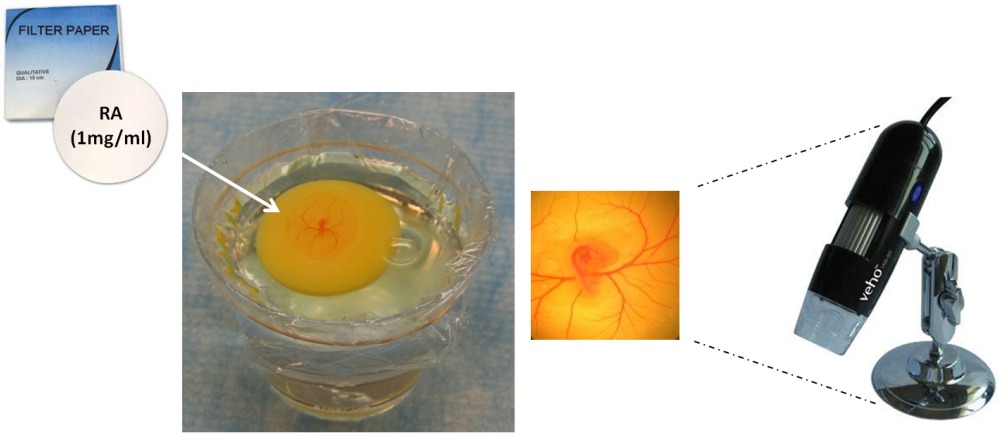

Figure 6.6: Experimental design consists of soaking filter paper in different concentrations of retinoic acid (RA) and placing it on the embryonic vasculature. Following several days of incubation, a USB-microscope can capture the downstream effects on development.

Analysis & Interpretation of RA Treatment Results

An essential part of the scientific process, and often the most challenging, is to quantitatively analyze and correctly interpret the data. To assist with this task, we recommend that the students plot the data, either digitally or by hand, for each output measured (Figure 6.7). Instruct the students to use the data to confirm or deny their initial hypothesis. If the hypothesis is confirmed, the students must prepare a series of arguments from the data to support their claim. If the hypothesis fails, the students must generate a new hypothesis based on the results of the study. It is also important to consider the implications of these results in a broader context. For instance, ask the students how these results might relate to human development, or how the other unmeasured features of the embryo, such as the internal organs, might be affected by the treatment.

Example Data Analysis & Interpretation Worksheet

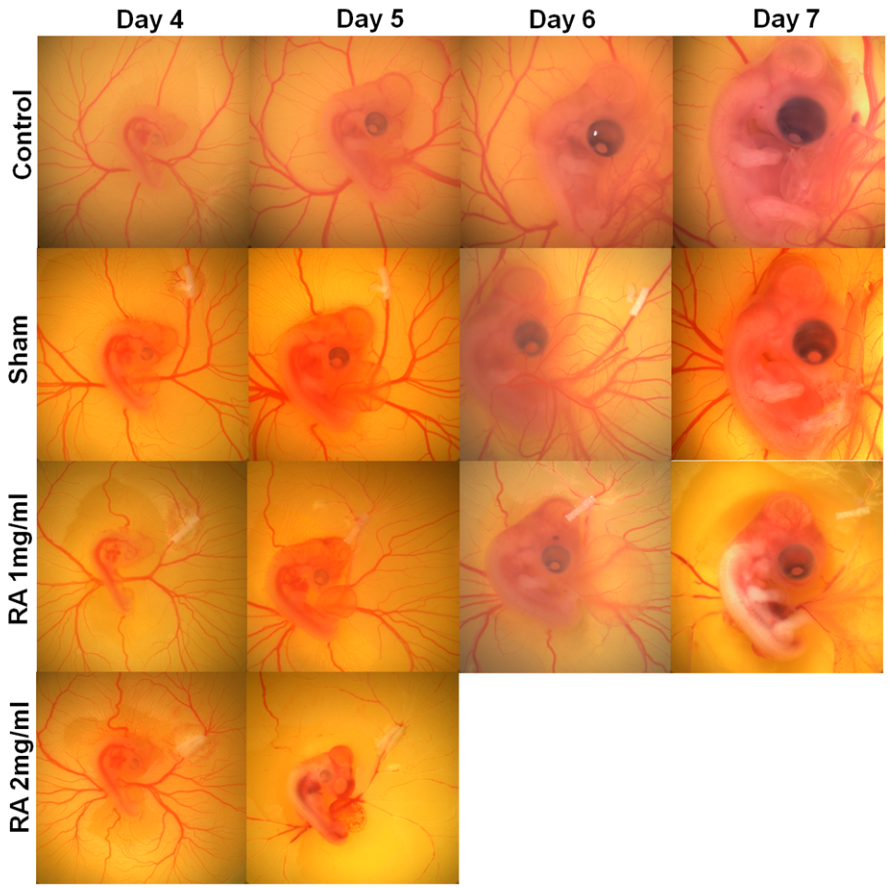

Figure 6.7: Retinoic Acid Perturbation Study Data Set. Array of ex-ovo chick images across treatment and over time. RA treatment stunted embryo development and even resulted in embryo lethality at higher dosages

Using the generated tables, line graphs, and previous understanding of embryonic development and RA, work through the following questions as you analyze the data (Figure 6.8).

- Q#1) Compare the "tip-to-tail" length and eye diameter between the control and RA treatments. Did addition of retinoic acid stimulate or stunt growth?

  - While the control and treated embryos had roughly the same starting tip-to-tail length, by day 7 the control tip-to-tail length was 25% greater than the embryos with 1mg/ml RA treatment. The 2mg/ml RA treatment embryo died before day 7. These results suggest that RA stunted and/or terminated the growth of the embryo.

- Q#2) Are the sham results different from the control? What do the sham results indicate about our method of treatment?

  - The sham results do not appear to be significantly different from the control. This indicates that the defects were not induced by the filter paper or DMSO, but instead can be wholly attributed to the addition of retinoic acid.

- Q#3) Approximate the growth rate of each treatment by determining the slope of the "tip-to-tail" curves. Which condition had the fastest growth rate? Which was the slowest?

  - Control - 0.39 mm/day, Sham - 0.34 mm/day, RA 1mg/ml - 0.25 mm/day, RA 2mg/ml - 0.2 mm/day. The control embryo had the fastest growth rate and the 2mg/ml RA treatment had the slowest. The control growth rate was roughly twice as fast as the 2mg/ml RA treatment. This result agrees with the conclusion in question #1, that RA stunted the embryo's growth.

- Q#4) From our data, we see that RA treatment affected the global development of the embryo, yet the treatment was applied locally. Why do you think this is?

  - Even though the retinoic acid is applied over a small area away from

the embryo, it was placed on a blood vessel of the vasculature network. This particular placement on a vessel facilitated the spread, and uptake, of RA in the embryo body. This emphasizes the substantial role the circulatory system plays in nutrient consumption and trafficking, demonstrating how high local concentrations of harmful agents can have global consequences due to rapid transport throughout the developing embryo.

- Q#5) Explain how an optimum (not too high and not too low) human exposure to vitamin A measurement could be determined from similar experiments.
  - The upper-bound dosages for human embryos could be approximated from this studies data by scaling according to body weight or blood volume.

6.4.4 Discussion

The embryo chick provides a unique lens through which to study general (cell activity, organ systems) and development-specific (cell differentiation, morphogenesis) processes in biology and physics. Watching the embryo induces fundamental questioning of why some structures develop first vs. later on, how the embryo is feeding itself, and how processes change with growth. The effects of physics such as diffusion, transport, and mechanical forces can be incorporated into our lesson framework. Instructional versatility enables the breadth of content to be appropriately scaled to student ability or knowledge base. For instance, observation, measurement, and prediction of normal development may

Tip-to-Tail Length (mm)	Day 4	Day 5	Day 6	Day 7
Control	0.76	1.22	1.62	1.92
Sham	0.85	1.14	1.52	1.85
RA (1mg/ml)	0.79	0.96	1.19	1.56
RA (2mg/ml)	0.72	0.92	N/A	N/A

Eye Diameter (µm)	Day 4	Day 5	Day 6	Day 7
Control	96	221	334	443
Sham	120	195	315	419
RA (1mg/ml)	78	150	253	328
RA (2mg/ml)	95	116	N/A	N/A

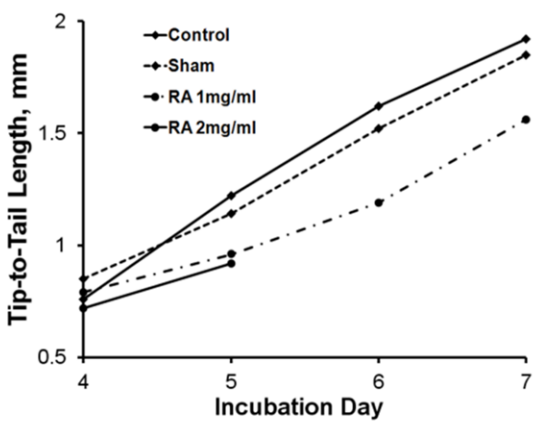

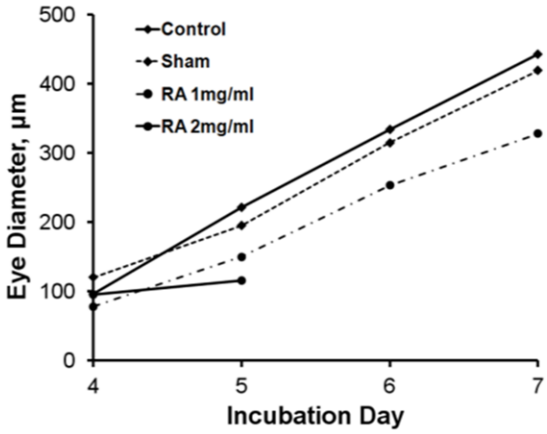

Figure 6.8: Quantification of Eye diameter and Tip-to-Tail length for RA perturbation study using open source software (ImageJ) provided by the NIH.

be sufficient for middle school biology students, while the RA perturbation model may be more appropriate for upper level high school students. In the following, we present further background information and ethical issues with animal research to extend the applicability of this lesson (Figure 6.9).

Metabolic and Molecular Aspects of Study - Mechanism of Action

Vitamin A is broken down into all-trans-RA and 9-cis-RA which is then transported to the nucleus of the cell. Within the nucleus, all-trans-RA binds to retinoic acid receptors (RAR) and 9-cis-RA binds to retinoid receptors (RXR). RAR and RXR form RAR/RXR heterodimers, which bind to regulatory regions

Figure 6.9: Engagement of students during the ex-ovo chick culture and analysis of experimental results.

of the chromosome called retinoic acid response elements (RARE). Binding of all-trans-RA and 9-cis-RA to RAR and RXR respectively allows the complex to regulate the rate of gene transcription. In the case of all-trans-RA applied systemically to a developing chick embryo, complexity arises since cells/tissues will respond to the retinoic acid differently. For example, in the developing limb bud, tissue regression has been largely associated with the molecular control of self-induced cell death (apoptosis). Brain defects have been largely associated with the molecular control of cell migration. Therefore, we suggest a generalized mechanism of action be used for explanation. Upon excess RA administration, stunted growth may be the result of abnormal cell migration or apoptosis which is regulated directly by the transcriptional complex (all-trans-RA and 9-cis-RA to RAR and RXR) (Figure 6.10, adapted from http://lpi.oregonstate.edu/infocenter/vitamins).

Bioethics of Animal Research

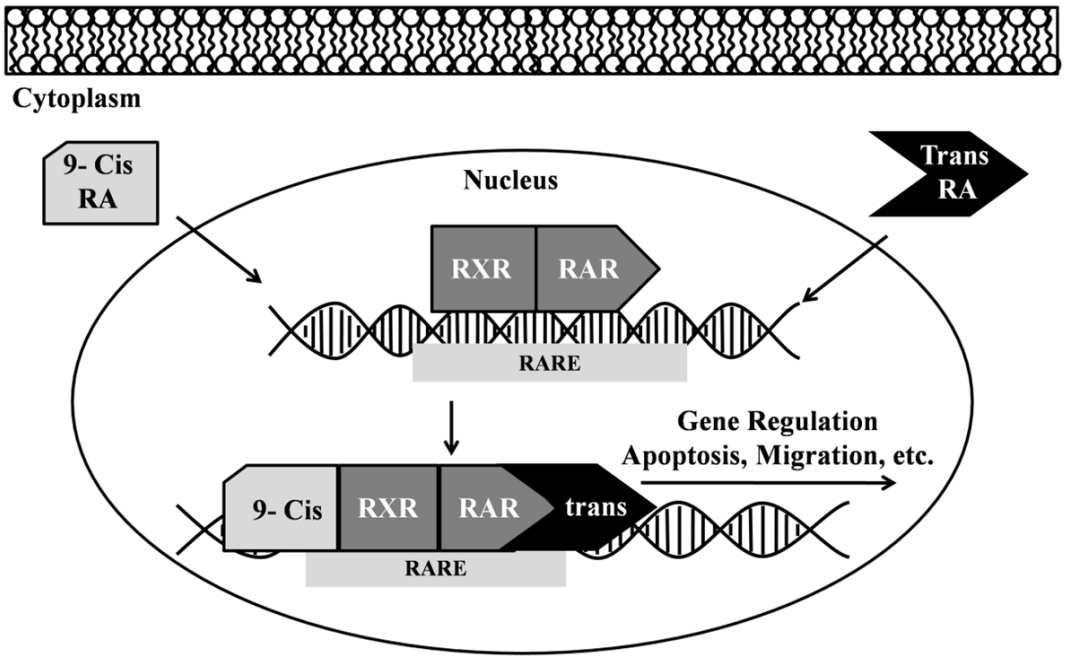

Figure 6.10: Metabolic and molecular pathway of RA (advanced student classrooms) describing the mechanism through which RA regulates gene expression.

Using live embryos within the classroom will inevitably spark a conversation about humane treatment and ethics. We feel this is an extremely important aspect, and should not be overlooked. From a purely regulatory standpoint, all use of vertebrate animals in research, teaching and testing is regulated by the Institutional Animal Care and Use Committee (IACUC, http://www.iacuc.org/). Chick embryos younger than embryonic day 15 (E15) are assumed to be unable to experience pain, because of limited neural development. It is recommended that E14 or younger embryos be euthanized by hypothermia, typically by placing the eggs in a 20 °C freezer. Chick embryos from E15 to pre-hatching should be euthanized by decapitation, anesthetic agents, or another rapid and humane method. Studies using embryos within three days of hatching or hatchlings must be reviewed by the normal IACUC procedure for vertebrate animals. In our experiments, embryos will be euthanized at day 7, which is only 1/3 of

the way through its 3 week hatching cycle. Therefore, the embryos cannot experience pain and are exempt from any IACUC protocols. This however, will not limit conversation about the ethics of animal research within the classroom. We encourage teachers to lead a classroom discussion on the role of animals in scientific research, and use this time effectively to discuss humane treatment and ethics. From our experience, the level of concern and opinions will vary from class to class. It is imperative to guage student sensitivity in a considerate and objective manner before conducting the experiments. Resources for animal research ethics can be found on the web: www.ethics.org.

6.5 GK-12 Experience Summary

The GK-12 program has been as much a learning experience for me as a teaching one. Students face social and family difficulties that supersede their academic challenges, something I didn't fully appreciate before the GK-12 program. The baggage from broken homes and relationships makes its way into the classroom, disrupting the students' focus and confidence. The GK-12 fellowship is not designed to address these family issues, however, by sharing positive, affirming, and educational moments with students, we create a safe place for students to think and achieve. In all, I think the approach our teacher-fellow team took to engage students, through open Q & A sessions, informal lectures, and a unique curriculum module, was successful. Support for this statement comes from student comments about our curriculum:"This is awesome! I want to know everything about the body!" and "I like science now!". Another indicator of program success was that four students asked me for information about attending Cornell, and others started thinking about college, quite possibly for

the first time. Though intangible, it is these student interactions that I will remember, and I know that the GK-12 program benefited everyone involved.

CHAPTER 7
CONCLUSION

The formation of the embryonic heart is truly a complex and fascinating process regulated by mechanical and molecular feedback. In this study, we have identified some specific mechanisms of mechano-molecular feedback, developed tools to measure mechanical properties, and implemented a computational framework of growth and remodeling on which to further explore valve development. We now summarize the conclusions and contributions of this research. Remaining research questions and future directions are discussed.

Quantification of avian embryonic AV valves

The mechanical properties of post-EMT valves were previously not characterized. Through this work, we have quantified how valve stiffness increases and how the valve transitions from a globular to a planar geometry during this period of valvulogenesis. We developed a new method for interpreting the pipette aspiration experiment for soft, nonlinear materials using an analytic expression. This extends the use of the method beyond the linear elastic range and eliminates the need for computational simulations to evaluate each data set. Our exponential material law sufficiently captures the nonlinearity observed in early stage embryonic valve tissues. The deformable post technique was also implemented to test the planar valve at the later stages of development. We anticipate that these techniques may be of use to development biology labs interested in measuring mechanical properties.

This study demonstrated a significant level of anisotropy present in the valve by stage HH36 (Day 10). The origin of this anisotropy is an important follow-up

research question. The role of molecular and/or mechanical signals in stimulating these microstructural changes is still unknown, although the valve community does know some of the ECM proteins involved [88, 94]. Preliminary data from the lab suggests that increases in ECM fiber density and orientation are primarily responsible for the anisotropy (see Appendix A Figure A.1), but these features have not been quantified. Mechanical aspiration with a circular pipette is an isotropic technique. We hypothesize that a rectangular pipette may be able to distinguish effects of tissue anisotropy. FE simulation is needed to validate this hypothesis. Developing a constitutive law with ECM fiber details is another direction for this work

Biomechanical Remodeling by TGFβ3 and 5-HT in post-EMT Valves

The biomechanical remodeling capacity of two key signaling pathways was identified through this study. TGFβ3 stimulated 2-fold increases in tissue stiffness and proliferation rates in AV cushion hanging drops. 5-HT potentiated the effect of TGFβ3 through the 5-HT2b receptor, but may also act through other downstream interactions. We identified an interesting dynamic between the remodeling processes of cell contraction, proliferation, and ECM synthesis. TGFβ3 treatment increased cell contractile behavior, but the AV cushion appeared less compacted than the control because proliferation and ECM synthesis compensated for the volume change due to compaction. The interaction of 5-HT and TGFβ3 was further demonstrated *in vivo* through system 5-HT treatment of avian embryos. These results provide a specific molecular mechanism for stiffness generation, and may have implications for the how the anisotropy discussed in the previous section occurs.

Two different lines of research are motivated by this study. First, we have established a novel *in vitro* culture system which can be used to investigate the effect of other molecular signals on AV cushion mechanics. A natural follow-up study would be to investigate downstream points of interaction between TGFβ and 5-HT signaling. Alternatively, the system could be used to study non-molecular stimuli such as osmotic pressure changes.

Second, having established that TGFβ is important in the biomechanical remodeling process, it would be interesting to see the effect of removing TGFβ. We have begun to investigate this question using a TGFβ2 KO mouse model. The TGFβ2 isoform was chosen for the mouse because it appears to perform the same function as TGFβ3 does in the chick during EMT [29]. TGFβ2 KO valves have an odd morphology, characterized by an increased, "butterfly-shaped" volume (see Appendix A Figure A.2) [14]. This morphology is hypothesized to be the continuation of EMT into what are normally considered post-EMT stages [11]. Our preliminary data shows that the KO valves are stiffer than WT valves (see Appendix A Figure A.3). This neither agrees with the avian cushion remodeling data, nor with the histology results of other groups that show the KO valves have increased glycoaminoglycan content, which is a structurally weak constituent [11, 10]. Although hard to interpret, the stiffness result does confirm that TGFβ regulates valve mechanics, but not in a binary way. More research is needed to reconcile these differences.

A Model of Mechanically Stimulated Growth and Remodeling

The role of mechanical stimulation in tissue growth and remodeling will increasingly be a focus of research in the developmental biology and biome-

chanics communities. We have derived an evolution equation for tissue growth and shape change using the conservation laws of continuum mechanics and the entropy inequality. Our formulation includes a remodeling force balance law, which was previously proposed in a different form [42]. We introduce a homeostatic stress state, which is the stress at which growth ceases, as a biological force through this balance law. The mechanical energy of newly created tissue is still an open question in the growth mechanics field. We propose that the free energy of this new tissue is non-zero, but not necessarily equal to the current free energy of the body. Our numerical examples indicated that varying the free energy term adjusts the rate of isotropic volume growth or modulates the hydrostatic pressure, depending on whether problem is stress-controlled or displacement-controlled.

Future work on this growth model should include both theoretical and experimental components. The model currently assumes that the tissue is a single constituent, but in reality tissues consist of several constituents. Although the single constituent theory adequately models the bulk mechanical behavior, the microstructural details, such as a shift in constituent volume fractions, are absent from the model. Histology data from our lab indicates that the shift from GAGs to collagen during valvulogenesis is significant [94, 28]. Incorporating these details would increase the biological relevance of the growth model. The mechanical nature of homeostasis is an important and largely open question. Novel experiments are needed to characterize the homeostatic mechanical stimulus to which cells respond and attempt to mitigate. Molecular signaling may also affect biomechanics, either through direct activation of remodeling processes or indirectly by reprogramming the preferred homeostatic mechanical state. Experimental insights of this nature are needed in order for the concept

of a homeostat to move from a descriptive to a mechanistic feature of growth models.

Computational Model of AV Valvulogenesis

We then applied our growth theory to the specific application of modeling the development of AV valves. We showed that the distribution of fluid pressure and shear tractions was sufficient to generate a valve-like shape. This required the assumption of a compressive, isotropic, homeostatic state, which was justified by the compressive loading the valve experiences during these stages. As the valve remodeled, the fluid forces on the new shape promoted further elongation and condensation of the leaflet. This suggested that fluid-driven valve growth may be a positive feedback system. Residual stress developed at the valve/myocardial interface due to the discontinuity in growth rate across that line. Significant circumferential residual stress developed at the leading edge of the cushion due to radial growth toward the axis of symmetry. Residual shear stress was localized to the inflow and outflow valve surfaces near the myocardium. We also demonstrated the importance of inelastic shear deformation in generating the leaflet-like shape. These simulations support the hypothesis that mechanical forces are key drivers of valve morphogenesis.

Our focus was on modeling normal valve development, but this computational framework could naturally be extended to understanding defect formation. Future work for this project is to use fluid loading profiles from flow perturbation studies to model the defective morphology seen in experiments. The significance of the homeostatic state can also be investigated with this model. For example, the enlarged "butterfly-shaped" valves observed in the TGFβ2 KO

mouse can be generated by adjusting the spatial distribution of the homeostatic stress (see Appendix A Figure A.4). Simulations of this nature may provide insight into where, or what, to look for when trying to identify what defines homeostasis. More biological details could also be incorporated into the model. For example, *in vivo* AV canal geometries quantified using micro-CT could be imported into ANSYS. Similarly, the 3D geometry of defective AV canals could also be simulated in this way. This would evaluate the dependence of valve growth on initial geometry, and potentially provide some clinically relevant insights.

Conclusion

The mechanical and molecular signaling results of this work have implications for congenital heart defects (CHDs). We have characterized the normal mechanical properties of AV valves, which can now be used to identify defective valves. Our results establish the efficacy of TGFβ3 and 5-HT to regulate tissue mechanics, which motivates including these genes in future studies of specific CHDs. Then through a theoretical growth law, we demonstrated the potential capacity of mechanical signaling to direct normal valve formation. Our computational growth model can be extended to analyze experimental models of CHD formation. In all, this dissertation contributes to the current understanding of heart valve mechanics and molecular signaling, and provides new directions for future research.

APPENDIX A - FUTURE WORK/PRELIMINARY DATA

Formation of ECM Anisotropy in AV Valve

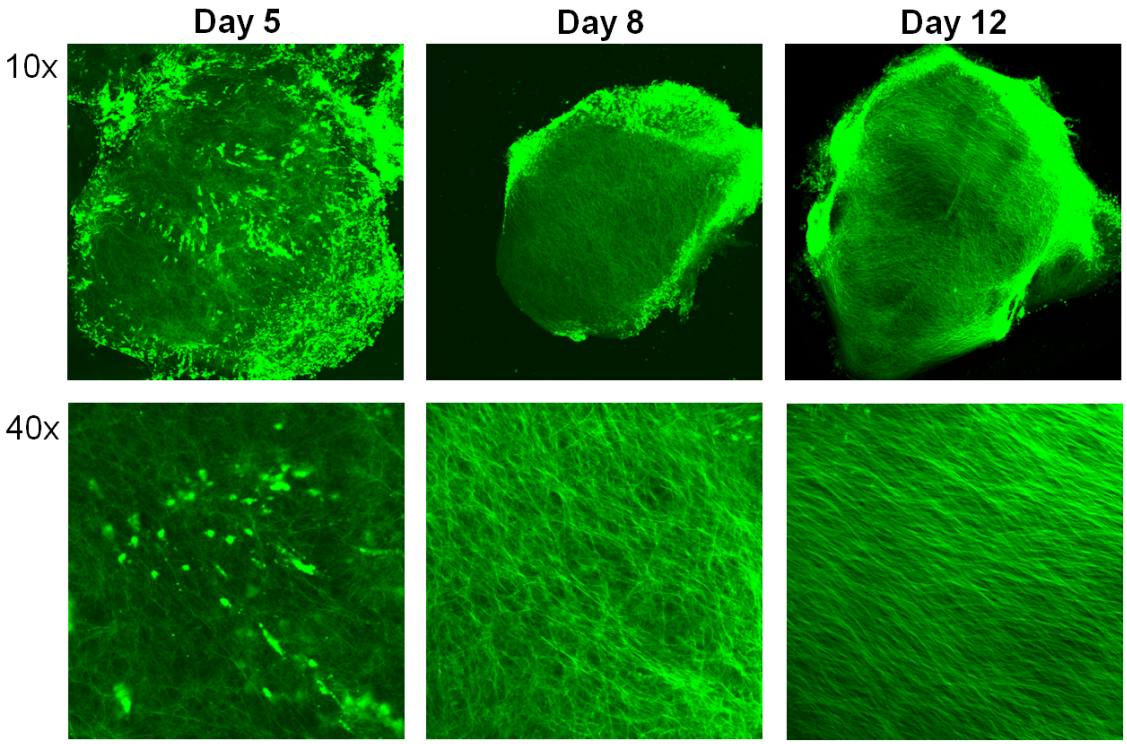

Figure A.1: AV cushion transitions from an isotropic ECM at day 5 to significantly anisotropic ECM by day 12. Left AV leaflets at 10x and 40x maginication. Leaflets stained with general amino acid stain 5-(4,6-dichlorotriazinyl)aminofluorescein (5-DTAF), 50 μM for 30 min

Defective valve morphology in TGFβ2 KO mice

TGFβ2 deficient AV valves were larger than WT valves with approximately a 3.6 fold increase in cross-sectional area. KO valves were irregularly shaped and demonstrated delayed formation of the fibrous ventricular septum. Cell

count was 3-fold higher in KO valves, but no statistical difference in cell density was observed.

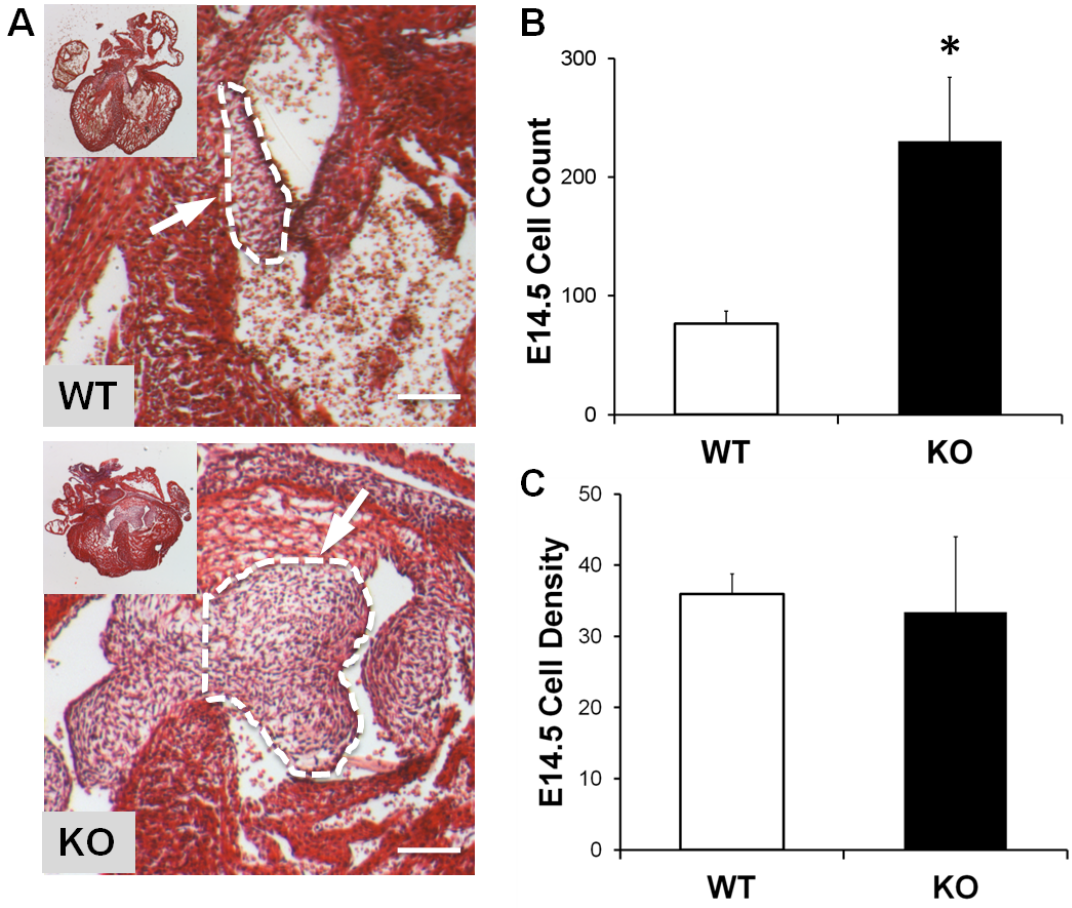

Figure A.2: TGFβ2 KO Morphology A) Massons trichrome stain of E14.5 wildtype (WT) and knockout (KO) whole hearts (70x scale bar = 200 μm) and AV valves(150x scale = 100 μm) B) Significant increase in valve cell number in KO over WT. mean $\pm$ SD, *p $<$ 0.05 t-test, n = 3 C) Cell density was not statistically different between WT and KO. mean $\pm$ SD, t-test, n = 3, density units cells(10^4 μm^2) n = 3, mean $\pm$ SD, *p$<$0.05 t-test

TGFβ2 KO mice have stiffer AV valves at stages E12.5 & E14.5

Pipette aspiration demonstrated that post-EMT AV valve stiffness is elevated

over WT and HET embryos. KO strain energy density was approximately 1.3 fold over WT at E12.5 and 1.5 fold at E14.5.

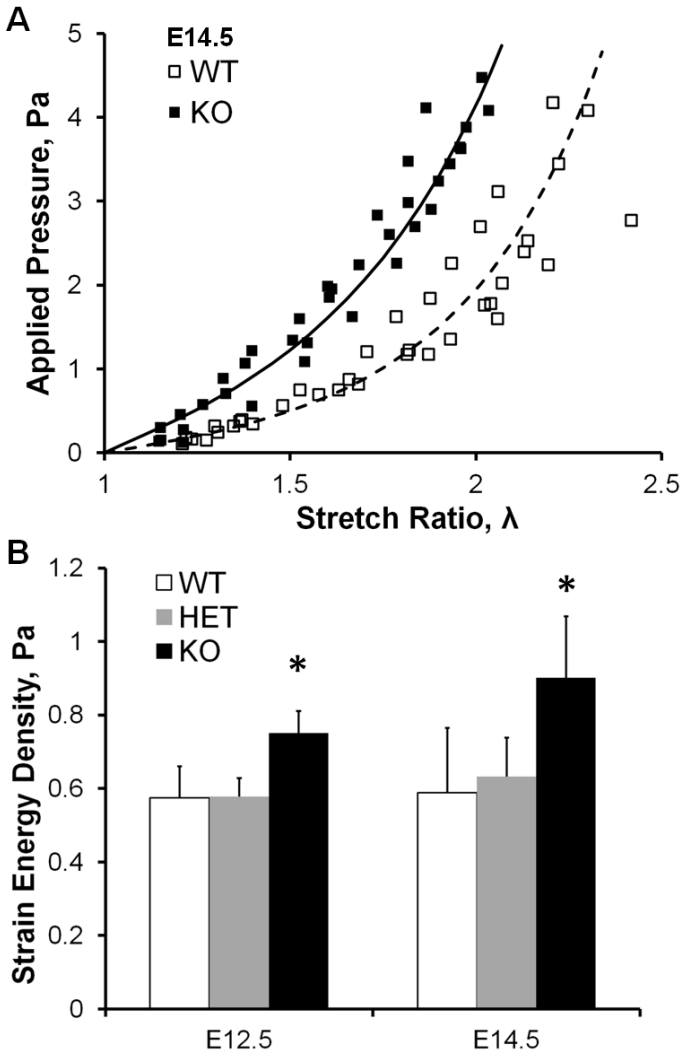

Figure A.3: Valve stiffness is elevated in TGFβ2 KO A) Representative ΔP vs λ curves for E14.5 WT and KO embryos. B) Calculated strain energy densities of WT, HET, and KO genotypes at stages E12.5 and E14.5. mean $\pm$ SD, n = 6, *p < 0.01 wrt to WT and HET, 1-way ANOVA wrt genotype

TGFβ2 KO morphology can be modeled by varying the homeostatic stress

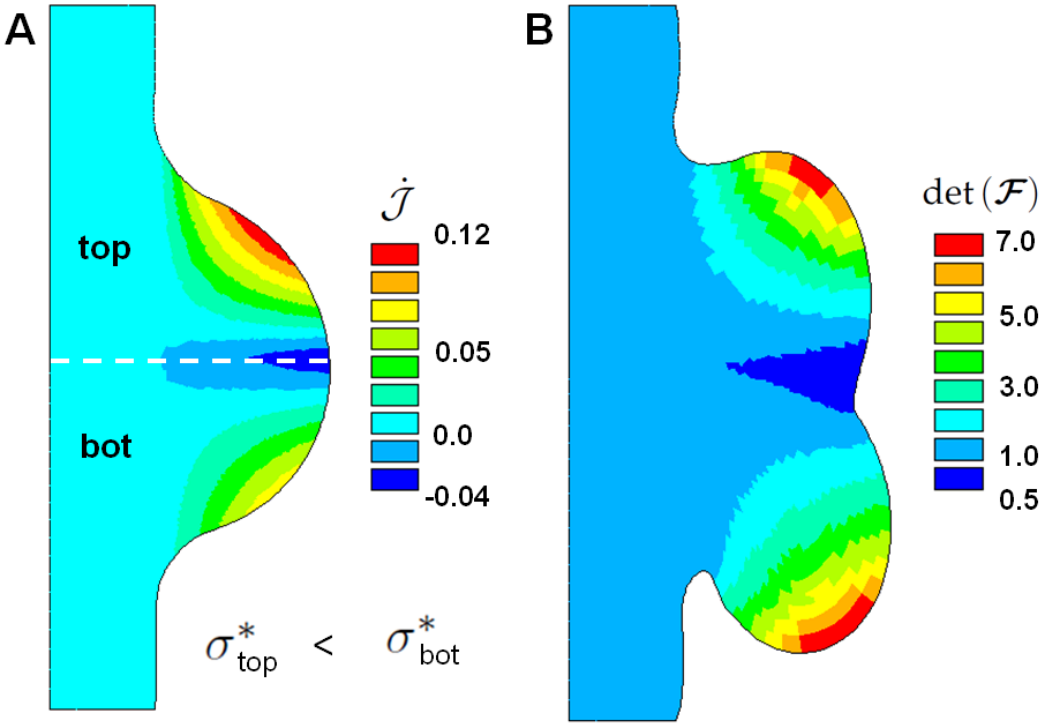

Figure A.4: "Butterfly" morphology of TGFβ2 KO can be simulated by having a more compressive homeostatic stress (σ^*) on the inflow (top) side relative to the outflow (bot) A) Color map of the dilatation rate after initial loading B) Inelastic Jacobian which represents the change in volume

APPENDIX B

APPENDIX B - MATLAB FILES

Appendix B contains the key Matlab files that were used to either generate numerical data presented in the thesis, or to aid my understanding of how the FE algorithms worked. All supporting function files are in the Matlab folder attached with the thesis. All executable files have the word "Run" in the filename.

B.1 Fixed Stress Growth

Purpose: Determine the evolution of the inelastic deformation under a fixed elastic stress, $\boldsymbol{f} = const$, with a homeostatic stress, and two possible incoming free energies, $\Delta\bar{\psi} = 0$ or $\Delta\bar{\psi} = -\bar{\psi}$. Results are presented in Chapter 5.

B.1.1 Fixed Stress Run

```
1 %Fixed Elastic Stress                              PB 5.21.12
2 clear;clc;close all
3
4 %Assume components of b = f*f' are constant
5 %with respect to time. Therefore the elastic
6 %stretches and the stress are constant in time.
7 %This code looks at the evolution of the growth
8 %tensor G under such a loading. Hydrostatic strain
```

```
%theta determined using S33=0 BC

%Homeostatic Stress can be changed in the ode file

%Evaluate 2 Incoming Free Energies
%1) Wh = 0 --> dW=-W
%2) Wh = W --> dW=0

%Parameters
mu = 10;         %Shear Modulus
a  = 0.01;       %Integration Factor
L1 = 1;          %Axial Stretch Ration
k = 0.3;         %Shear Parameter
%f0 = [cos(phi) sin(phi) 0; -sin(phi) cos(phi) 0; 0 0 1];
f0 = [L1 k 0; 0 1/sqrt(L1) 0; 0 0 1/sqrt(L1)];
b0 = f0*f0';

IC = [1,1,1,0,0,0,0,0,0];
tspan = [0,1];
for j = 1:2
IC = [1,1,1,0,0,0,0,0,0];
theta = b0(3,3);
MAT = [mu,a,j];
[t,f] = ode45(@remod_shear_traction_ode2b,...
    tspan,IC,[],f0,MAT,theta);
if j==1  %dW = -W
    f1 = f;
    t1 = t;
% [theta1,TRb1] = back_solve(t,f,F0,MAT);
elseif j==2 %dW = 0
    f2 = f;
    t2 = t;
```

```
% [theta2,TRb2] = back_solve(t,f,F0,MAT);
end
end
%Plot Results
det1 = f1(:,1).*f1(:,2).*f1(:,3) - f1(:,4).*f1(:,5).*f1(:,3);
det2 = f2(:,1).*f2(:,2).*f2(:,3) - f2(:,4).*f2(:,5).*f2(:,3);
fixed_f_G_stretch2(t,[f1(:,1),f2(:,1)]) %G11
fixed_f_G_stretch2(t,[f1(:,2),f2(:,2)]) %G22
fixed_f_G_stretch2(t,[f1(:,4),f2(:,4)]) %G12
fixed_f_G_stretch2(t,[det1,det2])       %det(G)
```

B.1.2 Fixed Stress ode

```
function [dydt] = remod_shear_traction_ode2b(t,y,f0,MAT,theta)

mu = MAT(1); a = MAT(2); j = MAT(3);
%Solve for Growth Tensor
G11 = y(1);G22 = y(2);G33 = y(3);
G12 = y(4);G21 = y(5);G13 = y(6);
G31 = y(7);G23 = y(8);G32 = y(9);

G = [G11 G12 G13; G21 G22 G23; G31 G32 G33];
f = f0;          %Elastic Deformation
%-------------------------------------------------
%Homeostatic Stress - Sigma_33 = 0
Lh = 1;
fh  = diag([Lh,1/sqrt(Lh),1/sqrt(Lh)]);
%-------------------------------------------------
%Elastic Stress - Sigma_33 = 0
```

```
Lab = Elsheby(f,fh,mu,j,theta);
Gdot = a*det(G)*Lab*G;
dydt = [Gdot(1,1);
        Gdot(2,2);
        Gdot(3,3);
        Gdot(1,2);
        Gdot(2,1);
        Gdot(1,3);
        Gdot(2,3);
        Gdot(3,1);
        Gdot(3,2)];

    function Lab = Elsheby(f,fh,mu,j,theta)
    b = f*f';
    bh = fh*fh';
    W = mu*(trace(b)-3);
    if j==1
        Wh = 0;
    elseif j==2
        Wh = W;
    end
    sig = 2*mu*(b - theta*eye(3));
    sigh = 2*mu*(bh - bh(3,3)*eye(3));
    Lab = f'*(sig-sigh)/f' +(Wh-W)*eye(3);
```

B.2 Fixed Displacement Remodeling

Purpose: Determine the evolution of the inelastic deformation under a fixed displacement, $\boldsymbol{F} = const$, with a homeostatic stress, and two possible incom-

ing free energies, $\Delta\bar{\psi} = 0$ or $\Delta\bar{\psi} = -\bar{\psi}$. At $t = 0$, an incompressible, purely elastic deformation is applied to a solid cube and held. The inelastic deformation evolves to return the current stress to the homeostatic level. Results are presented in Chapter 5.

B.2.1 Fixed Displacment Run

```
%Remodeling in Shear                PB 6.03.12
clear;clc;close all

%Assume a fixed shear deformation and simulate
%tissue remodeling.
%Evaluate 2 Incoming Free Energies
%1) Wh = 0 --> dW=-W
%2) Wh = W --> dW=0

%Homeostatic stress can be adjusted within
%the ode file


%Parameters
k = 0.5;          %Shear Parameter
mu = 10;          %Shear Modulus
a = 0.1;          %Integration Factor
L2=1;             %Axial Stretch Ration
F0 = [L2 k 0;0 1/sqrt(L2) 0; 0 0 1/sqrt(L2)];
%F0 = [1 0 0; k 1 0; 0 0 1];

```

```
%IC = [G11, G22, G33, G12, G21]
IC = [1,1,1,0,0,0,0,0,0];
tf = 1;
tspan = [0 tf];
%W Loop - Free Energy
for j = 1:2
    MAT = [mu,a,j];
[t,f] = ode45(@remod_shear_ode,tspan,IC,[],F0,MAT);

if j==1
    f1 = f;
G11 = f(:,1);
G22 = f(:,2);
G12 = f(:,4);
t1 = t;
[theta1,TRb1,S1] = back_solve(t,f,F0,MAT);
elseif j==2
    f2 = f;
G11_2 = f(:,1);
G22_2 = f(:,2);
G12_2 = f(:,4);
t2 = t;
[theta2,TRb2,S2] = back_solve(t,f,F0,MAT);
end
end

%Hydrostatic Pressure w/ Zero Homeostatic stress
W = mu*(TRb1-3);
frac = [0,1,2];
THETA = zeros(length(W),length(frac));
for k = 1:length(frac)
THETA(:,k) = 1/3*TRb1 + W*(frac(k)-1)/(2*mu);
```

```
54 end
55
56 fixed_f_G_stretch2(t1,[S1(:,1),S2(:,1)]/(2*mu));
57 fixed_f_G_stretch2(t1,[S1(:,2),S2(:,2)]/(2*mu));
58 fixed_f_G_stretch2(t1,[S1(:,3),S2(:,3)]/(2*mu));
59 fixed_f_G_stretch2(t1,[S1(:,4),S2(:,4)]/(2*mu));
60 fixed_f_G_stretch2(t1,[theta1,theta2]);
61
62 figure
63 plot(t1,THETA,t1,theta1,t2,theta2,'o')
64 xlabel('Time'); ylabel('P/(2␣\mu)');
65 legend('\Delta␣W␣=␣-W','\Delta␣W␣=␣0','\Delta␣W␣=␣W')
66
67 %Initialize Structures
68 Lt = length(t);
69 b11 = zeros(Lt,1);b22 = zeros(Lt,1);
70 b12 = zeros(Lt,1);b33 = zeros(Lt,1);
71 GG11 = zeros(Lt,1);GG22 = zeros(Lt,1);
72 GG12=zeros(Lt,1);GG33=zeros(Lt,1);
73 Sig11=zeros(Lt,1);Sig22=zeros(Lt,1);
74 Sig12=zeros(Lt,1);Sig33=zeros(Lt,1);
75 JG = zeros(Lt,1);Jb = zeros(Lt,1);
76
77
78 %Generate Movie of Deformation
79 for i=1:length(t)-10
80     G11 = f(i,1);G22 = f(i,2);G33 = f(i,3);
81     G12 = f(i,4);G21 = f(i,5);G13 = f(i,6);
82     G31 = f(i,7);G23 = f(i,8);G32 = f(i,9);
83     G = [G11 G12 G13; G21 G22 G23; G31 G32 G33];
84     GG = G*G';
85
```

```
86      ff = F0/G;  %Elastic Deformation
87      b = ff*ff'; %Left-Cauchy Green
88
89      b11(i) = b(1,1);
90      b22(i) = b(2,2);
91      b33(i) = b(3,3);
92      b12(i) = b(1,2);
93      Jb(i) = det(b);
94
95      SX1 = G*[1,0,0]';       %Line 1-2
96      SY1 = G*[0,1,0]';       %Line 1-4
97      S13 = G*[1,1,0]';       %Line 1-3
98
99    x1 = F0*[1,0,0]';
100   y1 = F0*[0,1,0]';
101   x13 = F0*[1,1,0]';
102
103   LX1x = [0,SX1(1)]; LX1y = [0,SX1(2)];
104   LY1x = [0,SY1(1)]; LY1y = [0,SY1(2)];
105   LXY1x = [SX1(1),S13(1)]; LXY1y = [SX1(2),S13(2)];
106   LYX1x = [SY1(1),S13(1)]; LYX1y = [SY1(2),S13(2)];
107
108
109   Lx1x = [0,x1(1)];  Lx1y = [0,x1(2)];
110   Ly1x = [0,y1(1)];  Ly1y = [0,y1(2)];
111   Lxy1x = [x1(1),x13(1)];  Lxy1y = [x1(2),x13(2)];
112   Lyx1x = [y1(1),x13(1)];  Lyx1y = [y1(2),x13(2)];
113
114   clf
115
116   line(Lxy1x,Lxy1y,'Color','b','LineWidth',2,'LineStyle','--')
117   line(LX1x,LX1y,'Color','g','LineWidth',2) %Growth deformation
```

```
118     line(LY1x,LY1y,'Color','g','LineWidth',2)
119     line(LXY1x,LXY1y,'Color','g','LineWidth',2)
120     line(LYX1x,LYX1y,'Color','g','LineWidth',2)
121     line(Lx1x,Lx1y,'Color','b','LineWidth',2,'LineStyle','--')
122     line(Ly1x,Ly1y,'Color','b','LineWidth',2,'LineStyle','--')
123     line(Lyx1x,Lyx1y,'Color','b','LineWidth',2,'LineStyle','--')
124     xlabel('X','FontSize',20)
125     ylabel('Y','FontSize',20)
126     axis([0 2 0 2])
127     axis square
128
129     h = legend('$F$','$\mathcal{F}$');
130     set(h,'Interpreter','Latex','FontSize',16,...
131         'YColor',[1 1 1],'XColor',[1 1 1])
132
133     text(0.1,1.75,'$f_\,=$','Interpreter','Latex','FontSize',18)
134     text(0.25,1.75,num2str(ff(1:2,1:2),2),'FontSize',18)
135
136      M(:,i) = getframe;
137      %Store Inelastic Deformation
138      GG11(i) = GG(1,1);
139      GG22(i) = GG(2,2);
140      GG33(i) = GG(3,3);
141      GG12(i) = GG(1,2);
142      JG(i) = det(G);
143
144      %Store Cauchy Stress
145      Sig = 2*mu*(b - 1/3*trace(b)*eye(3));
146      Sig11(i) = Sig(1,1);
147      Sig22(i) = Sig(2,2);
148      Sig33(i) = Sig(3,3);
149      Sig12(i) = Sig(1,2);
```

```
150 end
```

B.2.2 Fixed Displacement ode

```
1  function [dydt] = remod_shear_ode(t,y,F0,MAT)
2
3  mu = MAT(1); a = MAT(2); j = MAT(3);
4
5  %Solve for Growth Tensor
6  G11 = y(1);G22 = y(2);G33 = y(3);
7  G12 = y(4);G21 = y(5);G13 = y(6);
8  G31 = y(7);G23 = y(8);G32 = y(9);
9
10 G = [G11 G12 G13; G21 G22 G23; G31 G32 G33];
11
12 f = F0/G;
13
14 %Homeostatic State
15 Lh = 1; kh = 0;
16 fh = [Lh kh 0;0 1/sqrt(Lh) 0; 0 0 1/sqrt(Lh)];
17
18 Lab = Elsheby(f,fh,mu,j);
19 Gdot =a*det(G)*Lab*G;
20 dydt = [Gdot(1,1);
21          Gdot(2,2);
22          Gdot(3,3);
23          Gdot(1,2);
24          Gdot(2,1);
25          Gdot(1,3);
```

```
26          Gdot(2,3);
27          Gdot(3,1);
28          Gdot(3,2)];
29
30      function Lab = Elsheby(f,fh,mu,j)
31      b = f*f'; c = f'*f;
32      bh = fh*fh';
33      W = mu*(trace(b)-3);
34      if j==1
35          Wh = 0;
36      elseif j==2
37          Wh = W;
38      elseif j==3
39          Lh = 1;
40          fh  = diag([Lh,1/sqrt(Lh),1/sqrt(Lh)]);
41          bh = fh*fh';
42          Wh = mu*(trace(bh)-3);
43          bh = diag([1 1 1]);
44      end
45      dW = Wh-W;
46      theta = 1/3*trace(c) + dW/(2*mu);
47      sig = 2*mu*(b - theta*eye(3));
48      sigh = 2*mu*(bh - trace(bh)/3*eye(3));
49      Lab = f'*(sig-sigh)/f' +(Wh-W)*eye(3);
```

B.2.3 Fixed Displacement backsolve

Calculates the hydrostatic pressure neccesary to ensure the evolution is volume preserving, $\mathcal{L}_{\alpha\alpha} = 0$.

```
1  function [Theta,TRb,S] = back_solve(t,f,F0,MAT)
```

```
%Solve for the Cauchy stresses and
%hydrostatic pressure using the inelastic
%deformation results from the ode solver

Lt = length(t); mu = MAT(1); j = MAT(3);
WW = zeros(Lt,1);
TRb = zeros(Lt,1); Theta= zeros(Lt,1);
S = zeros(Lt,4);
for i=1:Lt
    G11 = f(i,1);G22 = f(i,2);G33 = f(i,3);
    G12 = f(i,4);G21 = f(i,5);G13 = f(i,6);
    G31 = f(i,7);G23 = f(i,8);G32 = f(i,9);
    G = [G11 G12 G13; G21 G22 G23; G31 G32 G33];
    ff = F0/G;
    b = ff*ff';
    WW(i) = mu*(trace(b)-3);
    if j==1
    dW=-WW(i);
    elseif j==2
    dW = 0;
    end
    TRb(i) = trace(b);
    Theta(i) = 1/3*TRb(i) + dW/(2*mu);
    sig = 2*mu*(b - Theta(i)*eye(3));
    Theta(i) = dW/(2*mu);
    S(i,1) = sig(1,1); S(i,2) = sig(2,2); S(i,3) = sig(3,3);
    S(i,4) = sig(1,2);
end
```

B.3 3D Single Element FE Model

Purpose: Implement a nonlinear FE model of a single element to, 1) validate constitutive-relation derivations, 2) to better understand the construction of the tangent elasticity matrix, and 3) see how the Newton Raphson iteration is implemented in ANSYS. The model consists of a single, 4-node cube element with four Gauss integration points in each dimension. This is a Lagrangian formulation. The cube is under a uni-axial load in the x-direction which is initially ramped with no growth, and then held with growth active. The inelastic deformation is stored using a Matlab <struct>, similar to the user state variables in ANSYS. A pseudo-code of the Newton Raphson method in the context of

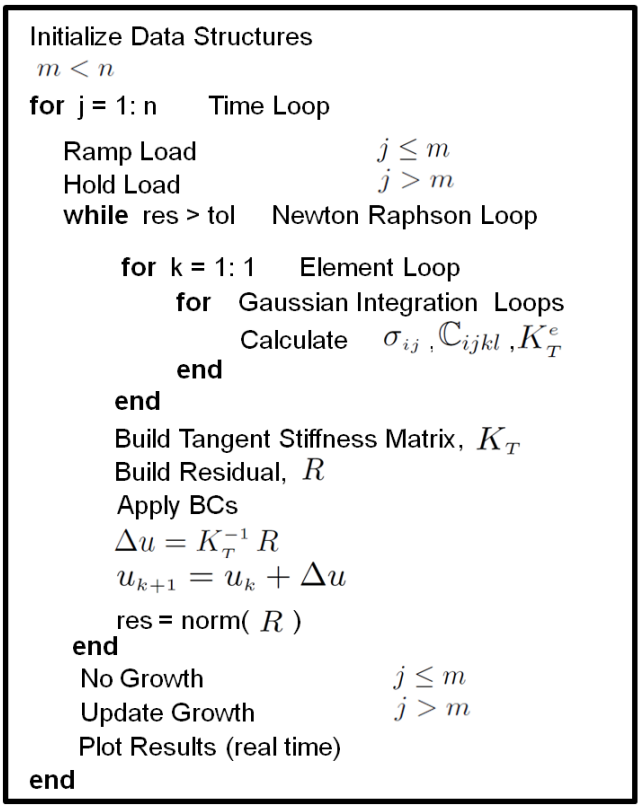

Figure B.1: Pseudo-code of nonlinear FEs using the Newton Raphson algorithm

nonlinear FEs is presented in Figure B.1. The "run" file plots a 3D image of a growing cube in real time during the simulation (Figure B.2). Only key Matlab files for the algorithm are presented. Supporting files, such as shape functions and storage routines, are included in the attached folder.

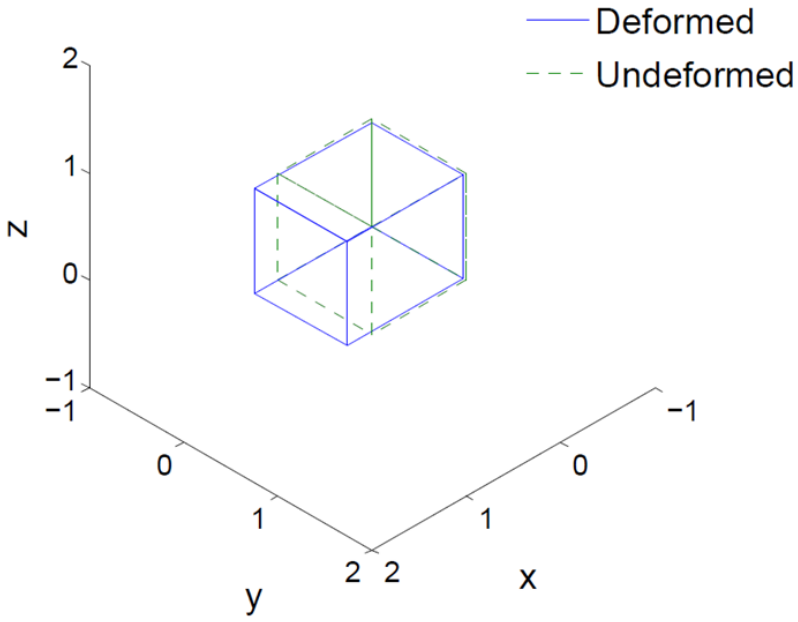

Figure B.2: Pseudo-code of nonlinear FEs using the Newton Raphson algorithm

B.3.1 3D Cube Nonlinear FE Run

```
1 %3D Stress-based Growth Element          10/17/11
2 clear; clc; close all; tic
```

```
3
4  %3D FEM algorithm for a stress based growth
5  %law using a Neo-hookean material.  Algorithm
6  %details a single element only.  Lagrangian
7  %implementation, hence 2nd PK stress calculated.
8
9  %Uniaxial Loading
10
11 %-----------------------------------------------
12 %Initial Element Nodes & Material Parameters
13 mu = 20;         %Initial Shear Modulus
14 D1 = 0.002;      %Inverse Bulk Modulus
15 a  = 0.05;       %Numerical Integration Factor
16 MAT = [mu,D1,a];
17 %Initial Node Coordinates (cube [0,1])
18 [XYo,XY] = init_node_coords();
19 xy_n = XY;
20 %Initial Growth Tensor & Displacement Profile
21 [G,F0] = init_G(); ue=zeros(24,1); %tou=[0;0;0];
22 %-----------------------------------------------
23 %Figure Setup
24 scrsz = get(0,'ScreenSize');
25 h1 = figure('Position',...
26     [200 300 scrsz(4)/2 scrsz(4)/2]);
27 h2 = figure('Position',...
28     [700 300 scrsz(4)/1.5 scrsz(4)/2]);
29 %-----------------------------------------------
30 [z,w] = gauss4();   %Gauss Nodes & Wieghts
31 %-----------------------------------------------
32 n = 20;          %total # time steps
33 t = 0;           %Start time
34 T = 1;           %End time
```

```
35 del_t = T/n;     %Step Size
36 T_load = 1;      %Load Time Final
37 mm = 5;         %# of load steps
38 tou = 0; touf = 5/4;     %Inital & Final Load
39 del_tou = (touf-tou)/mm;     %Load Ramp
40 %-------------------------------------------------
41 %Initialize Storage Structures
42 u2x = zeros(n,1); C11 = zeros(n,1);
43 Time = zeros(n,1); Sigxx = zeros(n,1);
44 Sigyy = zeros(n,1); Sigzz = zeros(n,1);
45 Sigxz = zeros(n,1); Sigxx_F = zeros(n,1);
46 B11 = zeros(n,1); e11 = zeros(n,1);
47 ux_n4=zeros(n,1);Cse = zeros(6,6);
48 P = zeros(24,1); KK = zeros(n,1);
49 B11_F = zeros(n,1); Sigxx_all = zeros(n,1);
50 JL=1; iii=1;
51 %Time Loop
52 for jj=1:n
53 %Apply Load Increment
54    if jj < mm
55    tou = tou + del_tou;
56    else
57    tou = tou;
58    end
59    t = t + del_t;
60 %-----------------------------------------------
61 %Newton-Rhaphson Loop
62 tol=10^-5; maxiter=200; del=3;kk=1;
63 while kk< maxiter && del>tol
64    %Load Vector - no load increment
65    %x-axis normal load
66
```

```
67      P(1)= tou/JL; P(4)=tou/JL;
68      P(7)=tou/JL; P(10)=tou/JL;
69      %x face,y-direction
70      %P(3)= tou; P(6)=tou; P(9)=tou; P(12)=tou;
71  %-----------------------------------------------
72  %Loop over Elements (just one in this case)
73       xyV = XYo' + ue;     %Current Node Locations
74       xy  = Voight_Trans(xyV);
75  %-----------------------------------------------
76  %Gauss Integration
77  I=zeros(24,1);   Kmat=zeros(24,24);
78  Kgeom=zeros(24,24);
79  Sb = zeros(9,9);  P1 = zeros(24,1);
80  for i=1:4        %x coordinate loop
81       I1 = zeros(24,1);
82       Kmat1 = zeros(24,24);
83       Kgeom1 = zeros(24,24);
84
85       for l=1:4   %z coordinate loop
86       Ie=zeros(24,1);
87       K1=zeros(24,24);
88       K2=zeros(24,24);
89
90       for j=1:4   %y coordinate loop
91       %Volume Integral
92       Be=quadB3(z(i),z(j),z(l));      %dN/de
93       N=quadNV3(z(i),z(j),z(l));      %Voight N
94       Fex=Be*xy;                      %dx/de
95       Feo=Be*XY;                      %dX/de
96       Jeo=det(Feo);        %Jacobian-Undeformed to Parent
97       F = Feo\Fex;         %dx/dX - Deformation Gradient
98       B = Feo\Be;          %dN/dX
```

```
99      Bo=quadBo3(F,B);     %Total Lagrangian Diff Operator
100     Bgeom=quadBgeom3(B);%Undeformed Gradient Operator
101     JL = F(2,2)*F(3,3);
102
103     %Inner Loop Stress Update
104     [S,Sb,Cse,G,F0] =...
105     Stress_Calc_NeoHookean_Calg(F,G,F0,MAT,i,l,j,t,Cse,kk);
106
107     %Internal Force Stiffness
108         Ie=Ie+w(j)*Bo'*S*Jeo;
109     %Material Stiffness
110         K1=K1+w(j)*Bo'*Cse*Bo*Jeo;
111     %Geometric Stiffness
112         K2=K2+w(j)*Bgeom'*Sb*Bgeom*Jeo;
113     end
114     I1=I1+w(l)*Ie;  Kmat1=Kmat1+w(l)*K1; Kgeom1=Kgeom1+w(l)*K2;
115     end
116     I=I+w(i)*I1; Kmat=Kmat+w(i)*Kmat1; Kgeom=Kgeom+w(i)*Kgeom1;
117  end
118 %-----------------------------------------------------------------
119 %Tangent Stiffness Assembly
120 Kt=Kmat+Kgeom;              %Tangent Stiffness, Kt
121 R=I-P;                      %Residual = Internal - Applied
122 %-----------------------------------------------------------------
123 if kk<2  %Store Initial Residual
124    Ro=R;
125 end
126 %-----------------------------------------------------------------
127 %Apply Boundary Conditions
128
129 %Uniaxial load of cube element with displacements of
130 %side opposing the loaded surface fixed
```

```
131 % %Apply BCs - Fixed yz face  @ x=0,  Nodes 5-8 Fixed
132 %  R(13:24)=0; %Node 5-8
133 %  Kt(:,13:24)=0; Kt(13:24,:)=0;
134 %Kt(13:24,13:24)=diag(ones(12,1));
135
136 %Apply BCs - Fixed yz face  @ x=0,  Nodes 5,8 Fixed
137  R(13:16)=0; %Node 5 Fixed, 6 ux=0
138  Kt(:,13:16)=0; Kt(13:16,:)=0;
139  Kt(13:16,13:16)=diag(ones(4,1));
140  R(22)=0; R(19)=0; %Node 7,8 ux=0
141  Kt(:,22)=0; Kt(22,:)=0; Kt(22,22)=1;
142  Kt(:,19)=0; Kt(19,:)=0; Kt(19,19)=1;
143
144  R(18)=0; R(23)=0; %Node 6 uz=0 Node 8 uy=0
145  Kt(:,23)=0; Kt(23,:)=0; Kt(23,23)=1;
146  Kt(:,18)=0; Kt(18,:)=0; Kt(18,18)=1;
147
148  R(3)=0; R(11)=0; %Node 1 uz=0 Node 4 uy=0
149  Kt(:,3)=0; Kt(3,:)=0; Kt(3,3)=1;
150  Kt(:,11)=0; Kt(11,:)=0; Kt(11,11)=1;
151
152  R(6)=0;  %Node 2 uz
153  Kt(:,6)=0; Kt(6,:)=0; Kt(6,6)=1;
154  R(2)=0; Kt(:,2)=0; Kt(2,:)=0; Kt(2,2)=1;
155
156 % %Shear BCs
157 % R(13:24)=0; %Node 5-8
158 % Kt(:,13:24)=0; Kt(13:24,:)=0;
159 %Kt(13:24,13:24)=diag(ones(12,1));
160 %-------------------------------------------------------------
161 %Plot Results before new F,
162 %evaluated at gauss node (3,3,3)
```

```
drawnow
[Sig,B,F,Fg,Sig_F,u2] = Neo_output(G,xy,XY,ue,MAT,3,3,3);
xyp = [xy(1:4,:);xy([1,5:8,5,8,4,3,7,6,2],:)];
XYp = [XY(1:4,:);XY([1,5:8,5,8,4,3,7,6,2],:)];

C = F'*F; B_F = F*F';
u2x(jj) = u2(1);
ux_n4(jj) = ue(10);
C11(jj) = C(1,1);
Time(jj) = t;
Sigxx_all(iii) = Sig(1,1);
Sigxx(jj) = Sig(1,1);
Sigyy(jj) = Sig(2,2);
Sigzz(jj) = Sig(3,3);
Sigxz(jj) = Sig(1,3);
Sigxx_F(jj) = Sig_F(1,1);
B11(jj) = B(1,1);
e11(jj) = 1/2*(B(1,1)-1);
B11_F(jj) = B_F(1,1);

 set(0,'CurrentFigure',h1)
 plot3(xyp(:,1),xyp(:,2),xyp(:,3),XYp(:,1),...
     XYp(:,2),XYp(:,3),'--');
 view([1,1,1])
 axis([-1 2 -1 2 -1 2])
 xlabel('x'); ylabel('y'); zlabel('z');
 title('NeoHookean Cube Element under surface traction')
 legend('Deformed','Undeformed','Location','Southeast')

set(0,'CurrentFigure',h2)
subplot(1,2,1)
plot(u2x(1:jj),Sigxx(1:jj)/mu,u2x(1:jj),Sigxz(1:jj)/mu)
```

```
xlabel('Time')
ylabel('Cauchy Stress, $T_{xx}$','Interpreter','latex')
axis([0 0.25 -.2 1])
% h2 = legend('$\sigma_{xx}(F)$','$\sigma_{xy}(f)$');
% set(h2,'Interpreter','latex')

subplot(1,2,2)
plot(sqrt(B11_F(1:jj)),Sigxx_F(1:jj)/mu,...
    sqrt(B11(1:jj)),Sigxx(1:jj)/mu,...
    sqrt(B11_F(1:jj)),Sigxx(1:jj)/mu)
xlabel('Stretch Ratio')
ylabel('Cauchy Stress, $T_{xx}$','Interpreter','latex')
axis([1 1.3 0 1])
h3 = legend('$\lambda_{total} \sigma_{total}$',...
    '$\lambda_{elastic} \sigma_{elastic}$',...
    '$\lambda_{total} \sigma_{elastic}$');
set(h3,'Interpreter','latex')

%-------------------------------------------------------------
%Solve delT
delu=Kt\(-R);                    %Delta ug
ue=ue+delu;                      %Update Displacement
del=norm(R)/norm(Ro);
kk=kk+1;
iii = iii+1;
cond(Kt);       %Condition of Tangent Stiffness Matrix
%-------------------------------------------------------------
end
kk;
KK(jj) = kk;
if jj > mm
G = growth_update(G,xy,XY,MAT,del_t);
```

```
227 else
228 G=G;
229 end
230 xy_n = xy;                    %Node Locations at tn
231 end
232 toc
```

B.3.2 3D Cube Nonlinear FE Stress Calc

```
function [S,Sb,Cab,G,F0,JL] = Stress_Calc_NeoHookean_Calg(F...
    ,G,F0,MAT,i,l,j,t,Cab,kk)

%Update 2nd PK stress tensor, and build tangent
%elasticity tensor. NeoHookean Material w/
%Bulk Modulus Parameter
%-------------------------------------------------------------
%Initialize Subroutine Structures
Sb = zeros(9,9);
%Material Parameters
mu = MAT(1); %Shear Modulus
D1 = MAT(2); %Inverse Bulk Modulus
%-------------------------------------------------------------
%Decompose Growth and Elastic Deformation Components
Fg = growth_call(G,i,l,j);   %Call current integration pt Fg
Fe = F/Fg;                   %Elastic Deformation Gradient
%-------------------------------------------------------------
%Kinematics
Je = det(Fe);        %Jacbian Elastic
Ce = Fe'*Fe;         %Right Cauchy Green(RCG) Tensor
I = eye(3);          %Identity Tensor
Cinv = I/Ce;         %Inverse RCG
I_c = Je^(-2/3)*trace(Ce);  %1st Invariant
Cinv_b = Cinv*Je^(2/3);     %Deviatoric C^{-1}
%-------------------------------------------------------------
%NeoHookean Material Law: W = (mu/2)(I_c -3)+(1/D1)(J-1)^2
Sm = mu*(Je^(-2/3)*I-1/3*I_c*Cinv')...
    + 2/D1*Je*(Je-1)*Cinv'; %Second P-K Stress
```

```
29 S=[Sm(1,1);Sm(2,2);Sm(3,3);Sm(2,3);...
30     Sm(1,3);Sm(1,2)]; %Voight Notation
31 %Stress for Geometric Stiffness Tensor
32 Sb(1:3,1:3) = Sm; Sb(4:6,4:6) = Sm; Sb(7:9,7:9) = Sm;
33 %-------------------------------------------------------
34 %Build Elasticity Tensor
35 Cab  = Elast_tensor_NeoHookean_Calg(Fe,MAT);
36 %Material Subroutine Complete - Return to FEM Loop
```

B.3.3 3D Cube Nonlinear FE Elasticity Tensor

```
function Cab = Elast_tensor_NeoHookean_Calg(F,MAT)
%Calculate Material Elasticity Tensor dS/dE
%Represent in 6x6 tensor using symmetry
%      1      2      3      4      5      6
%1  C1111 C1122 C1133 C1123 C1113 C1112
%2  C2211 C2222 C2233 C2223 C2213 C2212
%3  C3311 C3311 C3333 C3323 C3313 C3312
%4  C2311 C2322 C2333 C2323 C2313 C2312
%5  C1311 C1322 C1333 C1323 C1313 C1312
%6  C1211 C1222 C1233 C1223 C1213 C1212


%-----------------------------------------------------------
%Initialize Subroutine Structures
Cab = zeros(6,6);  Cab2 = zeros(6,6);


mu = MAT(1); D1 = MAT(2);   %Material Parameters
C = F'*F;  Cinv = C\eye(3); %RCG Stretch Tensor & Inverse
J = det(F); I_c = J^(-2/3)*trace(C);
Ic = trace(C);
JJ = J^(-2/3);
%-----------------------------------------------------------
%Elasticity Coefficients
a5 = -(1/3)*mu*J^(-2/3);
a7 = -(1/18)*mu*I_c + 1/(2*D1)*J*(2*J-1);
a8 = (1/6)*mu*I_c - (1/D1)*J*(J-1);

%Voight Notation
Cvi = [Cinv(1,1);Cinv(2,2);Cinv(3,3);...
```

```
    Cinv(2,3);Cinv(1,3);Cinv(1,2)];
Iv = [1;1;1;0;0;0];
for a = 1:6
    for b = 1:6
%[i,j,l,m] = index(a,b);
% Cab2(a,b) = -(2/3)*mu*JJ*Cvi(b)*Iv(a) + ...
%     (2/9)*mu*I_c*Cvi(b)*Cvi(a)- (2/3)*mu*JJ*Iv(b)*Cvi(a)...
%     + (1/3)*mu*I_c*(Cinv(i,l)*Cinv(j,m)+Cinv(i,m)*Cinv(j,l))...
%     + (2/D1)*J*(J-1)*Cvi(b)*Cvi(a) + (2/D1)*J^2*Cvi(b)*Cvi(a)...
%     - (4/D1)*J*(J-1)*Cinv(j,l)*Cinv(m,i);
[i,j,k,l] = index(a,b);
Cab(a,b) = -2/3*mu*JJ*(Iv(a)*Cvi(b) + Cvi(a)*Iv(b)...
    -1/3*Ic*Cinv(j,i)*Cinv(l,k) - Ic*Cinv(j,l)*Cinv(k,i))...
    +2/D1*J*(2*J-1)*Cinv(l,k)*Cinv(j,i)...
    -4/D1*J*(J-1)*Cinv(j,l)*Cinv(k,i);

    end
end

%Index between Vioght and Full Notation
function [i,j,k,l] = index(a,b)
    if a==1
        i=1; j=1;
    elseif a==2
        i=2; j=2;
    elseif a==3
        i=3; j=3;
    elseif a==4
        i=2; j=3;
    elseif a==5
        i=1; j=3;
    elseif a==6
```

```
63          i=1; j=2;
64      end
65      if b==1
66          k=1; l=1;
67      elseif b==2
68          k=2; l=2;
69      elseif b==3
70          k=3; l=3;
71      elseif b==4
72          k=2; l=3;
73      elseif b==5
74          k=1; l=3;
75      elseif b==6
76          k=1; l=2;
77      end
```

B.3.4 3D Cube Nonlinear FE Growth

```
function G = Stress_Calc_NeoHookean_Growth(F,G,MAT,i,l,j,del_t)
%Update Growth Deformation
%NeoHookean Material w/ Bulk Modulus Parameter
% (i,l,j) -> (x,z,y)
%-------------------------------------------------
%Initialize Subroutine Structures
Sb = zeros(9,9);
%Material Parameters
mu = MAT(1); %Shear Modulus
D1 = MAT(2); %Bulk Modulus
a  = MAT(3); %Numerical Integration Factor
%-------------------------------------------------
%Decompose Growth and Elastic Deformation Components
Fg = growth_call(G,i,l,j);
Fe = F/Fg;  %Elastic Deformation Gradient
%-------------------------------------------------
%Kinematics
Je = det(Fe);    %Jacobian Elastic
Ce = Fe'*Fe;     %Right Cauchy Green(RCG) Tensor
I = eye(3);      %Identity Tensor
Cinv = I/Ce;     %Inverse RCG
I_c = Je^(-2/3)*trace(Ce);  %1st Invariant
Ic = trace(Ce);
Cinv_b = Cinv*Je^(2/3);
%-------------------------------------------------
%NeoHookean Material Law:
%W = (mu/2)(I_c -3) + (1/D1)(J-1)^2
Sig = mu*Je^(-5/3)*(Fe*Fe' - 1/3*trace(Fe*Fe')*I)...
```

```
29      + 2/D1*(Je-1)*I;
30
31  %Integration of Evolution Equation
32  Ls = Fe'*Sig/(Fe');          %Growth Deformation Rate
33  Fg = Fg + a*Ls*Fg*del_t;     %Explict Time Integration
34
35  %Store Updated Growth Tensor(x,z,y)
36  G = growth_store(Fg,G,i,l,j);
```

APPENDIX C

APPENDIX C - ANSYS FILES

C.1 ANSYS USERHYPER

ANSYS allows users to implement custom constituitive material behavior. For hyperelastic materials, the implementation is streamlined by the built-in subroutine USERHYPER. At every integration point, ANSYS will access USERHYPER to evaluate the hyperelastic potential and the 1st and 2nd partial derivatives with respect to the strain invariants. The USERHYPER subroutine is capable of enforcing an incompressibility constraint using hybrid displacement - pressure (u-p) elements. Hybrid elements include an extra degree of freedom which approximates the pressure neccesary to enforce incompressibility. To ensure this pressure field is only associated with the volumetric deformation, the deformation gradient (F_{iA}) is decomposed into a deviatoric/volumetric split, specifically,

$$\bar{F}_{iA} = J^{-\frac{1}{3}} F_{iA} \tag{C.1.1}$$

where $J = det(F_{iA})$ is the Jacobian of the deformation gradiant. From this decomposition we see that $det(\bar{\boldsymbol{F}}) = 1$, and consequently the constitutive relations can now be defined uniquely in terms of these deviatoric and volumetric variables. Therefore the arguments of an isotropic, hyperelastic material law include only the 1st and 2nd invariants of the modified left Cauchy-Green stretch tensor,

$\bar{\boldsymbol{B}} = \bar{\boldsymbol{F}}\bar{\boldsymbol{F}}^T$, and the Jacobian as listed below:

$$\begin{aligned} \bar{I}_B &= tr(\bar{\boldsymbol{B}}) \\ \bar{I}I_B &= \frac{1}{2}\left[tr(\bar{\boldsymbol{B}})^2 - tr(\bar{\boldsymbol{B}^2})\right] \\ J &= det(\boldsymbol{F}) \end{aligned}$$

ANSYS requires the 1st and 2nd partial derivatives of the material law in order to calculate the Cauchy stress, σ_{ij}, and tangent elasticity tensor, $\mathcal{C}_{ijkl}$, at every integration point. The tangent elasticity tensor, called the material Jacobian in the ANSYS documentation (Sec 6.4.1.2), predicts the next step of the Newton-Raphson iteration used to solve each load step. The material law and partial derivatives implemented in the USERHYPER for both the incompressible and nearly incompressible cases are outlined below.

C.1.1 Fully Incompressible Case

We implemented in ANSYS the following exponential, isotropic, incompressible hyperelastic material law with linear and nonlinear material parameters C and α, respectively.

$$\psi\left(\bar{I}_B\right) = \frac{C}{2}\left\{exp\left[\alpha(\bar{I}_B - 3)\right] - 1\right\} \tag{C.1.2}$$

Below are the 1st and 2nd partial derivatives required by the ANSYS USERHYPER subroutine.

$$\begin{aligned} \frac{\partial\psi}{\partial\bar{I}_B} &= \frac{\alpha\, C}{2} exp\left[\alpha(\bar{I}_B - 3)\right] \\ \frac{\partial^2\psi}{\partial\bar{I}_B^2} &= \frac{\alpha^2\, C}{2} exp\left[\alpha(\bar{I}_B - 3)\right] \end{aligned}$$

The Cauchy stress in this case has the following form,

$$\sigma_{ij} = \frac{\alpha C}{J}\, exp\left[\alpha\left(\bar{I}_B - 3\right)\right]\left(\bar{B}_{ij} - \frac{1}{3}\bar{B}_{kk}\,\delta_{ij}\right) + p\,\delta_{ij} \tag{C.1.3}$$

where we have used the relation,

$$\frac{\partial \bar{I}_B}{\partial F_{iA}} = -\frac{2}{3}J^{-\frac{2}{3}}F^{-1}_{Ai}\,B_{kk} + 2J^{-\frac{2}{3}}F_{iA}$$

and where p is the pressure associated with the incompressibility constraint.

C.1.2 Nearly Incompressible Case

For a nearly incompressible material, the free energy is identical to Eq C.1.2 except for the additional term containing the jacobian, J. Nearly incompressible materials are implemented through a lagrange multiplier, or penalty method. The paramter d_1 is the inverse of the bulk modulus, κ, which is a measure of a material's resistance to volumetric expansion or contraction. The selection of d_1 determines the strictness of the incompressibility condition. J goes to 1 as $\kappa = \frac{1}{d_1}$ goes to ∞. Near this limit, the material is ultra sensitive to changes in volume which can result in a large Cauchy stresses and, consequently, an ill-conditioned tangent elasticity tensor. Therefore the penatly method technique can only model nearly incompressible materials, which in many situations is sufficiently accurate. Below is the nearly incompressible hyperelastic potential and respective derivatives.

$$\psi\left(\bar{I}_B, J\right) = \frac{C}{2}\left\{exp\left[\alpha(\bar{I}_B - 3)\right] - 1\right\} + \frac{1}{d_1}\left(J-1\right)^2 \tag{C.1.4}$$

1st and 2nd partial derivatives:

$$\begin{aligned}
\frac{\partial \psi}{\partial \bar{I}_B} &= \frac{\alpha\, C}{2} exp\left[\alpha(\bar{I}_B - 3)\right] \\
\frac{\partial \psi}{\partial J} &= \frac{2}{d_1}\,(J-1) \\
\frac{\partial^2 \psi}{\partial \bar{I}_B^2} &= \frac{\alpha^2\, C}{2} exp\left[\alpha(\bar{I}_B - 3)\right] \\
\frac{\partial^2 \psi}{\partial J^2} &= \frac{2}{d_1} \\
\frac{\partial^2 \psi}{\partial J\, \partial \bar{I}_B} &= 0
\end{aligned}$$

The Cauchy stress for the nearly incompressible case is a slightly modified form of Eq. (C.1.3), due to the additional term in the free energy.

$$\sigma_{ij} = \frac{\alpha C}{J}\, exp\left[\alpha\left(\bar{I}_B - 3\right)\right]\left(\bar{B}_{ij} - \frac{1}{3}\bar{B}_{kk}\,\delta_{ij}\right) + \frac{2}{d_1}\,(J-1)\;\delta_{ij} \tag{C.1.5}$$

C.1.3 Validation of USERHYPER Routine

The USERHYPER implementation was validated against analytical results for the homogeneous deformations of uniaxial extension, uniaxial compression, (Figure C.1) and simple shear (Figure C.2). The simulations were initialy performed on an single 3D 8-node brick element. The problem was then solved with a mesh. The fully incompressible results are presented in Figure C.1 & C.2. For the uniaxial load simulation, the hydrostatic pressure p was determine by assuming $\sigma_{\text{yy}} = \sigma_{\text{zz}} = 0$. With this assumption and the corresponding uniaxial load deformation,

$$\boldsymbol{F} = \text{diag}\left(\lambda, \lambda^{-1/2}, \lambda^{-1/2}\right)$$

the analytical stress-strain relation for the axial stress reduces to,

$$\sigma_{\text{xx}} = \alpha C\, exp\left[\alpha\left(\lambda^2 + \frac{2}{\lambda} - 3\right)\right]\left(\lambda^2 - \frac{1}{\lambda}\right) \tag{C.1.6}$$

Similarly, using the simple shear deformation gradient,

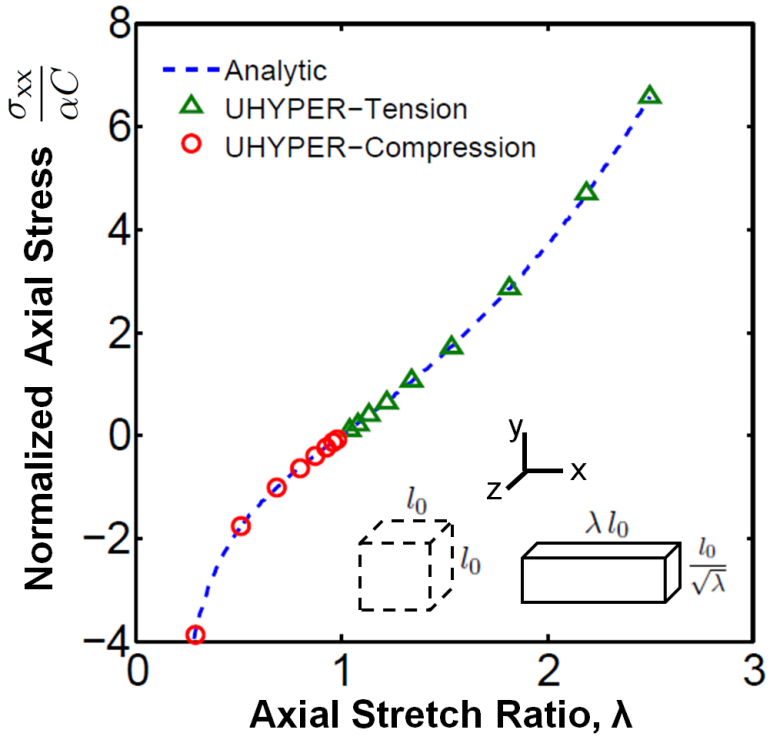

Figure C.1: Plot of normalized axial stress, $\sigma_{xy}/\alpha C$, versus axial stretch ratio, λ for a uniaxial tension and compression test. The plot compares the ANSYS USERHYPER output with the analytical result. C=10, $\alpha = 0.03$

$$\mathbf{F} = \begin{bmatrix} 1 & 0 & 0 \\ k & 1 & 0 \\ 0 & 0 & 1 \end{bmatrix}$$

we can derive the analytical expression for the Cauchy shear stress.

$$\sigma_{xy} = \alpha C\, exp\left[\alpha k^2\right] k \tag{C.1.7}$$

The ANSYS results agreed well with the analytical results (Figure C.1 & C.2), indicating that the material was correctly implemented.

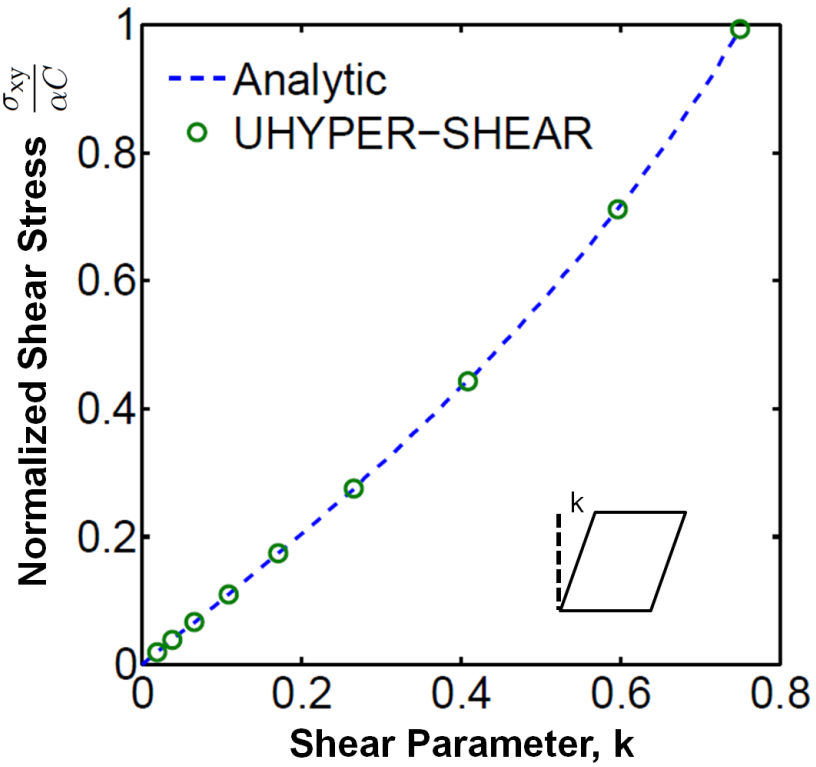

Figure C.2: Plot of normalized shear stress, $\sigma_{xy}/\alpha C$, versus shear parameter, k, comparing the ANSYS USERHYPER output with the analytical result. C=10, $\alpha = 0.5$

C.1.4 USERHYPER Fortran Code

```
1  *deck,UserHyper    USERDISTRIB  parallel                          gal
2        subroutine UserHyper(
3       &                        prophy, incomp, nprophy, invar,
4       &                        potential, pInvDer)
5  c**********************************************************************
6  c
7  c     *** Example of user hyperelastic routine
8  c
9  c           This is an exponential material law of the 1st
10 c           invariant used for the isotropic modeling of
11 c           the pipette experiment
```

```
c
c     input arguments
c     ===============
c      prophy      (dp,ar(*),i)     material property array
c      nprophy     (int,sc,i)       # of material constants
c      invar       dp,ar(3)         invariants
c
c     output arguments
c     ================
c      incomp      (log,sc,i)    fully incompressible or compressible
c      potential    dp,sc        value of potential
c      pInvDer       dp,ar(10)   der of potential wrt i1,i2,j
c                                 1 - der of potential wrt i1
c                                 2 - der of potential wrt i2
c                                 3 - der of potential wrt i1i1
c                                 4 - der of potential wrt i1i2
c                                 5 - der of potential wrt i2i2
c                                 6 - der of potential wrt i1j
c                                 7 - der of potential wrt i2j
c                                 8 - der of potential wrt j
c                                 9 - der of potential wrt jj
c*********************************************************************
c --- parameters
#include "impcom.inc"
      DOUBLE PRECISION ZERO, ONE, TWO, THREE, HALF, TOLER
      PARAMETER       (ZERO  = 0.d00,
     &                 ONE   = 1.0d0,
     &                 HALF  = 0.5d0,
     &                 TWO   = 2.d0,
     &                 THREE = 3.d0,
     &                 TOLER = 1.0d-12)
      EXTERNAL         erhandler
```

```
c
c --- argument list
c
      INTEGER          nprophy
      DOUBLE PRECISION prophy(*), invar(*),
     &                 potential, pInvDer(*)
      LOGICAL          incomp
c
c --- local variables
c
      INTEGER          i
      DOUBLE PRECISION i1, i1i2, d1, jj,
     &                 alpha, C, Q

      i1    = invar(1)
      jj    = invar(3)
      alpha = prophy(1)
      C     = prophy(2)
      d1    = prophy(3)

c          Incompressible Potential and Derivatives
      Q = exp(alpha*(i1-THREE))
      potential = C/TWO*(Q-ONE)

      pInvDer(1) = alpha*C/TWO*Q
      pInvDer(2) = ZERO
      pInvDer(3) = (alpha**TWO)*C/TWO*Q
      pInvDer(4) = ZERO
      pInvDer(5) = ZERO
      pInvDer(6) = ZERO
      pInvDer(7) = ZERO
      pInvDer(8) = ZERO
```

```
76        pInvDer(9) = ZERO
77
78        incomp = .TRUE.
79  c          Nearly Incompressible Potential and Derivatives
80        IF(d1 .gt. TOLER) THEN
81           incomp = .FALSE.
82           potential = potential + ONE/d1*(jj-ONE)**2
83           pInvDer(8) = TWO/d1*(jj-ONE)
84           pInvDer(9) = TWO/d1
85        END IF
86        RETURN
87        END
```

C.2 ANSYS USERMAT

The USERMAT subroutine allows for the incorporation of general material behaviour. Inelastic and viscoelastic material behavior can be implemented through this subroutine. At every integration point, ANSYS accesses the USERMAT to determine the current Cauchy stress, σ_{ij}, and material jacobian matrix, $\mathbb{C}_{ijkl}$, which is used to approximate the next iteration step. The subroutine allows for the input and output of user-defined state variables (ustatev). Our purpose for using the USERMAT subroutine was to integrate the evolution equations for the inelastic deformation of the growth model.

C.2.1 Outline of ANSYS Solver Routine

At the every time step, ANSYS would input the current total deformation gradient, F^n_{iA}, where superscript n represents the nth (current) iteration. Given that $\boldsymbol{F}^n = \boldsymbol{f}^n\boldsymbol{\mathcal{F}}^n$ and that the current inelastic deformation, $\boldsymbol{\mathcal{F}}^n$, was known, we solved for the current elastic deformation, $\boldsymbol{f}^n$. The Cauchy stress and the material jacobian matrix were then calculated using this elastic deformation. Then each component of the inelastic deformation was updated using a forward Euler integration of the prescribed inelastic deformation rate, $\boldsymbol{\mathcal{L}}$.

$$\mathcal{F}_{ij}\left(t+\Delta t\right) = \mathcal{F}_{ij}\left(t\right) + \mathcal{L}_{im}(t)\mathcal{F}_{mj}(t)\Delta t. \tag{C.2.1}$$

ANSYS would then take the stress and elasticity tensor and build the global tangent stiffness matrix and the iteration residual. Table C.1 lists the built-in ANSYS fortran functions that were used to perform these calculations.

Table C.1: Built-in ANSYS Fortran Functions

Name	Description	Operation
maxb(A,B,C,..)	matrix multiplication	C = A*B
matxb(A,B,C,..)	matrix multiplication	C = A'*B
symeqn	linear system solver	see ANSYS Sec 8.4.11

ANSYS solved the nonlinear FE problem using the Newton-Raphson (NR) iteration scheme, which is outlined in the Matlab pseudo-code of Figure B.1 of Appendix B.2. ANSYS used a Sparse Direct solver to calculate the displacement increment for each NR loop, specifically,

$$\left[K_T\right]\left\{\Delta u\right\} = \left\{R\right\} \tag{C.2.2}$$

where $[K_T]$ is the global tangent stiffness matrix, $\{\Delta u\}$ the displacement increment, and $\{R\}$ is the residual. The residual is the difference between the external force vector and the internal force vector for the current NR iteration. ANSYS solved Eq. C.2.2 using a Cholesky decomposition of $[K_T]$ which is,

$$\begin{aligned}[K_T] &= [L]\left[L^t\right] \\ &= \left[\bar{L}\right][D]\left[\bar{L}^t\right]\end{aligned}$$

where $[L]$ and $\left[\bar{L}\right]$ are a lower triangular matrices and $[D]$ is a diagonal matrix. ANSYS then back substitutes to solve for $\{\Delta u\}$ using,

$$\begin{aligned}\left[\bar{L}\right]\{w\} &= \{R\} \\ [D]\left[\bar{L}^t\right]\{\Delta u\} &= \{w\}\end{aligned}$$

ANSYS reorders the rows and columns to reduced the amount of fill-in required during the Cholesky decomposition. The Minimum Degree ordering and the METIS ordering methods are used for the reordering. For complete details, see ANSYS Theory Reference Sec. 15.9.

C.2.2 Material Jacobian Derivation

For nonlinear material analysis, the material Jacobian matrix (also known as the spatial elasticity tensor), $\mathbb{C}_{ijkl}$, is required to predict the material properties of the next iteration. In ANSYS, the elasticity tensor is defined as,

$$\mathring{\boldsymbol{\tau}} = J\mathbb{C} : \boldsymbol{d} \tag{C.2.3}$$

where $\mathring{\boldsymbol{\tau}}$ is the Jaumann rate of the Kirchoff stress and $\boldsymbol{d}$ is the symmetric part of the elastic deformation rate tensor, $\boldsymbol{l} = \dot{\boldsymbol{f}}\boldsymbol{f}^{-1}$. The Jaumann rate is a objective

time derivative expressed in terms of the spin tensor, $\boldsymbol{\omega}$, which is the asymmetric part of $\boldsymbol{l}$.

$$\mathring{\boldsymbol{\tau}} = \dot{\boldsymbol{\tau}} - \boldsymbol{\omega\tau} + \boldsymbol{\tau\omega} \tag{C.2.4}$$

The general form of $\mathbb{C}$ for an isotropic material is presented in Lubarda and Hoger (2002) [114], Eq 11.9 as,

$$\mathbb{C}_{ijkl} = 4\, f_{i\alpha} f_{j\beta} \frac{\partial^2 \psi}{\partial c_{\alpha\beta} \partial c_{\gamma\xi}} f_{k\gamma} f_{l\xi} + \frac{1}{2} \left(\tau_{lj}\delta_{ik} + \tau_{ik}\delta_{jl} + \tau_{li}\delta_{jk} + \tau_{kj}\delta_{il} \right) \tag{C.2.5}$$

where $c_{\alpha\beta} = f_{i\alpha} f_{i\beta}$ is the right Cauchy Green stretch tensor. For the growth model, we implemented an exponential material,

$$\psi\left(I_c, j\right) = \frac{C}{2} \left\{ exp\left[\alpha(I_c - 3)\right] - 1 \right\} + \frac{1}{d_1} \left(j - 1\right)^2 \tag{C.2.6}$$

where $I_c = tr(\boldsymbol{c})$ and $j = det(\boldsymbol{f})$. Note that the deviatoric-volumetric split of the invariants was not used in this formulation.

We now evaluate the partial derivatives of the 1st term of the elasticity tensor in Eq. (C.2.5), where

$$\begin{aligned} S_{\alpha\beta} &= 2\frac{\partial \psi}{\partial c_{\alpha\beta}} \\ &= 2\alpha C\, exp\left[\alpha\left(I_c - 3\right)\right] \delta_{\alpha\beta} + \frac{2}{d_1} j\ \left(j - 1\right) c^{-1}_{\beta\alpha} \end{aligned} \tag{C.2.7}$$

defines the 2nd Piola-Kirchoff stress, $S_{\alpha\beta}$. We now calculate the 2nd partial of ψ starting from the 2nd PK stress using $K \equiv \alpha C\, exp\left[\alpha\left(I_c - 3\right)\right]$.

$$\frac{\partial S_{\alpha\beta}}{\partial c_{\gamma\xi}} = \alpha K \frac{\partial c_{mm}}{\partial c_{\gamma\xi}} \delta_{\alpha\beta} + \frac{2}{d_1}(2j - 1)\frac{\partial j}{\partial c_{\gamma\xi}} c^{-1}_{\beta\alpha} + \frac{2}{d_1} j(j - 1)\frac{\partial c^{-1}_{\beta\alpha}}{\partial c_{\gamma\xi}} \tag{C.2.8}$$

The partial derivatives in Eq (C.2.8) are as follows,

$$\begin{aligned} \frac{\partial c_{mm}}{\partial c_{\gamma\xi}} &= \delta_{\gamma\xi} \\ \frac{\partial j}{\partial c_{\gamma\xi}} &= \frac{1}{2} j\, c^{-1}_{\xi\gamma} \\ \frac{\partial c^{-1}_{\beta\alpha}}{\partial c_{\gamma\xi}} &= \frac{1}{2}\left(c^{-1}_{\beta\xi} c^{-1}_{\alpha\gamma} + c^{-1}_{\beta\gamma} c^{-1}_{\alpha\xi} \right) \end{aligned}$$

which after insertion into Eq C.2.8 yields,

$$\frac{\partial S_{\alpha\beta}}{\partial c_{\gamma\xi}} = \alpha K \delta_{\alpha\beta}\delta_{\gamma\xi} + \frac{1}{d_1} j(2j-1) c^{-1}_{\beta\alpha} c^{-1}_{\xi\gamma} - \frac{1}{d_1} j(j-1)\left(c^{-1}_{\beta\xi} c^{-1}_{\alpha\gamma} + c^{-1}_{\beta\gamma} c^{-1}_{\alpha\xi}\right) \quad \text{(C.2.9)}$$

Finally, by plugging in the Kirchoff stress,

$$\tau_{ij} = \alpha C \, exp\left[\alpha\left(I_c - 3\right)\right] b_{ij} + \frac{2}{d_1} j\left(j-1\right)\delta_{ij} \quad \text{(C.2.10)}$$

and Eq. (C.2.9) into Eq. (C.2.5) we arrive at the elasticity tensor,

$$\begin{aligned}
\mathbb{C}_{ijkl} &= 2\, f_{i\alpha} f_{j\beta} \frac{\partial S_{\alpha\beta}}{\partial c_{\gamma\xi}} f_{k\gamma} f_{l\xi} + \frac{1}{2}\left(\tau_{lj}\delta_{ik} + \tau_{ik}\delta_{jl} + \tau_{li}\delta_{jk} + \tau_{kj}\delta_{il}\right) \\
&= 2\alpha K b_{ij} b_{kl} + \frac{2}{d_1} j(2j-1)\delta_{ij}\delta_{kl} - \frac{2}{d_1} j(j-1)\left(\delta_{ik}\delta_{jl} + \delta_{jk}\delta_{il}\right) \\
&+ \frac{K}{2}\left(b_{lj}\delta_{ik} + b_{ik}\delta_{jl} + b_{li}\delta_{jk} + b_{kj}\delta_{il}\right) + \frac{2j(j-1)}{d_1}\left(\delta_{jl}\delta_{ik} + \delta_{il}\delta_{jk}\right)
\end{aligned}$$

with the final form of,

$$\mathbb{C}_{ijkl} = 2\alpha K b_{ij} b_{kl} + \frac{2}{d_1} j(2j-1)\delta_{ij}\delta_{kl} + \frac{K}{2}\left(b_{lj}\delta_{ik} + b_{ik}\delta_{jl} + b_{li}\delta_{jk} + b_{kj}\delta_{il}\right) \quad \text{(C.2.11)}$$

C.2.3 USERMAT Fortran Code

```
1  *deck,usermat3d    USERDISTRIB  parallel                          gal
2        subroutine usermat3d_exp_growth3(
3       &                   matId, elemId,kDomIntPt, kLayer, kSectPt,
4       &                   ldstep,isubst,keycut,
5       &                   nDirect,nShear,ncomp,nStatev,nProp,
6       &                   Time,dTime,Temp,dTemp,
7       &                   stress,ustatev,dsdePl,sedEl,sedPl,epseq,
8       &                   Strain,dStrain, epsPl, prop, coords,
9       &                   var0, defGrad_t, defGrad,
10      &                   tsstif, epsZZ,
11      &                   var1, var2, var3, var4, var5,
12      &                   var6, var7, var8)
13 c**************************************************************
14 c     *** primary function ***
15 c
16 c           user defined material constitutive model
17 c
18 c      Attention:
19 c           User must define material constitutive law properly
20 c           according to the stress state such as 3D, plane strain
21 c           and axisymmetry, plane stress and beam.
22 c
23 c           a 3D material constitutive model can use for
24 c           plane strain and axisymmetry cases.
25 c
26 c           When using shell elements, a plane stress algorithm
27 c           must be used.
28 c
29 c       The following demonstrates a USERMAT subroutine for
30 c       a nearly incompressible exponential hyperelastic model
```

```
c       of 3D solid elements or plane elements in plane strain
c       or axisymmetric stress state.
c
c       See "ANSYS user material subroutine USERMAT" for detailed
c       description of how to write a USERMAT routine.
c
c*******************************************************************
c
c     input arguments
c     ===============
c      matId     (int,sc,i)             material #
c      elemId    (int,sc,i)          element #
c      kDomIntPt (int,sc,i)          "k"th domain integration point
c      kLayer    (int,sc,i)          "k"th layer
c      kSectPt   (int,sc,i)          "k"th Section point
c      ldstep    (int,sc,i)          load step number
c      isubst    (int,sc,i)          substep number
c      nDirect   (int,sc,in)         # of direct components
c      nShear    (int,sc,in)         # of shear components
c      ncomp     (int,sc,in)         nDirect + nShear
c      nstatev   (int,sc,l)          Number of state variables
c      nProp     (int,sc,l)          Number of material ocnstants
c
c      Temp      (dp,sc,in)          temperature at beginning of
c                                    time increment
c      dTemp     (dp,sc,in)          temperature increment
c      Time      (dp,sc,in) time at beginning of increment (t)
c      dTime     (dp,sc,in)          current time increment (dt)
c
c      Strain   (dp,ar(ncomp),i)     Strain
c      dStrain  (dp,ar(ncomp),i)     Strain increment
c      prop     (dp,ar(nprop),i)     Material constants
```

```
c      coords    (dp,ar(3),i)         current coordinates
c      defGrad_t(dp,ar(3,3),i)       Def gradient at time t
c      defGrad   (dp,ar(3,3),i)      Defgradient at time t+dt
c
c     input output arguments
c     ======================
c      stress    (dp,ar(nTesn),io)          stress
c      ustatev    (dp,ar(nstatev),io)       user state variable
c      sedEl     (dp,sc,io)                 elastic work
c      sedPl     (dp,sc,io)                 plastic work
c      epseq     (dp,sc,io)           equivalent plastic strain
c
c     output arguments
c     ================
c      keycut    (int,sc,io)        loading bisect/cut control
c                                   0 - no bisect/cut
c                                   1 - bisect/cut
c
c      dsdePl    (dp,ar(ncomp,ncomp),io)  jacobian matrix
c      epsZZ     (dp,sc,o)    strain epsZZ for plane stress,
c*****************************************************************
c      ncomp   6   for 3D  (nshear=3)
c      ncomp   4   for plane strain or axisymmetric (nShear = 1)
c      ncomp   3   for plane stress (nShear = 1)
c      ncomp   3   for 3d beam      (nShear = 2)
c      ncomp   1   for 1D (nShear = 0)
c
c      stresss and strains, plastic strain vectors
c          11, 22, 33, 12, 23, 13    for 3D
c          11, 22, 33, 12        for plane strain or axisymmetry
c          11, 22, 12                for plane stress
c          11, 13, 12                for 3d beam
```

```
c          11                          for 1D
c
c      material jacobian matrix
c        3D
c           dsdePl    |  1111   1122   1133   1112   1123   1113 |
c           dsdePl    |  2211   2222   2233   2212   2223   2213 |
c           dsdePl    |  3311   3322   3333   3312   3323   3313 |
c           dsdePl    |  1211   1222   1233   1212   1223   1213 |
c           dsdePl    |  2311   2322   2333   2312   2323   2313 |
c           dsdePl    |  1311   1322   1333   1312   1323   1313 |
c        plane strain or axisymmetric (11, 22, 33, 12)
c           dsdePl    |  1111   1122   1133   1112 |
c           dsdePl    |  2211   2222   2233   2212 |
c           dsdePl    |  3311   3322   3333   3312 |
c           dsdePl    |  1211   1222   1233   1212 |
c        plane stress (11, 22, 12)
c           dsdePl    |  1111   1122   1112 |
c           dsdePl    |  2211   2222   2212 |
c           dsdePl    |  1211   1222   1212 |
c        3d beam (11, 13, 12)
c           dsdePl    |  1111   1113   1112 |
c           dsdePl    |  1311   1313   1312 |
c           dsdePl    |  1211   1213   1212 |
c        1d
c           dsdePl    |  1111 |
c
c***********************************************************************
#include "impcom.inc"
c
       INTEGER
     &                 matId, elemId,
     &                 kDomIntPt, kLayer, kSectPt,
```

```
127       &                 ldstep,isubst,keycut,
128       &                 nDirect,nShear,ncomp,nStatev,nProp
129        DOUBLE PRECISION
130       &                 Time,    dTime,   Temp,    dTemp,
131       &                 sedEl,   sedPl,   epseq,   epsZZ
132        DOUBLE PRECISION
133       &                 stress  (ncomp), ustatev (nStatev),
134       &                 dsdePl  (ncomp,ncomp),
135       &                 Strain  (ncomp), dStrain (ncomp  ),
136       &                 epsPl   (ncomp), prop    (nProp  ),
137       &                 coords  (3),
138       &                 defGrad (3,3),defGrad_t(3,3),
139       &                 tsstif  (2)
140  c
141  c***************** User defined part *************************
142        INTEGER           mcomp, n, info
143        DOUBLE PRECISION HALF, THIRD, ONE, TWO, FOUR, SMALL,
144       &                 ZERO, TWOTHIRD, ONEDM02, ONEDM05,
145       &                              ONEHALF, sqTiny, THREE
146        PARAMETER        (ZERO       = 0.d0,
147       &                 HALF       = 0.5d0,
148       &                 THIRD      = 1.d0/3.d0,
149       &                 ONE        = 1.d0,
150       &                 TWO        = 2.d0,
151       &                              FOUR           = 4.d0,
152       &                 SMALL      = 1.d-08,
153       &                 sqTiny     = 1.d-20,
154       &                 ONEDM02    = 1.d-02,
155       &                 ONEDM05    = 1.d-05,
156       &                 ONEHALF    = 1.5d0,
157       &                              THREE          = 3.d0,
158       &                 TWOTHIRD   = 2.0d0/3.0d0,
```

```
159       &                  mcomp      = 6,
160       &                                     n                  = 3)
161   c
162   c       defGrad_F(dp,ar(3,3),l)  total deformation gradient
163   c       a         (dp,sc,i)            growth rate parameter a(r)
164   c       alpha     (dp,sc,i)                nonlinear material parameter
165   c       C10           (dp,sc,i)            linear material parameter
166   c       D1            (dp,sc,i)            inverse bulk modulus
167   c       G         (dp,ar(3,3),io) Inelastic Deformation
168   c
169   c --- temperary variables for solution purpose
170   c       i, j
171   c       BBAR - Deviatoric Left Cauchy Green Strain
172   c       BBARP - Principal Values of BBAR
173   c       BBARN - Principal direction of BBAR
174   c       DISTGR - Deviatoric Deformation Gradient
175   c       DET - determinant of deformation gradient
176         EXTERNAL          vzero, vmove, get_ElmData, eigen_calc,
177       &                   mctac, maxb, polar_decomp, svars_write,
178       &                   matxb, matba, felastic_write, symeqn
179         DOUBLE PRECISION sigElp(mcomp), dsdeEl(mcomp,mcomp),
180       &                   sigDev(mcomp), JM(mcomp,mcomp),
181       &                                  dfds(mcomp),
182       &                   sigi   (mcomp), strainEl(mcomp)
183         DOUBLE PRECISION var0, var1, var2, var3, var4, var5,
184       &                   var6, var7, var8
185         INTEGER           i, j , k1, k2, IERR, indic
186         DOUBLE PRECISION C10, alpha, D1, a,
187       &                   DET_F, DET, DET_G,
188       &                   EG, EK, PR, EG23,
189       &                   BBAR(6), DISTGR(3,3),
190       &                   TRBBAR, DDSDDE(ncomp,ncomp),
```

```
191       &                   AA(3,6), dG(3,3), IG(3,3),
192       &                   G(3,3), T(3,3), Iden(3,3),
193       &                   defGrad_F(3,3), IdefGrad(3,3)
194 c*************************************************************
195        keycut = 0
196 c          Define Identity Matrix - "Iden"
197        call vzero(Iden(1,:),3)
198        call vzero(Iden(2,:),3)
199        call vzero(Iden(3,:),3)
200        Iden(1,1) = 1.d0; Iden(2,2) = 1.d0; Iden(3,3) = 1.d0;
201
202 c**** Get C10, alpha, and Bulk Modulus^-1, D1,
203        C10   = prop(2)
204        alpha = prop(3)
205        D1    = prop(4)
206        a     = prop(5)
207 c      Overall Deformation Gradient, F
208        defGrad_F = defGrad;
209 c      Calculate the deteminant: J=det(F)
210        DET_F = defGrad_F(1,1)*defGrad_F(2,2)*defGrad_F(3,3)
211       & -defGrad_F(1,2)*defGrad_F(2,1)*defGrad_F(3,3)
212           IF (nShear .EQ. 3) THEN
213        DET_F = DET_F + defGrad_F(1,2)*defGrad_F(2,3)*defGrad_F(3,1)
214       &          +defGrad_F(1,3)*defGrad_F(3,2)*defGrad_F(2,1)
215       &          -defGrad_F(1,3)*defGrad_F(3,1)*defGrad_F(2,2)
216       &          -defGrad_F(2,3)*defGrad_F(3,2)*defGrad_F(1,1)
217           end IF
218 C-------------------------------------------------------------
219 C     Initialize Growth Tensor, G
220        G(1,1) = ustatev(1); G(2,2) = ustatev(2); G(3,3) = ustatev(3);
221        G(1,2) = ustatev(4); G(1,3) = ustatev(5); G(2,1) = ustatev(6);
222        G(2,3) = ustatev(7); G(3,1) = ustatev(8); G(3,2) = ustatev(9);
```

```
C-----------------------------------------------------------------------
C          Calculate G^-1 = inv(G)
       AA(1:3,1:3) = G
       call symeqn(AA,3,3,-3,1)
       IG = AA(1:3,4:6)

C      Calculate f = F*inv(G)
       call maxb(defGrad,IG,defGrad,3,3,3,3,3,3)
C-----------------------------------------------------------------------
C   Calculate the Elastic Cauchy Stress and Elasticity Tensor
C   Calculate the Determinant of Elastic Deformation Gradient, j=det(f)
       DET = defGrad(1,1)*defGrad(2,2)*defGrad(3,3)
     & -defGrad(1,2)*defGrad(2,1)*defGrad(3,3)
          IF (nShear.EQ.3) THEN
              DET = DET + defGrad(1,2)*defGrad(2,3)*defGrad(3,1)
     &           +defGrad(1,3)*defGrad(3,2)*defGrad(2,1)
     &           -defGrad(1,3)*defGrad(3,1)*defGrad(2,2)
     &           -defGrad(2,3)*defGrad(3,2)*defGrad(1,1)
          end IF
C   Calculate the Determinant of Inelastic Deformation Gradient, det(G)
       DET_G = G(1,1)*G(2,2)*G(3,3)-G(1,2)*G(2,1)*G(3,3)
          IF (nShear.EQ.3) THEN
              DET_G = DET_G + G(1,2)*G(2,3)*G(3,1)
     &           +G(1,3)*G(3,2)*G(2,1)-G(1,3)*G(3,1)*G(2,2)
     &           -G(2,3)*G(3,2)*G(1,1)
          end IF

C   Re-label Elastic Deformation Gradient
          do k1=1,3
           do k2=1,3
             DISTGR(k2,k1) = defGrad(k2,k1)
           end do
```

```
255           end do
256   c   Calculate Left Cauchy Green Strain, b = ff^t
257           BBAR(1)=DISTGR(1,1)**2+DISTGR(1,2)**2+DISTGR(1,3)**2
258           BBAR(2)=DISTGR(2,1)**2+DISTGR(2,2)**2+DISTGR(2,3)**2
259           BBAR(3)=DISTGR(3,3)**2+DISTGR(3,1)**2+DISTGR(3,2)**2
260           BBAR(4)=DISTGR(1,1)*DISTGR(2,1)+DISTGR(1,2)*DISTGR(2,2)
261        & +DISTGR(1, 3)*DISTGR(2, 3)
262           IF(nShear.EQ.3) THEN
263           BBAR(6)=DISTGR(1, 1)*DISTGR(3, 1)+DISTGR(1, 2)*DISTGR(3, 2)
264        & +DISTGR(1, 3)*DISTGR(3, 3)
265           BBAR(5)=DISTGR(2, 1)*DISTGR(3, 1)+DISTGR(2, 2)*DISTGR(3, 2)
266        & +DISTGR(2, 3)*DISTGR(3, 3)
267           end if
268
269   c               Calculate 1st Invariant of b, Ib
270           TRBBAR = BBAR(1) + BBAR(2) + BBAR(3)
271                   EG = TWO*alpha*C10*exp(alpha*(TRBBAR - THREE))
272           EK = TWO*DET/D1*(TWO*DET-ONE)
273           PR = TWO/D1*(DET-ONE)
274   c       call defG_write(Time,defGrad_F,defGrad,DET_F,DET,PR)
275   30         format (3f9.2)
276   c          Calculate Cauchy Stress
277         do k1=1,nDirect
278           stress(k1) = HALF*EG*BBAR(k1)/DET + PR
279         end do
280         do k1 = nDirect+1, nDirect+nShear
281           stress(k1) = HALF*EG*BBAR(k1)/DET
282         end do
283
284   C      CALCULATE THE TANGENT Elasticity Matrix
285   C        EG23=EG*TWO*THIRD
286          DDSDDE(1, 1)= EG*(alpha*BBAR(1)**2+BBAR(1))+EK
```

```
287         DDSDDE(2, 2)= EG*(alpha*BBAR(2)**2+BBAR(2))+EK
288         DDSDDE(3, 3)= EG*(alpha*BBAR(3)**2+BBAR(3))+EK
289         DDSDDE(1, 2)= alpha*EG*(BBAR(1)*BBAR(2))   +EK
290         DDSDDE(1, 3)= alpha*EG*(BBAR(1)*BBAR(3))   +EK
291         DDSDDE(2, 3)= alpha*EG*(BBAR(2)*BBAR(3))   +EK
292         DDSDDE(1, 4)= alpha*EG*(BBAR(1)*BBAR(4)) + EG/TWO*BBAR(4)
293         DDSDDE(2, 4)= alpha*EG*(BBAR(2)*BBAR(4)) + EG/TWO*BBAR(4)
294         DDSDDE(3, 4)= alpha*EG*(BBAR(3)*BBAR(4))
295         DDSDDE(4, 4)= alpha*EG*(BBAR(4)**2) + EG/TWO*(BBAR(1)+BBAR(2))
296         IF(nShear.EQ.3) THEN
297         DDSDDE(1, 6)= alpha*EG*(BBAR(1)*BBAR(6)) + EG/TWO*BBAR(6)
298         DDSDDE(2, 6)= alpha*EG*(BBAR(2)*BBAR(6))
299         DDSDDE(3, 6)= alpha*EG*(BBAR(3)*BBAR(6)) + EG/TWO*BBAR(6)
300         DDSDDE(1, 5)= alpha*EG*(BBAR(1)*BBAR(5))
301         DDSDDE(2, 5)= alpha*EG*(BBAR(2)*BBAR(5)) + EG/TWO*BBAR(5)
302         DDSDDE(3, 5)= alpha*EG*(BBAR(3)*BBAR(5)) + EG/TWO*BBAR(5)
303         DDSDDE(5, 5)= alpha*EG*(BBAR(5)**2) + EG/TWO*(BBAR(2)+BBAR(3))
304         DDSDDE(6, 6)= alpha*EG*(BBAR(6)**2) + EG/TWO*(BBAR(1)+BBAR(3))
305         DDSDDE(4,6)= alpha*EG*(BBAR(4)*BBAR(6)) + EG/FOUR*BBAR(5)
306         DDSDDE(4,5)= alpha*EG*(BBAR(4)*BBAR(5)) + EG/FOUR*BBAR(6)
307         DDSDDE(5,6)= alpha*EG*(BBAR(5)*BBAR(6)) + EG/FOUR*BBAR(4)
308         END IF
309 c     Symmetry of Elasticity Matrix
310       DO K1=1, ncomp
311       DO K2=1, K1-1
312       DDSDDE(K1, K2)=DDSDDE(K2, K1)
313       END DO
314       END DO
315
316       dsdePl = DDSDDE
317
318 C-----------------------------------------------------------------
```

```
C       Update Growth Tensor, dG = a ft*T*f^-t*G
C   Write Cauchy Stress in matrix form
            T(1,1) = stress(1); T(2,2)=stress(2); T(3,3)=stress(3);
            T(1,2) = stress(4); T(1,3)=ZERO; T(2,3)=ZERO;
            T(2,1) = T(1,2); T(3,1) = T(1,3); T(3,2)=T(2,3);
       IF(nShear.EQ.3) THEN
            T(1,3)=stress(6); T(2,3)=stress(5);
            T(2,1) = T(1,2); T(3,1) = T(1,3); T(3,2)=T(2,3);
       endif

C       Isotropic Homeostatic Reference Stress
        T(1,1) = T(1,1) - prop(8)
        T(2,2) = T(2,2) - prop(8)
        T(3,3) = T(3,3) - prop(8)

c       Calculate f^t*T
       call matxb(defGrad,T,T,3,3,3,3,3,3)
c       Calculate f^-1
           AA(1:3,1:3) = defGrad
       call symeqn(AA,3,3,-3,1)
       IdefGrad = AA(1:3,4:6)

c    Calculate f^-t
       call matxb(IdefGrad,Iden,IdefGrad,3,3,3,3,3,3)
c        Calculate f^t*T*f^-t
       call maxb(T,IdefGrad,IdefGrad,3,3,3,3,3,3)

c        Calculate f^t*T*f^-t*G
       call maxb(IdefGrad,G,dG,3,3,3,3,3,3)

C        Gradient in Growth Rate Parameter, a
       if (coords(1) .ge. prop(6)) then
```

```
351               a = 0.d0
352         else
353               a = prop(5)*(prop(6)-coords(1))/(prop(10))
354         endif
355
356         if (Time .ge. prop(7)) then
357          G(1,1) = G(1,1) + a*dTime*dG(1,1);
358          G(2,2) = G(2,2) + a*dTime*dG(2,2);
359          G(3,3) = G(3,3) + a*dTime*dG(3,3);
360          G(1,2) = G(1,2) + a*dTime*dG(1,2);
361          G(2,1) = G(2,1) + a*dTime*dG(2,1);
362            if (nShear.EQ.3) THEN
363            G(1,3) = G(1,3) + a*dTime*dG(1,3);
364            G(3,1) = G(3,1) + a*dTime*dG(3,1);
365            G(3,2) = G(3,2) + a*dTime*dG(3,2);
366            G(2,3) = G(2,3) + a*dTime*dG(2,3);
367            else
368            G(1,3) = ZERO; G(2,3) = ZERO; G(3,1) = ZERO; G(3,2) = ZERO;
369                endif
370         endif
371
372   c   Store State Variable Quanities
373             ustatev(1) = G(1,1)
374             ustatev(2) = G(2,2)
375             ustatev(3) = G(3,3)
376             ustatev(4) = G(1,2)
377             ustatev(5) = G(1,3)
378             ustatev(6) = G(2,1)
379             ustatev(7) = G(2,3)
380             ustatev(8) = G(3,1)
381             ustatev(9) = G(3,2)
382             ustatev(10) = DET_F
```

```
383           ustatev(11) = DET
384           ustatev(12) = DET_G
385         ustatev(13) = DET_G*(IdefGrad(1,1) + IdefGrad(2,2)
386          &              + IdefGrad(3,3))
387           ustatev(14) = IdefGrad(1,1) + IdefGrad(2,2)
388          &       + IdefGrad(3,3)
389           ustatev(15) = a*ustatev(14)
390           ustatev(16) = a*ustatev(13)
391           ustatev(17) = a
392         return
393         end
```

C.3 ANSYS Input Files

ANSYS has its own scripting language for building and solving the FE models. Each file is stand only and can be run in ANSYS using the "Read input File" option under the File directory, or can be run as a batch file. Loop and if statements are coded using Fortran syntax.

C.3.1 Material Behaviour Validation ANSYS Input File

```
1
2 finish
3 /clear
4 !Validation File for ANSYS custom material las
5 !Uni-axial load of a single cube, to increase mesh
6 !density parameter "eSize" under the mesh section
7
8 !usermat3d_exp_growth1.f
```

```
!       C10   = prop(2)
!       alpha = prop(3)
!       D1    = prop(4)
!       a     = prop(5)
!       Ro*   = prop(6)
!       to    = prop(7)

/TITLE,GrowthExp_Uni
/FILNAME,GrowthExp_Uni,0

!Geometry Parameter Set
*SET,a,1         !Cube Side Dimension
*SET,p,5                 !Applied Traction
*SET,Force,100  !Shear Displacement

!GUI Preferences
/NOPR
/NERR,0,500,,0,0
/PMETH,OFF,0

KEYW,PR_SET,1
KEYW,PR_STRUC,1
KEYW,PR_THERM,0
KEYW,PR_FLUID,0
KEYW,PR_ELMAG,0
KEYW,MAGNOD,0
KEYW,MAGEDG,0
KEYW,MAGHFE,0
KEYW,MAGELC,0
KEYW,PR_MULTI,0
KEYW,PR_CFD,0
/GO
```

```
41
42 /PREP7
43 !Element Type
44 ET,1,solid185,,,1
45 KEYOPT,1,2,0                    !Full Integration
46 KEYOPT,1,6,0                    !Pure Displacement Formulations
47
48 !Material Properties
49 !TB,HYPER,1,,,NEO       !Neo-Hookean data table
50 !TBDATA,1,4             !Define mu shear modulus
51 !TBDATA,2,0.000002      !Define incompressibility parameter
52
53 TB,USER,1,1,8,                  !Exponential - Inelastic User Material
54 TBTEMP,1
55 TBDATA,1,2,20,1.5,0.002,0,0 !grow file #, C, alpha,d1,a=0,bb
56 TBDATA,,0,0
57 TB,STATE,1,,20                  !Number of UserState Variables
58 TBDATA,1,1,1,1,0,0,0    !Init. SVars G11,G22,G33,G12,G13,G21
59 TBDATA,,0,0,0,0,0,0     !7-12   G23,G31,G32
60 TBDATA,,0,0,0,0,0,0         !13-18
61 TBDATA,,0,0,0,0,0,0         !19-24
62
63 !Create Geometry
64 Block,0,a,0,a,0,a                      !Cube Test Element
65
66 !Mesh Regions
67 esize,0.1          !Distance btw nodes
68 type,1             !Element type 1 (Solid185)
69 mat,1                       !Material type 1 (Neo or User)
70 vmesh,1            !Mesh Cube
71 ALLSEL,ALL
72
```

```
73  FINISH                    !End PREP7 preprocessing
74
75  !-----------------------------------------------------
76  /SOLU               ! Enter SOLUTION
77  ANTYPE,0                        !Static Analysis
78  NLGEOM,1                        !Nonlinear Geometry Effects
79  !  Load Step 1: Perturbation
80  NSEL,S,LOC,X,-0.05,0.05
81  NSEL,R,LOC,Y,-0.05,0.05
82  D,ALL,UX,0
83  ALLSEL,ALL
84  NSEL,S,LOC,Z,-0.05,0.05
85  NSEL,R,LOC,X,-0.05,0.05
86  D,ALL,UZ,0
87  ALLSEL,ALL
88  NSEL,S,LOC,Y,-0.05,0.05
89  NSEL,R,LOC,Z,-0.05,0.05
90  D,ALL,UY,0
91  ALLSEL,ALL
92  SFA,6,,PRES,-Force
93  ALLSEL,ALL
94
95  SOLCONTROL,ON
96  AUTOST,ON                !ANSYS Automatic Time Stepping
97  TIME,1               !Solution Total Time Step
98  OUTRES,ALL,ALL   !Output all
99  OUTRES,SVAR,ALL  !Store state variables
100 NLDIAG,NRRE,ON   !Nonlinear Diagnostics - NR Residuals
101
102 solve
```

C.3.2 Valve Simulation ANSYS Input File

The following ANSYS input file is representative of the input files used for the embryonic AV valve simulation. ANSYS uses time to parameterize the load increment in nonlinear analyses. Since I am modeling an inelastic evolution, time actually has physical significance. I was not able to disable growth during the elastic loading step because ANSYS doesn't allow on-the-fly changes to the material properties. I therefore applied the load over a time, Δt_e, much smaller than the inelastic load step, Δt_g. Below is a pseudo-code to help with reading the file.

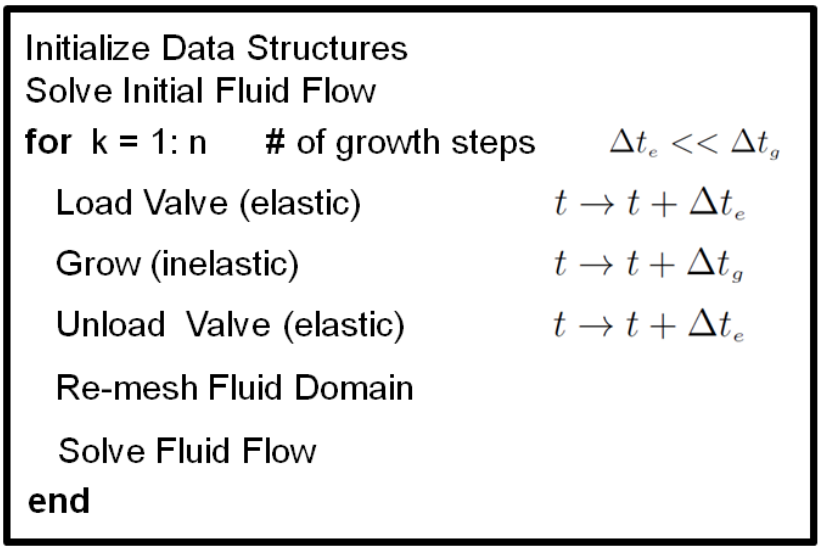

Figure C.3: Psuedo-code of Valve Growth Simulation. $\Delta t_e = 0.1$, $\Delta t_g = 5$

```
1 /batch
2 !finish
3 /clear
4 !ANSYS script for axi-symmetric model of initial
5 !semi-circle cushion under shear and normal
6 !tractions undergoing stress prescribed inelastic
```

```
!deformation.  USERMAT files required.
!Cushion growth only, no myo growth

!Pseudo Code
!       *DO
!         Fluid
!                 Solid - Load
!                 Solid - evolve
!                 Solid - unload
!                 upgeom - define new reference config
!                 damorph - match solid/fluid interface
!    *ENDDO


!usermat3d_exp_growth3
!Isotropic Reference Stress [prop(7)]
!Growth Gradient in r dir   [prop(5)]
!Velocity specified fluid
!Fluid Parameters in CGS Units [g,cm,s]
!Reference stress - T0 = 0

!      C10  = prop(2)/TWO
!      D1   = prop(3)
!          a    = prop(4)
!      R*       = prop(5)
!      to   = prop(6)
!      T*   = prop(7)

/FILNAME,HH27_Avg_T02,1

!Geometry Parameter Set
*SET,LFACT,1.E-01
```

```
*SET,base,1*LFACT           !Base length
*SET,r_c,0.25*LFACT     !Cushion Radius
*SET,R,0.5*LFACT        !Canal Radius
*SET,t_w,0.15*LFACT             !Myocardial Thickness
*SET,Flow_ex,4*R                !Flow Exit Length
*SET,Flow_en,4*R                !Flow Entrance Length
*SET,mu,200
*SET,d1,0
*SET,alpha,18

!GUI Preferences
/NERR,0,500,,0,0
/UNITS,CGS
/PMETH,OFF,0
KEYW,PR_SET,1
KEYW,PR_STRUC,1
KEYW,PR_THERM,0
KEYW,PR_FLUID,0
KEYW,PR_ELMAG,0
KEYW,MAGNOD,0
KEYW,MAGEDG,0
KEYW,MAGHFE,0
KEYW,MAGELC,0
KEYW,PR_MULTI,0
KEYW,PR_CFD,0
/GO

/PREP7
!------------------------------Element Type------------
ET,1,141                                ! Fluid - static mesh
KEYOPT,1,3,1                            !Axisymmetric about y-axis
ET,2,182                                !Hyperelastic element
```

```
KEYOPT,2,3,1                                !Axisymmetric about y-axis
ET,3,SURF153,,,1
KEYOPT,3,2,0                                !Element Coord. Sys.
KEYOPT,3,3,1                                !Axisymmetric
KEYOPT,3,4,1    !No midside node - to match Fluid domain
!------------------------------Create Geometry---------
*AFUN,DEG                !Use DEG for Angular functions
K,1,0,0,0,                                  !Origin
K,2,R-r_c,0,0,0,
K,3,R,-base/2,0,
K,4,R+t_w,-base/2,0,
K,5,R,base/2,0,
K,6,R+t_w,base/2,0
K,7,R,-r_c,0,
K,8,R,r_c,0,
K,9,0,0,1,               !(0,0,1) for normal vector
K,10,R-r_c*sin(alpha),-cos(alpha)*r_c,0
K,11,R-sin(alpha)*r_c,cos(alpha)*r_c,0
K,12,R,1.4*r_c,0
K,13,R,-1.4*r_c,0
K,14,0,-2*r_c,0
K,15,0,2*r_c,0
K,16,0,-base/2,0
K,17,0,base/2,0
K,18,R,Flow_ex,0
K,19,R,-Flow_en,0
K,20,R+t_w,Flow_ex,0
K,21,R+t_w,-Flow_en,0
K,22,0,Flow_ex,0
K,23,0,-Flow_en,0
K,24,R+t_w,base/2,0
K,25,R+t_w,-base/2,0
```

```
103
104 !--------Cushion & Myocardium Region--------------
105 L,3,13                                    !Line #1 - bot edge1
106 L,3,19                                    !Line #2 - bot edge2
107 L,19,21                                   !Line #3 - bot cap
108 L,21,25                                   !Line #4 - bot back
109 L,25,24                                   !Line #5 - cent back
110 L,24,20                                   !Line #6 - top back
111 L,20,18                                   !Line #7 - top cap
112 L,18,5                                    !Line #8 - top edge2
113 LARC,13,10,14,r_c/1.9   !Line #9 - bot fillet
114
115
116 !Cushion Initial Arcs
117 LARC,10,2,8,r_c,                    !Line #10 - bot arc
118 LARC,2,11,7,r_c,                        !Line #11 - top arc
119 LARC,11,12,15,r_c/1.9           !Line #12 - top fillet
120 L,12,5                                      !Line #13 - top edge1
121
122 L,24,5                                         !Line #14
123 L,3,25                                         !Line #15
124
125 lsel,s,LINE,,9,15,1
126 lsel,a,LINE,,1,,
127 lsel,a,LINE,,5,,
128 AL,ALL                  !Area #1 AV Cushion & Myocardium
129 ALLSEL,ALL
130 !----Morphing Region Geometry-------------------------
131 L,1,16                                    !Line #16 - Sym Axis neg
132 L,16,3                                    !Line #17 - Inflow
133 L,1,17                                    !Line #18 - Sym Axis pos
134 L,17,5                                    !Line #19 - Outflow
```

```
135
136 AL,16,17,1,12,10,11,13,9,19,18    !Area#2 Morphing Fluid Region
137 ALLSEL,ALL
138 !-------Fluid Domain-----------------------------------
139 L,17,22                                  !Line #20 - Sym Axis pos 2
140 L,16,23                                  !Line #21 - Sym Axis neg 2
141 L,22,18                                  !Line #22 - Flow Exit
142 L,23,19                                  !Line #23 - Flow Entrance
143
144 AL,20,22,8,19                    !Area #3 Exit Fluid Area
145 ALLSEL,ALL
146 AL,21,23,2,17                    !Area #4 Entrance Fluid Area
147 ALLSEL,ALL
148
149 AL,6,7,8,14                             !Area #5
150 AL,2,3,4,15                             !Area #6
151 ALLSEL,ALL
152 AGLUE,ALL
153
154 !-----------Meshing Criteria---------------
155 !Parameters
156 nEntx = 20
157 nEnty = 30
158 sEnty = 2
159 nExty = 30
160 sExty = 2
161 nMorph = 20
162 nMyo   = 10
163 ncush = 50
164 nBase = 2*(nEnty+nExty+nMorph)
165 nCaps = 4
166 nfillet = 25
```

```
167
168 lesize,23,,,nEntx,,,                    !Entrance Mesh x
169 lesize,2,,,nEnty,sEnty
170 lesize,4,,,nEnty,1/sEnty
171 lesize,21,,,nEnty,sEnty
172
173 lesize,22,,,nEntx,,,
174 lesize,8,,,nExty,1/sExty
175 lesize,6,,,nExty,sExty
176 lesize,20,,,nExty,sExty
177
178 lsel,s,LINE,,10,11,1,
179 lesize,ALL,,,ncush,
180 ALLSEL,ALL
181 lsel,s,LINE,,12
182 lsel,a,LINE,,9
183 lesize,ALL,,,nfillet,
184 ALLSEL,ALL
185 lesize,1,,,nMyo,0.4
186 lesize,13,,,nMyo,1/0.4
187 ALLSEL,ALL
188
189 lsel,s,LINE,,16,19,
190 lesize,ALL,,,nMorph,1
191 ALLSEL,ALL
192
193 lesize,5,,,2*nMorph,-0.75
194
195 lesize,3,,,nCaps,
196 lesize,7,,,nCaps,
197 lesize,14,,,nCaps,
198 lesize,15,,,nCaps,
```

```
199 ALLSEL,ALL
200
201 lsel,s,LINE,,16,19,1
202 cm,morph_Ln_ex,line              !Lines to exclude during morphing
203 ALLSEL,ALL
204
205 !-----------!Assign Area Characteristics----------------
206 lsel,s,,,9,13,1          !Select BC Lines - MAT2,REAL3,TYPE3
207 lsel,a,,,1,1,1
208 latt,2,3,3
209 lmesh,all
210
211 allsel,all
212 lsel,s,,,9,12,1                          !Select BC Lines
213 nsll,,1                                          !Select BC nodes
214 CM,BC_NODES,NODE                         !BC_NODES - component
215 allsel,all
216
217 asel,s,AREA,,2,4,1
218 aatt,1,1,1      !AREA #2-4 Fluid (MAT,REAL,TYPE) 2
219 amesh,all
220 ALLSEL,ALL
221
222 asel,s,AREA,,1,1,1      !AREA #1 Solid (MAT,REAL,TYPE) 1
223 !asel,a,AREA,,5,6,1
224 aatt,2,2,2
225 amesh,all
226 allsel,all
227
228 !               Create Fluid Physics Environment
229 ET,3,0                           !Surf153 Null
230 ET,2,0                           !Cushion is Null Element
```

```
231 ET,1,FLUID141,,,1        !Fluid Element
232 KEYOPT,1,3,1             !Axisymmetric about y-axis
233
234 dens = 1.060             !g/cm^3  Density
235 visc = 0.030             !g/cm s  Viscosity
236
237 !                           CFD Solution Control
238 flda,solu,flow,T                        !Flow (Laminar) - ON
239 flda,solu,turb,T                        !Turbulent Flow - ON
240 flda,iter,exec,400      !Steady-state solution # global iterations
241 flda,outp,sumf,50                       !Summary output interval
242 flda,outp,tauw,T                       !Output Wall Shear Stress
243
244 !                           CFD Property Information
245 flda,prot,dens,constant
246 flda,prot,visc,constant
247 flda,nomi,dens,dens     ! (g/cm3) for density - water
248 flda,nomi,visc,visc             ! (g/cm-s) (viscosity of water)
249 flda,conv,pres,1.E-8    ! Tighten pressure equation convergence
250 flda,conv,vy,1.E-4
251 flda,conv,vx,1.E-4
252 flda,MIR,MOME,0                 !Momentum Relaxation Factor
253 !flda,pres,refe,1               !Change Reference Pressure
254
255 !                                 CFD Boundary Conditions
256 lsel,s,LINE,,16,18,2
257 lsel,a,LINE,,20,21,1
258 dl,all,,vx,0,1
259 allsel,all
260
261 lsel,s,LINE,,1,2,1
262 lsel,a,LINE,,8,13,1
```

```
dl,all,,vx,0.,1 !Cush/Myo Surface Vx=0 (include ends)
dl,all,,vy,0.,1 !Cush/Myo Surface Vy=0 (include ends)
allsel,all

dl,23,,vx,0.,0                  !Inlet Flow Vx=0
dl,23,,PRES,62,1                !Inlet Pressure
dl,22,,pres,0,0                 !Outlet Press Po=0
allsel,all
!--------Cushion Component---------------------------
/title,Fluid Analysis
physics,write,fluid,fluid
physics,clear

!----------Create Solid Physics Environment-----------
ET,1,0                          !Fluid is Null Region
ET,2,PLANE182       !Hyperelastic element
KEYOPT,2,3,1            !Axisymmetric about y-axis
ET,3,SURF153,,,1        !Shear Traction Element
KEYOPT,3,2,0            !Element Coord. Sys.
KEYOPT,3,3,1            !Axisymmetric
KEYOPT,3,4,1            !No midside node - to match Fluid domain


TB,USER,2,1,11,                 !Mat#2 - USERMAT/Growth
TBTEMP,1
TBDATA,1,4,1000,0.3,0.00002,1/1000,R   !Exp-1, C, alpha, d1, a, R*
TBDATA,,0.1,-62/2,0,R,0                             !t0, T*, 0, R, 0
TB,STATE,2,,20                  !Number of UserState Variables
TBDATA,1,1,1,1,0,0,0    !Initilized SVars G11,G22,G33,G12,G13,G21
TBDATA,,0,0,0,0,0,0     !7-12   G23,G31,G32
TBDATA,,0,0,0,0,0,0         !13-18  DET_F, DET, DET_G
TBDATA,,0,0,0,0,0,0         !19-24
```

```
295 AllSEL,ALL
296
297 !       Boundary Conditions
298 lsel,s,line,,5,5,1
299 lsel,a,line,,14,15,1 !New Selections for lower number of elements
300 dl,all,,ux,0                              !Fixed Base Ux=0
301 dl,all,,uy,0                              !Fixed Base Uy=0
302 allsel,all
303
304 /title, Cushion Evolution
305 finish
306 /solu
307 antype,static
308 nlgeom,on
309 AUTOTS,ON
310 DELTIM,0.01,0.0001,0.01,OFF     !Fixed Time Step
311 rescontrol,,none
312 !cnvtol,f,,,,-1
313 physics,write,struc,struc
314 physics,clear
315 save
316 finish
317
318 !-----------Fluid Solid Interaction Loop--------------------
319 nloops = 17   !# of Fluid update loops
320 GStep = 5               !Growth Increments
321 TM = 0                                          !Initial Time
322 cmsel,s,BC_NODES,,                      !Select BC Nodes
323 *GET,F_len,NODE,,COUNT          !F_len = #BC nodes
324 *dim,NODE_F,array,F_len,3       !Array of BC Node #s
325 *dim,Shear,array,F_len,5        !Array of BC Node #s
326 *dim,TauW_Store,array,F_len,nloops
```

```
*dim,Press_Store,array,F_len,nloops

nn=0
*DO,jj,1,F_len
     *GET,NODE_F(jj,1),NODE,nn,NXTH             !Store BC Node #s
         nn = NODE_F(jj,1)
*ENDDO
!-------------------------------------------------------
!-------------------------------------------------------
*DO,i,1,nloops          !Fluid/Solid Evolution Loop

/solu
physics,read,fluid      !Read in Fluid Problem
flocheck,1                      !Initialize Fluid Problem
*IF,i,ne,1,then
flda,iter,exec,600
*ENDIF
solve                           !Solve Fluid Problem
finish
*IF,i,gt,1,THEN
/COPY,HH27_Avg_T02,rfl,,HH27_Avg_T02_%i%,rfl,,
*ENDIF
!-------------------------------------------------------------
/post1          !Store PRES and SHEAR Tractions
set,last
*DO,jj,1,F_len
*GET,NODE_F(jj,2),NODE,NODE_F(jj,1),TAUW
*GET,Press_Store(jj,i),NODE,NODE_F(jj,1),PRES
*GET,TauW_Store(jj,i),NODE,NODE_F(jj,1),TAUW
*GET,NODE_F(jj,3),NODE,NODE_F(jj,1),LOC,Y
*ENDDO
finish
```

```
!-----------------------------------------------------------
physics,read,struc                          !Resume Solid Problem
/assign,esave,struc,esav!Files Restarting nonlinear structure
/assign,emat,struc,emat
*IF,i,gt,1,then                             !Structural Restart Loop
parsave,all                                             !Save Parameters
resume                    !Resume DB - to return original node positions
parresume                                               !Resume Parameters
/prep7
antype,stat,rest
finish
*ENDIF
!---------------------------Define Cushion BC Array-----------
*DO,jj,1,F_len
        nsel,s,NODE,,NODE_F(jj,1)
        esln,s,0,ALL
        esel,r,TYPE,,3
        *GET,Shear(jj,1),ELEM,0,NUM,MAX         !Surf153 Element #
        Shear(jj,2) = TauW_Store(jj,i)          !Wall Shear Stress
        Shear(jj,3) = Press_Store(jj,i)         !Pressure
        ALLSEL,ALL
*ENDDO
!-------------------------------------------------------------
/solu

AllSEL,ALL
!---------------------------Solid - Load BCs-------------------
tt = 0                                                  !Initial Ramp increment
nRamp = 1                                               !# of Load Ramp Steps
*DO,kk,1,nRamp
    tt = 0.1*(kk)/nRamp                 !Ramp Increment
        jj = 0
```

```
391         *DO,jj,1,F_len
392 SFE,Shear(jj,1),1,PRESS,1,(kk)/(nRamp)...
393 *(Shear(jj,3)-Shear(jj,5)) + Shear(jj,5)
394 SFE,Shear(jj,1),2,PRESS,1,(kk)/(nRamp)*...
395 (Shear(jj,2)-Shear(jj,4)) + Shear(jj,4)
396         *ENDDO
397 solcontrol,ON                           !Solution Control ON
398 rescontrol,,none                        !Deny Multi-frame Restart
399 NEQIT,50,                                       !Max # NR Iterations
400 DELTIM,tt,0.00001,tt,OFF        !Fixed Time Step
401 !cnvtol,f,,,,-1                        !Force Convergence Tolerance
402 TIME,TM+tt                              !apriori Time Interval
403 OUTRES,ALL,last                        !Output ALL substep solutions
404 OUTRES,SVAR,last                    !Output ALL SVAR
405 NLDIAG,NRRE,ON                        !Nonlinear Diagnostics
406 solve
407 save
408 antype,stat,rest                      !Restart Analysis
409 *ENDDO
410 TM = TM + tt                          !Update Total Time Variable
411
412 !---------------------------Growth Deformation-------------------
413 solcontrol,off          !Solution Control Off
414 NEQIT,50,                       !Max # NR Iterations
415 rescontrol,,none        !Deny Multi-frame Restart
416 AUTOTS,ON                       !Automatic Time Increment
417 DELTIM,0.01,0.00001,0.01,OFF!Fixed Time Step Max 0.1, Min 0.0001
418 cnvtol,f,,,,-1          !Force Convergence Tolerance
419 TIME,TM + GStep         !Growth for Time = GStep
420 OUTRES,ALL,100          !Output every 10 substep solutions
421 OUTRES,SVAR,100         !Output every 10 substep solutions
422 NLDIAG,NRRE,ON          !Nonlinear Diagnostics
```

```
423 solve
424 save
425 TM = TM+GStep                              !Update Total Time Variable
426 finish
427 !------------------Store Current Load as Previous Load-----
428 *DO,jj,1,F_len
429         Shear(jj,4) = TauW_Store(jj,i)          !Wall Shear Stress
430         Shear(jj,5) = Press_Store(jj,i)         !Pressure
431 *ENDDO
432 !---------------------------Unload Solid ----------------------
433 /solu
434 AllSEL,ALL
435 antype,stat,rest                            !Restart Analysis
436 tt = 0                                              !Initial Ramp increment
437 nRamp = 1                                           !# of Load Ramp Steps
438 *DO,kk,1,nRamp
439     tt = 0.1*(kk)                           !Ramp Increment
440         jj = 0
441         *DO,jj,1,F_len
442         SFE,Shear(jj,1),1,PRESS,1,0
443         SFE,Shear(jj,1),2,PRESS,1,0
444         *ENDDO
445 solcontrol,ON                               !Solution Control ON
446 rescontrol,,none                            !Deny Multi-frame Restart
447 NEQIT,50,                                           !Max # NR Iterations
448 DELTIM,0.01,0.00001,0.01,OFF!Fixed Time Step
449 TIME,TM + tt                        !apriori Time Interval
450 OUTRES,ALL,LAST                              !Output ALL substep solutions
451 OUTRES,SVAR,LAST                        !Output ALL SVAR
452 solve
453 save
454 antype,stat,rest                            !Restart Analysis
```

```
455 *ENDDO
456 TM = TM + tt                                !Update Total Time Variable
457 finish
458 !---------------------------Morph/Remesh Fluid Domain-----------
459 /prep7
460 *if,i,ne,nloops,then
461 !0 - remesh if morph fails, 1 - remesh only, 2 - morph only
462 mkey = 1
463 damorph,2,morph_Ln_ex,mkey
464 !Morph A2 exclude "morph_Ln_ex" component lines
465 *endif
466 finish
467 !RETURN & SOLVE FLUID PROBLEM
468 *ENDDO
469
470 save
471 finish
```

Bibliography

[1] M. M. Ackermans, H. Zhou, C. E. Carels, F. A. Wagener, and J. W. Von den Hoff. Vitamin A and clefting: putative biological mechanisms. *Nutrition Reviews*, 69(10):613–624, Oct 2011.

[2] S. Al-Roubaie, E. D. Jahnsen, M. Mohammed, C. Henderson-Toth, and E. A. Jones. Rheology of embryonic avian blood. *American Journal of Physiology.Heart and Circulatory Physiology*, 301(6):H2473–81, Dec 2011.

[3] L. G. Alexopoulos, M. A. Haider, T. P. Vail, and F. Guilak. Alterations in the mechanical properties of the human chondrocyte pericellular matrix with osteoarthritis. *Journal of Biomechanical Engineering*, 125(3):323–333, Jun 2003.

[4] M. Ben Amar and A. Goriely. Growth and instability in elastic tissues. *Journal of the Mechanics and Physics of Solids*, 53(10):2284–2319, 10 2005.

[5] D. Ambrosi, G. A. Ateshian, E. M. Arruda, S. C. Cowin, J. Dumais, A. Goriely, G. A. Holzapfel, J. D. Humphrey, R. Kemkemer, E. Kuhl, J. E. Olberding, L. A. Taber, and K. Garikipati. Perspectives on biological growth and remodeling. *Journal of the Mechanics and Physics of Solids*, 59(4):863–883, Apr 1 2011.

[6] D. Ambrosi and F. Guana. Stress-modulated growth. *Mathematics and Mechanics of Solids*, 12:319–342, 2007.

[7] D. Ambrosi and A. Guillou. Growth and dissipation in biological tissues. *Continuum Mechanics and Thermodynamics*, (5):245–251, Oct 01 2007.

[8] T. Aoki, T. Ohashi, T. Matsumoto, and M. Sato. The pipette aspiration ap-

plied to the local stiffness measurement of soft tissues. *Annals of Biomedical Engineering*, 25(3):581–587, May-Jun 1997.

[9] L. Attisano, J. L. Wrana, F. Lopez-Casillas, and J. Massague. TGF-beta receptors and actions. *Biochimica et Biophysica Acta*, 1222(1):71–80, May 26 1994.

[10] M. Azhar, K. Brown, C. Gard, H. Chen, S. Rajan, D. A. Elliott, M. V. Stevens, T. D. Camenisch, S. J. Conway, and T. Doetschman. Transforming growth factor beta2 is required for valve remodeling during heart development. *Developmental Dynamics*, 240(9):2127–2141, Sep 2011.

[11] M. Azhar, R. B. Runyan, C. Gard, L. P. Sanford, M. L. Miller, A. Andringa, S. Pawlowski, S. Rajan, and T. Doetschman. Ligand-specific function of transforming growth factor beta in epithelial-mesenchymal transition in heart development. *Developmental Dynamics*, 238(2):431–442, Feb 2009.

[12] K. Balachandran, S. Hussain, C. H. Yap, M. Padala, A. H. Chester, and A. P. Yoganathan. Elevated cyclic stretch and serotonin result in altered aortic valve remodeling via a mechanosensitive 5-ht(2a) receptor-dependent pathway. *Cardiovascular Pathology*, page in press, Aug 22 2011.

[13] T. Bartman, E. C. Walsh, K. K. Wen, M. McKane, J. Ren, J. Alexander, P. A. Rubenstein, and D. Y. Stainier. Early myocardial function affects endocardial cushion development in zebrafish. *PLoS Biology*, 2(5):E129, May 2004.

[14] U. Bartram, D. G. Molin, L. J. Wisse, A. Mohamad, L. P. Sanford, T. Doetschman, C. P. Speer, R. E. Poelmann, and A. C. Gittenberger de Groot. Double-outlet right ventricle and overriding tricuspid valve

reflect disturbances of looping, myocardialization, endocardial cushion differentiation, and apoptosis in tgf-beta(2)-knockout mice. *Circulation*, 103(22):2745–2752, Jun 5 2001.

[15] L. V. Beloussov and V. I. Grabovsky. Morphomechanics: goals, basic experiments and models. *The International Journal of Developmental Biology*, 50(2-3):81–92, 2006.

[16] L. V. Beloussov and N. N. Luchinskaia. Biomechanical feedback in morphogenesis, as exemplified by stretch responses of amphibian embryonic tissues. *Biochemistry and Cell Biology*, 73(7-8):555–563, Jul-Aug 1995.

[17] LV Beloussov. *The dynamic architecture of a developing organism: an interdisciplinary approach to the development of organisms.* Kluwer, Dordrecht, 1998.

[18] S. V. Biechler, J. D. Potts, M. J. Yost, L. Junor, R. L. Goodwin, and J. W. Weidner. Mathematical modeling of flow-generated forces in an *in vitro* system of cardiac valve development. *Annals of Biomedical Engineering*, 38(1):109–117, Jan 2010.

[19] A. L. Bookout and D. J. Mangelsdorf. Quantitative real-time pcr protocol for analysis of nuclear receptor signaling pathways. *Nuclear Receptor Signaling*, 1:e012, 2003.

[20] T. Boudou, J. Ohayon, Y. Arntz, G. Finet, C. Picart, and P. Tracqui. An extended modeling of the micropipette aspiration experiment for the characterization of the young's modulus and poisson's ratio of adherent thin biological samples: numerical and experimental studies. *Journal of Biomechanics*, 39(9):1677–1685, 2006.

[21] A. S. Boyer, I. I. Ayerinskas, E. B. Vincent, L. A. McKinney, D. L. Weeks, and R. B. Runyan. Tgfbeta2 and tgfbeta3 have separate and sequential activities during epithelial-mesenchymal cell transformation in the embryonic heart. *Developmental Biology*, 208(2):530–545, Apr 15 1999.

[22] N. P. Burrows, A. C. Nicholls, J. R. Yates, G. Gatward, P. Sarathachandra, A. Richards, and F. M. Pope. The gene encoding collagen alpha1(v)(col5a1) is linked to mixed ehlers-danlos syndrome type i/ii. *The Journal of Investigative Dermatology*, 106(6):1273–1276, Jun 1996.

[23] P. R. Buskohl, J. T. Jenkins, and J. T. Butcher. Computational simulation of hemodynamic driven growth and remodeling of embryonic atrioventricular valves. *Biomechanics and Modeling of Mechanobiology*, 2013.

[24] Philip R. Buskohl, Russell A. Gould, and Jonathan T. Butcher. Quantification of embryonic atrioventricular valve biomechanics during morphogenesis. *Journal of Biomechanics*, 45(5):895–902, 3/15 2012.

[25] Philip R. Buskohl, Russell A. Gould, and Jonathan T. Butcher. Quantification of embryonic atrioventricular valve biomechanics during morphogenesis. *Journal of Biomechanics*, 45(5):895–902, 3/15 2012.

[26] J. T. Butcher, G. J. Mahler, and L. A. Hockaday. Aortic valve disease and treatment: the need for naturally engineered solutions. *Advanced Drug Delivery Reviews*, 63(4-5):242–268, Apr 30 2011.

[27] J. T. Butcher and R. R. Markwald. Valvulogenesis: the moving target. *Philosophical Transactions of the Royal Society of London.Series B, Biological Sciences*, 362(1484):1489–1503, Aug 29 2007.

[28] J. T. Butcher, T. C. McQuinn, D. Sedmera, D. Turner, and R. R. Markwald. Transitions in early embryonic atrioventricular valvular function correspond with changes in cushion biomechanics that are predictable by tissue composition. *Circulation Research*, 100(10):1503–1511, May 25 2007.

[29] T. D. Camenisch, D. G. Molin, A. Person, R. B. Runyan, A. C. Gittenberger de Groot, J. A. McDonald, and S. E. Klewer. Temporal and distinct tgf-beta ligand requirements during mouse and avian endocardial cushion morphogenesis. *Developmental Biology*, 248(1):170–181, Aug 1 2002.

[30] Q. Chen, H. Chen, D. Zheng, C. Kuang, H. Fang, B. Zou, W. Zhu, G. Bu, T. Jin, Z. Wang, X. Zhang, J. Chen, L. J. Field, M. Rubart, W. Shou, and Y. Chen. Smad7 is required for the development and function of the heart. *The Journal of Biological Chemistry*, 284(1):292–300, Jan 2 2009.

[31] Y. N. Chiu, R. A. Norris, G. Mahler, A. Recknagel, and J. T. Butcher. Transforming growth factor beta, bone morphogenetic protein, and vascular endothelial growth factor mediate phenotype maturation and tissue remodeling by embryonic valve progenitor cells: Relevance for heart valve tissue engineering. *Tissue Engineering.Part A*, 16(11):3375–85, Jul 14 2010.

[32] D. S. Choi, S. J. Ward, N. Messaddeq, J. M. Launay, and L. Maroteaux. 5-ht2b receptor-mediated serotonin morphogenetic functions in mouse cranial neural crest and myocardiac cells. *Development*, 124(9):1745–1755, May 1997.

[33] C. J. Chuong and Y. C. Fung. On residual stresses in arteries. *Journal of Biomechanical Engineering*, 108(2):189–192, May 1986.

[34] S. Cleja-Tigoiu and G. Maugin. Eshelby's stress tensors in finite elasto-plasticity. *Acta Mechanica*, 139:231–249, 2000.

[35] M. D. Combs and K. E. Yutzey. Heart valve development: regulatory networks in development and disease. *Circulation Research*, 105(5):408–421, Aug 28 2009.

[36] S. C. Cowin and W. C. Van Buskirk. Surface bone remodeling induced by a medullary pin. *Journal of Biomechanics*, 12(4):269–276, 1979.

[37] B. J. Damon, M. C. Remond, M. R. Bigelow, T. C. Trusk, W. Xie, R. Perucchio, D. Sedmera, S. Denslow, and R. P. Thompson. Patterns of muscular strain in the embryonic heart wall. *Developmental Dynamic*, 238(6):1535–1546, Jun 2009.

[38] M. V. Danilchik, E. E. Brown, and K. Riegert. Intrinsic chiral properties of the xenopus egg cortex: an early indicator of left-right asymmetry? *Development*, 133(22):4517–4526, Nov 2006.

[39] M. G. Davey and C. Tickle. The chicken as a model for embryonic development. *Cytogenetic and Genome Research*, 117(1-4):231–239, 2007.

[40] F. J. de Lange, A. F. Moorman, R. H. Anderson, J. Manner, A. T. Soufan, C. de Gier-de Vries, M. D. Schneider, S. Webb, M. J. van den Hoff, and V. M. Christoffels. Lineage and morphogenetic analysis of the cardiac valves. *Circulation Research*, 95(6):645–654, Sep 17 2004.

[41] A. DiCarlo. *Surface and Bulk Growth Unified*, pages 53–64. Mechanics of Material Forces. Advances in Mechanics and Mathematics. Springer, 2005.

[42] Antonia DiCarlo and Sara Quiligotti. Growth and balance. *Mechanics Research Communications*, 29:449, 2002.

[43] H. C. Dietz, G. R. Cutting, R. E. Pyeritz, C. L. Maslen, L. Y. Sakai, G. M. Corson, E. G. Puffenberger, A. Hamosh, E. J. Nanthakumar, and S. M. Curristin. Marfan syndrome caused by a recurrent de novo missense mutation in the fibrillin gene. *Nature*, 352(6333):337–339, Jul 25 1991.

[44] S. Disatian and E. C. Orton. Autocrine serotonin and transforming growth factor beta 1 signaling mediates spontaneous myxomatous mitral valve disease. *The Journal of Heart Valve Disease*, 18(1):44–51, Jan 2009.

[45] H. Dolk, M. Loane, and E. Garne. The prevalence of congenital anomalies in europe. *Advances in Experimental Medicine and Biology*, 686:349–364, 2010.

[46] L. M. Eisenberg and R. R. Markwald. Molecular regulation of atrioventricular valvuloseptal morphogenesis. *Circulation Research*, 77(1):1–6, Jul 1995.

[47] I. El-Hamamsy, K. Balachandran, M. H. Yacoub, L. M. Stevens, P. Sarathchandra, P. M. Taylor, A. P. Yoganathan, and A. H. Chester. Endothelium-dependent regulation of the mechanical properties of aortic valve cusps. *Journal of the American College of Cardiology*, 53(16):1448–1455, Apr 21 2009.

[48] C. S. Elangbam, L. E. Job, L. M. Zadrozny, J. C. Barton, L. W. Yoon, L. D. Gates, and N. Slocum. 5-hydroxytryptamine (5ht)-induced valvulopathy: compositional valvular alterations are associated with 5ht2b receptor and 5ht transporter transcript changes in Sprague-Dawley rats. *Experimental and Toxicologic Pathology*, 60(4-5):253–262, Aug 2008.

[49] M. Epstein and G. A. Maugin. Thermomechanics of volumetric growth

in uniform bodies. *International Journal of Plasticity*, 16(7-8):951–978, 6/1 2000.

[50] J. D. Eshelby. The force on an elastic singularity. *Phil. Trans. Roy. Soc. Lond.*, A244:87–112, 1951.

[51] J. D. Eshelby. *Energy relations and the energy -momentum tensor in continuum mechanics*, volume A244 of *Inelastic Behavior of Solids*, pages 77–114. McGraw-Hill, New York, 1970.

[52] J.D. Eshelby. The elastic field of a crack extending non-uniformly under general anti-plane loading. *Journal of the Mechanics and Physics of Solids*, 17(3):177 – 199, 1969.

[53] E. A. Evans and R. Waugh. Osmotic correction to elastic area compressibility measurements on red cell membrane. *Biophysical Journal*, 20(3):307–313, Dec 1977.

[54] A. K. Ewart, C. A. Morris, D. Atkinson, W. Jin, K. Sternes, P. Spallone, A. D. Stock, M. Leppert, and M. T. Keating. Hemizygosity at the elastin locus in a developmental disorder, Williams syndrome. *Nature Genetics*, 5(1):11–16, Sep 1993.

[55] A. S. Forouhar, M. Liebling, A. Hickerson, A. Nasiraei-Moghaddam, H. J. Tsai, J. R. Hove, S. E. Fraser, M. E. Dickinson, and M. Gharib. The embryonic vertebrate heart tube is a dynamic suction pump. *Science*, 312(5774):751–753, May 5 2006.

[56] J. Fu, Y. K. Wang, M. T. Yang, R. A. Desai, X. Yu, Z. Liu, and C. S. Chen. Mechanical regulation of cell function with geometrically modulated elastomeric substrates. *Nature Methods*, 7(9):733–736, Sep 2010.

[57] T. Fukumoto, R. Blakely, and M. Levin. Serotonin transporter function is an early step in left-right patterning in chick and frog embryos. *Developmental Neuroscience*, 27(6):349–363, 2005.

[58] Y. C. Fung. What are the residual stresses doing in our blood vessels? *Annals of Biomedical Engineering*, 19(3):237–249, 1991.

[59] Y. C. Fung and S. Q. Liu. Change of residual strains in arteries due to hypertrophy caused by aortic constriction. *Circulation Research*, 65(5):1340–1349, Nov 1989.

[60] YC Fung. *Biomechanics: Motion, Flow, Stress, and Growth*. Springer, New York, 1990.

[61] L. Fusi, A. Farina, and D. Ambrosi. Mathematical modeling of a solid-liquid mixture with mass exchange between constituents. *Mathematics and Mechanics of Solids*, 11:575, 2006.

[62] J. F. Ganghoffer. Mechanical modeling of growth considering domain variationpart ii: Volumetric and surface growth involving eshelby tensors. *Journal of the Mechanics and Physics of Solids*, 58(9):1434–1459, 9 2010.

[63] K. Garikipati, E. M. Arruda, K. Grosh, H. Narayanan, and S. Calve. A continuum treatment of growth in biological tissue: mass transport coupled with mechanics. *Journal of the Mechanics and Physics of Solids*, 52(7):1595–1625, 2004.

[64] K. K. Garikipati, H. Narayanan, EM Arruda, K. Grosh, and S. Calve. *Material forces in the context of biotissue remodelling*, volume 11 of *Mechanics of Material Forces*. Springer, 2005.

[65] I. H. Gessner, A. E. Lorincz, and H. Bostrom. Acid mucopolysaccharide content of the cardiac jelly of the chick embryo. *The Journal of Experimental Zoology*, 160(3):291–298, Dec 1965.

[66] R. L. Gleason and J. D. Humphrey. A 2D constrained mixture model for arterial adaptations to large changes in flow, pressure and axial stretch. *Mathematical Medicine and Biology*, 22(4):347–369, Dec 2005.

[67] A. Gonzalez-Sanchez and D. Bader. *In vitro* analysis of cardiac progenitor cell differentiation. *Developmental Biology*, 139(1):197–209, May 1990.

[68] J. A. Goodship, D. Hall, A. Topf, C. Mamasoula, H. Griffin, T. J. Rahman, E. Glen, H. Tan, J. Palomino Doza, C. L. Relton, J. Bentham, S. Bhattacharya, C. Cosgrove, D. Brook, J. Granados-Riveron, F. A. Bu'lock, J. O'Sullivan, A. G. Stuart, J. Parsons, H. J. Cordell, and B. Keavney. A common variant in the ptpn11 gene contributes to the risk of tetralogy of fallot. *Circulation Cardiovascular Genetics*, 5(3):287–292, Jun 1 2012.

[69] B. C. Groenendijk, B. P. Hierck, J. Vrolijk, M. Baiker, M. J. Pourquie, A. C. Gittenberger de Groot, and R. E. Poelmann. Changes in shear stress-related gene expression after experimentally altered venous return in the chicken embryo. *Circulation Research*, 96(12):1291–1298, Jun 24 2005.

[70] C. Guilluy, M. Rolli-Derkinderen, P. L. Tharaux, G. Melino, P. Pacaud, and G. Loirand. Transglutaminase-dependent rhoa activation and depletion by serotonin in vascular smooth muscle cells. *The Journal of Biological Chemistry*, 282(5):2918–2928, Feb 2 2007.

[71] V. Gupta and K. J. Grande-Allen. Effects of static and cyclic loading in

regulating extracellular matrix synthesis by cardiovascular cells. *Cardiovascular Research*, 72(3):375–383, Dec 1 2006.

[72] B. I. Gustafsson, K. Tommeras, I. Nordrum, J. P. Loennechen, A. Brunsvik, E. Solligard, R. Fossmark, I. Bakke, U. Syversen, and H. Waldum. Long-term serotonin administration induces heart valve disease in rats. *Circulation*, 111(12):1517–1522, Mar 29 2005.

[73] S. Hafizi, P. M. Taylor, A. H. Chester, S. P. Allen, and M. H. Yacoub. Mitogenic and secretory responses of human valve interstitial cells to vasoactive agents. *The Journal of Heart Valve Disease*, 9(3):454–458, May 2000.

[74] TP Harrigan and JJ Hamilton. An analytical and numerical study of the stability of bone remodeling theories: dependence on microstructural stimulus. *Journal of Biomechanics*, 25(5):477–488, 1992.

[75] RT Hart. A theoretical study of the influence of bone maturation rate on surface remodeling predictions: idealized models. *Journal of Biomechanics*, 23(3):241, 1990.

[76] O. Hauso, B. I. Gustafsson, J. P. Loennechen, A. K. Stunes, I. Nordrum, and H. L. Waldum. Long-term serotonin effects in the rat are prevented by terguride. *Regulatory Peptides*, 143(1-3):39–46, Oct 4 2007.

[77] J. I. Hoffman and S. Kaplan. The incidence of congenital heart disease. *Journal of the American College of Cardiology*, 39(12):1890–1900, Jun 19 2002.

[78] B. Hogers, M. C. DeRuiter, A. C. Gittenberger de Groot, and R. E. Poelmann. Unilateral vitelline vein ligation alters intracardiac blood flow patterns and morphogenesis in the chick embryo. *Circulation Research*, 80(4):473–481, Apr 1997.

[79] J. R. Hove, R. W. Koster, A. S. Forouhar, G. Acevedo-Bolton, S. E. Fraser, and M. Gharib. Intracardiac fluid forces are an essential epigenetic factor for embryonic cardiogenesis. *Nature*, 421(6919):172–177, Jan 9 2003.

[80] N. Hu and E. B. Clark. Hemodynamics of the stage 12 to stage 29 chick embryo. *Circulation Research*, 65(6):1665–1670, Dec 1989.

[81] N. Hu, D. M. Connuck, B. B. Keller, and E. B. Clark. Diastolic filling characteristics in the stage 12 to 27 chick embryo ventricle. *Pediatric Research*, 29(4 Pt 1):334–337, Apr 1991.

[82] J. D. Humphrey and K. R. Rajagopal. A constrained mixture model for arterial adaptations to a sustained step change in blood flow. *Biomechanics and Modeling in Mechanobiology*, 2(2):109–126, Nov 2003.

[83] J. M. Hurle, J. M. Icardo, and J. L. Ojeda. Compositional and structural heterogenicity of the cardiac jelly of the chick embryo tubular heart: a TEM, SEM and histochemical study. *Journal of Embryology and Experimental Morphology*, 56:211–223, Apr 1980.

[84] F. Jaffre, P. Bonnin, J. Callebert, H. Debbabi, V. Setola, S. Doly, L. Monassier, B. Mettauer, B. C. Blaxall, J. M. Launay, and L. Maroteaux. Serotonin and angiotensin receptors in cardiac fibroblasts coregulate adrenergic-dependent cardiac hypertrophy. *Circulation Research*, 104(1):113–123, Jan 2 2009.

[85] M. Jastrzebska, J. Zalewska-Rejdak, I. Mroz, B. Barwinski, R. Wrzalik, A. Kocot, and J. Nozynski. Atomic force microscopy and ft-ir spectroscopy investigations of human heart valves. *General Physiology and Biophysics*, 25(3):231–244, Sep 2006.

[86] B. Jian, J. Xu, J. Connolly, R. C. Savani, N. Narula, B. Liang, and R. J. Levy. Serotonin mechanisms in heart valve disease I: serotonin-induced up-regulation of transforming growth factor-beta1 via g-protein signal transduction in aortic valve interstitial cells. *The American Journal of Pathology*, 161(6):2111–2121, Dec 2002.

[87] R. B. Hinton Jr, G. H. Deutsch, J. M. Pearl, H. H. Hobart, C. A. Morris, and D. W. Benson. Bilateral semilunar valve disease in a child with partial deletion of the williams-beuren syndrome region is associated with elastin haploinsufficiency. *The Journal of Heart Valve Disease*, 15(3):352–355, May 2006.

[88] R. B. Hinton Jr, J. Lincoln, G. H. Deutsch, H. Osinska, P. B. Manning, D. W. Benson, and K. E. Yutzey. Extracellular matrix remodeling and organization in developing and diseased aortic valves. *Circulation Research*, 98(11):1431–1438, Jun 9 2006.

[89] B. B. Keller, N. Hu, P. J. Serrino, and E. B. Clark. Ventricular pressure-area loop characteristics in the stage 16 to 24 chick embryo. *Circulation Research*, 68(1):226–231, Jan 1991.

[90] C. B. Kern, R. A. Norris, R. P. Thompson, W. S. Argraves, S. E. Fairey, L. Reyes, S. Hoffman, R. R. Markwald, and C. H. Mjaatvedt. Versican proteolysis mediates myocardial regression during outflow tract development. *Developmental Dynamics*, 236(3):671–683, Mar 2007.

[91] S. M. Klisch, T. J. Van Dyke, and A. Hoger. A theory of volumetric growth for compressible elastic biological materials. *Mathematics and Mechanics of Solids*, 6:551, 2001.

[92] S. M. Klisch and A. Hoger. Volumetric growth of thermoelastic materials and mixtures. *Mathematics and Mechanics of Solids*, 8:377–402, 2003.

[93] V. K. Krishnamurthy, F. Guilak, D. A. Narmoneva, and R. B. Hinton. Regional structure-function relationships in mouse aortic valve tissue. *Journal of Biomechanics*, 44(1):77–83, Jan 4 2011.

[94] B. P. Kruithof, S. A. Krawitz, and V. Gaussin. Atrioventricular valve development during late embryonic and postnatal stages involves condensation and extracellular matrix remodeling. *Developmental Biology*, 302(1):208–217, Feb 1 2007.

[95] K. E. Kubow, E. Klotzsch, M. L. Smith, D. Gourdon, W. C. Little, and V. Vogel. Crosslinking of cell-derived 3d scaffolds up-regulates the stretching and unfolding of new extracellular matrix assembled by reseeded cells. *Integrative Biology*, 1(11-12):635–648, Dec 2009.

[96] E. J. Lammer, J. S. Chak, D. M. Iovannisci, K. Schultz, K. Osoegawa, W. Yang, S. L. Carmichael, and G. M. Shaw. Chromosomal abnormalities among children born with conotruncal cardiac defects. *Birth Defects Research Part A, Clinical and Molecular Teratology*, 85(1):30–35, Jan 2009.

[97] D. J. Lanska. Chapter 29: historical aspects of the major neurological vitamin deficiency disorders: overview and fat-soluble vitamin A. *Handbook of Clinical Neurology*, 95:435–444, 2010.

[98] O. Latinovic, L. A. Hough, and H. Daniel Ou-Yang. Structural and micromechanical characterization of type I collagen gels. *Journal of Biomechanics*, 43(3):500–505, Feb 10 2010.

[99] J. M. Lauder. Neurotransmitters as morphogens. *Progress in Brain Research*, 73:365–387, 1988.

[100] J. M. Lauder, M. B. Wilkie, C. Wu, and S. Singh. Expression of 5-ht(2a), 5-ht(2b) and 5-ht(2c) receptors in the mouse embryo. *International Journal of Developmental Neuroscience*, 18(7):653–662, Nov 2000.

[101] EH Lee. Elastic-plastic deformation at finite strain. *Journal of Applied Mechanics*, 36(1), 1969.

[102] W. R. Legant, J. S. Miller, B. L. Blakely, D. M. Cohen, G. M. Genin, and C. S. Chen. Measurement of mechanical tractions exerted by cells in three-dimensional matrices. *Nature Methods*, 7(12):969–971, Dec 2010.

[103] W. R. Legant, A. Pathak, M. T. Yang, V. S. Deshpande, R. M. McMeeking, and C. S. Chen. Microfabricated tissue gauges to measure and manipulate forces from 3d microtissues. *Proceedings of the National Academy of Sciences of the United States of America*, 106(25):10097–10102, Jun 23 2009.

[104] C. A. Lemmon, C. S. Chen, and L. H. Romer. Cell traction forces direct fibronectin matrix assembly. *Biophysical Journal*, 96(2):729–738, Jan 2009.

[105] M. Levin, G. A. Buznikov, and J. M. Lauder. Of minds and embryos: left-right asymmetry and the serotonergic controls of pre-neural morphogenesis. *Developmental Neuroscience*, 28(3):171–185, 2006.

[106] D. Y. Li, A. E. Toland, B. B. Boak, D. L. Atkinson, G. J. Ensing, C. A. Morris, and M. T. Keating. Elastin point mutations cause an obstructive vascular disease, supravalvular aortic stenosis. *Human Molecular Genetics*, 6(7):1021–1028, Jul 1997.

[107] R. M. Liberfarb and A. Goldblatt. Prevalence of mitral-valve prolapse in the stickler syndrome. *American Journal of Medical Genetics*, 24(3):387–392, Jul 1986.

[108] I. E. Lin and L. A. Taber. A model for stress-induced growth in the developing heart. *Journal of Biomechanical Engineering*, 117(3):343–349, Aug 1995.

[109] J. Lincoln, C. M. Alfieri, and K. E. Yutzey. Development of heart valve leaflets and supporting apparatus in chicken and mouse embryos. *Developmental Dynamics*, 230(2):239–250, Jun 2004.

[110] J. Lincoln, J. B. Florer, G. H. Deutsch, R. J. Wenstrup, and K. E. Yutzey. Colva1 and colxia1 are required for myocardial morphogenesis and heart valve development. *Developmental Dynamics*, 235(12):3295–3305, Dec 2006.

[111] S. E. Lindsey and J. T. Butcher. The cycle of form and function in cardiac valvulogenesis. *Aswan Heart Centre Science & Practice Series*, 2(10), 2011.

[112] S. Q. Liu and Y. C. Fung. Material coefficients of the strain energy function of pulmonary arteries in normal and cigarette smoke-exposed rats. *Journal of Biomechanics*, 26(11):1261–1269, 11 1993.

[113] Y. Liu, L. Wei, D. L. Laskin, and B. L. Fanburg. Role of protein transamidation in serotonin-induced proliferation and migration of pulmonary artery smooth muscle cells. *American Journal of Respiratory Cell and Molecular Biology*, 44(4):548–55, Jun 17 2010.

[114] V. A. Lubarda and A. Hoger. On the mechanics of solids with a growing mass. *International Journal of Solids and Structures*, 39(18):4627–4664, 9 2002.

[115] J. Manner. Cardiac looping in the chick embryo: a morphological review with special reference to terminological and biomechanical aspects of the looping process. *Anatomical Record*, 259:248, 2000.

[116] J. Massague and Y. G. Chen. Controlling TGF-beta signaling. *Genes and Development*, 14(6):627–644, Mar 15 2000.

[117] G. A. Maugin. *Material Inhomogeneities in Elasticity*. Chapman & Hall, London, first edition, 1993.

[118] A. Mekontso-Dessap, F. Brouri, O. Pascal, P. Lechat, N. Hanoun, L. Lanfumey, I. Seif, N. Benhaiem-Sigaux, M. Kirsch, M. Hamon, S. Adnot, and S. Eddahibi. Deficiency of the 5-hydroxytryptamine transporter gene leads to cardiac fibrosis and valvulopathy in mice. *Circulation*, 113(1):81–89, Jan 3 2006.

[119] P. Merlob, E. Birk, L. Sirota, N. Linder, M. Berant, B. Stahl, and G. Klinger. Are selective serotonin reuptake inhibitors cardiac teratogens? echocardiographic screening of newborns with persistent heart murmur. *Birth Defects Research.Part A, Clinical and Molecular Teratology*, 85(10):837–841, Oct 2009.

[120] W. D. Merryman, P. D. Bieniek, F. Guilak, and M. S. Sacks. Viscoelastic properties of the aortic valve interstitial cell. *Journal of Biomechanical Engineering*, 131(4):041005, Apr 2009.

[121] W. D. Merryman, H. D. Lukoff, R. A. Long, G. C. Engelmayr Jr, R. A. Hopkins, and M. S. Sacks. Synergistic effects of cyclic tension and transforming growth factor-beta1 on the aortic valve myofibroblast. *Cardiovascular Pathology*, 16(5):268–276, Sep-Oct 2007.

[122] F. A. Millan, F. Denhez, P. Kondaiah, and R. J. Akhurst. Embryonic gene expression patterns of TGF beta 1, beta 2 and beta 3 suggest different developmental functions *in vivo*. *Development*, 111(1):131–143, Jan 1991.

[123] C. E. Miller, R. P. Thompson, M. R. Bigelow, G. Gittinger, T. C. Trusk, and D. Sedmera. Confocal imaging of the embryonic heart: how deep? *Microscopy and Microanalysis*, 11(3):216–223, Jun 2005.

[124] L. A. Miller. Fluid dynamics of ventricular filling in the embryonic heart. *Cell Biochemistry and Biophysics*, 61(1):33–45, Sep 2011.

[125] J. R. Moiseiwitsch and J. M. Lauder. Serotonin regulates mouse cranial neural crest migration. *Proceedings of the National Academy of Sciences of the United States of America*, 92(16):7182–7186, Aug 1 1995.

[126] L. Monassier, M. A. Laplante, T. Ayadi, S. Doly, and L. Maroteaux. Contribution of gene-modified mice and rats to our understanding of the cardiovascular pharmacology of serotonin. *Pharmacology and Therapeutics*, 128(3):559–567, Dec 2010.

[127] J. J. Munoz, V. Conte, and M. Miodownik. Stress-dependent morphogenesis: continuum mechanics and truss systems. *Biomechanics and Modeling in Mechanobiology*, 9(4):451–467, Aug 2010.

[128] B. R. Munson, D. F. Young, and T. H. Okiishi. *Fundamentals of Fluid Dynamics*. John Wiley & Sons, USA, 4th edition, 2002.

[129] Y. Nakajima, K. Miyazono, M. Kato, M. Takase, T. Yamagishi, and H. Nakamura. Extracellular fibrillar structure of latent TGF beta binding protein-1: role in TGF beta-dependent endothelial-mesenchymal transfor-

mation during endocardial cushion tissue formation in mouse embryonic heart. *The Journal of Cell Biology*, 136(1):193–204, Jan 13 1997.

[130] C. G. Nebigil, P. Hickel, N. Messaddeq, J. L. Vonesch, M. P. Douchet, L. Monassier, K. Gyorgy, R. Matz, R. Andriantsitohaina, P. Manivet, J. M. Launay, and L. Maroteaux. Ablation of serotonin 5-ht(2b) receptors in mice leads to abnormal cardiac structure and function. *Circulation*, 103(24):2973–2979, Jun 19 2001.

[131] N. L. Nerurkar, A. Ramasubramanian, and L. A. Taber. Morphogenetic adaptation of the looping embryonic heart to altered mechanical loads. *Developmental Dynamics*, 235(7):1822–1829, Jul 2006.

[132] R. A. Newbury-Ecob, R. Leanage, J. A. Raeburn, and I. D. Young. Holt-oram syndrome: a clinical genetic study. *Journal of Medical Genetics*, 33(4):300–307, Apr 1996.

[133] R. A. Norris, R. A. Moreno-Rodriguez, Y. Sugi, S. Hoffman, J. Amos, M. M. Hart, J. D. Potts, R. L. Goodwin, and R. R. Markwald. Periostin regulates atrioventricular valve maturation. *Developmental Biology*, 316(2):200–213, Apr 15 2008.

[134] R. A. Norris, J. D. Potts, M. J. Yost, L. Junor, T. Brooks, H. Tan, S. Hoffman, M. M. Hart, M. J. Kern, B. Damon, R. R. Markwald, and R. L. Goodwin. Periostin promotes a fibroblastic lineage pathway in atrioventricular valve progenitor cells. *Developmental Dynamics*, 238(5):1052–1063, May 2009.

[135] G. M. Odell, G. Oster, P. Alberch, and B. Burnside. The mechanical basis of morphogenesis. I Epithelial folding and invagination. *Developmental Biology*, 85:446–462, 1981.

[136] T. Ohashi, H. Abe, T. Matsumoto, and M. Sato. Pipette aspiration technique for the measurement of nonlinear and anisotropic mechanical properties of blood vessel walls under biaxial stretch. *Journal of Biomechanics*, 38(11):2248–2256, Nov 2005.

[137] T. Olsson and A. Klarbring. Residual stresses in soft tissue as a consequence of growth and remodeling: application to an arterial geometry. *European Journal of Mechanics A*, 27(6):959–974, 0 2008.

[138] M. A. Oyama and R. J. Levy. Insights into serotonin signaling mechanisms associated with canine degenerative mitral valve disease. *Journal of Veterinary Internal Medicine*, 24(1):27–36, Jan-Feb 2010.

[139] L. M. Pavone, A. Spina, S. Rea, D. Santoro, V. Mastellone, P. Lombardi, and L. Avallone. Serotonin transporter gene deficiency is associated with sudden death of newborn mice through activation of TGF-beta1 signalling. *Journal of Molecular and Cellular Cardiology*, 47(5):691–697, Nov 2009.

[140] A. D. Person, S. E. Klewer, and R. B. Runyan. Cell biology of cardiac cushion development. *International Review of Cytology*, 243:287–335, 2005.

[141] C. K. Phoon. Circulatory physiology in the developing embryo. *Current Opinion in Pediatrics*, 13(5):456–464, Oct 2001.

[142] G. D. Pins, D. L. Christiansen, R. Patel, and F. H. Silver. Self-assembly of collagen fibers. Influence of fibrillar alignment and decorin on mechanical properties. *Biophysical Journal*, 73(4):2164–2172, Oct 1997.

[143] J. D. Potts and R. B. Runyan. Epithelial-mesenchymal cell transformation in the embryonic heart can be mediated, in part, by transforming growth factor beta. *Developmental Biology*, 134(2):392–401, Aug 1989.

[144] J. D. Potts, E. B. Vincent, R. B. Runyan, and D. L. Weeks. Sense and antisense TGF beta 3 mrna levels correlate with cardiac valve induction. *Developmental Dynamics*, 193(4):340–345, Apr 1992.

[145] R. E. Pyeritz. The marfan syndrome. *Annual Review of Medicine*, 51:481–510, 2000.

[146] X. Qi, G. Yang, L. Yang, Y. Lan, T. Weng, J. Wang, Z. Wu, J. Xu, X. Gao, and X. Yang. Essential role of smad4 in maintaining cardiomyocyte proliferation during murine embryonic heart development. *Developmental Biology*, 311(1):136–146, Nov 1 2007.

[147] A. Rachev and R. L. Gleason Jr. Theoretical study on the effects of pressure-induced remodeling on geometry and mechanical nonhomogeneity of conduit arteries. *Biomechanics and Modeling in Mechanobiology*, 10(1):79–93, Feb 2011.

[148] K. R. Rajagopal and A. R. Srinivasa. A thermodynamic frame work for rate type fluid models. *Journal of Non-Newtonian Fluid Mechanics*, 88:207–227, 2000.

[149] A. Ramasubramanian, N. L. Nerurkar, K. H. Achtien, B. A. Filas, D. A. Voronov, and L. A. Taber. On modeling morphogenesis of the looping heart following mechanical perturbations. *Journal of Biomechanical Engineering*, 130(6):061018, Dec 2008.

[150] A. Ramasubramanian and L. A. Taber. Computational modeling of morphogenesis regulated by mechanical feedback. *Biomechanics and Modeling in Mechanobiology*, 7(2):77–91, Apr 2008.

[151] M. D. Reller, M. J. Strickland, T. Riehle-Colarusso, W. T. Mahle, and A. Correa. Prevalence of congenital heart defects in metropolitan atlanta, 1998-2005. *The Journal of Pediatrics*, 153(6):807–813, Dec 2008.

[152] O. W. Richards and A. J. Kavanagh. The analysis of the relative growth gradients and changing form of growing organisms. *The American Naturalist*, 77(772):385–399, 1943.

[153] H. E. Ritchie, P. D. Brown-Woodman, and A. Korabelnikoff. Effect of co-administration of retinoids on rat embryo development *in vitro*. *Birth Defects Research.Part A, Clinical and Molecular Teratology*, 67(6):444–451, Jun 2003.

[154] E. K. Rodriguez, A. Hoger, and A. D. McCulloch. Stress-dependent finite growth in soft elastic tissues. *Journal of Biomechanics*, 27(4):455–467, Apr 1994.

[155] V. L. Roger, A. S. Go, D. M. Lloyd-Jones, R. J. Adams, J. D. Berry, T. M. Brown, M. R. Carnethon, S. Dai, G. de Simone, E. S. Ford, C. S. Fox, H. J. Fullerton, C. Gillespie, K. J. Greenlund, S. M. Hailpern, J. A. Heit, P. M. Ho, V. J. Howard, B. M. Kissela, S. J. Kittner, D. T. Lackland, J. H. Lichtman, L. D. Lisabeth, D. M. Makuc, G. M. Marcus, A. Marelli, D. B. Matchar, M. M. McDermott, J. B. Meigs, C. S. Moy, D. Mozaffarian, M. E. Mussolino, G. Nichol, N. P. Paynter, W. D. Rosamond, P. D. Sorlie, R. S. Stafford, T. N. Turan, M. B. Turner, N. D. Wong, J. Wylie-Rosett, on behalf of the American Heart Association Statistics Committee, and Stroke Statistics Subcommittee. Heart disease and stroke statistics–2011 update: A report from the american heart association. *Circulation*, Dec 15 2010.

[156] B. L. Roth, D. L. Willins, K. Kristiansen, and W. K. Kroeze. 5-

hydroxytryptamine2-family receptors (5-hydroxytryptamine2a, 5-hydroxytryptamine2b, 5-hydroxytryptamine2c): where structure meets function. *Pharmacology and Therapeutics*, 79(3):231–257, Sep 1998.

[157] K. J. Rothman, L. L. Moore, M. R. Singer, U. S. Nguyen, S. Mannino, and A. Milunsky. Teratogenicity of high vitamin A intake. *The New England Journal of Medicine*, 333(21):1369–1373, Nov 23 1995.

[158] T. W. Sadler. Selective serotonin reuptake inhibitors (SSRIs) and heart defects: Potential mechanisms for the observed associations. *Reproductive Toxicology*, 32(4):484–9, Sep 24 2011.

[159] A. Santhanakrishnan and L. A. Miller. Fluid dynamics of heart development. *Cell Biochemistry and Biophysics*, 61(1):1–22, Sep 2011.

[160] F. M. Sasoglu, A. J. Bohl, and B. E. Layton. Design and microfabrication of a high-aspect-ratio PDMS microbeam array for parallel nanonewton force measurement and protein printing. *Journal of Micromechanics and Microengineering*, 17(3):623, 2007.

[161] M. Sato, D. P. Theret, L. T. Wheeler, N. Ohshima, and R. M. Nerem. Application of the micropipette technique to the measurement of cultured porcine aortic endothelial cell viscoelastic properties. *Journal of Biomechanical Engineering*, 112(3), Aug 1990.

[162] P. J. Scambler. The 22q11 deletion syndromes. *Human Molecular Genetics*, 9(16):2421–2426, Oct 2000.

[163] J. A. Schroeder, L. F. Jackson, D. C. Lee, and T. D. Camenisch. Form and function of developing heart valves: coordination by extracellular matrix

and growth factor signaling. *Journal of Molecular Medicine*, 81(7):392–403, Jul 2003.

[164] D. Sedmera, T. Pexieder, V. Rychterova, N. Hu, and E. B. Clark. Remodeling of chick embryonic ventricular myoarchitecture under experimentally changed loading conditions. *The Anatomical Record*, 254(2):238–252, Feb 1 1999.

[165] Y. Shi and J. Massague. Mechanisms of TGF-beta signaling from cell membrane to the nucleus. *Cell*, 113(6):685–700, Jun 13 2003.

[166] WK Silk and RO Erickson. Kinematics of plant growth. *Journal of Theoretical Biology*, 76:481–501, 1979.

[167] S. Sivanandam, J. S. Glickstein, B. F. Printz, L. D. Allan, K. Altmann, D. E. Solowiejczyk, L. Simpson, A. Perez-Delboy, and C. S. Kleinman. Prenatal diagnosis of conotruncal malformations: diagnostic accuracy, outcome, chromosomal abnormalities, and extracardiac anomalies. *American Journal of Perinatology*, 23(4):241–245, May 2006.

[168] R. Skalak, G. Dasgupta, M. Moss, E. Otten, P. Dullemeijer, and H. Vilmann. Analytical description of growth. *Journal of Theoretical Biology*, 94:555–577, 1982.

[169] R. Skalak, S. Zargaryan, RK Jain, PA Netti, and A. Hoger. Compatibility and the genesis of residual stress by volumetric growth. *Journal of Mathematical Biology*, 34:889–914, 1996.

[170] M. L. Smith, D. Gourdon, W. C. Little, K. E. Kubow, R. A. Eguiluz, S. Luna-Morris, and V. Vogel. Force-induced unfolding of fibronectin in the extracellular matrix of living cells. *PLoS Biology*, 5(10):e268, Oct 2 2007.

[171] P. Snider, R. B. Hinton, R. A. Moreno-Rodriguez, J. Wang, R. Rogers, A. Lindsley, F. Li, D. A. Ingram, D. Menick, L. Field, A. B. Firulli, J. D. Molkentin, R. Markwald, and S. J. Conway. Periostin is required for maturation and extracellular matrix stabilization of noncardiomyocyte lineages of the heart. *Circulation Research*, 102(7):752–760, Apr 11 2008.

[172] L. A. Taber. Biomechanics of growth, remodeling, and morphogenesis. *Applied Mechanics Reviews*, 48:487–545, 1995.

[173] L. A. Taber. Theoretical study of beloussov's hyper-restoration hypothesis for mechanical regulation of morphogenesis. *Biomechanics and Modeling in Mechanobiology*, 7(6):427–441, Dec 2008.

[174] L. A. Taber. Towards a unified theory for morphomechanics. *Philosophical Transactions.Series A, Mathematical, physical, and engineering sciences*, 367(1902):3555–3583, Sep 13 2009.

[175] L. A. Taber and D. W. Eggers. Theoretical study of stress-modulated growth in the aorta. *Journal of Theoretical Biology*, 180(4):343–357, Jun 21 1996.

[176] L. A. Taber and J. D. Humphrey. Stress-modulated growth, residual stress, and vascular heterogeneity. *Journal of Biomechanical Engineering*, 123(6):528–535, Dec 2001.

[177] L. A. Taber, D. A. Voronov, and A. Ramasubramanian. The role of mechanical forces in the torsional component of cardiac looping. *Annals of the New York Academy of Sciences*, 1188:103–110, Feb 2010.

[178] L. A. Taber, J. Zhang, and R. Perucchio. Computational model for the

transition from peristaltic to pulsatile flow in the embryonic heart tube. *Journal of Biomechanical Engineering*, 129(3):441–449, Jun 2007.

[179] J. L. Tan, J. Tien, D. M. Pirone, D. S. Gray, K. Bhadriraju, and C. S. Chen. Cells lying on a bed of microneedles: an approach to isolate mechanical force. *Proceedings of the National Academy of Sciences of the United States of America*, 100(4):1484–1489, Feb 18 2003.

[180] D. P. Theret, M. J. Levesque, M. Sato, R. M. Nerem, and L. T. Wheeler. The application of a homogeneous half-space model in the analysis of endothelial cell micropipette measurements. *Journal of Biomechanical Engineering*, 110(3):190–199, Aug 1988.

[181] V. Todorovic, E. Finnegan, L. Freyer, L. Zilberberg, M. Ota, and D. B. Rifkin. Long form of latent tgf-beta binding protein 1 (ltbp1l) regulates cardiac valve development. *Developmental Dynamics*, 240(1):176–187, Jan 2011.

[182] J. Vermot, A. S. Forouhar, M. Liebling, D. Wu, D. Plummer, M. Gharib, and S. E. Fraser. Reversing blood flows act through klf2a to ensure normal valvulogenesis in the developing heart. *PLoS Biology*, 7(11):e1000246, Nov 2009.

[183] M. von Dassow, J. A. Strother, and L. A. Davidson. Surprisingly simple mechanical behavior of a complex embryonic tissue. *PloS One*, 5(12):e15359, Dec 28 2010.

[184] N. J. Waitzman, P. S. Romano, and R. M. Scheffler. Estimates of the economic costs of birth defects. *Inquiry*, 31(2):188–205, Summer 1994.

[185] G. A. Walker, K. S. Masters, D. N. Shah, K. S. Anseth, and L. A. Leinwand. Valvular myofibroblast activation by transforming growth factor-beta: implications for pathological extracellular matrix remodeling in heart valve disease. *Circulation Research*, 95(3):253–260, Aug 6 2004.

[186] J. N. Warnock, C. A. Gamez, S. A. Metzler, J. Chen, S. H. Elder, and J. Liao. Vasoactive agents alter the biomechanical properties of aortic heart valve leaflets in a time-dependent manner. *The Journal of Heart Valve Disease*, 19(1):86–95; discussion 96, Jan 2010.

[187] S. W. Watts, J. R. Priestley, and J. M. Thompson. Serotonylation of vascular proteins important to contraction. *PloS One*, 4(5):e5682, May 25 2009.

[188] G. Xu, P. S. Kemp, J. A. Hwu, A. M. Beagley, P. V. Bayly, and L. A. Taber. Opening angles and material properties of the early embryonic chick brain. *Journal of Biomechanical Engineering*, 132(1):011005, Jan 2010.

[189] J. Xu, B. Jian, R. Chu, Z. Lu, Q. Li, J. Dunlop, S. Rosenzweig-Lipson, P. McGonigle, R. J. Levy, and B. Liang. Serotonin mechanisms in heart valve disease II: the 5-ht2 receptor and its signaling pathway in aortic valve interstitial cells. *The American Journal of Pathology*, 161(6):2209–2218, Dec 2002.

[190] S. Yabanoglu, M. Akkiki, M. H. Seguelas, J. Mialet-Perez, A. Parini, and N. Pizzinat. Platelet derived serotonin drives the activation of rat cardiac fibroblasts by 5-ht2a receptors. *Journal of Molecular and Cellular Cardiology*, 46(4):518–525, Apr 2009.

[191] H. C. Yalcin, A. Shekhar, T. C. McQuinn, and J. T. Butcher. Hemodynamic

patterning of the avian atrioventricular valve. *Developmental Dynamics*, 240(1):23–35, Jan 2011.

[192] H. C. Yalcin, A. Shekhar, N. Nishimura, A. A. Rane, C. B. Schaffer, and J. T. Butcher. Two-photon microscopy guided femtosecond-laser photoablation of avian cardiogenesis: Noninvasive creation of localized heart defects. *American Journal of Physiology:Heart and Circulatory Physiology*, Aug 13 2010.

[193] M. S. Yavarone, D. L. Shuey, H. Tamir, T. W. Sadler, and J. M. Lauder. Serotonin and cardiac morphogenesis in the mouse embryo. *Teratology*, 47(6):573–584, Jun 1993.

[194] E. A. Zamir and L. A. Taber. On the effects of residual stress in microindentation tests of soft tissue structures. *Journal of Biomechanical Engineering*, 126(2):276–283, Apr 2004.

[195] R. Zhao, K. L. Sider, and C. A. Simmons. Measurement of layer-specific mechanical properties in multilayered biomaterials by micropipette aspiration. *Acta Biomaterialia*, 7(3):1220–1227, Mar 2011.

[196] R. Zhao, K. Wyss, and C. A. Simmons. Comparison of analytical and inverse finite element approaches to estimate cell viscoelastic properties by micropipette aspiration. *Journal of Biomechanics*, 42(16):2768–2773, Dec 11 2009.

[197] M. H. Zile. Vitamin A-not for your eyes only: requirement for heart formation begins early in embryogenesis. *Nutrients*, 2(5):532–550, May 2010.